DEPARTMENT OF PHYSICS

Effects of Electrical Resistivity on Fast Electron Transport in Relativistic Laser-Solid Interactions

by

David Andrew MacLellan

in partial fulfilment of the requirements for the degree of
Doctor of Philosophy in Physics

2014

Copyright Declaration

Signed:

Date:

For my family.

Abstract

This thesis reports on experimental and numerical investigations of relativistic electron transport in solids irradiated by intense (i.e. $I_L > 10^{19}$ Wcm^{-2}) laser pulses. Specifically, the effect of electrical resistivity on fast electron transport is explored.

The first investigation explores fast electron transport in allotropes of carbon by measuring the spatial-intensity distribution of the beam of protons accelerated from the target rear-surface. An analytical model is developed which accounts for the rear-surface fast electron sheath dynamics, ionisation and projection of the resulting beam of protons, and is used (in conjunction with the experimental measurements) to infer annular fast electron beam transport with filamentary structure in 200 μm-thick diamond targets. The important role that material lattice structure has in defining electrical resistivity, which in turn defines the fast electron transport properties, is established utilising three-dimensional hybrid particle-in-cell (3D hybrid-PIC) simulations together with an analytical model of the resistive filamentation instability.

The second investigation explores fast electron transport in silicon utilising both experimental measurements and 3D hybrid-PIC simulations. Annular fast electron transport is demonstrated and explained by resistively generated magnetic fields. The results indicate the potential to completely transform the beam transport pattern by tailoring the resistivity-temperature profile at temperatures as low as a few eV. Additionally, the sensitivity of annular fast electron beam transport is explored by varying the drive laser pulse parameters (i.e. energy, focal spot radius and pulse duration) and is found to be particularly sensitive to the peak laser pulse intensity. An ability to optically 'tune' the properties of an annular fast electron transport pattern may be important for applications.

In the final investigation the effect that initial target temperature, and thus lattice melt, has on fast electron transport properties is demonstrated. Laser-accelerated proton beams are used to isochorically heat silicon for several tens-of-picoseconds prior to the propagation of fast electrons through the pre-heated target. This enables the influence of resistivity gradients, generated by proton-induced lattice melt, on fast electron transport properties to be explored. The experimental observation of an annular proton beam after $t_{heat} = 30$ ps of proton pre-heating, which corresponds to annular electron transport within the target, is in excellent qualitative agreement with 3-D hybrid-PIC simulations of fast electron transport in a target containing an initial temperature (and thus, resistivity) gradient.

Acknowledgements

As scientists we draw our pleasure from making new discoveries, in doing so uncovering a fresh understanding of nature. To paraphrase a famous physicist, we don't do research only for the practical results. However, I have come to the conclusion that scientific discovery comes second to the relationships and friendships built with your colleagues and collaborators. Indeed, in my opinion, a project as challenging as a PhD would not be a complete experience without these relationships; it would certainly not be as much fun! To this end, there are a number of people who deserve immense thanks.

Firstly, my supervisor Prof. Paul McKenna deserves the most thanks. He has consistently provided me with advice, guidance, encouragement and support. Moreover, his continual pursuit of the highest standard of scientific excellence has been inspiring. From him I have learned perhaps the two most important skills that a scientist should possess: 1) asking the correct questions; and, 2) communicating the answers clearly and effectively.

Next, to my friends with whom I've worked most closely in both the laboratory and office. To Ross – it's been a genuine pleasure to study and work with you all these long years, and a privilege to watch you develop from a student into a physicist of the highest calibre. To David – your meticulous attention to detail and extensive knowledge of laser-plasma physics have been so important. To Haydn – your skill in the lab and general banter have been excellent; TAP experiments just won't be the same without us arguing in the chamber! A big thanks also to all the other researchers I've had the pleasure of working with over the years – you know who you are! Additionally, the world-class expertise at the Central Laser Facility has made all of this work possible – thanks!

Finally, and most importantly, to my friends and family. To my parents, Andy and Karen, sister Charlene, and brother Calum. Without you, I wouldn't be where I am today. You've encouraged me every step of the way, challenging me continually and providing every possible form of support. I hope that this thesis gives you even a small appreciation of how much you mean to me. Here's to all the future holds!

Role of the author

The results presented in this thesis are the work of the author over several experimental campaigns, performed as part of a team of researchers led by Prof. McKenna. The author was involved at each step: experimental planning and execution, data analysis, numerical simulations and interpretation of results. In addition, the author, together with Prof. McKenna, led the preparation of the publications arising from this work, with input from co-authors.

Chapter 5: The author actively contributed to the planning and execution of the experiment. The proton dosimetry film stacks were designed, assembled and scanned by the author, in addition to other diagnostics. The author took a leading role in the analysis of all data. The analytical model used to estimate the proton spatial intensity distribution from the TNSA electric field distribution was based on a code originally written by Dr. M. N. Quinn (University of Strathclyde), and subsequently developed by the author. The calculation of the carbon resistivity curves was performed by Dr M. P. Desjarlais, Sandia National Laboratory. The 3D hybrid-PIC simulations were performed by the author under the supervision of Dr. A. P. L Robinson and Prof. P. McKenna.

Chapter 6: The author actively contributed to the planning and execution of the experimental campaign as Deputy Target Area Operator. The author was responsible for installing and running the RCF film stack detectors, in addition to other diagnostics and operator duties. The author took a leading role in the analysis of all data. The calculation of the silicon resistivity curve was performed by Dr. M. P. Desjarlais, Sandia National Laboratory. The 3D hybrid-PIC simulations were performed by the author under the supervision of Dr. A. P. L. Robinson and Prof. P. McKenna.

Chapter 7: The author actively contributed to the planning and execution of the experiment. The proton dosimetry film stacks were designed, assembled and scanned by the author, in addition to other diagnostics. The author took a leading role in the analysis of all data. The calculation of the disordered silicon resistivity curve was performed by Dr M. P. Desjarlais, Sandia National Laboratory. The 1D hydrodynamic and 3D hybrid-PIC simulations were performed by the author under the supervision of Dr. A. P. L Robinson and Prof. P. McKenna.

List of publications

Publications directly resulting from the work presented in this thesis

1. **"Annular fast electron transport in silicon arising from low-temperature resistivity"**.
   D. A. MacLellan, D. C. Carroll, R. J. Gray, N. Booth, M. Burza, M. P. Desjarlais, F. Du, B. Gonzalez-Izquierdo, D. Neely, H. W. Powell, A. P. L. Robinson, D. R. Rusby, G. G. Scott, X. H. Yuan, C.-G. Wahlström, and P. McKenna, *Physical Review Letters*, **111**, 095001, (2013).

2. **"Tunable mega-Ampere electron current propagation in solids by dynamic control of lattice melt"**.
   D. A. MacLellan, D. C. Carroll, R. J. Gray, N. Booth, M. Burza, M. P. Desjarlais, F. Du, D. Neely, H. W. Powell, A. P. L. Robinson, G. G. Scott, X. H. Yuan, C.-G. Wahlström, and P. McKenna, *Physical Review Letters*, At press (2014).

3. **"The influence of laser-drive parameters on annular fast electron transport in silicon"**.
   D. A. MacLellan, D. C. Carroll, R. J. Gray, A. P. L. Robinson, M. P. Desjarlais, D. Neely and P. McKenna, *Plasma Physics and Controlled Fusion*, **56**, 084002 (2014).

4. **"Fast electron transport patterns in intense laser-irradiated solids diagnosed by modelling measured multi-MeV proton beams"**.
   D. A. MacLellan, D. C. Carroll, R. J. Gray, N. Booth, B. Gonzalez-Izquierdo, H. W. Powell, G. G. Scott, D. Neely and P. McKenna, *Laser and Particle Beams*, **31**, 475-480, (2013)

5. **"Effects of target pre-heating and expansion on terahertz radiation production from intense laser-solid interactions"**.
   X. H. Yuan, Y. Fang, D. C. Carroll, **D. A. MacLellan**, F. Du, N. Booth, M. Burza, M. Chen, R. J. Gray, Y. F. Jin. Y. T. Li, Y. Liu, D. Neely, H. W. Powell, G. G. Scott, C.-G. Wahlström, J. Zhang, P. McKenna and Z. M. Sheng, *High Power Laser Science and Engineering*, **2**, e5, (2014)

Additional publications resulting from PhD work

1. **"Multi-pulse enhanced laser ion acceleration using plasma half cavity targets"**.
   G. G. Scott, J. S. Green, V. Bagnoud, C. Brabetz, C. M. Brenner, D. C. Carroll, **D. A. MacLellan**, A. P. L. Robinson, M. Roth, C. Spindloe, F. Wagner, B. Zielbauer, P. McKenna and D. Neely, *Applied Physics Letters*, **101**, 024101, (2012).

2. **"Injection and transport properties of fast electrons in ultraintense laser-solid interactions."**.
   M. Coury, D. C. Carroll, A. P. L. Robinson, X. H. Yuan, C. M. Brenner, M. Burza, R. J. Gray, K. L. Lancaster, Y. T. Li, X. X. Lin, **D. A. MacLellan**, H. W. Powell, M. N. Quinn, O. Tresca, C.-G. Wahlström, D. Neely, and P. McKenna, *Physics of Plasmas*, **20**, 043104, (2013).

3. **"Single shot, temporally and spatially resolved measurements of fast electron dynamics using a chirped optical probe"**.
   J. S. Green, C. D. Murphy, N. Booth, R. J. Dance, R. J. Gray, **D. A. MacLellan**, P. McKenna, D. Rusby and L. Wilson, *Journal of Instrumentation*, **9**, P03003, (2014).

4. **"High efficiency proton beam generation through target thickness control in femtosecond laser-plasma interactions"**.
   J. S. Green, A. P. L. Robinson, N. Booth, D. C. Carroll, R. J. Dance, R. J. Gray, **D. A. MacLellan**, P. McKenna, C. D. Murphy, D. Rusby, and L. Wilson, *Applied Physics Letters* **104**, 214101(2014).

5. **"Modified thomson spectrometer design for high enegy, multi-species ion sources"**.
   D. Gwynne, S. Kar, D. Doria, H. Ahmed, M. Cherchez, J. Fernandez, R. J. Gray, J. S. Green, F. Hanton, **D. A. MacLellan**, P. McKenna, Z. Najmudin, D. Neely, J. A. Ruiz, M. Streeter, M. Swantusch, O. Willi, M. Zepf, and M. Borghesi, *Review Scientific Instruments*, **85**, 033304, (2014).

6. **"Azimuthal asymmetry in collective electron dynamics in relativistically transparent laserfoil interactions"**.
   R. J. Gray, **D. A. MacLellan**, B. Gonzalez-Izquierdo, H. W. Powell, D. C. Carroll, C. D. Murphy, L. Stockhausen, D. R. Rusby, G. G. Scott, R. Wilson, N. Booth, D. R. Symes, S. J. Hawkes, R. Torres, M. Borghesi, D. Neely, and P. McKenna, *New Journal of Physics*, **16** 093027, (2014).

7. **"Enhancement of ion acceleration in the multi-pulse regime"**.
   H. W. Powell, R. J. Gray, M. King, **D. A. MacLellan**, B. Gonzalez-Izquierdo, D. C. Carroll, L. Stockhausen, D. R. Rusby, R. Torres, N. Dover, Z. Najmudin, G. Hicks, R. Wilson, N. Booth, M. Borghesi, D. Neely, and P. McKenna,, *Submitted*, (2014).

Contents

List of Figures

Chapter 1

Introduction

1.1 History and Motivation

When Theodore Maiman produced the first laser light using a ruby crystal and flashlamp in 1960 [1], building upon the previously demonstrated *maser* developed in the early 1950's [2], he could have been forgiven for not fully appreciating the extent to which his discovery would revolutionise both fundamental physics and modern technology. Indeed, at the time he remarked that "the laser is a solution looking for a problem[3]." The unique properties of laser light, namely it's monochromaticity, coherency and high directionality (in addition to high brightness), have enabled it's use in a startlingly broad and diverse range of applications; from optical devices (e.g. CD players), industrial applications (e.g. welding and laser cutting) to medical applications (e.g. surgical incisions and cauterisation) and fundamental physics (e.g. laser cooling for creation of Bose-Einstein condensates [4]). The laser has become ubiquitous in modern times — no longer can it be considered a "solution looking for a problem".

Building upon the initial demonstration by Maiman, researchers quickly developed and improved the original laser design; the demonstration of Q-switching in 1961 [5] ushered in the generation of laser pulses with kilo-Joule energies and nanosecond duration, while the development of mode-locking in 1964 enabled pulses of ultra-short duration to be generated (i.e. 10^{-15} s) [6]. The development of such laser pulses initiated the growth of a new field of physics: exploring the

interaction of intense laser pulses with matter. This burgeoning field of intense laser-solid (or, more generally, laser-plasma) interactions, whilst active in the late 1970's and early 1980's, primarily explored laser-matter interactions at intensities of $10^{14} - 10^{16}$ Wcm^{-2} [7–9]. However, the field made a considerable leap forward in 1985 with the invention of the technique chirped pulse amplification [10] which enabled laser intensities to increase from the order of 10^{15} Wcm^{-2} to $> 10^{20}$ Wcm^{-2} in as little as a decade. In recent years, a wide variety of high intensity lasers are available, each possessing a wide range of pulse properties. For example, the Astra-Gemini and Vulcan lasers at the Rutherford Appleton Laboratory both produce high intensity pulses but with distinct pulse parameters; the former delivers tens-of-femtosecond (i.e. 4×10^{-14} s) pulses of 15 J energy, while the latter produces picosecond duration (i.e. 10^{-12} s) pulses with 500 J of energy — operating close to their peak intensities, these lasers generate pulses with intensities close to 10^{21} Wcm^{-2}.

Such rapid developments in laser technology have stimulated significant research effort devoted to understanding and optimising two particular applications of high intensity lasers interacting with dense plasma: 1) inertial confinement fusion; and 2) laser-driven ion acceleration. This thesis explores physics relevant to both of these applications.

1. Inertial confinement fusion

The use of lasers to drive a controlled nuclear fusion reaction, while suggested in the 1960's [11], was most popularly proposed by Nuckolls *et al.* [12] in 1972, although the idea originated from a series of meetings in 1957 which explored peaceful applications of nuclear energy, chaired by Edward Teller [13]. In contrast to the other most common technique by which controlled nuclear fusion is realised (i.e. magnetic confinement fusion, in which a toroidal-shaped plasma is maintained at low density and high pressure by strong magnetic fields in a device known as a tokamak) laser-driven nuclear fusion involves heating and compressing a millimetre-sized pellet of fuel by intense laser pulses. The scheme relies on the requirement that the inward inertia of the fuel pellet, generated as the

incident lasers ablate material from the capsule surface, compresses the fuel – the fuel subsequently burns (i.e. ignites), releasing more energy than was used to compress it, before the target has time to disassemble. Thus, laser-driven fusion is known as inertial confinement fusion (ICF).

In the original scheme proposed by Nuckolls *et al.*, intense lasers (of UV or X-ray wavelength) are used to heat and compress a spherical fuel capsule, a method known as 'hot-spot' direct-drive ICF. This capsule consists of an outer ablator shell and an inner region containing cryogenic deuterium-tritium (DT) fuel. The laser is incident onto the surface of the fuel pellet (i.e. the ablator shell), resulting in heating and expansion of the ablator material. Due to momentum conservation, this outward expansion produces a corresponding rocket-like inward acceleration of the fuel, resulting in significant compression. As the interior fuel compresses, the fuel exhibits two distinct regions: 1) a central 'hot spot' containing $\sim 2-5\%$ of the main fuel mass; and 2) a dense (i.e. 1000 gcm^{-3}), relatively cold region constituting the remaining fuel mass [14] - see Fig. 1.1(a). Thus, direct-drive ICF is referred to as isobaric compression [15]. However, due to the nanosecond duration of the laser pulses used to drive the compression phase [12] the subsequent implosion dynamics of the fuel occur on hydrodynamical timescales. This invariably results in the growth of instabilities (particularly the Rayleigh-Taylor class of instabilities [16]) which lead to the degradation of the confinement process, thereby reducing the efficiency of the fusion reaction.

The invention of the CPA technique [10] enabled the generation of high intensity lasers (i.e. $I_L > 10^{18}$ Wcm^{-2}), delivered in an ultrashort pulse of picosecond to several tens-of-femtosecond duration. This innovation provided the method by which an alternative approach to controlled thermonuclear fusion was proposed: fast ignition ICF. First suggested by Tabak *et al.* [17] in 1994, the fast ignition (FI) ICF scheme separates the compression and ignition phases of the fusion process by utilising a secondary high intensity laser to initiate the fusion reaction – the igniter beam. The fuel is initially compressed, in much the same way as in conventional direct-drive ICF, but the generation of a central hot-spot (as in direct-drive ICF) is not necessary (the hot spot is typically produced off-centre –

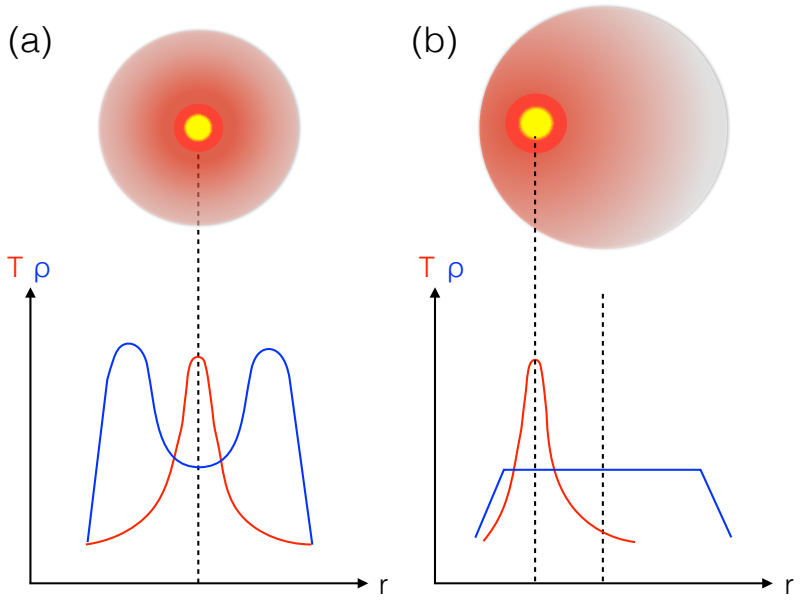

Figure 1.1: Schematic picture of the temperature and density as a function of radius for: (a) 'hot-spot' ICF; and (b) fast ignition ICF.

see Fig. 1.1(b)) and thus the density requirements are relaxed, from 1000 gcm^{-3} for direct-drive ICF to a uniform (i.e. isochoric) value of 300 gcm^{-3} for FI – the density and temperature profiles of hot-spot direct-drive and fast ignition ICF schemes are shown in Fig. 1.1(a) and (b) respectively.

The vital stage of the FI process involves an intense laser (of estimated energy $\sim$ 100 kJ and 10 ps duration [18]) injected into the pre-compressed fuel. This intense laser couples it's energy into the generation of a population of 'fast' (i.e. moving close to the speed of light) electrons which propagate to the high-density core and deliver the 'spark' that ignites the fusion process. This process is shown schematically in Fig. 1.2(a).

The advantages of fast ignition over conventional (i.e. 'hot-spot') ICF arise from the reduction in fuel compression required. The isochoric compression characteristic of FI means that more fuel mass can be compressed to a much lower average density than in conventional ICF. The consequence is that both a higher fusion gain can be achieved in conjunction with a reduction of the overall laser energy required for compression. In addition, FI is less susceptible to hydrodynamic instabilities (e.g. Rayleigh-Taylor instabilities) due to being less dependent on compression symmetry, together with a uniformly lower density.

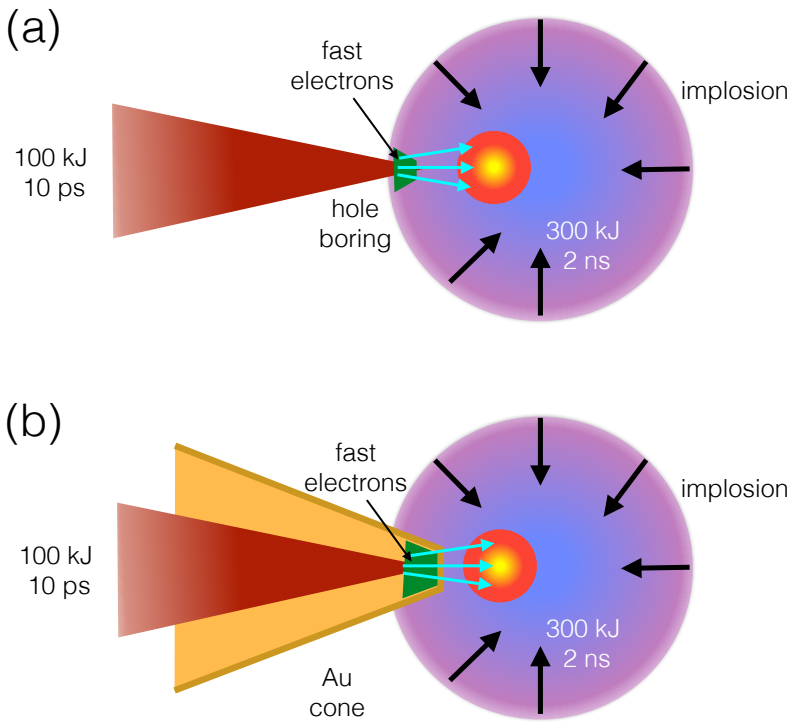

Figure 1.2: The fast ignition approach to ICF: (a) hole-boring fast ignition; and (b) cone-guided fast ignition.

The main challenge of the FI scheme involves the delivery of energy from the high intensity ignitor pulse via the generation and transport of fast electrons to the compressed fuel. The fast electrons (which ignite the fusion process via their energy deposition in the compressed DT fuel) must propagate through 100 - 300 μm of compressed fuel to the ignition region. Thus, efficient transfer of this energy is critical to achieving ignition. There are currently two main techniques proposed to do this: hole boring and cone-guided FI.

Hole-boring FI involves the direct interaction of the ignitor pulse with the compressed fuel, shown schematically in Fig. 1.2(a). However, due to the low-density plasma surrounding the fuel the laser is susceptible to propagation losses and deflection arising from instabilities in this region [19]. In order to minimise beam energy loss in the low-density plasma region encasing the fuel, the innovative technique of cone-guided FI was proposed [20], shown schematically in Fig. 1.2(b). In this scheme, a hollow guiding cone (typically of high Z material e.g. gold) is embedded within the fuel capsule. The high intensity pulse is then focussed into

the gold cone (thereby avoiding the low-density plasma) and the fast electrons are generated by the interaction of the ignitor pulse with the tip of the cone. The first proof-of-principle experimental demonstration of cone-guided ignition was made by Kodama *et al.* in 2002 [21], in which increased rates of fusion reactions (indicated by an enhanced neutron yield) occurred when the ignition pulse was fired in conjunction with compression.

Since the fast electrons are generated at the tip of the cone, the transport properties of electrons through both the cone tip and compressed fuel to the ignition region, typically a 'stand-off' distance of 100 - 300 μm [22], is of vital importance to FI. Thus, new schemes have been proposed to control the fast electron transport by embedding structures within the cone tip. For example, the 'magnetic switchyard' approach may offer an increase in coupling efficiency to the fuel core [23]. Therefore, a better understanding of the conditions which determine, and techniques which control, the transport of fast electrons in dense plasmas will have a direct influence on optimising the fast ignition approach to ICF.

2. Laser-driven ion acceleration

In addition to ICF, a particularly unique application of laser-solid interactions is the generation of energetic ions (i.e. MeV energies) from solids irradiated by intense laser pulses. While early observations were made of energetic ions (sub-MeV energies) arising from solids irradiated by moderated intensity CO_2 lasers [24, 25], the high intensity regime heralded by CPA lasers has enabled laser-driven ion sources of unprecedented energy and beam quality to be produced [26–30]. For current laser intensities ($> 10^{19}$ Wcm^{-2}) the dominant acceleration mechanism is target normal sheath acceleration (TNSA) [31].

The acceleration of these ions arises from strong electric fields, created by fast electron sheaths generated at the solid's surfaces. The strength of such electric sheath fields are on the order of TV/m, large enough to ionise atoms on the target surface and accelerate them to multi-MeV/nucleon energies. Since the ions originate from the action of the sheath field, the properties of the ion beam

are a direct consequence of this field evolution, which in turn is directly affected by the fast electron propagation inside the target.

The ion beams produced in laser-solid interactions have particularly noteworthy properties, including high energy [32], low emittance [33], high laminarity and directionality, and find application in a wide range of fields, from ion sources for proton oncology [34] to proton driven fast ignition ICF [35] and high energy density investigations [36]. Therefore, improvement in our understanding and control of the propagation of fast electrons inside the target will have a direct impact on the quality of the sheath-accelerated ion beam for such applications.

1.2 Fast electron transport

As has been discussed, the controlled generation and transport of mega-Ampère currents of fast electrons in intense laser-solid interactions is particularly important for applications such as fast ignition ICF and laser-driven ion sources.

One of the unresolved issues critical to the realisation and optimisation of these applications is the extent to which cold material properties influence electron transport properties. In recent years, work has investigated fast electron transport in metals and plastics [37, 38], concluding that transport in conductors and insulators is different; this has been generally attributed to differences in room temperature resistivity (i.e. availability of free electrons)[37] between different materials.

However, a recent investigation by McKenna *et al.* [39] offered a radically new insight into material effects on fast electron transport. By investigating fast electron transport in various carbon samples, McKenna *et al.* demonstrated that fast electron transport is strongly affected by the material's lattice structure, via the role that lattice structure has in defining resistivity, which in turn governs the development of self-generated resistive magnetic fields which can influence the fast electron beam propagation.

During an intense laser-solid interaction, a fraction of the incident laser energy is converted into the generation of energetic (i.e. 'fast') electrons. To enable

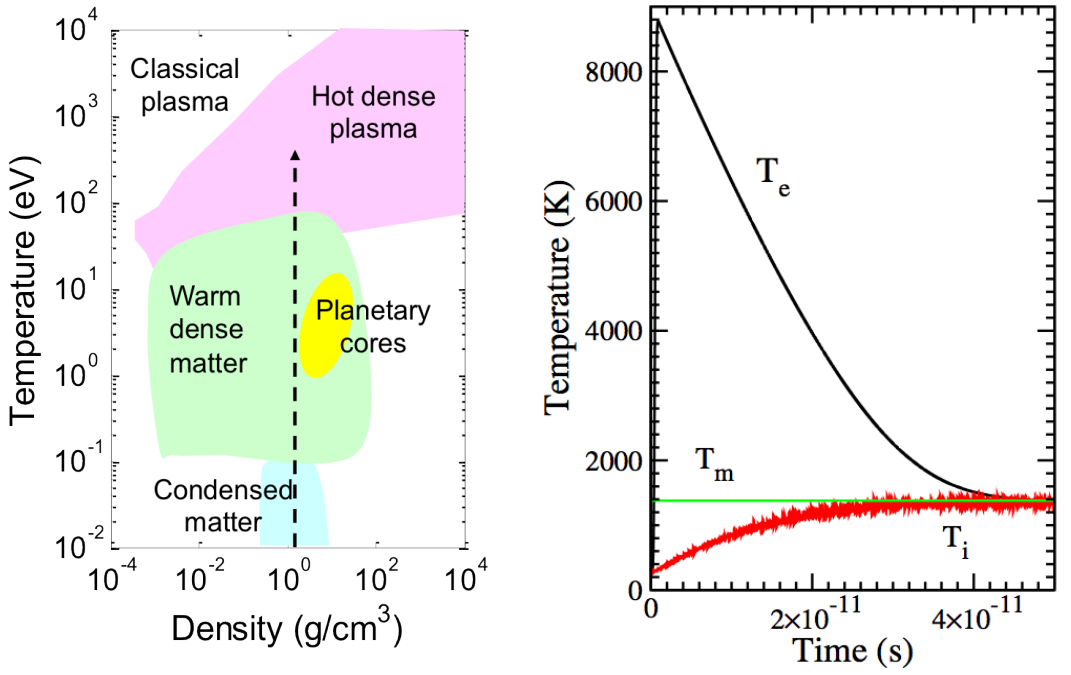

Figure 1.3: Transient states induced during intense laser-solid interactions: (a) ultrafast isochoric heating drives a transition between cold solid to hot plasma; and (b) electron-ion equilibration time, extracted from Mazevet *et al.* [40].

propagation of these electrons, a return current is drawn from the background material. The action of this return current is to neutralise the fast electron beam current such that propagation into the dense material is possible. One of the key properties of the return current electrons is that they are highly collisional and rapidly, on a femtosecond timescale, heat the background material to very high temperatures – the material subsequently undergoes a transition from cold solid to hot plasma (see Fig. 1.3(a)).

The timescale of return current heating (i.e. femtoseconds) is considerably shorter than typical hydrodynamic timescales (i.e. nanoseconds), and thus the bulk target material undergoes electron-driven heating to high temperatures (i.e. $\sim$ 1 - 100 eV) while temporarily remaining at solid density (i.e. isochoric heating). Key to the physics of this transient state of matter is the electron-ion equilibrium time. During the heating process, the background target electrons undergo heating on a femtosecond timescale, while the background ions typically take considerably longer to experience significant heating; the electrons (due to

their smaller mass) experience the heating first and subsequently mediate their energy to the background ions, with both populations eventually reaching thermal equilibrium on timescales typically of the order of tens-of-picoseconds [40] (see Fig. 1.3(b)). Therefore, for electron transport driven by sub-picosecond laser pulses, the material's lattice temporarily retains its cold-state structure while the background electrons are thermally excited.

In the work presented by McKenna *et al.* [39] it was the lattice structure in this transient 'warm dense matter' (WDM) regime that defined the material's resistivity, which subsequently determined the global fast electron transport properties. Indeed, the quite remarkable observation of smooth, uniform electron beam transport in diamond (a room-temperature insulator) — smooth transport is characteristic of metals; insulators typically exhibit disrupted beam transport [37] — was attributed to the metallic-like resistivity of diamond at temperatures in the region of 1 - 10 eV, which is directly correlated with the transient well-ordered diamond lattice structure.

This crucial revelation re-opens the debate on the extent to which material properties influence fast electron transport. To obtain a clearer understanding of the fundamental relationship between material properties and fast electron transport, this thesis presents several experimental and numerical investigations of fast electron transport in solids, specifically focussing on the role that low-temperature (i.e. 1 - 60 eV) electrical resistivity has on the transport properties of the fast electron beam.

This thesis consists of eight chapters, summarised as follows:

- **Chapter 2:** Discusses the basic physics of laser-plasma interactions.
- **Chapter 3:** Describes the detailed physics of fast electron transport, providing a detailed discussion of resistivity models and magnetic field generation.
- **Chapter 4:** Presents the experimental and numerical techniques used to investigate fast electron transport in solids.

- **Chapter 5:** Fast electron transport in carbon is explored in this chapter via experimental measurements, analytical modelling and numerical simulation results.

- **Chapter 6:** Investigations of fast electron transport properties in silicon are presented in this chapter using a combination of experimental measurements and 3-D hybrid PIC simulations.

- **Chapter 7:** The role of target temperature gradients, induced by proton-heating, on fast electron transport in silicon is explored in this chapter. Experimental results are presented, along with hydrodynamic modelling of proton-heating in silicon. Finally, 3-D hybrid PIC simulations are used to interpret the experimental measurements.

- **Chapter 8:** Summarises the results of the investigations presented in Chapter 5, 6 and 7. Potential directions for future research are discussed.

Chapter 2

Fundamentals of Laser-Plasma Interactions

2.1 Introduction

The interaction of a sufficiently high intensity laser pulse with a solid target results in ionisation of the material, leading to the formation of a plasma − this state plays a key role in defining the physics of laser absorption and in the subsequent generation of energetic particles (e.g. hot, 'fast' electrons and multi-MeV ions). Therefore it is important to understand the underlying physics of laser-plasma interactions to enable a deeper understanding of the source of these.

In this chapter, the physics of laser-plasma interactions is presented by exploring electron dynamics and the mechanisms governing energetic electron generation in intense (i.e. $I_L > 10^{18}$ Wcm^{-2}) laser-solid interactions. This creates an important foundation to aid understanding of the physics presented in the results sections of Chapter's 5, 6 and 7.

2.2 Electron motion in an electromagnetic field

2.2.1 Describing an electromagnetic wave

Fundamentally, laser-solid interactions involve electron dynamics (i.e. acceleration) in an electromagnetic field. The action of the field (i.e. laser pulse) is to liberate electrons through the process of ionisation, and subsequently accelerate them. Thus, the relation between the fields and particles underpins the related physical processes.

An electromagnetic wave can be described by it's vector potential $\mathbf{A}(z,t)$, where the electromagnetic wave (i.e. laser pulse) propagates in the $\hat{\mathbf{e}}_z$ direction (i.e. longitudinal z-direction), is linearly polarised in the $\hat{\mathbf{e}}_x$ direction (i.e. the electric field is orientated in the transverse x-direction) and the magnetic field is orientated along the $\hat{\mathbf{e}}_y$-direction. The vector potential is given by:

$$\mathbf{A}(z,t) = \hat{\mathbf{e}}_x \cdot A_0 \sin(k_L z - \omega_L t) \tag{2.1}$$

where $k_L = 2\pi n/\lambda_L$ is the wavenumber of the laser, ω_L is the laser frequency, $\lambda_L = 2\pi c/\omega_L$ (where c is the speed of light) is the wavelength of the laser and n is the refractive index of the medium through which the electromagnetic wave propagates.

Assuming that there is no external electrostatic potential, the electric, $\mathbf{E}$, and magnetic, $\mathbf{B}$, fields are given by:

$$\mathbf{E} = -\frac{\partial \mathbf{A}}{\partial t} = \mathbf{E_0} \cos(k_L z - \omega_L t) \tag{2.2}$$

$$\mathbf{B} = \nabla \times \mathbf{A} = \mathbf{B_0} \cos(k_L z - \omega_L t) \tag{2.3}$$

where $\mathbf{E_0} = \omega_L A_0 \hat{\mathbf{e}}_x$ and $\mathbf{B_0} = k_L A_0 \hat{\mathbf{e}}_y$. Note that the fields are orientated orthogonal to each other according to the relation $|B_0| = \frac{1}{c}|E_0|$.

In vacuum (i.e. where the refractive index $n = 1$), the laser intensity, I_L, is given by the magnitude of the Poynting vector, $\mathbf{P}$ (which corresponds to the energy flux density of the laser pulse), and is averaged over a laser period $T_L =$

$2\pi/\omega_L$ (denoted by the angled brackets $\langle ... \rangle$):

$$I_L = \langle |\mathbf{P}| \rangle = \frac{1}{\mu_o} \langle |\mathbf{E} \times \mathbf{B}| \rangle = \frac{\epsilon_0 c}{2} E_0^2 \tag{2.4}$$

where μ_0 is the permeability and ϵ_0 the permittivity of free space.

2.2.2 Ionisation

When incident on a solid target, an electromagnetic wave of sufficient intensity will liberate electrons from their constituent atoms through the process of ionisation. In order for ionisation to occur, the electric field of the laser must be sufficiently large to overcome the strong Coulomb forces that exist between the atom's nucleus and bound electrons - this energy is known as the binding, or ionisation, energy.

To overcome the binding energy, the applied laser field intensity must exceed the atomic intensity (defined as the intensity required to ionise hydrogen). The ionisation of ground state hydrogen is understood within the framework of the Bohr model, where the single electron present in hydrogen orbits the nucleus at specific distance, given by the Bohr radius a_B (which, for hydrogen, corresponds to : $a_B = 4\pi\varepsilon_0\hbar^2/m_e e^2 = 0.053\,\text{nm}$. The electric field, E_a, required to maintain the orbiting electron at this radius is calculated as: $E_a = e/4\pi\varepsilon_0 a_B^2 = 5 \times 10^{11}\,\text{Vm}^{-1}$, where e is the electronic charge. Using this electric field strength together with the Poynting vector (Eq. 2.4) enables an atomic intensity, I_a, to be defined as the intensity at which the laser field strength is equal to the strength of the electric field binding the electron to the atom:

$$I_a = \frac{\varepsilon_0 c}{2} E_a^2 \approx 10^{16}\ \ \text{Wcm}^{-2} \tag{2.5}$$

Thus, an incident laser intensity $I_L > 10^{16}\ \text{Wcm}^{-2}$ will ionise any target material. This intensity is relatively high and can be reduced by exploitation of a number of quantum mechanical processes. The ionisation processes relevant to laser-plasma interactions are multi-photon ionisation, tunnelling ionisation and barrier-suppression ionisation, shown in Fig. 2.1(a - c) respectively.

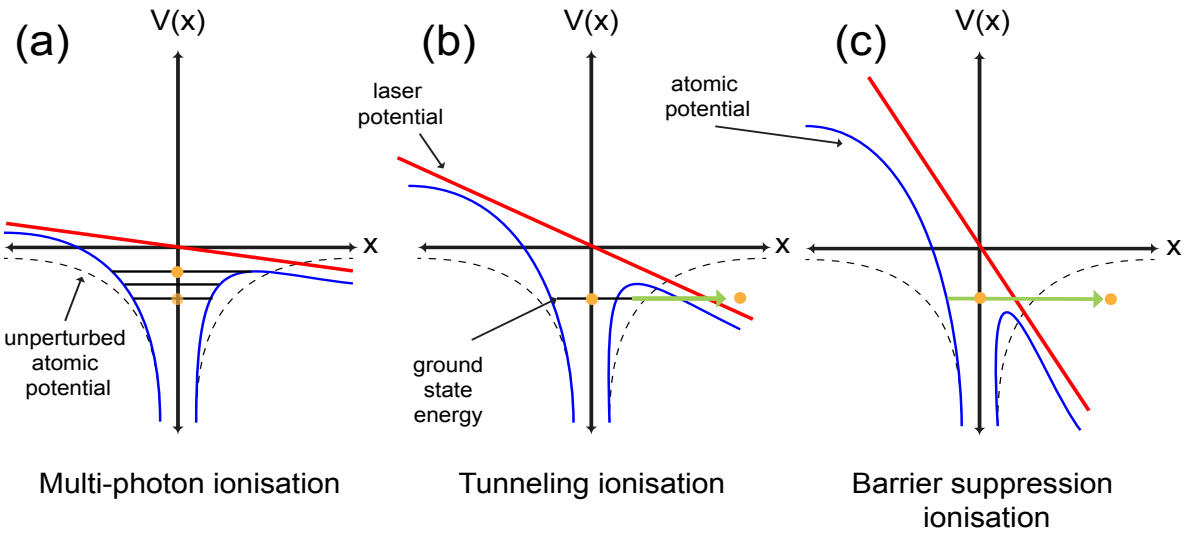

Figure 2.1: Ionisation processes relevant to laser-solid interactions: (a) multi-photon ionisation; (b) tunneling ionisation; and (c) barrier suppression ionisation.

To discriminate between ionisation processes at a given laser intensity, a useful parameter, known as the Keldysh [41] parameter, γ_K, is used:

$$\gamma_K = \omega_L \sqrt{\frac{2\epsilon_i}{I_L}} \sim \sqrt{\frac{\epsilon_i}{\Phi_{pond}}} \tag{2.6}$$

where ϵ_i is the ionisation energy and Φ_{pond} is the ponderomotive potential (which is explored in section 2.2.3).

Within the context of laser-solid interactions, a Keldysh parameter value of $\gamma_K \gg 1$ corresponds to a greater ionisation energy than ponderomotive potential; in this case, a large number of photons must be absorbed by a single electron in order to liberate the electron from it's potential well. This process is known as multi-photon ionisation (see Fig. 2.1(a)) and is dominant for low and moderate laser intensities, typical of that produced by nanosecond laser pulses. Multi-photon ionisation occurs when an electron gains energy due to absorbing a sufficiently high number (n) of photons over the duration of one laser cycle, where each photon possesses an energy of $E_\gamma = \hbar\omega_L$. After absorption, the final kinetic energy (E_k) of the electron may be greater than the photon energy ($E_k = (n+s)E_\gamma - \epsilon_i$; where s is the surplus absorbed photons), and thus the

electron is raised to a state from which it can escape (i.e. ionise). As previously noted, this processes is particularly important for lasers of longer pulse duration (i.e. nanosecond) and therefore is characteristic of ionisation induced by the laser pedestal (which is typically of a duration $\sim$ ns).

As the laser intensity increases, the Keldysh parameter becomes significantly smaller ($\gamma_K \ll 1$), and the ponderomotive potential begins to dominate over the ionisation energy. In particular, for ultraintense lasers (i.e. $I_L > 10^{18}$ Wcm^{-2}), ionisation occurs due to the laser electric field having a sufficiently large magnitude that it suppresses the nuclear binding potential (i.e. Coulomb potential); this 'warping' of the potential well, under the influence of the applied electric field, enables the electron to undertake two routes to ionisation: 1) tunnelling ionisation, where the suppression of the Coulomb barrier is sufficient for a high probability of electron tunnelling to occur (see Fig. 2.1(b)); and 2) over-the-barrier ionisation due to the Coulomb field becoming so distorted that electrons can freely escape (see Fig. 2.1(c)).

It is important to note than there are limitations in the use of the Keldysh parameter, as pointed out by Reiss [42]. These limitations occur for the case of ultra-high intensity laser fields (i.e. $I_L > 10^{18}$ Wcm^{-2}) where tunnelling is circumvented by barrier suppression effects. Moreover, the Keldysh theory does not include species dependency within the standard framework. A particularly rigorous extension made to the Keldysh model, known as ADK ionisation [43], accounts for larger atoms with a higher number of charge states, where the rate of ionisation, ν_{ADK}, is given by:

$$\nu_{ADK} \approx 6.6 \times 10^{16} \left(\frac{Z^2}{n_{ef}^{4.5}}\right) \left[10.87 \frac{Z^3}{n_{ef}^4} \left(\frac{E_a}{\mathbf{E}}\right)\right]^{2n_{ef}-1.5} \exp\left[-\frac{2Z^3}{3n_{ef}^3}\left(\frac{E_a}{\mathbf{E}}\right)\right] \quad (2.7)$$

where $\mathbf{E}$ is the electric field of the laser, Z is the ion charge and $n_{ef} = Z\sqrt{\epsilon_H/\epsilon_i}$ and ϵ_H is the ionisation potential of hydrogen.

These field ionisation mechanisms (i.e. tunnelling and barrier suppression ionisation) have been discussed within the context of the target front-surface (focal

spot region), where the atomic Coulomb potential is directly distorted by the action of the incident laser field. However, ionisation processes also occur within the target interior (driven by fast electron induced return currents) and at the target rear, where a strong electrostatic sheath field ionises the target rear-surface, subsequently accelerating ions [44]. The physics of field and collisional ionisation, induced by electrostatic sheath fields and collisional electrons respectively, is discussed in Chapter 3.

2.2.3 Electron motion in a laser field

The consequence of ionisation is that electrons (rather than ions, due to their greater mass than electrons), gain energy from the laser field and leave their parent atom. Thus, ionisation enables the electron to interact with the electromagnetic field and subsequently undergo a change of momentum (i.e. acceleration). The motion of an electron within an electromagnetic wave is typically an oscillation which arises due to the forces exerted on it by the electric and magnetic field components. These forces are described by the Lorentz equation:

$$\frac{d\mathbf{p}}{dt} = \frac{d}{dt}(\gamma m_e \mathbf{v}) = -e(\mathbf{E} + \mathbf{v} \times \mathbf{B}) \tag{2.8}$$

where $\mathbf{v}$ and $\mathbf{p}$ are the electron velocity and momentum respectively, and m_e is the electron mass. $\gamma = 1/\sqrt{1-\beta^2} = 1/\sqrt{1-v^2/c^2} = \sqrt{1+(p/m_e c)^2}$ is the relativistic Lorentz factor. Note also that the amplitudes of the electric and magnetic fields in vacuum are related by: $E = cB$ (using Faraday's law: $\nabla \times \mathbf{E} = -\partial \mathbf{B}/\partial t$).

By multiplying Eq. (2.8) by $\mathbf{p}$, and using the identities $\mathbf{p} \cdot (\mathbf{v} \times \mathbf{B}) = 0$ and $\mathbf{p} \cdot d\mathbf{p} = \frac{1}{2} d\mathbf{p}^2$, the rate of change of the electron kinetic energy ($E_K = m_e c^2(\gamma - 1)$) is obtained:

$$\frac{dE_K}{dt} = m_e c^2 \frac{d\gamma}{dt} = -e(\mathbf{v} \cdot \mathbf{E}) \tag{2.9}$$

At this point, it is useful to describe the intensity of a laser using the normalised

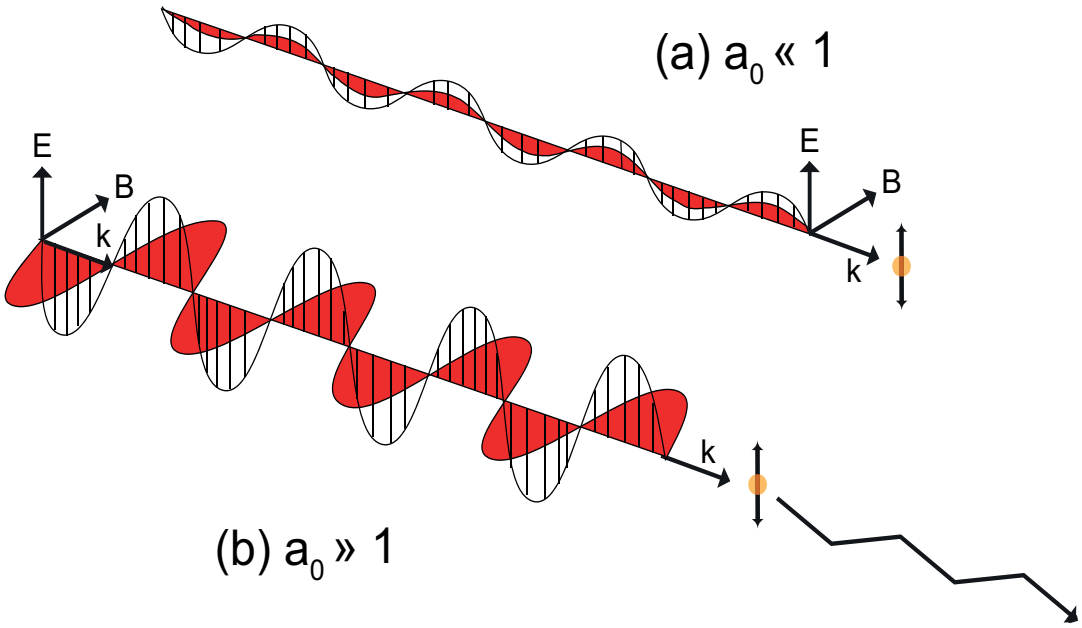

Figure 2.2: Single electron in an electromagnetic field for two intensity regimes: 1) $a_0 \ll 1$ - classical; and 2) $a_0 \gg 1$ - relativistic.

vector potential, a_0, defined by:

$$a_0 = \frac{\gamma v_{os}}{c} = \frac{eA}{m_e c} = \frac{eE_0}{m_e c \omega_L} \tag{2.10}$$

where $v_{os} = eE_0/m_e\omega_L$ is the transverse quiver velocity of an electron in an electric field amplitude E_0. Using a_0, the electric and magnetic field amplitudes can be rewritten as:

$$E_0 = \frac{a_0}{\lambda_L} \cdot 3.21 \times 10^{12} \text{ V m}^{-1}\mu m \tag{2.11}$$

$$B_0 = \frac{a_0}{\lambda_L} \cdot 1.07 \times 10^{4} \text{ T } \mu m \tag{2.12}$$

The normalised vector potential is used to determine when the amplitude of the electron velocity, v_{os}, approaches c, and thus can be used to characterise different regimes of laser-plasma interaction (i.e. classical and relativistic).

To understand these regimes, Fig. 2.2 displays the electron motion for both cases: (a) non-relativistic (i.e. classical); and (b) relativistic motion. In the

classical regime (i.e. lower laser intensities, $a_0 \ll 1$), where $v \ll c$ (and $\gamma \sim 1$), the electron motion is dominated by the electric field. At reduced laser irradiances (i.e. $I_L\lambda_L^2 < 10^{18}$ Wcm$^{-2}\mu$m^2), the magnetic force is a factor v_{os}/c less than the electric force and therefore it's influence on the electron motion is negligible. By integrating Eq. (2.8) for parameters corresponding to the non-relativistic case (i.e. $a_0 \ll 1$), with the initial conditions of an electron at rest ($v_0 = 0$) located at $(x_0, y_0) = (0, 0)$, the resulting electron velocity and displacement are given by: $\mathbf{v} = \hat{\mathbf{e}}_x \cdot eE_0/\omega_L m_e \cdot \sin(k_L z - \omega_L t)$ and $x = eE_0/\omega_L^2 m_e \cdot (cos(k_L z - \omega_L t) - 1)$ respectively. In this case, the electron oscillates under the action of the applied electric field with velocity and displacement amplitudes of $v_{os} = eE_0/\omega_L m_e$ and $x_{os} = eE_0/\omega_L^2 m_e$ respectively. Thus, for the non-relativistic regime the electron oscillates along the direction of the electric field (i.e. parallel to the field), as shown in Fig. 2.2 (a).

When an electron is influenced by a sufficiently strong laser field, it's resulting quiver velocity v_{os} approaches the speed of light c, and magnetic field effects become important. The onset of relativistic effects typically corresponds to laser irradiances given by:

$$I_L = \frac{a_0^2}{\lambda_L^2} \cdot 1.37 \times 10^{18}\,\mathrm{Wcm^{-2}}\mu\mathrm{m}^2 \tag{2.13}$$

$$I_L\lambda_L^2 > 1.37 \times 10^{18}\,\mathrm{Wcm^{-2}}\mu\mathrm{m}^2 \tag{2.14}$$

Note that the onset of relativistic motion also depends on the laser wavelength λ_L and thus a Nd:YAG glass-laser (which exhibit central wavelengths of $\lambda_L \sim 1\,\mu$m, e.g. the Vulcan laser) corresponds to a relativistic laser intensity of $\sim 10^{18}\,\mathrm{Wcm^{-2}}$. This intensity can be significantly lowered (by almost two orders of magnitude) by using a gas-laser system (i.e. CO_2 medium) which typically exhibit longer wavelengths ($\lambda_L \sim 10\,\mu$m).

For the relativistic regime (i.e. $a_0 > 1$), the solution of the Lorentz equation (Eq. (2.8)) leads to a distinctly different result from the classical regime. In this case, it can be shown that the electron motion is governed by the following

equations:

$$x(t) = \frac{a_0 c}{\omega} \sin(kz - \omega_L t) \tag{2.15}$$

$$z(t) = \frac{a_0^2 c}{4\omega_L} \left((kz - \omega_L t) + \frac{1}{2} \sin(2(kz - \omega_L t)) \right) \tag{2.16}$$

While motion in the x-direction is identical to the classical case (i.e. a transverse oscillation in the x-direction at the laser frequency), driven by the first term on the right-hand side of Eq. (2.16), the electron is strongly pushed in the laser propagation direction for $a_0 > 1$. In the laboratory reference frame (see Fig. 2.2(b)), the electron drifts in the laser propagation direction with velocity, $\mathbf{v}_D$, given by [45]:

$$\mathbf{v}_D = \frac{a_0^2}{4 + a_0^2} c \cdot \hat{\mathbf{e}}_z \tag{2.17}$$

Moreover, the electron undergoes motion at twice the laser frequency in the laser propagation direction (i.e. $\hat{\mathbf{e}}_z$-direction) due to the second term on the right-hand side of Eq. (2.16), which arises due to the $\mathbf{v} \times \mathbf{B}$ component of the Lorentz force (Eq. (2.8)). In a reference frame that is co-moving with the electron drift velocity $\mathbf{v}_D$, the electron undergoes a 'figure-of-eight' motion (see Fig. 2.2(b)).

It is important to point out that these solutions are only valid for a plane-wave (i.e. spatially infinite) that varies slowly with time. The physics changes significantly for the case of a laser pulse of finite spatial extent and temporal duration (i.e. focussed laser pulse), as would be used in a typical laser-solid interaction. The resulting spatial and temporal gradients in the laser field give rise to the so-called ponderomotive force.

The ponderomotive force

For an electron in an infinite plane wave, a free electron does not achieve net energy gain (i.e. the Lawson-Woodward theorem [46]). For laser intensities $I_L > 10^{18}$ Wcm^{-2}, the electron will drift from it's initial position due to the motion induced by the $\mathbf{v} \times \mathbf{B}$ component of the Lorentz force (see Eq. 2.8). However,

a defining characteristic of a focussing laser field is a spatially varying intensity profile. In this case, an electron is driven from regions of high to lower laser intensity during the first half of the laser cycle. When the field changes sign during the second half of the cycle, the electron will subsequently experience a weaker return force and will therefore not return to it's original position. Thus, the electron is driven out of regions of high laser intensity by a force arising from the time averaged spatial intensity gradients. This force is known as the ponderomotive force, $\mathbf{F}_P$, and is defined (for a single electron) as:

$$\mathbf{F}_P = -\frac{1}{4}\frac{e^2}{m_e\omega_L^2}\nabla E_s^2 = -\frac{e^2}{8\pi^2\epsilon_0 m_e c^3}\nabla\left(I_L\lambda_L^2\right) \tag{2.18}$$

where E_s is the spatial component of the electric field. This force originates from spatial electric field gradients (indicated by ∇E_s^2) and drives electrons from a higher to lower field position after each laser cycle with a velocity of $\sim v_{os}$. Moreover, since all charged quantities are squared there is no dependence on the sign of the charged particle, and thus the ponderomotive force drives all particles in the same direction (i.e. pushing them out of regions of high intensity).

In the relativistic intensity regime (i.e. as v_{os} approaches c; $a_0 > 1$), the time averaged kinetic energy gained by an electron over one cycle is the same as the ponderomotive potential, U_P:

$$U_P = m_e c^2(\langle\gamma\rangle - 1) = m_e c^2\left(\sqrt{1+\frac{a_0}{2}} - 1\right) \tag{2.19}$$

for a linearly polarised laser. Note that a linearly polarised pulse has $\gamma = \sqrt{1+a_0^2/2}$; for circular polarisation this becomes $\gamma = \sqrt{1+a_0^2}$.

At relativistic laser irradiances (i.e $I_L\lambda_L^2 > 10^{18}$ Wcm$^{-2}\mu$m^2), the magnetic field component of the ponderomotive force dominates electron motion (over the electric field component), acting to efficiently push fast electrons out of the oscillating laser field, subsequently launching them into the overdense target. This process is known as $\mathbf{j}\times\mathbf{B}$ heating and will described in detail in section **??**.

2.2.4 From a single particle to many particles

So far, only the motion of a single electron in an electromagnetic field has been considered. However, in a laser-solid interaction experiment the laser is focussed to a finite spot (of $\sim \mu$m radius), irradiating an area of the solid containing many electrons. The laser is absorbed in the skin depth of the solid target (see section 2.2.5) and the irradiated region undergoes a rapid change of state via laser absorption, heating and subsequently ionisation. Thus, many electrons will be influenced by the laser-field, resulting in collective electron motion.

As the material is heated beyond boiling temperature, ionisation of the gaseous atoms occurs as electrons are stripped from their constituent ions, and the material transitions to a plasma. A plasma can be described by considering it's local and long-range properties; these are known respectively as 'quasi-neutral' and 'collective behaviour'. Formally, a set of criteria [47] must be satisfied for matter to be described as a plasma:

1. $\lambda_D \ll L$ - the screening distance is smaller than the plasma dimension.
2. $N_D \gg 1$ - there are many particles contained within the screening distance.
3. $\omega_p \tau > 1$ - particle collisions are weak in comparison to collective effects.

Each of these criteria is explored in turn.

1. Debye length - $\lambda_D \ll L$

The first of these key characteristics represents a plasma's tendency to shield externally applied electric fields; the charged particles in a plasma (i.e. electrons and ions) will orientate in such a way that an oppositely-directed electric field is generated to cancel the external field on a macroscopic scale. Moreover, this ensures that the plasma maintains quasi-neutrality (i.e. the plasma is macroscopically charge neutral). In a plasma, the positive ions are surrounded by electrons that act to shield the Coulomb potential of the ions. To first order, the electric field due to a charge immersed in a plasma only interacts with other charged

particles in the plasma within a volume known as the 'Debye sphere', where the radius of the sphere is given by the Debye length λ_d.

$$\lambda_d = \sqrt{\frac{\epsilon_0 k_B T_e}{e^2 n_e}} \tag{2.20}$$

where k_B is Boltzmann's constant, T_e is the electron temperature and n_e is the electron density. The Debye length defines the minimum distance over which charge neutrality is ensured (i.e. a charged particle essentially feels no electric field effect from the other charges at distances greater than λ_D). Additionally, the Debye length is also a measure of the penetration depth of externally applied electromagnetic fields. For shielding effects to occur, the Debye sphere radius (i.e. Debye length) must be much less than the length of the linear dimension, L, of the plasma (i.e. $\lambda_d \ll L$).

2. Debye sphere - $N_D \gg 1$

Furthermore, Debye shielding is only valid if there are enough particles contained within the plasma. Specifically, the number of particles N_D contained within a Debye sphere is given by:

$$N_D = \frac{4}{3} n_e \pi \lambda_D^3 = 1.38 \times 10^6 \; T_e^{3/2} n_e^{-1/2} \tag{2.21}$$

For collective behaviour to apply, many particles must be contained within a Debye sphere:

$$N_D \gg 1 \tag{2.22}$$

3. Plasma frequency and collisions - $\omega_p \tau > 1$

One of the key characteristics of collective motion in a plasma is the oscillations set up in response to charge imbalances. When electrons are displaced from their original position, an electric field is generated which acts to restore the plasma quasi-neutrality by 'pulling' electrons back to their original position. This restoring force, coupled with the inertia of the electrons, causes the electrons to oscillate

(centred on the electron equilibrium position) at a characteristic frequency known as the plasma frequency, ω_p. Typically, the charge imbalance occurs over a distance of λ_D and therefore the plasma electron frequency may be expressed by:

$$\omega_p = \frac{(k_B T_e/m_e)^{1/2}}{\lambda_D} = \sqrt{\frac{n_e e^2}{\epsilon_0 m_e}} \tag{2.23}$$

To enable distinction between an ionised gas and a plasma, the product of the mean collision time τ with the electron plasma frequency must be greater than one (i.e. $\omega_L \tau > 1$), which represents plasma collisions being weak in comparison to the strong binary collisions characteristic of an ionised gas.

2.2.5 Laser propagation in a plasma

The property of a plasma to react to a perturbation with the oscillating plasma frequency ω_p is important when considering the interaction of electromagnetic waves with plasmas. To describe the propagation of electromagnetic fields ($\mathbf{E}$ and $\mathbf{B}$) in a plasma, Maxwell's equations are used:

$$\nabla \cdot \mathbf{E} = \frac{\rho_q}{\varepsilon_0} \qquad \textit{Gauss's law for electric field generation} \tag{2.24}$$

$$\nabla \cdot \mathbf{B} = 0 \qquad \textit{Gauss's law for magnetic field generation} \tag{2.25}$$

$$\nabla \times \mathbf{E} = -\frac{\partial \mathbf{B}}{\partial t} \qquad \textit{Faraday's law of induction} \tag{2.26}$$

$$\nabla \times \mathbf{B} = \mu_0 \mathbf{J} + \frac{1}{c^2}\frac{\partial \mathbf{E}}{\partial t} \qquad \textit{Ampère's circuital law} \tag{2.27}$$

where μ_0 is the vacuum permeability, ρ_q is the total charge density and $\mathbf{J}$ is the total current density.

In a laser-solid experiment, the laser pulse propagates through an expanding plasma created by the preceding laser pedestal (see section 2.2.6). For electromagnetic field propagation in a plasma, a wave equation can be derived using

Maxwell's equations:

$$\nabla^2 \mathbf{E} = \frac{1}{c^2}\frac{\partial^2 \mathbf{E}}{\partial t^2} + \mu_0 \frac{\partial \mathbf{J}}{\partial t} \tag{2.28}$$

which results in the plasma dispersion relation for plane waves:

$$\omega_L^2 = \omega_p^2 + k^2 c^2 \tag{2.29}$$

Moreover, if the laser field is sufficiently strong such that the electron quiver velocity, v_{sc}, approaches c during the interaction with the field, the electron mass, γm_e, increases. This, in turn, modifies the electron plasma frequency:

$$\omega_p = \sqrt{\frac{n_e e^2}{\langle\gamma\rangle \epsilon_0 m_e}} \tag{2.30}$$

where $\langle\gamma\rangle$ is time averaged over the fast electron oscillation period for a large number of electrons. Crucially, the electron plasma frequency depends on the (electron) plasma density.

When the laser field frequency exceeds the plasma frequency (i.e. $\omega_L > \omega_p$), the electrons move too slowly in response to the varying field and thus the laser propagates through the plasma. However, due to the density dependence of the plasma frequency, a laser propagating in a plasma density gradient will propagate until a specific density is achieved. At this so-called 'critical' density, the plasma becomes opaque to the laser, thus inhibiting propagation. The condition for this to occur is that the laser field frequency is equal to the plasma electron oscillation frequency, $\omega_L = \omega_P$. The corresponding density (i.e. critical density) is given by:

$$n_c = \frac{\epsilon_0 \langle\gamma\rangle m_e}{e^2}\omega_L^2 \approx 1.1 \times 10^{21} \left(\frac{\lambda_L}{\mu m}\right)^2 \left(\mathrm{cm}^{-3}\right) \tag{2.31}$$

Using this parameter enables the distinction of two regions of laser-plasma interaction:

1. Underdense plasma - $n_e < n_c$
2. Overdense plasma - $n_e > n_c$

By way of example, a laser of 1 μm wavelength (typical of the laser used in the experimental investigations presented in Chapter 5, 6 and 7) propagates to a critical density of $n_c \sim 10^{21}\text{cm}^{-3}$. The point at which the laser interacts with the critical density is defined as the critical surface.

The dispersion relation in Eq. 2.29 also implies that the phase velocity, v_{ph}, of the laser-field is greater in a plasma than in vacuum (c), for a plasma with $n_e < n_{cr}$. This can be expressed as:

$$v_{ph} = \frac{\omega_L}{k} = \frac{c}{\eta_r} \tag{2.32}$$

where η_r is the index of refraction expressed as:

$$\eta_r = \sqrt{1 - \frac{\omega_p^2}{\omega_L^2}} = \sqrt{1 - \frac{n_e}{n_c}} \tag{2.33}$$

Furthermore, the group velocity, v_g, (which for $n_e < n_c$ is less than c), is expressed as:

$$v_g = c\sqrt{1 - \frac{\omega_p^2}{\omega_L^2}} \tag{2.34}$$

However, for overdense interactions (i.e. $n_e > n_c$) the group velocity tends towards 0, and the laser is reflected from the critical density surface. The critical surface is particularly important for laser-solid interactions, as it is at this location that fast electrons are generated (see Chapter 3). However, the critical surface is not perfectly flat due to a number of processes, such as Rayleigh-Taylor instabilities that can cause surface rippling of the pre-formed plasma [48]. Moreover, reflection from the critical surface provides a mechanism by which harmonic are generated, the most efficient of which is the so-called Relativistic Oscillating Mirror (ROM) mechanism [49]. Additionally, for laser intensities in the relativistic regime (i.e. $a_0 > 1$), the plasma frequency increases with increasing laser intensity, resulting in the critical density increasing by a factor of γ, enabling the laser to propagate further into the plasma. This effect is known as self-induced transparency [50].

It is also important to note that an evanescent component of the laser is able to penetrate beyond the relativistically modified critical density. In this case, the laser field is exponentially attenuated over a distance which is defined as the collisionless skin depth, l_s, given by:

$$l_s = \frac{c}{\omega_p} \tag{2.35}$$

where c is the speed of light in vacuum and ω_p is the plasma frequency.

2.2.6 Solid target: front surface plasma

The creation of a laser-generated plasma is, unsurprisingly, critically dependant on the incident laser parameters (i.e. intensity, pulse duration and energy). Moreover, the laser contrast ratio, defined as the ratio between the peak intensity and pedestal intensity (which is typically produced by uncompensated spectral dispersion and amplified spontaneous emission) plays a key role in defining the front-surface plasma properties relevant to laser-solid interactions. This pedestal, which typically exhibits intensities in the region of $I_L = 10^{10} - 10^{15}$ Wcm^{-2} (dependant on the peak laser intensity), acts to ionise the front surface of the target prior to the arrival of the main peak (at which the intensity is highest). The incident laser continues to irradiate and interact with this plasma over it's pulse duration. To understand the processes that are involved when the pedestal interacts with the front surface of a solid-density target, Fig. 2.3 shows the result of a 1-D hydrodynamic simulation (using the HELIOS-CR code [51]).

In this simulation, a laser of intensity $I_L = 5 \times 10^{12}$ Wcm^{-2} (and $\sim$ few ns duration) is incident from left to right (Fig. 2.3 - green arrow) onto the surface of a silicon target. The laser-induced ionisation rapidly heats the front of the target to temperatures in the region of 1 - 140 eV (Fig. 2.3 - red line) over the first few tens-of-micron distance from the target-front surface. This creates a plasma, which extends over several hundred μm from the front surface, and also exhibits varying density over this distance (Fig. 2.3 - blue line). Also note the target compression and the formation of a shock wave propagating into the target.

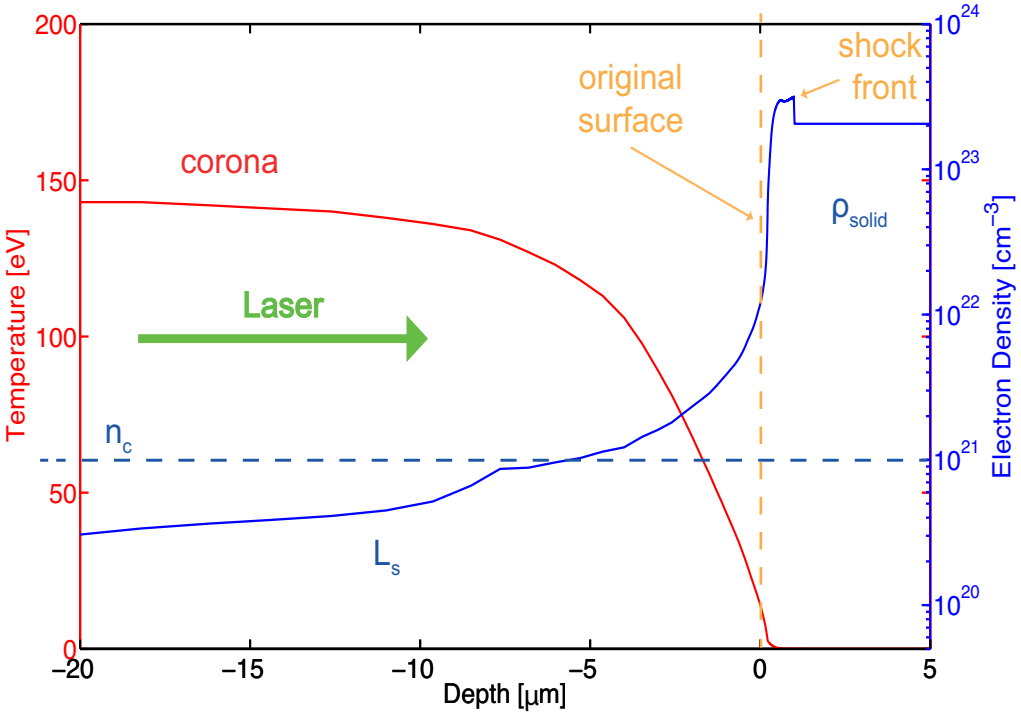

Figure 2.3: Hydrodynamic simulation (using HELIOS-CR) plot of temperature and density profiles produced for a solid-density target irradiated by a laser of intensity $I_L = 5 \times 10^{12}$ Wcm^{-2}.

Assuming a 1-D expansion, the density profile decreases exponentially. At a distance z from a target, with solid density n_0, the plasma density profile, $n_e(z)$, is given by [47]:

$$n_e(z) = n_0 \exp\left(-\frac{z}{L_s}\right) \tag{2.36}$$

The density scale length, L_s, is used to describe the density profile and is defined as the distance over which the density drops by a factor of $1/e$, where e is Euler's number. The scale length is an important parameter, as it essentially characterises the amount of pre-formed plasma, which in turn governs the mechanisms by which the laser energy is absorbed (see section 2.3).

The plasma density scale length is calculated approximately using the sound speed, c_s, and laser pulse duration, τ_L giving:

$$L_s \approx c_s \tau_L \tag{2.37}$$

where the ion sound speed, c_s, is given by:

$$c_s = \left(\frac{Z * k_B T_e}{m_i} \right)^{\frac{1}{2}} \tag{2.38}$$

where $Z*$ is the charge state of the ion and m_i is the ion mass.

As described in section 2.2.5, for relativistic laser fields the critical density increases by a factor of $\langle\gamma\rangle$, enabling the laser to propagate deeper. This, in turn, drives the critical surface backwards into plasma regions of increasing density (i.e. towards the solid density region). For a given pre-plasma scale length, the position of the critical surface, z_c, can be calculated by solving Eq. (2.36) for $n_e = n_c$, resulting in:

$$z_c = L_s \ln \left(\frac{\langle\gamma\rangle n_c}{n_0} \right) \tag{2.39}$$

where n_0 is solid density.

Having described the pre-plasma conditions, together with the subsequent influence on laser propagation, the mechanisms by which laser energy is absorbed into energetic particle generation (primarily at the critical surface) is now discussed.

2.3 Heating mechanisms: fast electron generation

The physical picture so far is understood as follows: the intrinsic laser pre-pulse (i.e. pedestal) is of sufficient intensity to generate a pre-plasma at the target front-surface. The laser irradiance at this point is quite moderate, typically in the region of $I_L \lambda_L^2 = 10^{10} - 10^{12}$ Wcm$^{-2}\mu$m^2. As the laser pedestal ionises the target front-surface, creating the pre-plasma, a plasma density (i.e. electron density) profile is produced. This profile exhibits a large variation of density, extending over some distance (typically between a few μm to several hundred μm, depending on pulse intensity and duration) from vacuum to solid density (i.e. 10^{23} cm^{-3}). As the main peak arrives at the target, the laser intensity

increases significantly to values of $I_L\lambda_L^2 = 10^{15} - 10^{20}$ Wcm$^{-2}\mu$m^2. This large span of intensities gives rise to a range of mechanisms which convert energy from the laser into the plasma electrons. In an ultra-intense laser-solid experiment, it is most likely that several of these mechanisms occur simultaneously; the most dominant mechanism largely depends on parameters such as the laser intensity, incidence angle and density scale-length, as will now be explored.

2.3.1 Collisional heating - inverse bremsstrahlung

At low to moderate laser irradiances (i.e. $I_L\lambda_L^2 = 10^{12} - 10^{15}$ Wcm$^{-2}\mu$m^2), the most dominant absorption mechanism arises from collisions between laser-driven electrons and plasma ions which constitute the background plasma. This mechanism, known as inverse bremsstrahlung, occurs due to the transfer of energy from the laser to the plasma when an oscillating electron (under the action of the laser pulse) collides with a plasma ion; the electron motion becomes damped during the collision, and thus energy from from the laser is converted into plasma heating.

A dispersion relation can be derived for inverse bremmsstralung by using the equation of motion for an electron in an oscillating electric field (i.e. Lorentz equation - Eq. (2.8)), together with an additional term which accounts for collisional damping and is proportional to the electron-ion collision frequency $\left(\nu_{ei} \propto \frac{n_e Z_i}{T_e^{3/2}}\right)$, given by [52]:

$$\left(\frac{kc}{\omega_L}\right)^2 = 1 - \frac{\omega_p^2}{\omega_L^2} + i\nu_{ei}\frac{\omega_p^2}{\omega_L^3} \tag{2.40}$$

Moreover, by using the imaginary part of the refractive index of a plasma (given by Eq. (2.33)) the collisional absorption coefficient, κ_{IB}, is given by:

$$\kappa_{IB} = \frac{\nu_{ei}}{2c}\left(\frac{n_e}{n_c}\right)\left(1 - \frac{n_e}{n_c}\right)^{-1/2} \tag{2.41}$$

$$\kappa_{IB} \propto \frac{Z_i n_e^2}{T_e^{3/2}}\left(1 - \frac{n_e}{n_c}\right)^{-1/2} \tag{2.42}$$

The absorption coefficient reveals that inverse bremsstrahlung is dominant when the electron temperature, T_e, is low while the plasma Z_i is large. Additionally, inverse bremsstrahlung is dominant for higher electron densities and therefore occurs primarily in the region close to the critical surface.

However, collisional effects diminish as the electron velocity (i.e. plasma temperature) increases, due to the electron mean free path increasing. For laser irradiances $I_L\lambda_L^2 > 10^{15}$ Wcm$^{-2}\mu$m^2, the plasma temperature rises significantly fast such that collisions between electrons and ions becomes an ineffectual mechanism of transferring energy from the laser field to the plasma.

To understand this, consider the following relation between intensity and temperature [45]. For lower intensity pulses the plasma temperature, T_e, varies with:

$$T_e \propto I_L^{4/9} t^{2/9} \tag{2.43}$$

where t is time. The collision frequency can be expressed as $\nu_{ei} \propto I_L^{-2/3} t^{-1/3}$; thus as the laser intensity increases the number of collisions falls, which in turn leads to an overall reduction in collisional absorption effects. Additionally, as the laser intensity increases such that the oscillation velocity of the electron approaches the electron thermal velocity, the collision frequency reduces even further, described by [45]:

$$\nu_{eff} \simeq \nu_{ei} \frac{v_{th}^2}{\left(v_{osc}^2 + v_{th}^2\right)^{3/2}} \tag{2.44}$$

where ν_{eff} is the effective collisional frequency and v_{th} is the thermal electron velocity. Therefore, collisional absorption contributes significantly less to electron heating at higher peak laser intensities; experiments [53] at irradiances of $I_L\lambda_L^2 > 10^{15}$ Wcm$^{-2}\mu$m^2 observed a high absorption that could not be accounted for by inverse bremsstrahlung (i.e. collisional heating mechanisms). Thus, alternative mechanisms must govern absorption at higher laser intensities which do not rely on collisions between electrons and ions.

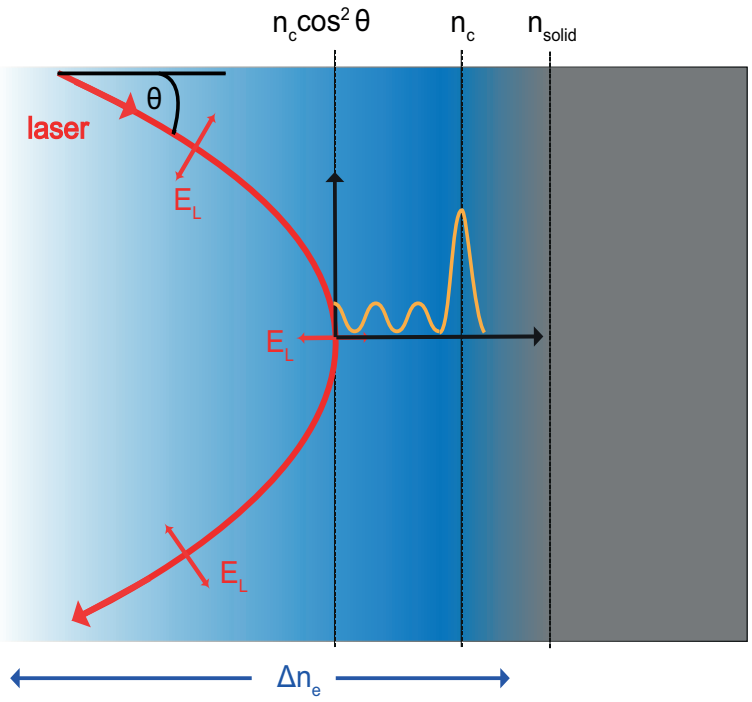

Figure 2.4: Schematic illustration of the resonance absorption process of p-polarised light (where **E** is orientated parallel to the density gradient) incident on a long plasma density scale length. Resonantly excited plasma waves transfer energy to the electrons at the critical surface.

2.3.2 Collisionless absorption

There are a number of collisionless processes by which energy from the laser pulse is coupled into the plasma electrons. The first of these is known as resonance absorption and occurs when energy is coupled to electrons at the critical surface in the form of resonant plasma waves. A schematic of the resonance absorption process is displayed in Fig. 2.4.

When a p-polarised laser is obliquely incident on a solid target (which exhibits a pre-plasma generated by the inherent pedestal preceding the main pulse) at some angle θ, the laser will be refracted in the pre-plasma and reflected at the critical surface. Note that the density at which the pulse is reflected is less than the critical density, n_c, by a factor of $\cos^2\theta$ (see Fig. 2.4). Moreover, for a linearly polarised laser, there is an electric field component which is parallel to the density gradient Δn_e. This electric field component can tunnel beyond the modified critical density (i.e. skin depth - see section 2.2.5), driving a plasma

wave in the form of electron density perturbations. Importantly, generation of the plasma wave is most efficient at resonance, which occurs when the plasma and laser frequency are equal (i.e. at the critical surface). The optimum laser-incidence angle, θ, for resonance absorption is given by [45]:

$$\sin\theta = (c/2\omega_L L_s)^{\frac{1}{3}} \tag{2.45}$$

where L_s is the plasma scale length.

Crucially, resonance absorption requires a plasma density of significant length (typically $L_s \gg \lambda_L$). However, as the laser intensity increases, the ponderomotive pressure also increases which can modify the density profile (e.g. profile steepening [54]). The consequence is that the density gradient becomes much shorter for more intense lasers. In the case of short scale lengths and more intense lasers (i.e. $a_0 > 1$), vacuum heating dominates over resonance absorption.

Also known as Brunel (or not-so-resonant) heating [55], vacuum heating occurs when a linearly polarised pulse is incident on a small density gradient (i.e. $L_s < \lambda_L$, in contrast to resonance absorption, where $L_s \gg \lambda_L$ - see Fig. 2.5). Moreover, this particular absorption mechanism is prevalent at relativistic laser irradiances (i.e. $a_0 > 1$; $I_L\lambda_L^2 > 10^{18}$ Wcm$^{-2}\mu$m^2). The absorption of energy from the laser into electrons occurs due to the electric field component of the laser being unable to propagate significantly beyond the critical surface. The incident laser 'drags' electrons from the target into vacuum over the first half of the laser cycle, and subsequently accelerates the electrons back into the target in the second half cycle (i.e. when the electric field changes direction). Note that the return velocity of these electrons is approximately given by the quiver velocity $v_{osc} \sim eE/m_e\omega_L$. Once the electrons are driven past the critical surface at n_c (and beyond the skin depth), having gained kinetic energy directly from the laser, they are subject to a weaker restoring force from the field. Thus, the electrons propagate into the target with a net energy gain. Vacuum heating is a more efficient absorption process than resonance absorption if the ratio of the quiver velocity to the laser frequency is greater than the density scale length (i.e. $v_{osc}/\omega_L > L_n$); this is a consequence of the minimum electric field shielding length being v_{osc}/ω_L, and

thus why vacuum heating is ineffective if the plasma density scale length is too long.

The fraction of laser energy converted into the electrons is given by the ratio of the absorbed power, f_{th}, to the incident power:

$$f_{th} = \frac{\eta_{osc}}{2\pi} \frac{v_{osc}^3}{v_L^2 c \cos\theta} \tag{2.46}$$

where η_{osc} is the efficiency factor (which indicates how much of the electron oscillatory motion is converted to heating the plasma) and $v_L = eE_L/m_e\omega_L$.

Another important absorption mechanism, which is particularly dominant at ultra-high laser intensities, underpins key electron properties and is most relevant to the results presented in this thesis. Known as $\mathbf{j} \times \mathbf{B}$ heating [56] (where $\mathbf{j} = en_e\mathbf{v}$), it is similar to vacuum heating but, crucially, depends on the electrostatic field driven by the oscillating component of the laser's ponderomotive force. At relativistic laser intensities (i.e. $a_0 > 1$; $I_L\lambda_L^2 > 10^{18}$ Wcm$^{-2}\mu$m^2), the $\mathbf{v} \times \mathbf{B}$ term in the Lorentz equation contributes significantly to the electron's motion (see Fig. 2.2). Thus, at the interface between the front surface plasma and vacuum, the electrons gain energy from the $\mathbf{v} \times \mathbf{B}$ component and are launched into the overdense plasma.

From a physical point of view, $\mathbf{j} \times \mathbf{B}$ heating is similar to vacuum heating in that both involve electrons being directly accelerated by a laser electric field incident on a sharp density profile. The key distinguishing features for $\mathbf{j} \times \mathbf{B}$ heating are that the electrons are ejected from regions of high intensity by the ponderomotive force, and thus directed along the laser k-direction, in addition to being rapidly heated by a fast oscillating component. For a linearly polarised laser, the resulting longitudinal force on an electron is given by:

$$F_z = -\frac{m_e}{4} \frac{dv_{osc}^2(x)}{dx} \left(1 - \cos(2\omega_L t)\right) \tag{2.47}$$

The first term on the right-hand side of Eq. 2.47 is the ponderomotive force (as described in section 2.2.3), which acts to drive the electron density profile inwards (i.e. towards the critical surface) by pushing electrons from areas of high field

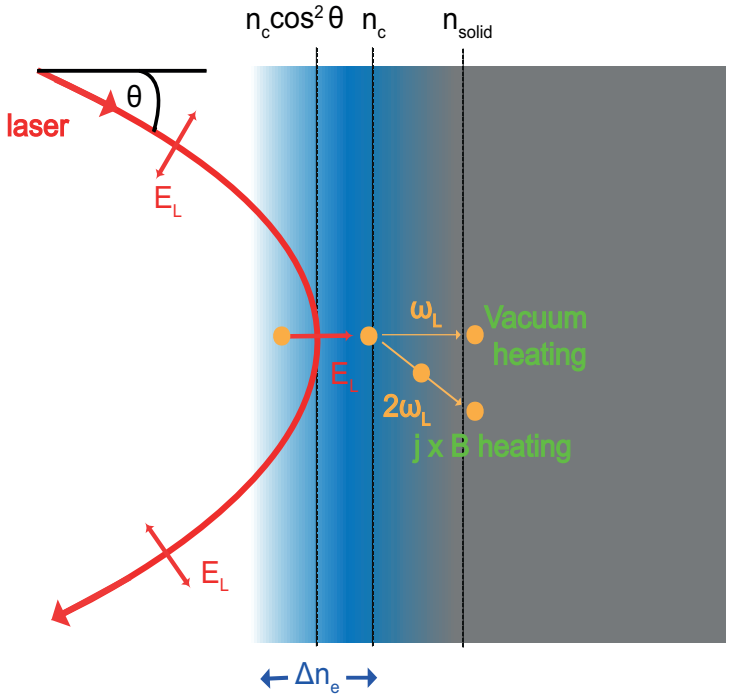

Figure 2.5: Schemetic showing vacuum and $\mathbf{j} \times \mathbf{B}$ heating mechanisms. For vacuum heating, the p-polarised laser is incident on a short density gradient (i.e. $L_s < \lambda_L$ accelerates electron beyond the critical surface along the target normal direction.For the $\mathbf{j} \times \mathbf{B}$ heating mechanism, a p-polarised laser is incident on a sharp density scale length where electron bunches are launched, at twice the laser frequency, into the overdense target along the laser direction.

intensity. The second term on the right-hand side of Eq. 2.47 is the oscillating component of the ponderomotive force, and contains the high-frequency component $\cos(2\omega_L t)$, arising from the $\mathbf{v} \times \mathbf{B}$ term of the Lorentz force (see Eq. 2.8). This term acts to oscillate the electorns at twice the laser frequency. Thus, the electrons are driven in bunches (at a frequency of $2\omega_L$) into the overdense plasma. Moreover, the direction of electron acceleration is different to vacuum heating; while vacuum heating accelerates electrons perpendicular to the density gradient, due to the electric field component being orientated parallel to the density gradient (i.e. along target normal), $\mathbf{j} \times \mathbf{B}$ heating drives electrons along the laser direction (see Fig. 2.5), as demonstrated experimentally by Santala *et al*[57]. In addition, $\mathbf{j} \times \mathbf{B}$ heating favours low incidence angles (i.e. approaching target normal), and also works for reasonably long density scale lengths (i.e. $L_s > \lambda_L$). Importantly, for the experimental conditions relevant to the results presented in Chapter 5, 6 and 7, $\mathbf{j} \times \mathbf{B}$ heating is likely to be the most dominant absorption mechanism, although resonance and vacuum heating will also contribute to a lesser degree.

2.3.3 Laser to fast electron conversion efficiency

The previous section described a number of mechanisms by which laser energy is coupled into energetic electrons. However, due to the complexity of a typical laser-solid interaction, as well as the dependency of each absorption mechanism on the pre-plasma scale length and density, laser incident angle, polarisation and intensity, it is not always clear as to exactly how much of the laser energy is converted into electron kinetic energy. Moreover, for the relativistic laser intensity regime there are (at present) no theoretical models that give an accurate quantitative prediction for absorption; rather, we use a qualitative approach to determine the absorption fraction, using a combination of experimental results and numerical simulations. The amount of energy converted from the laser into electrons is known as the conversion efficiency, $\eta_{L\rightarrow e}$. In recent decades, much work has focussed on both the experimental and numerical characterisation of the conversion efficiency. Experimentally, this is typically performed by measur-

ing secondary emitted sources, since direct characterisation of the absorption is virtually impossible; the very large electric fields within the target, as well as the strong electrostatic fields present at the target-vacuum boundaries, ensure that only a very small fraction of electrons escape. The consequence is that direct measurement of the escaping electron population may not reflect the dynamics and properties of the vast majority of the electrons, whose escape is inhibited by the strong fields. Therefore, indirect measurements of x-ray emission (utilising, for example, K_α emission [58]) enable the number of fast electrons to be characterised, albeit with a number of significant assumptions (i.e. electron beam divergence and temperature).

Measurements of the total absorbed energy (i.e. by measuring and comparing the reflected and scattered radiation) in the relativistic regime was made by Ping *et al*[59]. In this work, they utilised laser intensities of $I_L\lambda_L^2 = 10^{18} - 10^{20}$ Wcm$^{-2}\mu$m^2 for a variety of target and laser parameters. The key finding of this work is that the absorption coefficient varied with $(I_L\lambda_L^2)^{0.2}$ for the laser intensities explored, where the absorption percentage varied from $\eta_{L\rightarrow e} \sim 0.3$ at $I_L\lambda_L^2 = 10^{18}$ Wcm$^{-2}\mu$m^2 to $\eta_{L\rightarrow e} \sim 0.8$ at $I_L\lambda_L^2 = 10^{20}$ Wcm$^{-2}\mu$m^2. However, this result was a measurement of the total absorbed energy not necessarily only the energy converted into electron kinetic energy (at these intensities, energy will also have been converted into ion acceleration i.e plasma expansion).

A range of investigations specifically reporting on electron conversion efficiency (i.e. by inferring absorption from the properties of the 'fast' electron population) have been obtained [60], in which an intensity scaling of $\eta_{L\rightarrow e}(I_L) = 1.2 \times 10^{-15} I_L^{0.74}$ was derived; this scaling corresponds to $\eta_{L\rightarrow e} = 0.1$ at intensities of $I_L = 10^{18}$ Wcm^{-2} and $\eta_{L\rightarrow e} = 0.5$ at higher intensities of $I_L = 3\times10^{20}$ Wcm^{-2}. However, the results must be carefully interpreted as certain assumptions were made to obtain this scaling, namely that: 1) the fast electron source is isotropic (i.e. electrons are radiated in every direction); 2) there are no electric or magnetic fields to influence the electron transport; and 3) the contribution from refluxing electrons is neglected. These assumptions have been shown to be inaccurate for typical laser-solid interactions [61–63]. Moreover, including refluxing

for thin targets resulted in a conversion efficiency that was found to vary between $\eta_{L\to e} = (20 \pm 10)\%$ at intensities of $I_L = 10^{18} - 10^{20}$ Wcm^{-2}.

The collection of published results for laser absorption by overdense plasmas [64] for the intensity regime which is applicable to the investigations of this thesis (i.e. $I_L\lambda_L^2 = 10^{19} - 10^{20}$ Wμm^{2}cm^{-2}) indicate three general trends: 1) absorption increases with $I_L\lambda_L^2$; 2) absorption increases for lower plasma densities; and 3) absorption is greatest for an oblique angle of incidence. Furthermore, numerical simulation results also indicate that laser absorption into electrons peaks for near critical density plasmas [65].

The generally accepted values for laser-to-electron conversion efficiency typically fall within the region of $\eta_{L\to e} = 20\% - 40\%$ for ultraintense laser pulses ($I_L = 10^{18} - 10^{20}$ Wcm^{-2}). However, as previously indicated, these values are critically dependant on laser intensity, angle of incidence and pre-plasma scale length, and so at this time a full and quantitative theory of laser-to-fast electron conversion efficiency is still needed. A particularly useful review of experimental, numerical and theoretical investigations of laser absorption is given by Davies [64], in which the importance of the conversion efficiency for applications such as fast ignition is also addressed.

2.3.4 Fast electron spectrum and temperature

The absorption mechanisms discussed in section 2.3.1 and 2.3.2 result in the coupling of a fraction of the laser energy, $\eta_{L\to e}$, into the acceleration of a population of electrons to relativistic velocities with three typical hallmark signatures of collective high-intensity effects: angular-dependant absorption into hot (i.e. 'fast') electrons, hard x-ray emission and ion acceleration. Moreover, the accelerated population of electrons typically have much higher energies than the bulk plasma temperature T_e. In contrast to a monochromatic, beam-like electron energy spectrum that might be expected (since the electrons are accelerated by a coherent electric field - the incident laser field), Bezzerides *et al.* [66] demonstrated that the random (i.e. stochastic) nature of electron acceleration in the laser field results in strong variations of both the electron energy and trajectory. Averaging each

of these single-particle distributions over time leads to a Maxwellian velocity distribution. A single temperature Maxwellian distribution is defined as a function of the fast electron energy, E_f, and the fast electron temperature $k_B T_f$:

$$f(E_f) = N_f \sqrt{\frac{4E_f}{\pi (k_B T_f)^3}} \exp\left(-\frac{E_f}{k_B T_f}\right) \tag{2.48}$$

where N_f is the total number of fast electrons.

However, collective heating (and thus absorption) mechanisms can result in a significant departure from a single-temperature
Maxwellian distribution. In this case, a bi-Maxwellian electron distribution arises from collisionless heating effects [67, 68], as described in section 2.3.2. Furthermore, as the plasma heats (i.e. as $k_B T_f \rightarrow m_e c^2$) relativistic effects become important and the electron equilibrium distribution is described using the so-called Maxwell-Jüttner distribution [69]:

$$f(\gamma) = N_f \frac{\gamma^2 \beta}{\frac{k_B T_f}{m_e c^2} K_2(m_e c^2 / k_B T_f)} \exp\left(-\gamma / \frac{k_B T_f}{m_e c^2}\right) \tag{2.49}$$

where $\beta = v/c$, $\gamma = \frac{1}{\sqrt{1-\beta^2}}$ and K_n is the modified Bessel function of the second kind of order n.

Thus, the population of fast electrons generated at the target front-surface are driven over the critical density into the over-dense target, with some fraction of the laser energy $\eta_{L \rightarrow e}$ and a relativistic Maxwellian energy distribution. The mean energy of this distribution is known as the fast electron temperature ($k_B T_f$) and is a key parameter in fast electron physics. Over the years, a significant amount of effort has been dedicated to determining the scaling of $k_B T_f$ with the laser intensity, which are reviewed below.

At lower laser irradiances (i.e. $I_L \lambda_L^2 < 10^{17}$ Wcm$^{-2}\mu$m^2) , it has been demonstrated that the electron temperature scales as $k_B T_f \propto \left(\sqrt{I_L \lambda_L^2}\right)^{1/3}$, as discussed within the context of both resonance absorption [70] and the numerically derived scaling by Gibbon *et al.* [71]. Moreover, an experimentally derived electron temperature scaling was obtained by Beg *et al.* [27] which also exhibited an intensity dependance of $k_B T_f \propto \left(\sqrt{I_L \lambda_L^2}\right)^{1/3}$.

For higher laser intensities, the mean electron temperature typically scales as $k_B T_f \propto \sqrt{I_L \lambda_L^2}$. One of the first derivations of this scaling was by Wilks *et al.* [72] (also known as $\mathbf{j} \times \mathbf{B}$, or ponderomotive, scaling) in which numerical simulations demonstrated a temperature scaling of:

$$k_B T_f = m_e c^2 \left(\sqrt{1 + a_0^2} - 1 \right) \tag{2.50}$$

$$k_B T_f = 0.511 \text{ MeV} \left(\sqrt{1 + \frac{I_L \lambda_L^2}{1.37 \times 10^{18} \text{W} \mu\text{m}^2 \text{cm}^{-2}}} - 1 \right) \tag{2.51}$$

This particular intensity scaling is well reproduced by the analytical model of Haines *et al.* [73]. For the intensities explored within the framework of the investigations presented in Chapter 5, 6 an 7, the ponderomotive scaling of the mean electron temperature is used.

However, a word of caution must be made regarding these temperature scalings; $k_B T_f$ is typically derived using the peak laser intensity within a particular scaling law. As clearly demonstrated by Chen *et al.* [74], a single intensity-temperature parameter is an oversimplified approach. The spatial-intensity profile of the laser focal spot produces a range of electron temperatures, and thus the electron spectrum should be calculated such that the spatial variation of injected electron temperatures is accounted for.

The precise determination of both the number (i.e. laser-to-electron conversion efficiency) and temperature of the fast electron population poses one of the most important outstanding issues in ultraintense laser-solid interactions, and there is still much work needed for a precise quantitative understanding. In addition, the exact relationship between the escaped and initial electron distributions is not well understood. However, the excellent progress made so far in determining empirical (and numerical) scalings enables the interpretation of experimental and numerical results within a reasonable level of uncertainty.

Chapter 3

Fast Electron Transport and the Influence of Electrical Resistivity

3.1 Introduction

In Chapter 2, the mechanisms by which energy from the laser pulse is coupled into the generation, and subsequent acceleration, of a population of energetic electrons beyond the critical surface were presented. Building upon these concepts, this chapter discusses the subsequent propagation of the fast electrons within the solid target.

Of key importance to the physics of fast electron transport is the electrical resistivity of the solid, which influences the fast electron beam transport primarily via the generation of magnetic fields possessing significant strength. In addition, resistivity also plays an important role in beam instability processes (e.g. filamentation). This chapter begins with a fundamental description of how resistivity is defined for low-temperature solids (i.e. room temperature, 0.025 eV), plasmas (i.e. high temperature, > 100 eV) and transitionary states between solids and plasmas (i.e. states of 'warm dense matter', ~ 1 - 100 eV). The chapter concludes by detailing the role of resistivity in the context of influencing fast electron transport through self-generated magnetic fields.

3.2 Resistivity

An electric current represents a flow of electrons (i.e. electric charge); resistivity represents the ability of a material to inhibit this electron flow. Within the context of solids, ions exist in fixed locations arranged in a crystalline (i.e. lattice) or non-crystalline (i.e. amorphous) structure, and thus resistivity in solids is governed by the electron motion through the ionic structure. This section begins with a basic description of solid-state resistivity, before describing the resistivity of a plasma and finally detailing the resistivity of transitionary states of warm dense matter. A good understanding of both how electrons propagate in solids, as well as of the different descriptions of resistivity across a wide temperature regime, is relevant for the results presented in this thesis. This chapter therefore seeks to answer the question: what is electrical resistivity?

The Drude model [75] was one of the first models to explain the transport properties of electrons in solids. By proposing that a solid (in this case, a metal) is composed of ions (which are static and arranged in a lattice structure) and electrons (which can move freely throughout the solid), the electron motion was calculated by considering collisions with background ions.

Assuming that the free electrons can be described by the kinetic theory of an ideal gas, the average electron thermal velocity, v_{th}, as:

$$\frac{1}{2}m_e v_{th}^2 = \frac{3}{2}k_B T_e \tag{3.1}$$

$$v_{th} = \sqrt{\frac{3k_B T_e}{m_e}} \tag{3.2}$$

where m_e is the electron mass, T_e is the electron temperature and k_B is Boltzmann's constant. An important parameter to aid in describing resistivity across the temperature regime is the average distance over which an electron propagates before undergoing a collision, defined as the mean free path, λ_{mfp}:

$$\lambda_{mfp} = v_{th}\tau_c \tag{3.3}$$

where τ_c is the collision time.

When an electric field, E_{app} is applied to the metal (which acts to move the electrons, thereby creating a electrical current), the average velocity of the electrons is given by the drift velocity, $\hat{v}_D$, which is in the direction of the electric field and defined by:

$$\hat{v}_D = \frac{eE_{app}\tau_c}{m_e} \tag{3.4}$$

where e is the electronic charge. Note that the drift velocity is significantly smaller (i.e. ~ 7 orders of magnitude) than the electron thermal velocity; this is a consequence of the random motion electrons follow during collisions with the ions.

When an electron collides with an ion, the kinetic energy (gained from the electric field) is transferred from the electron to the ion leading to an increase in the temperature of the material (due to the increase in thermal vibrations). Thus, resistivity is indicative of how electron kinetic energy is converted into thermal energy (i.e. heat) due to the collisions between electrons and ions.

To derive the resistivity of a cold solid, let the electric current, I_e, be defined as the number of electrons propagating through a cross-sectional area, A, per unit time: $I_e = en_e\hat{v}_D A$, where n_e is the electron number density. The resulting electron current density is given by:

$$J_e = \frac{I_e}{A} = en_e\hat{v}_D = en_eE_{app}\mu \tag{3.5}$$

where $\mu = e\tau_c/m_e$ is a constant which defines the electron mobility. The product of the electron number density, n_e, mobility, μ, and electronic charge, e, is a constant for a given material, the inverse of which defines the resistivity, η:

$$\eta = \frac{1}{en_e\mu} \tag{3.6}$$

Thus, Eq. (3.5) can be written as:

$$J_e = \frac{E_{app}}{\eta} \tag{3.7}$$

This is the microscopic form of Ohm's law, which is equivalent to the more familiar $V = IR$. By way of example, the typical resistivity of a metal at room temperature (i.e. 295 K) assuming an electron mean free path of 1 nm and electron number density of 10^{29} m^{-3} is $\eta \sim 10^{-7}$ Ωm, which is in good agreement with experimental measurements for a wide variety of metals.

Despite the usefulness of the Drude model for describing some properties of metals (i.e. room temperature resistivity), as well as providing an intuitive explanation of resistivity, it fails to accurately describe the temperature dependence of resistivity. For example, the Drude model predicts the resistivity of metals to scale with temperature as $\propto \sqrt{T_e}$, whereas experimental measurements show that the resistivity of metals is proportional to T_e for a range of temperatures [76]. This arises from two key erroneous assumptions made in the Drude model: 1) the electrons in the solid are described as a gas (i.e. kinetic theory); and 2) the ions are assumed to be static, and electrostatic interactions between the electrons and ions (i.e. electron-ion interactions) and between the free electrons (i.e. electron-electron interactions) are ignored. While the contribution to resistivity arising from electron-electron collisions is negligible, electron-ion collisions do contribute significantly to the resistivity.

The inclusion of electron-ion collisions requires the electrons to be treated quantum mechanically, first calculated by Bloch [77]. In contrast to the Drude model, which assumes that the electrons collide with the ions, in the quantum case as the electron approaches the ion (due to both it's thermal velocity and attractive Coulomb forces between the nucleus and electron) it is repelled, not through collisions with the ion, but by the outer filled shell of electrons (valence band - see Fig. 3.1 (a)). Thus, resistivity arises due to scattering of the electrons by the electrons in energy orbitals surrounding the ion. As demonstrated by Bloch [77], a perfect ionic lattice structure (i.e. no imperfections) results in the solid possessing zero resistivity. Instead, resistivity arises due to imperfections in the ionic lattice which cause deflection of the electrons. Consequently, the mean free path of an electron in an imperfect lattice is not infinite and thus the material has a non-zero resistance. Since the mean free path is determined

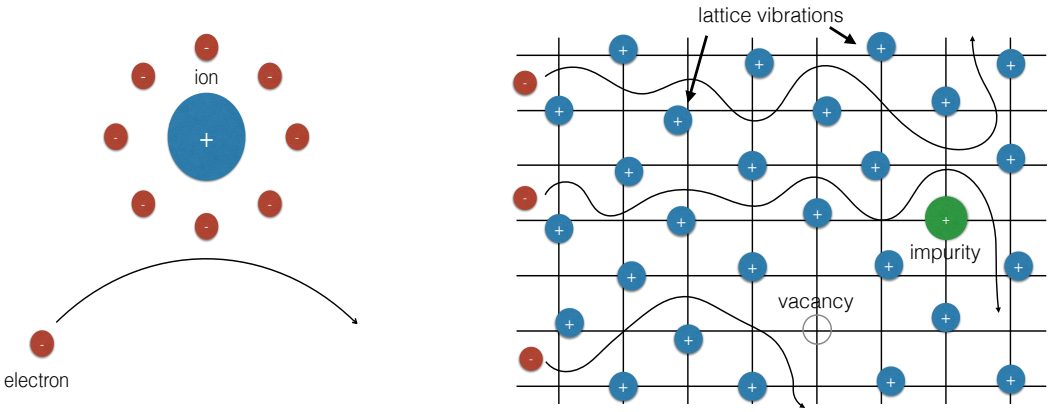

(a) (b)

Figure 3.1: Electron motion in an ionic lattice: (a) an electron approaching a positive ion is scattered by the outer valence electron shells; (b) an electron is scattered by ion thermal vibrations (i.e. phonons), impurities and vacancies of the lattice.

by scattering from the lattice sites, it is sensitive to the lattice structure of the solid and therefore important when describing the difference in resistivity between materials of different lattice structure – this is key to the results discussed in this thesis.

For solids, there are, in general, three types of lattice imperfection which give rise to resistivity: 1) thermal vibrations of the lattice (i.e. quantised units of lattice vibration – phonons); 2) impurities; and 3) crystal imperfections (i.e. vacancies at sites in the lattice). These are shown schematically in Fig. 3.1 (b), and each act to generate a finite electron mean path by scattering the electron which determines the resistivity of the solid.

3.2.1 Low temperature resistivity: band theory

A quantitative description of resistivity is obtained from the band structure theory of solids. The formation of a solid results in the individual atoms being arranged in a crystalline (or non-crystalline) structure. Note that a non-crystalline solid lacks the long-range order characteristic of a crystal lattice structure, but still exhibits some degree of local structure. Solids are characterised by the electron orbitals constituting the individual atoms combining to form a continuous band

of energies (i.e. an energy continuum) known as the valence band. In addition, energy regions form which are not enclosed by the valence band, due to the finite width of the individual energy bands. These regions of forbidden energy are known as band gaps with corresponding energy values (i.e. widths) determined by the material atomic structure. For conduction to occur, electrons must exist above the band gap in the region known as the conduction band. As will be described, it is the formation of these band gaps relative to the valence and conduction bands that enables the resistivity of metals, insulators and semiconductors to be characterised.

To describe the electronic band structure of solids in more detail, the free electron model of a solid is utilised [77, 78]. In this model, the average potential inside the material (which arises due to the valence electrons and ions) is constant throughout the solid, with a large potential formed at the sample edge which inhibits electrons from escaping the solid. Under normal conditions (i.e. room temperature) the average thermal energy of the orbital electrons is ~ 0.025 eV, and thus the probability of an electron escaping from the solid is infinitesimally small. Physically, this is envisaged as the well-known infinite potential well of length L (which corresponds to the size of the crystal), which is used to demonstrate the formation of orbital bands.

First, the allowed energy levels are obtained by solving the Schrödinger equation, which in 1-D is:

$$-\frac{\hbar^2}{2m_e}\frac{d^2\psi}{dx^2} = E\psi \tag{3.8}$$

where ψ is the eigenfunction (i.e. electron wavefunction), E is the allowed electron energies (i.e. eigenenergies). The solution of the Schrödinger equation generates a set of allowed eigenenergies, expressed by:

$$E = \frac{\hbar^2 k_x^2}{2m_e} = \frac{\hbar^2 \pi n_x^2}{2m_e L^2} \tag{3.9}$$

where n_x is an integer. Extending the solution to three dimensions (again for the case of an infinitely deep box of transverse dimension (i.e. width) L) results in a

range of allowed electron energies given by:

$$E = \frac{\hbar^2 k^2}{2m_e} = \frac{\hbar^2 \pi}{2m_e L^2}\left(n_x^2 + n_y^2 + n_z^2\right) \tag{3.10}$$

In k-space, many electron energy levels are made utilising a combination of $\left(n_x^2 + n_y^2 + n_z^2\right)$, where each combination corresponds to a point on a 3-D grid with the distance from the origin to a particular grid point given by $\left(n_x^2 + n_y^2 + n_z^2\right)^{1/2}$. Consequently, for the number of electrons present in a typical solid (i.e. $N \sim 10^{23}$ electrons), the energy of the highest occupied state is given by the the radius which encloses a sufficient number of grid points (i.e. orbital levels) to adequately accommodate the N electrons present in the solid. Since only integer values of n_x, n_y, and n_z are allowed, each grid point corresponds to a cube of unit volume, such that the number of grid points is equal to the volume under the surface. In k-space, this appears as a sphere of occupied states and a calculation of the density of states determines the energy of the highest occupied state, which is known as the Fermi energy, E_F, given by:

$$E_F = \frac{\hbar^2}{2m_e}\left[\frac{3\pi^2 N}{V}\right] \tag{3.11}$$

which also corresponds to the energy of the surface of this sphere. Thus, for conduction to occur electrons must be excited out of the valence band above the Fermi energy into the conduction band.

While this model is instructive for describing the general features of the band theory of solids, it doesn't account for the individual atomic potentials present in the crystal and instead assumes a constant potential within the solid (i.e. the potential is constant across the crystal dimension L). In a crystal, the potential varies periodically with the spacing of the atoms. More advanced models have been developed to include the effect of the lattice ions on the potential [78]. Nevertheless, the free electron model description of band theory presented above predicts that electrons in a solid form orbitals, which increase in energy with increasing distance from the atom, and the energy of the highest occupied state is given by the Fermi energy. For example, for a typical metal at solid density

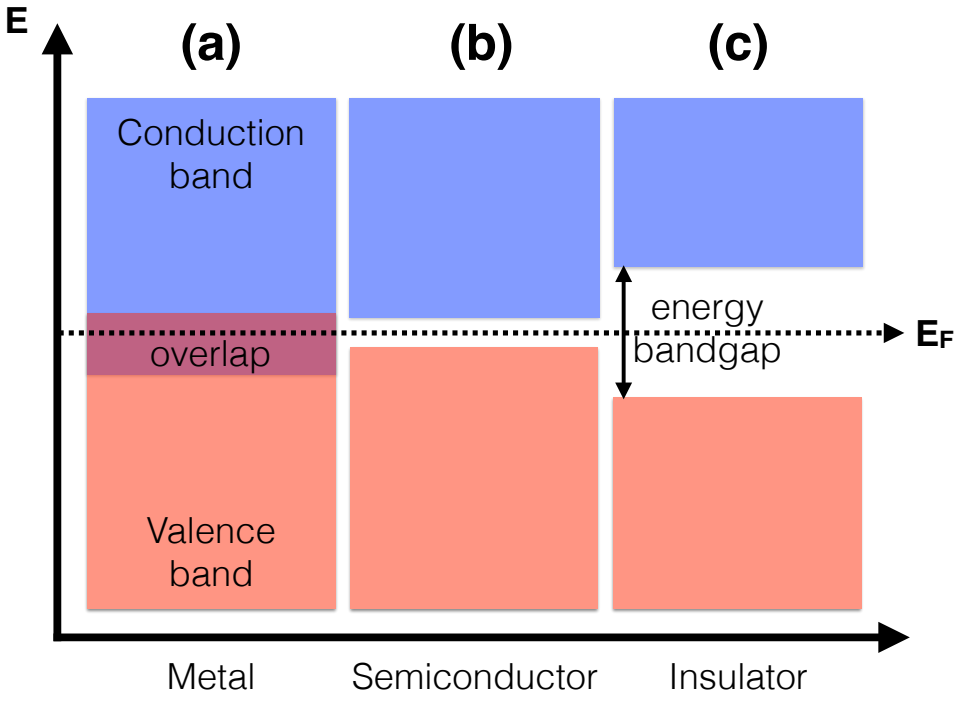

Figure 3.2: Band structure theory of solids: (a) metals are characterised by overlapping conduction and valence bands, resulting in free electrons in the conduction band; (b) semiconductors have a small bandgap that can be overcome by thermal excitation; and (c) insulators have a large bandgap which results in high resistivity.

(i.e. aluminium), the Fermi energy is around 10 eV.

Moreover, the band theory of solids enables an understanding of the distinct difference in resistivity between metals, insulators and semiconductors. This is shown schematically in Fig. 3.2. In this schematic, the occupied states are denoted as the valence band (in red) while the conduction band (blue region) represents de-localised electrons which are free to move throughout the solid. The Fermi energy is represented by the horizontal dotted line. The metallic bonds characteristic of metals result in free electrons moving within the metallic lattice. The corresponding band structure takes the form displayed in Fig. 3.2 (a), where there is an overlap region between the partially-filled valence band and conduction band (with the Fermi energy existing in this overlap region). Thus, metals have low resistivity at room temperatures, with the electrical resistivity arising from imperfections in the crystal lattice due to the presence of phonons

(i.e. quantised lattice vibrations). With increasing temperature, the resistivity of a metal increases linearly due to increased electron-phonon scattering.

For insulators, the covalent (or ionic) bonding present in the solid results in all electron orbitals being filled and therefore a distinct energy band gap exists between the valence and conductions bands (Fig. 3.2 (c)). Thus, insulators have a high resistivity at room temperature. To enable an insulator to conduct electrons, a large amount of energy (i.e. heat) must be supplied to excited electrons above the large bandgap energy.

Finally, semiconductors represent an intermediate stage between metals and insulators (Fig. 3.2 (b)). While similar to insulators in that they possess a partially filled valence band, the resulting energy band gap between the valence and conduction bands is sufficiently small that electrons can be thermally excited above the Fermi energy into the conduction band. For example, the band gap of silicon and germanium is 1.1 and 0.67 eV respectively (at room temperature). Thus, the resistivity of a semiconductor decreases with increasing temperature as electrons are excited above the relatively small band gap from the valence band into the conduction band.

The band theory of solids therefore provides a framework to explain the resistivity of solids at low temperature. In intense laser-solid interactions, the target is heated (by both the laser-field directly and collisional return current electrons) on very short timescales ($<$ picosecond) and therefore the solid transitions from low temperatures (in which the resistivity is described using the band theory of solids) to hot plasma temperatures. The resistivity of matter at plasma temperatures (i.e. $>$ 100 eV) is now discussed.

3.2.2 Plasma resistivity

When sufficient energy is supplied (e.g. using an intense laser pulse), a relatively thin solid (i.e. of thickness $< 30\mu$m) will reach temperatures of the order $>$ 100 eV, and subsequently become fully ionised. In this case, the resistivity arises from collisions between electrons and ions (i.e. Coulomb collisions). A schematic of Coulomb collisions in a plasma is displayed schematically in Fig. 3.3. The resis-

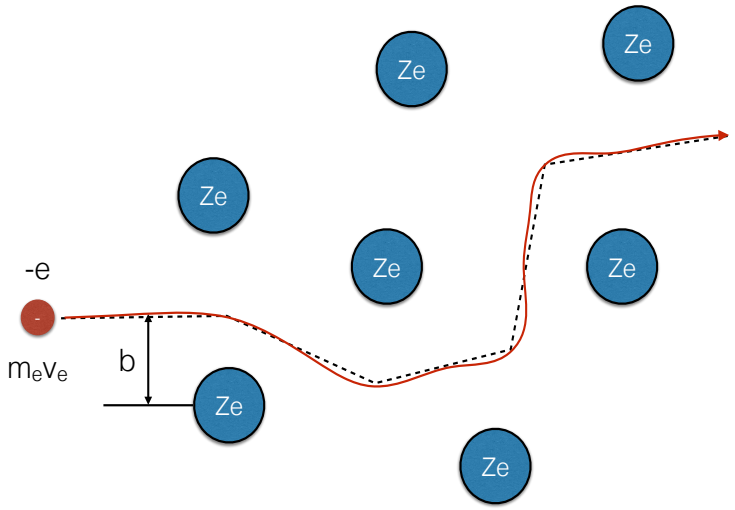

Figure 3.3: Plasma resistivity. Collisions between the electrons and ions result in an electron exhibiting continuous deflections, or scatterings, of its direction of motion, with the largest deflections occuring when it passes close to an ion.

tivity can be estimated by considering the case of an electron (with momentum $p_e = m_e v_e$ and charge $-e$), colliding with an ion (with charge Zq_e). The force arising from the collision between an electron and ion (i.e. the Coulomb force) is given by:

$$F_{e-i} = -\frac{Ze^2}{4\pi\varepsilon_0 r^2} \tag{3.12}$$

where r is the distance between the electron and ion. The distance of closest approach between the electron and ion is known as the impact parameter, b, and is defined as:

$$b = -\frac{e^2}{4\pi\varepsilon_0 m_e v_e^2}\frac{1}{\tan(\theta_s/2)} \tag{3.13}$$

For fully ionised plasmas the upper (b_{max}) and lower (b_{min}) limits of the impact parameter are set by the Debye length (i.e. $b_{max} = \lambda_D$) and the impact parameter corresponding to 90° scattering (i.e. $b_{min} = b_0$), respectively.

The impact parameter that arises from the lower limit (i.e. 90° scatter) is

given by:

$$b_0 = -\frac{e^2}{4\pi\varepsilon_0 m_e v_e^2} \tag{3.14}$$

with corresponding change of electron momentum:

$$m_e v_e = -\frac{Ze^2}{4\pi\varepsilon_0 m_e v_e^2} \tag{3.15}$$

By using Eq. 3.14 and Eq. 3.15 in conjunction with the Coulomb cross section $\sigma = \pi b_0^2$ and collision frequency $\nu_{e-i} = n_e \sigma_c v_e$ (assuming a Maxwellian distribution of electron velocities), the resistivity is given by:

$$\eta \approx \frac{Z\pi e^2\sqrt{m_e}}{(4\pi\varepsilon_0)^2 k_B T_e^{3/2}} \tag{3.16}$$

While this calculation assumes that large-angle electron-ion scattering is the dominant collision mechanism, small angle deflections will also contribute to the resistivity and are included by using the Coulomb logarithm, lnΛ, where Λ is the ratio of the maximum and minimum impact factors, $\Lambda = b_{max}/b_{min}$. The Coulomb logarithm also includes corrections for electron degeneracy and, as described by Lee and More [79], results in an estimated value of $\ln\Lambda \geq 2$. Incorporating the Coulomb logarithm correction factor into Eq. 3.16 results in the the Spitzer resistivity [80], η:

$$\eta \approx \frac{Z\pi e^2\sqrt{m_e}}{(4\pi\epsilon_0)^2 k_B T_e^{3/2}} \ln\Lambda \tag{3.17}$$

The Spitzer model predicts a resistivity which increases proportionally with temperature as $T_e^{-3/2}$. It is important to note that the Spitzer resistivity is only valid for a fully ionised, non-degenerate plasma (i.e. low density and high temperature state). Within the context of a laser-solid interaction, the resistivity of the background plasma in the region close to the focal spot (i.e. over the first few μm into the target) can be accurately described using the Spitzer model. However, deeper into the target (i.e. beyond $\sim 10\mu$m) where the background plasma is cooler, the Spitzer model is not applicable − application of the Spitzer

model to plasma temperatures of the order $T_e < 10$ eV gives incorrect resistivity predictions. Thus, a better understanding of the resistivity in the transient temperature regime between cold solid and hot plasma is required.

3.2.3 Resistivity of degenerate matter

Increasing the temperature of a cold solid (in which the resistivity is described within the framework of solid state theory, as outlined in section 3.2.1) to that of an ionised plasma (described in section 3.2.2) represents a temperature transition from 0.025 eV to $>$ 100 eV. A temperature change of this magnitude invariably results in a transition through a state of matter known as 'warm dense matter' (WDM), which exists at the interface between condensed matter (i.e. low temperature) and plasma (i.e. high temperature) physics.

This state is characterised by strong ion-ion coupling, partial electron degeneracy and partial ionisation. Qualitatively, this represents states in which the density is maintained at between 0.1-10 times solid density, and the temperature is in the region of 1-100 eV [81]. Quantitatively, WDM is characterised using the quantum degeneracy parameter Θ: $\Theta = T_{e/i}/T_F$, where $T_{e/i}$ is the temperature (either electron or ion) and T_F is the Fermi temperature ($T_F = E_F/k_B$); and the plasma coupling parameter Γ: $\Gamma = \langle E_P \rangle / \langle E_K \rangle$, where $\langle E_P \rangle$ is the average potential energy and $\langle E_K \rangle$ is the average kinetic energy. WDM is defined as having partially degenerate electrons (i.e. $\Theta \leq 1 -$ the thermal temperatures are of the order of the Fermi temperature) and being strongly coupled (i.e. $\Gamma \geq 1 -$ comparable thermal and kinetic energies).

The challenges associated with describing the physical properties of WDM (e.g. resistivity) arise from the inability of both standard condensed matter and plasma theory to account for the relevant physics needed to fully describe a partially degenerate, strongly coupled plasma. In recent years, much theoretical effort has been devoted to obtaining a better understanding and accurate description of the transport properties of WDM, utilising both analytical and simulation methods [82–84].

Of relevance to the results of fast electron transport presented in this thesis,

two methods of calculating the resistivity-temperature profile that account for the transitionary WDM state have been employed: the Lee-More resistivity model [79]; and quantum molecular dynamic (QMD) calculations coupled to the Kubo-Greenwood equation [85]. These are explored in turn.

1. The Lee-More model

The Lee-More model [79] is a wide-parameter range, semi-analytical model used to calculate transport coefficients in dense plasmas, which attempts to bridge the gap between plasma and non-plasma (i.e. solid and liquid) states by including electron degeneracy (i.e. low temperature effects) in conjunction with an accurate calculation of high temperature resistivity (i.e. Spitzer model).

The Lee-More model gives a consistent and complete set of transport coefficients, including electrical resistivity, for a wide range of temperatures and densities. The model obtains the transport coefficients from the solutions of the Boltzmann equation in the relaxation time approximation. The collision operator includes contributions from the scattering of electrons by ions and neutrals. The electron degeneracy effects on the transport coefficients are accounted for by using a Fermi-Dirac distribution to describe the electrons. The electron relaxation time τ is calculated using contributions from both electron-ion and electron-neutral scattering,

$$\frac{1}{\tau} = \frac{1}{\tau_{e-i}} + \frac{1}{\tau_{e-n}} \tag{3.18}$$

where

$$\tau_{e-i} = \frac{1}{n_i v_e \sigma_{e-i}} \tag{3.19}$$

$$\tau_{e-n} = \frac{1}{n_n v_e \sigma_{e-n}} \tag{3.20}$$

are the electron-ion and electron-neutral collision rates respectively, n_i is the ion density, n_n is the neutral density, and σ_{e-i} and σ_{e-n} are the electron-ion and neutral momentum transfer cross sections respectively.

For efficiency in the calculations, a Coulomb cross section with appropriate

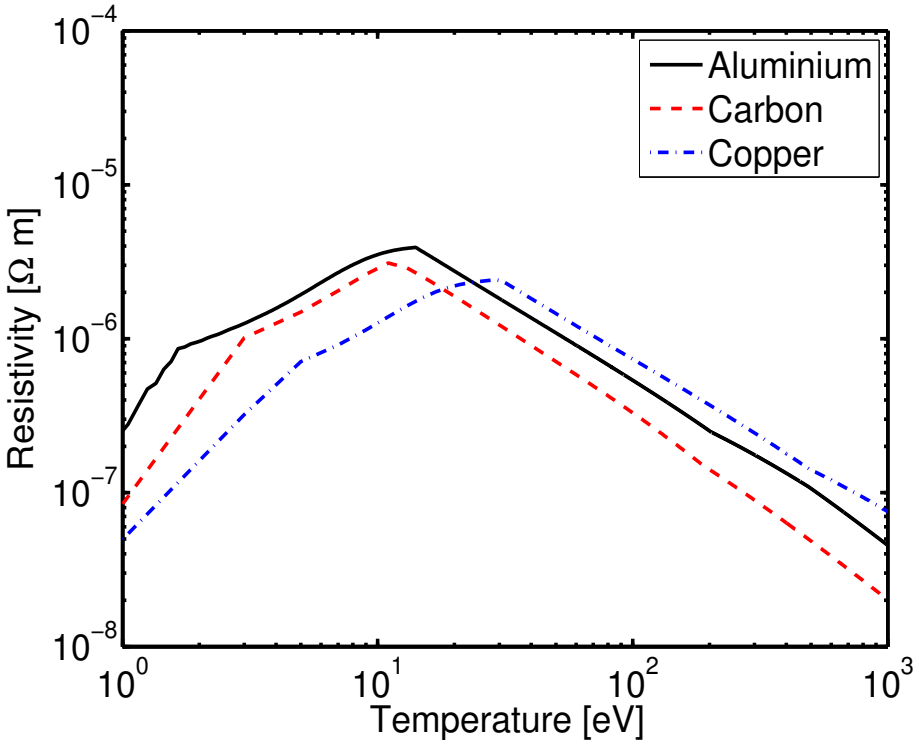

Figure 3.4: Resistivity-temperature profiles calculated using the Lee-More model for three example materials: aluminium (black curve); carbon (red curve) and copper (blue curve).

cut-off parameters is used which gives good approximation to the transport coefficients calculated from numerically derived cross sections; the cutoff parameters are obtained by comparing the Coulomb cross section to results from a partial wave calculation [79]. In the partial wave calculations, the electron-ion cross section is obtained by numerical solution of the Schrödinger equation for the Thomas-Fermi potentials [86]. The Coulomb cross section employed in the Lee-More model is given by [79]:

$$\sigma_{tr} = \frac{4\pi(Z^*)^2 e^4 \ln\Lambda}{m_e^2 v_e^4} \tag{3.21}$$

where Z^* is the ionisation state and $\ln\Lambda$ is the Coulomb logarithm given by:

$$\ln\Lambda = \frac{1}{2}\ln\left(1 + \frac{b_{max}^2}{b_{min}^2}\right) \tag{3.22}$$

where b_{max} and b_{min} are upper and lower impact parameter cutoffs for Coulomb

scattering. For the Lee-More model, b_{min} is limited to the mean inter-atomic distance, while the maximum impact parameter is again given by the Debye length [87], corrected for electron degeneracy. The resulting Coulomb logarithm is set to have a minimum value of 2 to overcome an inherent difficulty in the model that arises from the calculated electric field screening length becoming less than the inter-atomic spacing. Lee and More justified the minimum value of the Coulomb logarithm by comparing with the partial-wave calculations by Green and Lee [88]. Central to the Lee-More model is the utilisation of the Thomas-Fermi ionisation model to calculate the ionisation state, electron density, n_e, and chemical potential, μ, of the material. The resulting resistivity is given by:

$$\eta = \frac{m_e}{n_e \tau_c e^2} \left[A^\alpha \left(\frac{\mu}{k_B T_e} \right) \right]^{-1} \tag{3.23}$$

where the A^α coefficient is given by:

$$A^\alpha \left(\frac{\mu}{k_B T_e} \right) = \frac{4}{3} \left[\frac{F_2}{\left(1 + \exp\left(-\mu / k_B T_e \right) \left(F_{1/2} \right)^2 \right)} \right] \tag{3.24}$$

where $F_{1/2}$ and F_2 are Fermi-Dirac integrals of order 1/2 and 2 respectively. In addition, the inter-atomic spacing dependency of the resistivity is incorporated within the collision time τ_c.

Displayed in Fig. 3.4 are example resistivity-temperature curves calculated using the Lee-More model [79, 89] for three elements: aluminium, copper and carbon. While the Lee-More model is in good agreement with experimental measurements of the resistivity of metals [90], it fails to accurately account for the resistivity of both insulators and semiconductors. Moreover, the Lee-More model does not include ion-ion correlations; strong ion-ion correlations can have a defining effect on the electron collision frequency and mean free path, and thereby resistivity. Therefore a more accurate treatment of the resistivity of matter transitioning through the warm dense matter regime must account for ionic structure effects.

2. QMD-Kubo-Greenwood calculations

A method used to calculate resistivity which accounts for ion-ion correlations has been developed by Desjarlais *et al.* [85] utilising the plane-wave density functional theory code VASP [91, 92]. In this case, the resistivity is obtained by using a combination of *ab initio* molecular dynamics simulations and first principle resistivity calculations. The calculation consists of three main components: QMD simulations, precise resolution of the band structure and calculation of the resistivity utilising the Kubo-Greenwood equation.

Initially, atoms are placed into a 'supercell' which exhibits periodic boundary conditions that represent the ionic lattice. The QMD simulation is then run (at a given density and temperature) to obtain the independent ionic configurations which are then used for the calculation of the transport properties (i.e. electrical resistivity). Note that the technique also gives the optical properties and thermal resistivity in addition to the electrical resistivity. Ion configurations for the resistivity calculations are obtained by performing the *ab initio* QMD simulations within the framework of the finite temperature density functional theory [93]. For the QMD runs, the ions and their respective core wavefunctions are modelled using the Vanderbilt ultra-soft pseudopotentials [94]. The DFT exchange and correlation functionals are calculated at the level of the generalised gradient approximation [85]. Next, the Schröedinger equation is solved for an effective potential that includes contributions from the ions, the classical contribution of the electrons, and the quantum-mechanical exchange and correlation contributions.

The electron density, n_e, is constructed from the wavefunctions, Ψ_i, given by the solutions from the Schrödinger equation:

$$n_e = \sum_{i=1}^{N} |\Psi_i|^2 \tag{3.25}$$

and the equations are iterated until convergence is obtained [85]. The forces on the ions are computed and the molecular dynamics simulations are performed to obtain a precise calculation of the electronic band structure for the selected ion configuration. Next, a total of ten to twenty ionic configurations are selected

from an equilibrated (in an average sense) portion of the QMD simulation. For each of these configurations, the electrical resistivity is calculated using the Kubo-Greenwood formula.

The Kubo-Greenwood formula [95] gives the electrical resistivity directly from the electron wavefunctions that arise from the ion configurations sampled from the QMD simulations. Thus, it avoids the difficulties of calculating (or modelling), independently and consistently, the population of free electrons, the various relaxation times between the electrons and other species, and the proper form of the pseudopotential and screening models. In addition, it includes contributions to the resistivity from electron-atom, electron-ion, and electron-electron interactions. This enables a much more accurate calculation of the low-temperature (i.e. 0.025 eV - 20 eV) electrical resistivity than that obtained from the Spitzer and Lee-More models.

The Kubo-Greenwood formula for the electrical conductivity, as a function of the frequency ω for a particular $\mathbf{k}$ point in the Brillouin zone of the simulation supercell is given by:

$$\sigma_{\mathbf{k}}(\omega) = \frac{2\pi e^2\hbar^2}{2m_e^2\omega\Omega}\sum_{j=1}^{N}\sum_{i=1}^{N}\sum_{\alpha=1}^{3}\left[F(\epsilon_{i,\mathbf{k}}) - F(\epsilon_{j,\mathbf{k}})\right]|\left\langle\Psi_{j,\mathbf{k}}|\nabla_\alpha|\Psi_{i,\mathbf{k}}\right\rangle|^2\delta\left(\epsilon_{j,\mathbf{k}} - \epsilon_{i,\mathbf{k}} - \hbar\omega\right) \quad (3.26)$$

where the i and j summations are over the N discrete electron bands included in the triply periodic calculation of the cubic supercell volume element Ω. The α sum corresponds to the three spatial directions, $F(\epsilon_{i,\mathbf{k}})$ is the Fermi weight corresponding to the energy $\epsilon_{j,\mathbf{k}}$ for the ith band at $\mathbf{k}$ and $\Psi_{i,\mathbf{k}}$ is the corresponding wave function.

In general, the integration over the Brillioun zone is performed using the method of special $\mathbf{k}$ points [96]:

$$\sigma(\omega) = \sum_{\mathbf{k}}\sigma_{\mathbf{k}}(\omega)W(\mathbf{k}) \quad (3.27)$$

where $W(\mathbf{k})$ is the weighting factor for the point k in the Brillouin zone. The

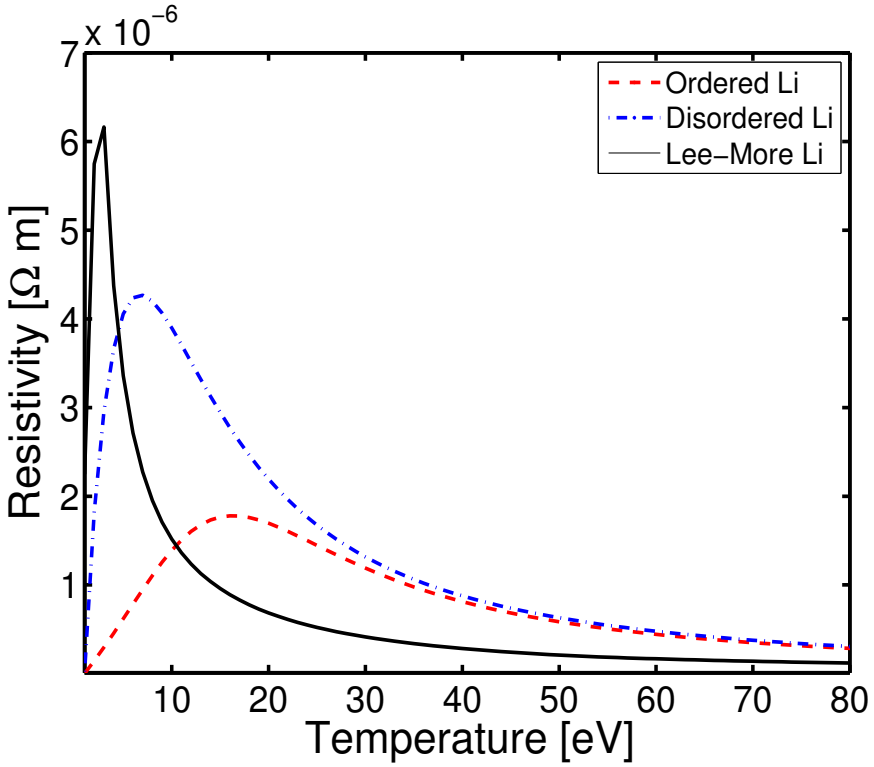

Figure 3.5: Resistivity-temperature profile of lithium obtained using the QMD-Kubo Greenwood method, by Dr M. P. Desjarlais at Sandia National Laboratories. The calculation is performed for ions in both an ordered (red curve) and amorphous (i.e. disordered) lattice (blue curve). The resistivity of lithium calculated using the Lee-More model is also shown (black curve).

final result is obtained by taking the average of $\sigma(\omega)$ over the ensemble of configurations sampled. Finally, the resistivity is obtained by taking the reciprocal of Eq. (3.27). Example resistivity curves calculated for lithium using the QMD-Kubo-Greenwood technique are shown in Fig. 3.5, for the case of a disordered (blue curve) and ordered (red curve) ionic lattice. Also shown is the resistivity of lithium calculated using the Lee-More model (black curve).

The form of the lithium resistivity-temperature profiles calculated using the QMD-Kubo-Greenwood method, for both ordered and disordered lattice structure, can be understood as follows. For metals (i.e. lithium or aluminium), there are free electrons (at room temperature) and thus a low resistivity. However, as the temperature of the solid is increased the ions will oscillate about their equilibrium position which results in an increased rate of electrons - phonon scattering. For lattice temperatures greater than the Debye temperature (i.e. the temper-

ature of the highest phonon vibration mode), a linear dependence of resistivity with temperature is predicted.

However, a maximum resistivity occurs when the electron mean free path is equal to the interatomic spacing. For example, lithium has a maximum resistivity of 4.2×10^{-6} Ωm and 1.9×10^{-6} Ωm for the disordered and ordered cases respectively − note that the mean free path in ordered lithium is longer than in disordered lithium, and thus the resistivity peak occurs at a higher value and lower temperature for the case of a disordered lattice. The minimum mean free path cannot be shorter than the mean interatomic distance, which therefore sets an upper limit to the value of the resistivity. As the temperature increases beyond this point (i.e. > 20 eV for lithium) the rate of collisions decreases with increasing energy and the resistivity is accurately described using the Spitzer model.

Finally, the Lee-More model (black curve - Fig. 3.5) calculation for lithium displays a significantly different result to both the ordered and disordered lithium cases. This primarily arises from the QMD-Kubo-Greenwood method accounting for the influence of the structure of the ionic lattice (i.e. ion-ion correlations). The extent to which lattice structure influences fast electron transport is explored in this thesis.

Summary - resistivity

This section has explored the resistivity-temperature variation across a wide range of temperatures, specifically focussing on three temperature regimes relevant to intense laser-solid interactions: 1) cold solid (i.e. condensed matter); 2) hot plasma; and 3) transitionary WDM. Of key importance to the results presented in this thesis is the distinctly different resistivity-temperature profile obtained for semiconductors, insulators and metals. Additionally, the physical explanation for the difference in resistivity for ordered and disordered lattices (see Fig. 3.5) plays a key role in the results presented in this thesis. The description of these results, together with the influence of resistivity arising from the transient WDM state on fast electron transport, forms the foundation of the results reported in Chapters 5, 6 and 7.

3.3 Fast electron transport

The intense laser-solid interaction generates a population of fast (i.e. MeV) electrons that are injected at the critical surface into the overdense target where the electrons undergo a range of physical effects. In Chapter 2, section 2.3.4, the fast electron beam source properties (i.e. fast electron density, energy spectrum and temperature) were discussed. In this section, the transport phenomena that the fast electrons are subject to are explored in detail, with emphasis placed upon the role of resistivity in defining the electron transport properties.

3.3.1 Current neutrality

The relation that is central to fast electron transport in conditions relevant to intense laser-solid interactions is the current balance relation (i.e. current neutrality) [97]:

$$\mathbf{j}_f + \mathbf{j}_r = 0 \tag{3.28}$$

where $\mathbf{j}_f$ and $\mathbf{j}_r$ are the fast electron and return current densities respectively. There are two key reasons which demonstrate the validity of charge neutrality.

The first of these is associated with the electric field generated by the fast electron beam current. For laser parameters used in a typical intense laser-solid interaction (i.e. $E_L \approx 100$ J and $\tau_L = 1$ ps), the fast electron velocity and density are approximately 10^8 ms^{-1} and 10^{26} m^{-3} respectively. The resulting current density is given by:

$$\mathbf{j}_f = -en_f\mathbf{v}_f \approx 10^{16}\ \text{Am}^{-2} \tag{3.29}$$

with corresponding fast electron current ~ 25 MA.

The electric field arising from this current density is calculated using:

$$\frac{\partial \mathbf{E}}{\partial t} = -\frac{\mathbf{j}_f}{\varepsilon_0} \tag{3.30}$$

resulting in an electric field magnitude of the order of 10^{15} Vm^{-1}. A field of

this magnitude is sufficiently large to halt the propagation of an MeV electron beam in a distance of $< \mu$m. In addition to the electric field, strong self-induced magnetic fields associated with this charge separation inhibit the propagation of the fast electron beam. The maximum current that can propagate before being deflected by the self-induced electromagnetic fields is given by the Alfvèn limit [98], I_A, expressed as:

$$I_A \simeq \frac{\beta\gamma m_e c^2}{e} = \beta\gamma\, 1.7 \times 10^4\,\mathrm{A} \tag{3.31}$$

where $\beta = v/c$ and γ is the Lorentz factor. For parameters typical of the laser-solid interactions investigated in this thesis, the Alfvèn limit is estimated to be $I_A = 70$ kA. By contrast, the fast electron beam current, I_f, is of the order of $I_f \approx 20\,\mathrm{MA}$, greatly exceeding the Alfvèn limit. Thus, a return current must exist to enable transport of the multi-MA current of fast electrons by neutralising the fast electron current density, thereby inhibiting the strong electromagnetic fields. Note that charge neutrality typically occurs on a time-scale given by $t_{j-r} = 2\pi/\omega_{pe}$ (where ω_{pe} is the electron plasma frequency), which is on the order of < 1 fs (although this is different for conductors and insulators due to the variation in availability of free electrons).

Moreover, Bell *et al*[99] used a simple energy conservation argument to demonstrate why current neutrality is also spatially localised with the fast electron beam. Firstly, consider the magnetic field generated around a column of fast electrons (of radius r_f). The corresponding radius of the return current electron population, R, is given by $R = r_f + \Delta R$, where ΔR is the difference in radius between the fast electron beam and return current beam. To ensure neutrality, both electron beam sources (i.e. fast and return current electrons) have the same current magnitude, $I_f = -I_r$. The current density of the fast electrons and return current electrons is given by: $\mathbf{j}_f = I_f/\pi r_f^2$; and $\mathbf{j}_r = I_f/\pi R^2$. The corresponding

magnetic field is given by:

$$\mathbf{B} = \frac{\mu_0 I_f}{2\pi} \begin{cases} r(\frac{1}{r_f^2} - \frac{1}{R^2}), & \text{if } r < r_f, \\ \frac{1}{r} - r\frac{1}{R^2}, & \text{if } r_f < r < R, \\ 0, & \text{if } r_f < r. \end{cases} \tag{3.32}$$

Assuming that $\Delta R \ll r_f$, the maximum magnetic field is given by: $B_{max} = \mu_0 I_f(\Delta R/r_f)/\pi r_f$. The corresponding magnetic energy contained within electron cylinder (per unit length) is given by: $E_{BL} = \mu_0 I_f^2(\Delta R/r_f)^2/4\pi$.

By way of example, a fast electron beam radius of $r_f = 10\mu$m and $I_f = 20$ MA, results in a maximum magnetic field of $B_{max} = \mu_0 I_f(\Delta R/r_f)/\pi r_f = 10^6(\Delta R/r_f)$ T, and corresponding magnetic energy per unit length given by: $E_{BL} = \mu_0 I_f^2(\Delta R/r_f)^2/4\pi = 40(\Delta R/r_f)^2$ Jμm^{-1}. Thus, ΔR must be much smaller than r_f (i.e. $\Delta R \ll r_f$) for conservation of energy to hold (i.e. so that the magnetic energy contained within the beam is not greater than the energy absorbed from the laser pulse). This clearly demonstrates why current neutrality must be locally true (i.e. $\mathbf{j}_f \approx -\mathbf{j}_r$). Additionally, while these simple analytical estimates provide clear evidence of the validity of the current balance relation, current neutrality has also been observed in 3D particle-in-cell (PIC - see Chapter 4) simulations [100, 101].

3.3.2 Collisions and target heating

As the fast electrons propagate into the solid-density target, energy is lost from the beam via collisions with the electrons and ions that constitute the background dense plasma. This occurs through a combination of scattering (both elastic − electron-electron collisions, and inelastic − electron-ion collisions), excitation (i.e. to higher band energies), ionisation and radiation emission (i.e. bremsstrahlung). To quantify the energy loss, the total stopping power, $(dE/ds)_{total}$, is calculated from the summation of the individual contributions arising from each energy loss

mechanism, given by:

$$\left(\frac{dE}{ds}\right)_{total} = \left(\frac{dE}{ds}\right)_{collisions} + \left(\frac{dE}{ds}\right)_{radiative} \tag{3.33}$$

Thus, the total stopping power is a function of the contribution of energy lost through collisional losses, which occur due to collisions between the fast electron beam and plasma particles, and radiative losses, which correspond to bremsstrahlung emission arising from the interaction of the fast electrons with the background ions.

To understand the energy loss mechanisms, example electron stopping curves are shown in Fig. 3.6 for two elements (carbon and silicon) that are relevant to the results described in this thesis. These profiles were obtained from the ESTAR stopping tables (available from the NIST database [102]). The calculation of the total stopping power involves utilising the Bethe theory of particle stopping [103, 104] to calculate the collisional power component, and theoretical bremsstrahlung cross sections [105] to obtain the radiative loss component.

The stopping curves reveal that collisional losses dominate for lower energy electrons (i.e. 0.01 - 1 MeV; blue region of Fig. 3.6) while higher energy electrons (i.e. $>$ 10 MeV; red region of Fig. 3.6) correspond to radiation losses. This characteristic electron stopping profile for increasing electron energy has important implications for how energy is converted from the fast electron beam into heating of the background target.

For electron energies produced in a typical intense laser-solid interaction, the mean electron energy is of the order of $>$ 1 MeV (see Chapter 2). Thus, the fast electron beam itself does not significantly contribute to target heating via collisions with the background plasma (see Fig. 3.6). Rather, it is the return current electrons which are the primary source of target heating.

The return current is drawn (via electromagnetic fields - section 2.2.5) to neutralise the fast electron beam current, thereby enabling the MeV beam to propagate. Initially, the energy from the fast electron beam is transferred to the fields which slow down the fast electron beam, and subsequently draw the return current. Due to the charge neutrality condition (i.e. $n_f \mathbf{v}_f = -n_r \mathbf{v}_r$) the

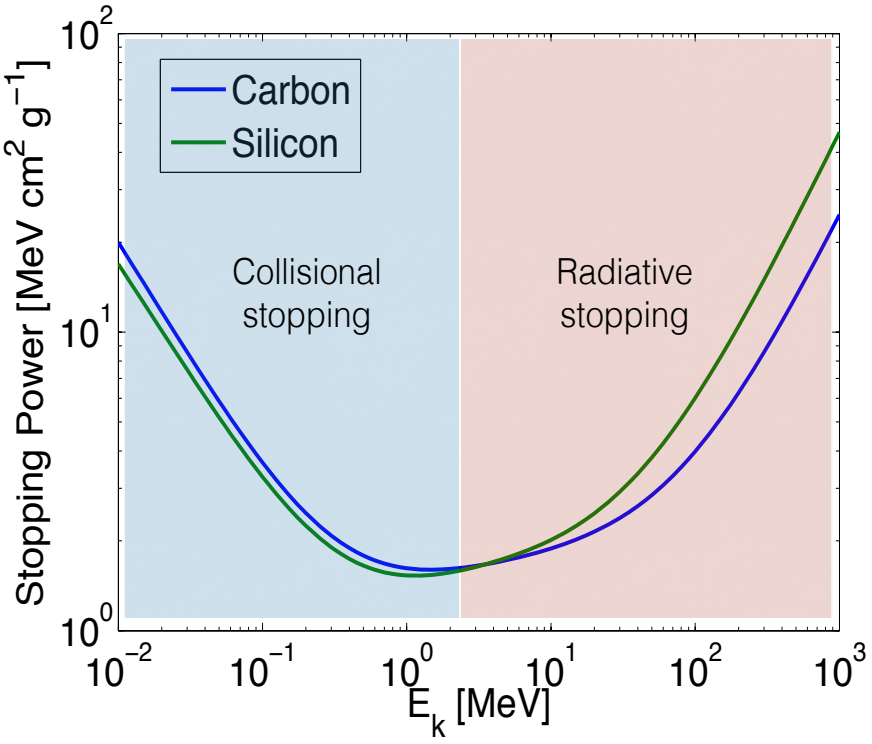

Figure 3.6: Stopping power calculated for carbon (blue curve) and silicon (green curve) as a function of fast electron energy. The blue and red regions given an indication the electron energy which corresponds to energy loss due to collisional and radiative stopping respectively.

return current electrons are slower and larger in number than the fast electron population. Thus, due to their lower energy (i.e. $\ll$ MeV), the return current electrons are highly collisional and couple energy to the plasma via Ohmic heating. The rate of Ohmic heating is given by [106]:

$$\frac{3}{2} n_b \left(\frac{dT_b}{dt} \right) = \mathbf{j_f^2} \eta \tag{3.34}$$

where T_b is the background electron temperature, η is the resistivity and n_b is the background electron density. Thus, heating occurs predominantly in regions of highest current density (i.e. along the fast electron propagation axis).

Furthermore, Ohmic heating of the background target by the return current electrons is of key importance to fast electron transport through it's role in changing the background plasma resistivity. The collisional return current heats the background electrons on very short (femtosecond) timescales, which acts to

transition the target temperature from cold solid to hot plasma. Importantly, heating induced by the return current gives rise to spatial variations of the target resistivity which seed the generation of large magnetic fields; these fields can significantly influence the fast electron transport properties, and are discussed in the next section.

3.3.3 Magnetic field generation

Although the current neutrality relation (i.e. $\mathbf{j}_f + \mathbf{j}_r \approx 0$) is a good approximation of the neutralisation of the fast electron current on a local scale, it is not an exact cancellation in a full 3-D situation (i.e. that present during MeV electron transport in a solid). The resulting imbalance between the densities of the fast electron and return current populations gives rise to the growth of large electromagnetic fields.

To demonstrate this, consider the electric field generated by the return current (obtained using Ohm's law) [106]:

$$\mathbf{E} = \eta \mathbf{j}_r \tag{3.35}$$

which, upon insertion into Faraday's induction law, gives rise to a magnetic field that temporally evolves as:

$$\frac{\partial \mathbf{B}}{\partial t} = -\nabla \times \mathbf{E} = -\nabla \times (\eta \mathbf{j}_r) \tag{3.36}$$

In addition, the magnetic field associated with the charge imbalance is given by Amperes law:

$$\nabla \times \mathbf{B} = \mu_0 (\mathbf{j}_f + \mathbf{j}_r) \tag{3.37}$$

where the displacement current is neglected. Thus, the origin of the magnetic field is the curl of the electric field that is required to draw the return current. This self-induced magnetic field can be shown to evolve with time as:

$$\mathbf{j}_f + \mathbf{j}_r = \frac{\nabla \times \mathbf{B}}{\mu_0} \tag{3.38}$$

$$\rightarrow \quad \mathbf{j}_r = \frac{\nabla \times \mathbf{B}}{\mu_0} - \mathbf{j}_f \tag{3.39}$$

$$\frac{\partial \mathbf{B}}{\partial t} = -\nabla \times \left(\frac{\eta}{\mu_0} \nabla \times \mathbf{B} - \eta \mathbf{j}_f \right) \tag{3.40}$$

$$\rightarrow \quad \frac{\partial \mathbf{B}}{\partial t} = -\nabla \times \left(\frac{\eta}{\mu_0} \nabla \times \mathbf{B} \right) + \nabla \times (\eta \mathbf{j}_f) \tag{3.41}$$

The first term on the right-hand side corresponds to the resistive diffusion of magnetic field, whereas the second term on the right-hand side corresponds to a magnetic field generated by the fast electron current density.

In the limit of strong heating (i.e. keV temperatures) resistive diffusion of the magnetic field becomes negligible and thus the magnetic field equation reduces to:

$$\frac{\partial \mathbf{B}}{\partial t} = \nabla \times (\eta \mathbf{j}_f) \tag{3.42}$$

$$\Rightarrow \quad \frac{\partial \mathbf{B}}{\partial t} = \eta (\nabla \times \mathbf{j}_f) + \nabla \eta \times \mathbf{j}_f \tag{3.43}$$

This equation determines resistive magnetic field generation arising from two principle sources: 1) variation in the fast electron current density (i.e. $\eta(\nabla \times \mathbf{j}_f)$); and 2) variation in the resistivity (i.e. $\nabla \eta \times \mathbf{j}_f$). Fig. 3.7 illustrates some of the main processes which occur during fast electron transport in a solid.

The first term (i.e. $\eta(\nabla \times \mathbf{j}_f)$) on the right-hand side of Eq. (3.43) arises from spatial variations of the fast electron current density and generates an azimuthal magnetic field which acts to push electrons into regions of highest current density. Since the injected electron beam profile follows the spatial profile of the laser focal spot (i.e. Gaussian), the highest current density occurs along the beam axis (i.e. longitudinal propagation direction) and thus the field forces the fast electrons towards the beam axis (i.e. pinching the beam).

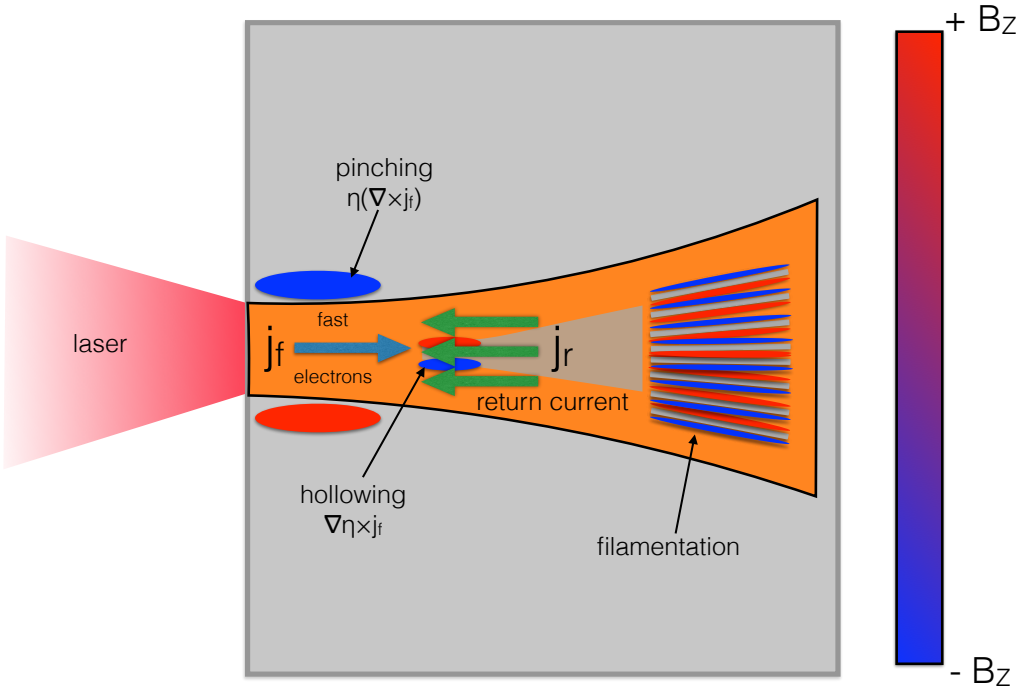

Figure 3.7: Fast electron transport. The various processes relevant to fast electron transport are displayed: fast electron current injection, spatially-overlapped return current, resistive magnetic field generation (both collimating and hollowing components) and beam filamentation. Note that the $\nabla\eta$ component can be either hollowing or pinching depending on the sign of the resistivity.

The tendency of the fast electron beam to effectively self-pinch has been explored by Bell and Kingham [107]. In this work, a condition was derived which revealed that the azimuthal magnetic field enveloping the fast electrons beam, of magnitude estimated from: $|B| \approx \frac{\eta j_f \tau_L}{r_f}$, causes the fast electrons to be deflected by an angle $\theta_{1/2}$ over a distance $r_f/\theta_{1/2}$, defined as the distance over which the electron beam radius doubles. If $\theta_{1/2}$ is relatively small, the ratio of the fast electron beam radius to the gyro-radius is:

$$\frac{r_f}{r_g} > \theta_{1/2}^2 \tag{3.44}$$

This ratio is then used to derive a condition that indicates when collimation

occurs − this collimation factor, Γ, is expressed as:

$$\Gamma = \frac{r_f eB}{\gamma_f m_e v_f \theta_{1/2}^2} \tag{3.45}$$

For collimation to occur, $\Gamma > 1$. Moreover, once initiated the process of collimating proceeds with positive feedback (i.e. the increase in current density driven by the magnetic field increases the rate of magnetic field generation).

The second term in Eq. (3.43) (i.e. $\nabla\eta \times \mathbf{j}_f$) generates a magnetic field which is derived from spatial gradients in the background plasma resistivity. These gradients are sourced from gradients in the background plasma temperature arising from return current-driven Ohmic heating. As described previously, the fast electron beam injected at the target front-surface exhibits the highest current density (and thereby background) temperature, on-axis. However, the spatial profile of the electron beam follows the spatial profile of the laser focal spot (i.e. Gaussian) and thus large temperature gradients are induced in the background plasma towards the edges of the fast electron beam (i.e. transverse to the electron beam propagation direction). These temperature gradients give rise to large resistivity gradients which, through the $\nabla\eta \times \mathbf{j}_f$ term, generates a magnetic field (which, depending on the sign of the resistivity gradient, will be hollowing or collimating) that drives electrons into regions of higher resistivity. This is typically in the direction transverse (i.e. perpendicular) to the fast electron beam propagation direction.

If the magnitude of the hollowing magnetic field component (i.e. $\nabla\eta \times \mathbf{j}_f$) exceeds the magnitude of the pinching magnetic field component (i.e. $\eta(\nabla \times \mathbf{j}_f)$) that surrounds the fast electron beam, this leads to the expulsion of fast electrons from the centre of the beam (i.e. beam axis) in a direction transverse to the propagation direction. The resulting global fast electron transport properties will be dominated by annular beam transport − this effect is referred to as beam hollowing. The effect of resistively generated magnetic fields on beam hollowing has been investigated numerically by Davies *et al.* [108, 109], using a rigid beam model in conjunction with the Spitzer resistivity model, and experimentally by

Norreys *et al.* [110].

At the core of all of these transport phenomena is the evolution of resistivity with temperature. Thus, understanding how resistivity varies across such a wide temperature range (i.e. from 0.025 eV to $>$ 100 eV) is fundamentally important to understanding fast electron − within the context of fast electron transport in solids, is the resistivity best described using solid state theory (section 3.2.1), plasma theory (section 3.2.2), or transient WDM theory (section 3.2.3). The implications of correctly accounting for the resistivity on defining fast electron transport properties form the foundation of the results presented in this thesis.

3.3.4 Fast electron beam instablities

As described in section 3.3.1, the fast electrons injected at the front surface (i.e. at the focal spot region) propagate into the target due to the drawing of a return current of electrons, sourced from the background target electrons, which is spatially overlapped with and propagates in the opposite direction to the forward streaming fast electrons. Thus, the two electron populations (i.e. forward streaming fast electrons and backward propagating return current) interact in a counter-streaming manner which in turn gives rise to a variety of beam instabilities. For intense laser-solid interactions the most dominant transport instability is the electromagnetic collisionless Weibel-like filamentation instability [111].

The collisionless Weibel instability is a transverse instability (i.e. it acts perpendicular to the propagation direction) that develops as a result of spatial modulations in the fast electron beam density (seeded by the interaction between the fast electrons and counter-propagating return current). Consequently, localised magnetic fields are generated around each perturbation which acts to 'pinch' and disrupt the beam into filaments; the electron beam subsequently breaks up. The generation of these filaments occurs on a time and spatial scale on the order of the fast electron beam plasma frequency, ω_{pf}, and plasma skin depth, $c\omega_{pf}$,

respectively, with the resulting growth rate, Γ_{wi}, given by [112]:

$$\Gamma_{wi} = \omega_{pf} \left(\frac{n_f}{\gamma n_e} \right)^{\frac{1}{2}} \times \frac{v_f}{c} \tag{3.46}$$

where v_f is the velocity of the fast electrons, n_f is the fast electron density and n_e is the background plasma density, which are key to determining the instablity growth rate.

A transverse instability that also arises from the counter-propagating electron beam currents, similar to the collisionless Weibel instability, is the resistive filamentation instability. In this case, the magnetic field growth rate surrounding each filament is related to the material's resistivity. Thus, regions of higher resistivity will seed an increased growth of magnetic fields and thus the growth rate of the resistive filamentation. Different to the collisionless Weibel, the resistive instability occurs on a timescale determined by the magnetic diffusion time, τ_D, given by:

$$\tau_d = \frac{\mu_0 r_F^2}{\eta} \tag{3.47}$$

where $r_F = 2\sqrt{\gamma}\,(\mathbf{v}_{th}/\mathbf{v}_f)\,(c/\omega_{pf})$ is the radius of a filament and η is the resistivity.

Work by Gremillet *et al.* [113] demonstrated that the resistive (and Weibel) instability growth rate varies with the transverse temperature of the electron beam, where a sufficiently high transverse temperature will generate an oppositely-directed force which dominates the magnetic fields acting to pinch the beam into filaments, thus reducing the growth rate. The influence of transverse temperature on filamentation growth rate is briefly explored in Chapter 5 via a linear resistive instability analysis [113, 114].

Ultimately, the action of beam instabilities is to break-up the fast electron beam into filaments, which propagate and spread throughout the target leading to energy loss and changes to the beam divergence angle. In Chapter 5, the role of beam instabilities on fast electron transport in carbon is investigated.

Chapter 4

Methods

4.1 Introduction

The fast electron transport investigations presented in this thesis utilise a complex combination of experimental facilities and diagnostics, together with interpretation of results using numerical simulation methods. In this chapter, the laser, diagnostic techniques and numerical methods most relevant to the results presented in Chapters 5, 6 and 7 are discussed.

4.2 The laser

The experimental investigations presented in this thesis were performed using the Vulcan laser at the Central Laser Facility (CLF), located within the Rutherford Appleton Laboratory (RAL) in Oxfordshire, UK. This section briefly describes the various components that constitute this laser, with emphasis placed on the typical laser parameters used in the investigations presented in Chapters 5, 6 and 7.

Vulcan is a Nd:glass laser consisting of 8 primary beam lines which can be directed into two target areas (excluding the decommissioned Target Area East). These target areas are known as Target Area West (TAW) and Target Area Petawatt (TAP).

In TAW, the 8 primary Vulcan beams can be utilised in a configuration con-

sisting of 6 long-pulse (i.e. nanosecond pulse duration) beams, each delivering up to 200 J of energy on target. The two remaining beams are short-duration (i.e. $\sim$ picosecond) pulses. One of these beams (labelled beam 7 - B7) delivers, via the technique of chirped pulse amplification (CPA)[10], up to 60 J (after compressor) in a 1 ps duration pulse. The final beam (labelled beam 8 - B8) is able to deliver up to 300 J pulses in a duration of 10 ps (again exploiting the technique of CPA). For all 8 beams, the central wavelength is $\lambda_L = 1.053$ μm.

In TAP, two of the 8 primary Vulcan beams are used. The first of these is a long pulse beam ($\sim$ 6 ns duration) with a typical delivered energy of 200 J. The primary laser for TAP is the ultra-high intensity 1 PW beam. The optimum laser parameters that the petawatt beam-line can deliver are 500 J in 500 fs, which is achieved through use of optical parametric chirped pulse amplification (OP-CPA) [115, 116] in conjunction with a large amplification chain consisting of rod and disk amplifiers. The resulting peak laser intensity is $I_L \approx 2\times10^{21}$ Wcm^{-2} (within a 3.5 μm radius spot). However, maintaining the laser at these peak conditions will result in rapid degradation of beam-line optics over the duration of a typical experimental campaign. Thus, the laser is operated at more sustainable parameters (e.g. pulse duration and energy on target of 1 ps and 300 J respectively), resulting in a peak intensity of $I_L \approx 7 \times 10^{20}$ Wcm^{-2}.

The laser pulse delivered to each target area (i.e. TAW and TAP) has it's own unique oscillator; this corresponds to a SEmiconductor Saturable Absorber Mirror (SESAM) oscillator and Ti:sapphire Kerr Lens Modelocked (KLM) oscillator for TAW and TAP respectively. Note that the method of mode-locking is different for each laser (i.e. passive mode-locking for each oscillator, but the TAW oscillator utilises the reflectivity of the absorber to produce pulse trains [117] while the TAP oscillator produces pulses via the non-linear Kerr effect in the laser medium [118]).

1. Producing high-intensity laser pulses

The peak laser intensity delivered to the target is ultimately constrained by the damage threshold of the optics used along the laser beam-line. A standard tech-

Laser Parameter	**Target Area West** (TAW B7)	**Target Area Petawatt** (TAP)
Energy on target E_L	60 J	300 J
Focal spot radius r_L	8 μm (FWHM)	3.5 μm (FWHM)
Pulse duration τ_L	1 ps	1 ps
Wavelength λ_L	1.053 μm	1.054μm
Polarisation	p	p
Intensity I_L	$\sim 7 \times 10^{19}$ Wcm^{-2}	$\sim 7 \times 10^{20}$ Wcm^{-2}

Table 4.1: Vulcan laser parameters for TAW and TAP, which are relevant to the investigations presented in this thesis.

nique is to increase the diameter of the beam, thereby increasing the beam area and thus reducing the energy density incident on each optical component to below the damage threshold. To do this, however, would eventually require optics that were both prohibitively large (i.e. the components would necessitate an unfeasibly large facility) and expensive. To overcome this difficulty, the technique of chirped pulse amplification is used [10], which involves the pulse being stretched (i.e. increasing the pulse duration) prior to amplification, thus reducing the intensity incident on the optical components. Before being directed to the target, the pulse is compressed to achieve a pulse duration closer to the original duration produced by the oscillator. This pulse stretching and compression technique (i.e. CPA) has been demonstrated to produce peak pulse powers of ~ 1 PW and within the context of the Vulcan laser, the technique of CPA is used on the TAW laser which, after using a reflective off-axis parabolic mirror to focus the pulse to the target, produces peak intensities of $\sim 7 \times 10^{19}$Wcm^{-2}.

For the TAP laser, the amplification technique is slightly different to that used for TAW. The shortest achievable pulse on Nd:glass systems is inherently limited using conventional amplification (i.e. CPA) due to gain-narrowing effects, which act to limit the maximum pulse bandwidth. To circumvent this limitation, the TAP beam line utilises the technique of OP-CPA to increase the pulse bandwidth,

thereby reducing the pulse length achievable from the system. In OP-CPA, the seed pulse from the oscillator (i.e. Ti:sapphire - large bandwidth) is chirped and passed through a non-linear crystal (i.e. β-barium borate (BBO)), which is simultaneously pumped by a high-energy long pulse laser (i.e. 'pump' pulse). Due to non-linear, parametric amplification processes, the oscillator seed pulse gains energy from the 'pump' pulse and is amplified with a typical total gain greater than 10^7 [115]. This stretched, pre-amplified pulse is then directed to the main amplification stage of the Petawatt beam, where a combination of Nd:silicon and Nd:phosphate crystals amplify the pulse. Finally, the amplified pulse is compressed to $\tau_L = 0.5-1$ ps and focussed to target using an f/3 off-axis parabola, giving a peak intensity of $I_L \sim 7 \times 10^{20}$ Wcm^{-2}. For the experiments described in this thesis, a summary of the laser parameters for each target area is given in Table 4.1.

2. Laser contrast

As discussed in Chapter 2, the laser intensity, I_L, is a key parameter in laser-solid interactions due to it's role in defining the interaction properties (i.e. plasma density and particle energies). However, the main pulse (i.e. peak intensity, short duration pulse) is not isolated; the laser exhibits a lower intensity, longer duration intensity profile preceding the highest intensity (and shortest duration) main pulse. This 'pedestal' intensity arises from amplified spontaneous emission (ASE - produced from amplified stray light) and uncompensated dispersion (generated by non-optimum compression of the main pulse). The ratio of peak pulse intensity to the intensity of the pedestal is known as the laser intensity contrast. Note that for ultra-high intensities, the intensity of both the peak pulse and pedestal increases and therefore the contrast ratio must be maintained high to reduce effects induced by the pedestal (i.e. target preheating, pre-plasma expansion and target compression). Laser contrast is typically characterised over two timescales: 1) tens of picoseconds before the main pulse; and 2) nanoseconds prior to the arrival of the main pulse. For the experimental investigations reported in this thesis, measurements made on the Vulcan laser indicate that the contrast is of

the order of $\sim 10^{10}$ (i.e. $I_L \sim 10^{10}$ Wcm^{-2}) at 0.1 - 1 ns and $\sim 10^{8}$ (i.e. $I_L \sim 10^{12}$ Wcm^{-2} at 50 - 100 ps [119].

4.3 Diagnosing fast electron transport

4.3.1 Introduction and brief review of diagnostic methods

Experimental investigations of fast electron transport in dense plasma typically aim to characterise specific properties of the electron beam (i.e. beam divergence, temperature and spatial profile). However, the direct measurement of fast electron transport in solids is extremely difficult and thus indirect probing techniques, based on secondary particle and radiation emission induced by the fast electrons, have been developed. In recent years, the fast electron beam has been predominantly characterised using four techniques: 1) X-ray emission; 2) optical probing; 3) transition radiation; and 4) proton emission. This section explores each of these techniques in turn, before providing a detailed description of the measurement technique used to obtain the results presented in Chapters 5, 6 and 7: target rear-surface proton emission.

1. X-ray emission - K_α imaging

Measuring X-ray emission from laser-solid interactions is performed utilising both imaging and spectroscopy, thus providing spatial and spectral information of the X-ray source (i.e. fast electrons). A particularly common technique used is known as K_α imaging.

For fast electrons, despite their mean free path being considerably longer than the target thickness, their energy stopping profile in matter (see Chapter 3) results in some energy being transferred to the background electrons via collisions. These collisions provide the background electrons with sufficient energy to enable transitions between atomic levels, resulting in the emission of photons of characteristic energy. The photon energy is dependent on the atomic levels over which the electrons have transitioned (i.e. K_β: M - K shell transition). These

transitions are determined by the atomic structure and are thus material dependent. For measurements relevant to fast electron transport, K_α transitions (i.e L - K shell transition) typically emit the most intense X-ray spectral lines and thus have been used most frequently. The emitted photons (e.g. for Cu-K_α the emitted photon energy is 8.05 keV, while for Ti-K_α the energy is 4.5 keV) leave the target and are collected and focussed (typically using a spherically-bent Bragg crystal) to a detector (image plate or a charge-coupled device (CCD) camera) [58]. The resulting magnified spatial profile corresponds to the K_α emission region and can be used to characterise the electron beam divergence [120], beam temperature [27] and conversion efficiency [64].

As described in Chapter 2, K_α measurements have been utilised to infer the mean electron temperature [61]. However, the results also provide information on the divergence of the electron beam. By measuring K_α emission from targets containing a buried fluorescence layer (across a range of depths, from 100 - 750 μm), the beam divergence half-angle was found to be $\sim 90^\circ$ for layers buried at shallower depths (i.e. 100 μm), and $\sim 30^\circ$ for layers deeper into the target (i.e. 750 μm). Moreover, K_α measurements made on both the Vulcan and LULI laser systems demonstrated an electron beam divergence half-angle of 20° for electrons with energy > 200 keV [121].

In addition, detailed studies of electron beam divergence utilising K_α emission have been made on the Vulcan laser, described by Green *et al.* [120] and Lancaster *et al.* [122]. These investigations explored two distinct intensity regimes: 1) longer pulse duration of $\tau_L = 5$ ps (relevant for fast ignition [22]), resulting in a peak laser intensity $I_L \sim 4 \times 10^{19}$ Wcm^{-2} - Green *et al.* [120]; and 2) short pulse duration $\tau_L = 0.5$ ps, with peak intensity $I_L \sim 5 \times 10^{20}$ Wcm^{-2} - Lancaster *et al.* [122]. For metallic targets (Cu and Ti) of < 75 μm thickness, the electrons were inferred to propagate through the targets with beam divergence half-angles of 35° and 27°, for Green *et al.* [120] and Lancaster *et al.* [122] respectively.

Finally, while K_α imaging provides spatial information of the X-ray source (and thus electron beam), more detailed information can be obtained by spectrally dispersing the emitted X-rays. This provides information of other spectral

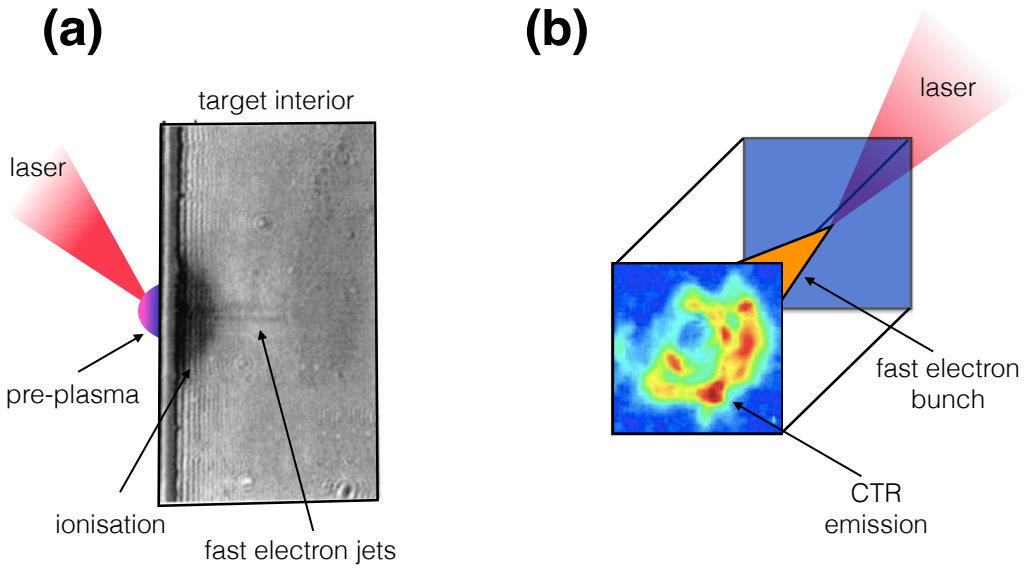

Figure 4.1: Common techniques used to characterise fast electron transport in solids: (a) transverse optical probing of transparent (i.e. glass) targets, where opaque regions correspond to fast electron induced ionisation (extracted from Gremillet *et al.* [113]); and (b) the principle of CTR, which is used to measure spatial features of the escaping fast electrons, displayed a measured CTR (extracted from Storm *et al.* [124]).

emission lines which, in turn, can be used to obtain information on the fast electron beam temperature [123].

2. Optical probing

Optical probing of fast electron transport in solids has been employed to primarily investigate the 2-D longitudinal electron transport profile. The technique involves collecting a portion of the main pulse (to ensure that the probe and main pulse are temporarily synchronised) and directing it across the target surface along the transverse (i.e. side-on) direction. The probe beam is imaged onto a CCD camera and the resulting images represent a time-resolved 'shadowgram' of the laser-induced plasma expansion profile. If probing occurs in a transparent target (e.g. glass), the edge-on 2-D transport profile of the fast electrons is imaged. In addition, the time-resolved probe images can be temporarily varied by incorporating a movable 'time-slide' into the beam-path before the target; adding

or subtracting path length (i.e. by moving the time-slide) enables optical probing to be performed at different time-steps.

One of the first implementations of optical probing to investigate fast electron transport within solid-density targets was performed by Borghesi *et al.* [125], where Al-coated glass targets were probed after $\sim$ 5 ps of irradiation by a picosecond laser pulse of intensity $I_L > 10^{19}$ Wcm^{-2}. The resulting shadowgrams revealed filamentary jet-like structures, evidenced by opaque regions (caused by ionisation) within the transparent target. The observed tracks extended to 700 μm in length and $\sim$ 20 μm in width and, using 3-D particle-in-cell and 2-D Vlasov-Fokker-Planck (VFP) hybrid codes, were inferred to be consistent with fast electron induced ionisation of the glass target.

The first experimental investigation to demonstrate the importance of resistive magnetic fields on fast electron transport was by Tatarakis *et al.* [126]. In this work, plastic targets irradiated by laser pulses of intensity $I_L \sim 1 \times 10^{19}$ Wcm^{-2} were optically probed and the resulting shadowgrams revealed an electron density distribution within the ablated (i.e. target front-surface) plasma exhibiting a minimum along the target normal direction. Additionally, a narrow plasma jet was observed (after a few picoseconds) at the target rear-surface. Tatarakis *et al.* attributed these features to the collimation of the fast electron beam within the target by large magnetic fields

Another important study from around the same time was reported by Gremillet *et al.* [127], in which thick ($>$ 400 μm) glass targets were irradiated by 350 fs duration pulses of peak intensity $I_L > 10^{19}$ Wcm^{-2}, and subsequently optically probed at time-resolved steps between 1.2 - 3 ps after the laser irradiation. The shadowgraphy measurements revealed two distinct electron populations: 1) filamentary, jet-like structures (of hundred-micron length) propagating in the forward direction; and 2) a hemi-spherical shaped ionisation front located near the target front-surface moving slower than the jet-like fast electron channels, consistent with K_α measurements obtained by Wharton *et al.* [61]. Moreover, the observation of a high-velocity ($\sim c$) collimated electron beam structure suggests the presence of strong magnetic-fields within the target.

In addition to internal target probing, the divergence of the fast electron beam has been characterised by Green *et al.* [120] and Lancaster *et al.* [122] using shadowgraphy measurements of the plasma expansion at the target rear-surface, in conjunction with K_α measurements. In these investigations, laser-irradiation of $< 75\mu$m-thick metallic targets revealed an electron beam divergence angle of up to $\theta_{1/2} = 56°$.

Moreover, transverse optical probing has also been used to measured a signature of annular transport in plastic targets. In this work, Norreys *et al.* [110] irradiated 175 μm-thick Mylar targets (of transverse dimension 5 mm $\times$ 5 mm) with intense picosecond duration laser pulses (of peak intensity $I_L = 5 \times 10^{19}$ Wcm^{-2}), and optically probed the rear-surface plasma expansion 200 ps after laser-irradiation of the target front-surface. The resulting shadowgrams revealed a transition between a strongly collimated electron profile, which was observed at intensities of $I_L = 1 \times 10^{19}$ Wcm^{-2}, to an annular electron pattern at intensities of $I_L = 5 \times 10^{19}$ Wcm^{-2}, with a 20° full-width divergence angle.

Recently, a new approach to rear-surface optical probing has been demonstrated by Green *et al.* [128]. In this work, a chirped optical probe beam was reflected from the target rear-surface and, exploiting the broad bandwidth of the Ti:Sapphire laser used, a series of narrow-band interference filters were employed to preferentially select specific wavelengths (and thus time-steps). This, in turn, enables multiple time-resolved 2-D spatial measurements (with spatial resolution of 6 μm and temporal resolution of 100 fs - 1.5 ps) of target rear-surface plasma formation and expansion to be made on a single shot which can be used to infer the fast electron transport properties.

3. Coherent transition radiation (CTR)

Another optical technique used to image the spatial profile of fast electrons propagating through solids exploits the emission of transition radiation induced by the most energetic (i.e. fastest) electrons escaping from the target rear-surface. Transition radiation is emitted when a charged particle passes through a refractive index interface [129], as occurs when the fastest electrons escape from the

target rear-surface into vacuum. For a single electron making this transition, the emitted radiation is weak. However, ultra-intense laser-solid interactions produce a large number of fast electrons. The summation of the transition radiation emitted by the many individual electrons provides a measurable signal.

Transition radiation can be divided into two components: 1) incoherent transition radiation (ITR); and 2) coherent transition radiation (CTR). ITR corresponds to the summation of transition radiation produced by individual electrons, while CTR is emitted when an electron beam (consisting of bunches accelerated at $2\omega_L$), exhibiting electron density modulations along the direction of its propagation (i.e. longitudinally), crosses the rear-surface target-vacuum interface [130, 131]. Due to each electron bunch containing a distribution of velocities, each bunch disperses as it propagates through the target, reducing the coherency of the beam. Thus the emitted CTR energy is sensitive to both target thickness and the fast-electron beam temperature. A detailed discussion of transition radiation is given by Ginzburg *et al.* [129].

The application of this technique to fast electron transport was first explored by Santos *et al.* [132], in which aluminium targets of 400 μm thickness were irradiated by laser pulses of intensity $I_L \sim 10^{19}$ Wcm^{-2} and the CTR radiation was imaged onto a 12-bit CCD camera. The results revealed that the electron beam inside the target propagated with a constant divergence half-angle of $\theta_{1/2} = 17^0$. In another study, Storm *et al.* [124] measured CTR from Al and Cu of several tens-of-μm thickness under laser irradiation of intensity $I_L \sim 10^{19}$ Wcm^{-2} and reported the mean electron beam temperature and half-angle divergence to be 1.4 MeV and $\theta_{1/2} = 16^\circ$, respectively. To support the experimental measurements, 3-D hybrid-particle-in-cell simulations were used to reproduce the details of the CTR images and it was found that this was only achievable when an initial half-angle divergence of 56^0 was assumed. Electron beam collimation, induced by self-generated resistive magnetic fields, was concluded to be responsible for the difference between the initial divergence angle of $\theta_{1/2} = 56^\circ$ and the experimentally measured beam divergence half-angle of $\theta_{1/2} = 16^\circ$.

4.4 Using proton emission to characterise the spatial properties of fast electron transport

While techniques involving X-ray emission and optical probing provide some insight into the transport properties, there are a number of drawbacks. For example, optical diagnostics are inhibited from probing overdense plasmas (i.e. above critical density) due to the target being opaque to the laser pulse. Moreover, the large electric (and magnetic) fields produced within μm-thick targets largely confine the majority of electrons (excluding the most energetic electrons which escape into vacuum) to re-circulate within the target, which can make interpretation of K_α emission data difficult. Furthermore, even time-resolved imaging of transition radiation from electrons exiting the target rear surface does not resolve the spatial features of the lower energy electrons that are confined to reflux within the target.

In recent years, a technique used to particular success for characterising the spatial properties of fast electron transport in solids is the measurement of proton emission from the target rear-surface [37–39, 133], in which the proton beam arising from the action of the rear (i.e. non-irradiated) target surface electric sheath-field is detected using a stack of radiochromic film (RCF). This technique offers two key advantages: 1) it enables the time-integrated spatial characteristics of the rear-surface electron sheath (which is the source of the accelerated ion beam) to be measured which, in turn, enables the fast electron transport pattern within the target to be inferred; and 2) protons used for the imaging (i.e. $\sim$ MeV) are predominantly accelerated by electrons in the mean energy region of the fast electron spectrum, as described by Mora *et al.* [134], which are more susceptible to be influenced by self-generated magnetic fields within the target (see Chapter 3). By contrast, coherent transition radiation [132] arises from the escape of the most energetic electrons from the target rear-surface, which are less likely to be influenced by the self-generated fields within the target. Moreover, since proton acceleration occurs at the local electric sheath-field surface, it has been demonstrated [37] that spatial modulations of the electric sheath spatial-

profile results in a corresponding modulation within the accelerated ion beam beam spatial-profile for all proton energies (i.e. in each RCF layer). By comparing experimentally measured proton spatial-intensity profiles with analytical modelling of sheath-field dynamics, and subsequent mapping into the accelerated proton beam spatial profile, the fast electron transport within the target can be inferred.

Previous work has shown that ions can originate from the front-surface [28] and rear-surface [29] of solids irradiated by intense laser pulses, with some debate as to the correct interpretation of when front or rear-surface acceleration dominates. For example, Wilks *et al.* [31] theoretically and numerically showed that rear-surface acceleration dominates for thicker (on the order of 100 μm-thick) targets, while Gibbon [135] argued that front-surface acceleration dominates for relatively thinner (i.e. few 10$'$s of micron thickness) targets.

In recent years, it has been experimentally demonstrated that the dominant ion acceleration mechanism in thick targets (i.e. hundreds of μm), at the laser intensities (i.e. $I_L > 5 \times 10^{19}$ Wcm^{-2}) explored in this thesis, is the target normal sheath acceleration (TNSA) mechanism, which occurs at the target rear surface see for example: Fuchs *et al.* [37]; Yuan *et al.* [136]; and Sentoku *et al.* [38]. Whereas for the case of thin (i.e. $\sim \mu$m) and ultra thin (i.e. nanometer) targets other ion acceleration mechanisms at the target front surface, driven by the collisionless shock generated by the laser ponderomotive force, can contribute to the measured ion beam profile, these mechanisms are not relevant to the thick targets (i.e. > 100 μm) and linearly polarised laser pulses used in the investigations presented in this thesis.

4.4.1 Target Normal Sheath Acceleration (TNSA)

To explain TNSA qualitatively, a general description of the mechanism is outlined as follows. The interaction of an ultra-intense laser pulse (i.e. $I_L > 5 \times 10^{19}$ Wcm^{-2}) at the target front surface produces a source of hot, energetic electrons. As discussed in detail in Chapter 2, the electron source properties (i.e. energy spectrum and mean temperature) are determined by the incident laser

parameters (e.g. laser intensity), pre-plasma properties (e.g. scale length) and target properties. The fast electrons generated in the region of the focal spot propagate into the target with a divergence half-angle $\theta_{1/2} \sim 30^\circ - 50^\circ$ [137]. Within the target, the fast electrons are subject to a range of transport phenomena, as discussed in detail in Chapter 3. Upon reaching the target rear-surface vacuum boundary, the fast electrons can no longer draw a return current to enable them to propagate further forward and thus start to accumulate at the target rear-surface. This generates a strong electrostatic sheath field which reflects the remaining lower energy electrons back into the target. The sheath field extends longitudinally over a Debye length (i.e. the distance over which an electric field extends before being shielded − see Chapter 2). Note that once the reflected (i.e. re-circulated) electrons reach the target front-surface, an electrostatic sheath field is created there which acts to re-direct the electrons towards the rear-surface.

The electric field strength, E_s, can be estimated from:

$$E_s \approx \frac{k_B T_e}{e\lambda_D} \sim \mathrm{TVm}^{-1} \tag{4.1}$$

where $k_B T_e \sim$ MeV and $\lambda_D \sim \mu$m.

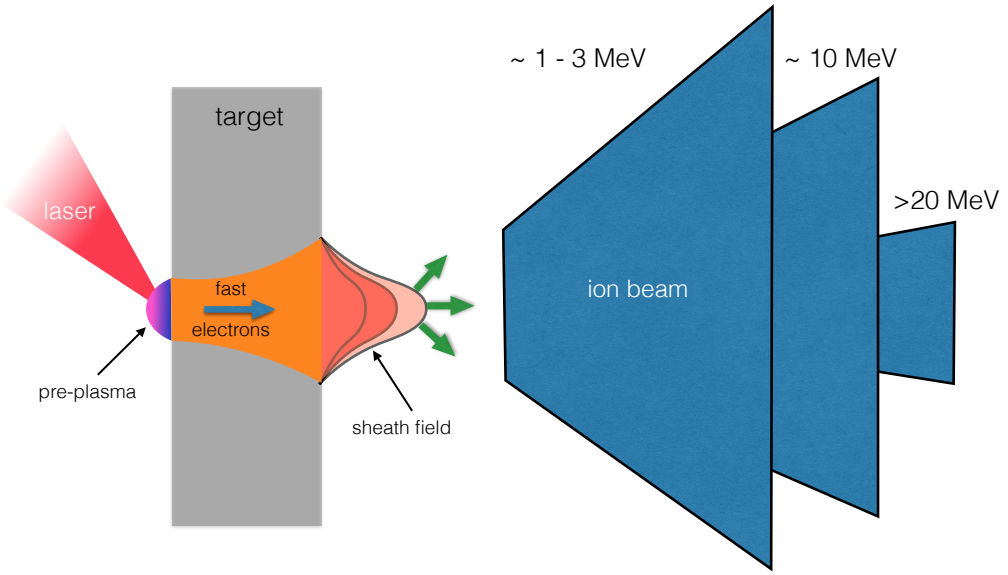

Figure 4.2: Acceleration of ions via the target normal sheath acceleration (TNSA) mechanism. The TV/m field formed at the target rear-surface by the fast electrons arriving there accelerates ions to multi-MeV energies, directed normal to the local sheath field profile. The ion beam divergence is energy dependant and is larger for lower energy ions and smaller for higher energy ions.

An electric field of this strength is sufficient to ionise atoms on the target rear-surface (which originate primarily from a hydrocarbon contaminant layer), and will subsequently accelerate ions to MeV energies over a distance of $\sim$ few μm, in conjunction with driving rapid plasma expansion. The resulting ions are preferentially accelerated according to their charge-to-mass ratio; ions with higher ratios (e.g. protons) will be preferentially accelerated to higher velocities, and thus stream ahead of heavier ions with lower charge-to-mass ratios (e.g. carbon ions). Moreover, because the sheath is shielded over such a short distance (i.e. Debye length - $\sim$ μm), only ions at the very front of the sheath layer will experience the strongest field for the greatest duration. The resulting ion trajectories are directed normal to the local orientation of the rear surface, in addition to being directed normal to the time-dependant spatial-profile of the electric sheath field. Thus, the spatial profile of the accelerated ion beam is

imprinted with both the spatial characteristics of the local target rear-surface and, importantly, the spatial profile of the electric sheath field driven by the fast electron density spatial distribution. A schematic of this process is shown in Fig. 4.2.

The acceleration of ions via the TNSA mechanism is a particularly complex process that is dependent on a number of factors, such as: 1) front surface physics (i.e. electron source properties − Chapter 2); 2) fast electron transport within the target (see Chapter 3); and 3) sheath field evolution and plasma expansion at the target rear-surface (in addition to ionisation and subsequent ion acceleration). To enable a more quantitative understanding of TNSA, a number of analytical and numerical models have been proposed [138–141]. One of the most widely used models is the fluid approach developed by P. Mora [138].

The Mora model is a 1-D isothermal plasma expansion model which describes plasma expansion into vacuum. Importantly, the model builds upon previous isothermal expansion models [142, 143] by incorporating a charge-separation layer (corresponding to the ion front) into the plasma expansion description. This enables an analytical description of the temporal evolution of the peak electric field to be obtained, where the accelerated ions gain energy from the fast electrons and both species subsequently propagate into vacuum in a quasi-neutral plasma 'cloud' − energy is transferred from the electrons to the ions and the accelerating field (which arises from the charge-separation layer) gradually decreases. The Mora model has been particularly successful when applied to a wide variety of experimental conditions [144], including results obtained from experiments performed on the Vulcan laser [32].

The Mora model is described as follows. After laser-irradiation, the fast electrons generated at the target front-surface propagate through the dense plasma before arriving at the target rear-surface, where the fastest electrons escape into vacuum. At time $t = 0$, the ions (of density n_i) are assumed to be initially cold and at rest, with a step-like spatial density distribution (i.e. $n_i = n_{i0}$ for $z \leq 0$ and $n_i = 0$ for $z > 0$), representative of the target rear-surface, where n_{i0} is the initial ion density, and z is the propagation direction. The electron density, $n_e(z)$,

at the rear surface is assumed to take the form of a Boltzmann distribution:

$$n_e(z) = n_{e0} \exp\left(\frac{e\Phi(z)}{k_B T_e}\right) \tag{4.2}$$

where n_{e0} is the initial electron density (i.e. injected electron density) estimated by $n_{e0} = \eta_{L\to e} E_L / c\tau_L \pi r_0^2 k_B T_e$, $\mathbf{\Phi}(z)$ is the electrostatic potential generated as the electrons exit the target and T_e is the electron temperature. The atoms (arising from hydrocarbon layers) are assumed to be field-ionised (see Chapter 2) and the resulting plasma is quasi-neutral (i.e. $n_e = Zn_i$, where n_i is the ion density and Z the ion charge). Charge separation occurs at the target rear-surface which acts to generate the electrostatic field potential, $\mathbf{\Phi}(z)$, which satisfies Poisson's equation:

$$\frac{\partial^2 \Phi}{\partial z^2} = \frac{e(n_e - Zn_i)}{\epsilon_0} \tag{4.3}$$

For $t > 0$ the electrons are assumed to be in thermal equilibrium, and thus equations Eq. (4.2) and Eq. (4.3) are still valid. The subsequent plasma expansion into vacuum is described using a fluid model, where the expansion dynamics are governed by the equations of continuity (Eq. (4.4)) and ion equation of motion (Eq. (4.5)):

$$\left(\frac{\partial}{\partial t} + v_i \frac{\partial}{\partial z}\right) n_i = -n_i \frac{\partial v_i}{\partial z} \tag{4.4}$$

$$\left(\frac{\partial}{\partial t} + v_i \frac{\partial}{\partial z}\right) v_i = -\left(\frac{Ze}{m_i}\right) \frac{\partial \Phi}{\partial z} \tag{4.5}$$

where v_i is the ion velocity and m_i is the ion mass.

A key limiting feature of the Mora model is the prediction that the energy and velocity of the ions indefinitely increase for increasing time; this prediction arises from the assumption of isothermal expansion. Thus, an upper limit is defined for the duration over which ion acceleration persists which, to first order, is given by the laser pulse duration τ_L. However, as demonstrated both experimentally and numerically by Fuchs *et al.* [144], for incident laser intensities greater than $3 \times 10^{19}\,\mathrm{Wcm^{-2}}$ the acceleration time is given approximately by $t_{acc} \approx 1.3(\tau_L +$

60 fs) [144].

Using the Mora model, the evolution of the electric field strength of the ion front, $E_{front}(t)$, the ion front position $x_{front}(t)$, and ion front velocity, $v_{front}(t)$, can be derived:

$$E_{front}(t) = \left(\frac{2n_{e0}k_BT_e}{\exp(1)\varepsilon_0}\frac{1}{1+\tau_p^2}\right)^{1/2} \tag{4.6}$$

$$x_{front}(t) \simeq 2\sqrt{2e\lambda_{D0}}\left[\tau_p \ln\left(\tau_p + \sqrt{\tau_p^2+1}\right) - \sqrt{\tau_p^2+1} + 1\right] \tag{4.7}$$

$$v_{front}(t) \simeq 2c_s \ln\left[\tau_p + \sqrt{\tau_p^2+1}\right] \tag{4.8}$$

where time is normalised to the ion plasma frequency, $\tau_p = \omega_{pi}t/2\exp(1)$, λ_{D0} is the initial Debye length and c_s is the ion sound velocity.

The resulting maximum energy, E_{max}, gained by the ions can be calculated using the equation derived by Mora [138]:

$$E_{max} = \frac{1}{2}m_i v_{front}^2 \simeq 2Zk_BT_e\left[\ln\left(\tau_p + \sqrt{\tau_p^2+1}\right)\right]^2 \tag{4.9}$$

The proton energy spectrum is given by [138]:

$$\frac{dN_{ion}}{dE_{ion}} = \left(\frac{n_{e0}c_s t_{acc}}{\sqrt{2EionZk_BT_e}}\right)\exp\left[-\sqrt{\frac{2E_{ion}}{Zk_BT_e}}\right] \tag{4.10}$$

where N_{ion} is the number of ions per energy E_{ion} which extends up to the maximum proton energy at the ion front, given by E_{max}.

Despite the success of the Mora model, it is inherantly limited by idealistic initial conditions (i.e. Boltzmann distribution of electron energies) and generalised assumptions (i.e. single electron temperature and isothermal expansion). Indeed, work by Passoni *et al.* [145] investigated the influence of including two electron populations (with different temperatures) in the expansion model and concluded that a two-temperature electron model results in a larger peak accelerating field that a one-temperature model. Moreover, the dynamics of the Mora expansion model are in 1-D, and thus limited to resolving 1-D features such as the proton

spectrum. To obtain a more complete picture of TNSA, multi-dimensional simulations must be performed utilising 3-D particle-in-cell (PIC - see section 4.5.2) codes.

Ion beam characteristics

Ion beams produced via the TNSA process exhibit key characteristics which enable their use in a wide range of applications, from cancer therapy [146] to isochoric heating of matter [147]. An important feature of the beams is their high particle number (i.e. $\sim 6 \times 10^{13}$ protons of $\sim$ MeV energy), which leads to relatively high laser-to-proton energy conversion efficiencies of ~ 15 % [148]. In addition, the beams also exhibit an energy-dependent divergence angle (i.e. opening angle), where the highest energy ions are emitted with the smallest opening angle and lower energy protons are emitted in larger opening angles (see Fig. 4.2). This effect arises from the Gaussian-shaped spatial profile of the sheath field which is due, in part, to the focal spot spatial-profile [149]. Thus, as the peak amplitude of the field evolves spatially (and temporarily), lower energy protons originate from larger radii while high proton energies are accelerated by the strongest region of the electric field (i.e. at the centre of the Gaussian).

In addition, the source size of the ion beam has been shown to be energy dependant, as demonstrated by Cowan *et al.* [33] and Roth *et al.* [150] (using modulations in the proton beam arising from grooves imprinted onto the target-rear surface), and Borghesi *et al.* [151] (using a mesh placed between the target rear-surface and RCF stack). The resulting source size was determined to exhibit a diameter of ~ 100 μm and corresponding virtual source size (located a few hundreds of μm in front of the target) of ~ 10 μm. Moreover, it was highlighted that the source size is derived from the early stages of the acceleration process [151].

The beam emittance enables the source size and divergence of the proton beam to be defined using the emission angle at a given transverse position. The key property relevant to the results presented in this thesis is the efficient mapping of rear-surface groove patterns into the proton beam [152], which provides

clear evidence that the accelerated proton beam possesses a high degree of laminarity (i.e. low emittance [33], where a high beam laminarity corresponds to the accelerated proton beam paths (i.e. trajectories) being orientated parallel to each other − they do not overlap). This important property of high laminarity means that the structure of the electric sheath field is directly mapped into the spatial-intensity profile of the accelerated ion beam, and is central to the experimental results presented in this thesis.

4.4.2 Measuring laser-accelerated protons - stacked RCF detector

In recent years, a number of techniques have been employed to measure the spatial-intensity profile and energy spectrum of beams of ions accelerated from the target rear-surface of solids irradiated by intense laser pulses, including contact radiography [153] and Cu-activation [154]. However, due to it's preferential sensitivity to protons (when used in a stack configuration), together with it's relative ease of experimental implementation (and almost immediate information retrieval), spatial and energy measurements of sheath-accelerated proton beams is most often made using stacks of radiochromic film (RCF). RCF is a plastic dosimetry film containing an organic, self-developing dye which turns blue when irradiated by ionising radiation (preferentially sensitive to protons). The optical density (OD) of the film is defined by:

$$OD = -\log_{10}\left(\frac{I}{I_{bd}}\right) \tag{4.11}$$

where I is the intensity of a given pixel and I_{bd} is the maximum signal value for a given bit depth (i.e. 65535 for a 16-bit scanner). The OD is directly correlated with the incident radiation flux (i.e. dose), in which a higher dose corresponds to a higher optical density (manifested by a darker blue colour on the RCF film).

There are a number of types of RCF available [155] which have been successfully fielded and characterised for laser-solid experiments. For the investigations described in this thesis, RCF type HD-810 was used, the composition of which is

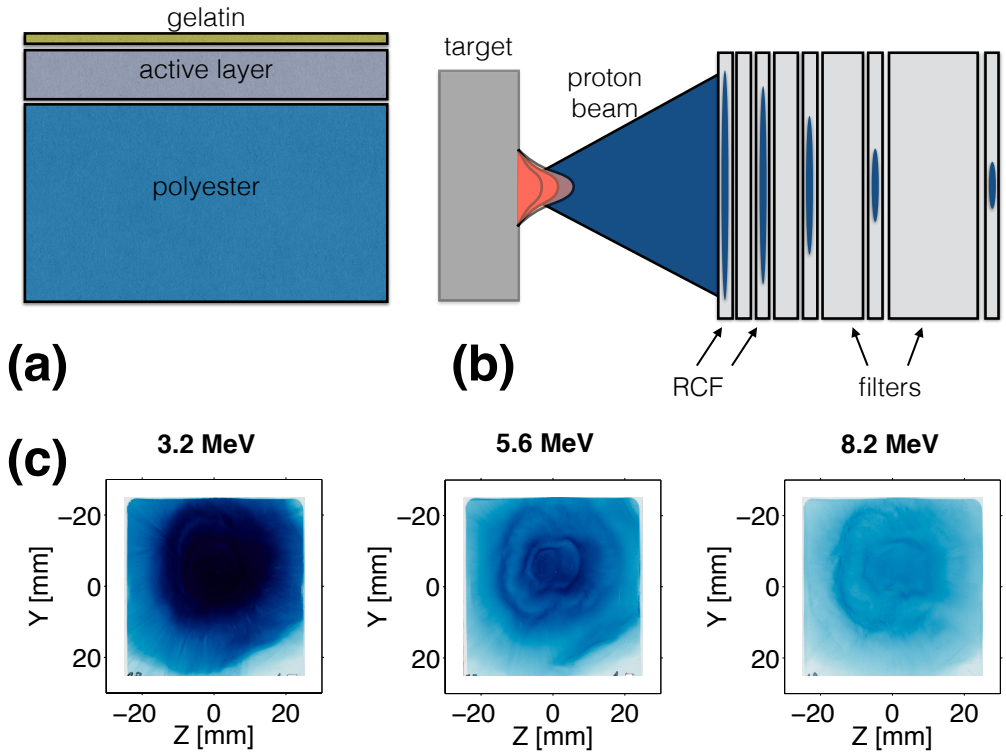

Figure 4.3: RCF stack diagnostic: (a) composition of radiochromic film (RCF); (b) typical experimental implementation of RCF to measure sheath-accelerated proton beams; and (c) representative measurements of a TNSA proton beam.

displayed in Fig. 4.3 (a).

The implementation of RCF in a typical laser-solid interaction experiment involves multiple layers of RCF interspersed with 'filter' layers, which are placed at some distance behind (or in-front, if measuring protons accelerated from the front-surface) the target, typically $\sim$ 3 - 7 cm to enable measurement of the entire beam, positioned along the target normal axis and parallel to the target rear-surface (see Fig. 4.3 (b), with an example proton spatial-intensity profile displayed in Fig. 4.3 (c)). Additionally, each stack is wrapped in a thin ($\sim$ 13 μm) Al layer to prevent heavier ions depositing energy in the RCF stack, in addition to preventing optical exposure of the RCF to the main pulse.

Using stacks of dosimetry film to measure both the spatial and energy profile of a laser-accelerated proton beam is possible due to the process by which ions deposit energy in matter. In contrast to electrons or photons, ions deposit the majority of their energy at the end of their propagation distance in a sharp peak

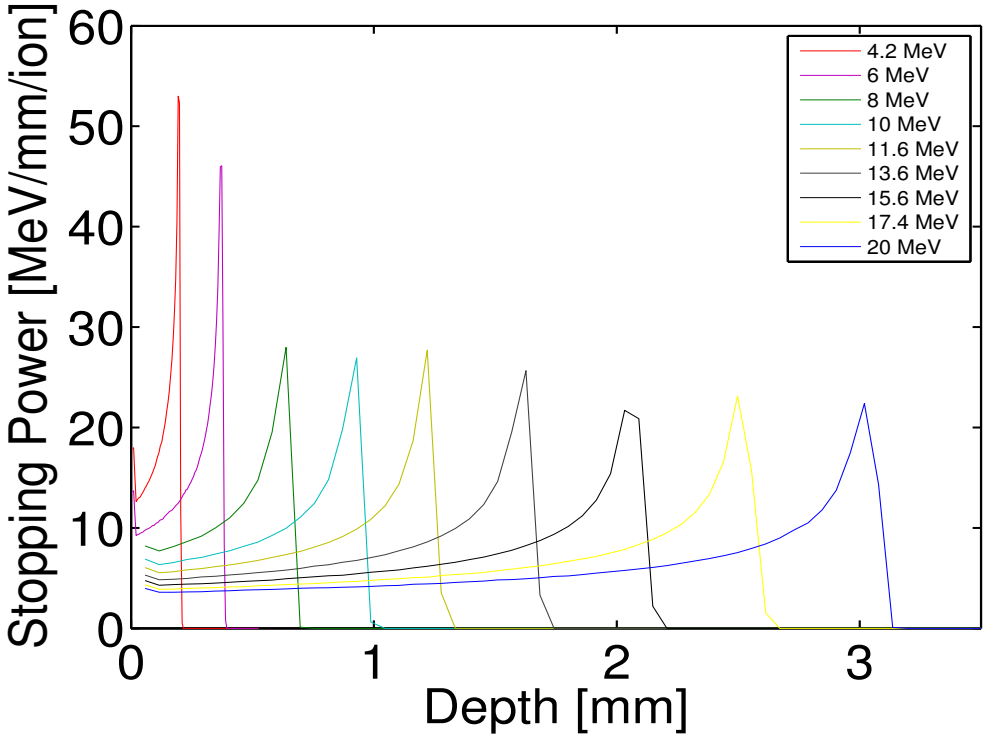

Figure 4.4: Stopping range for protons of various energies (highlighted in the legend) in Mylar, calculated using the SRIM (Stopping and Range of Ions in Matter) code.

known as the Bragg peak. The depth of the Bragg peak is energy dependent and thus low energy protons are stopped in the front layers of the stack, whereas higher energy protons propagate deeper into the stack, stopping at greater depths. Example stopping curve profiles for protons in a stack of Mylar (i.e. plastic) as is typically used in an experimental configuration, is displayed in Fig. 4.4. Using filters within the stack enables a range of proton Bragg peaks (and thus beam energies) to be resolved due to the modification of the stopping profile for increasing depth of material. In addition, using filter layers of different materiel (i.e. Cu or Fe), and thus different stopping power, enables the measurement of protons of an even greater range of energies. The proton stopping curves are calculated using the SRIM (Stopping and Range of Ions in Matter) code [156], which uses a Monte-Carlo algorithm to produce stopping range tables for a variety of materials.

The information that RCF stacks provide is important for characterising the

ion beam properties, electric sheath-field and fast electron transport properties. Specifically, RCF provides the following information: 1) proton beam divergence; 2) proton energy spectrum; 3) Laser-to-proton conversion efficiency; and 4) proton beam spatial-intensity distribution. These, in turn, provide information on the sheath-field and fast electron transport properties.

One of the first studies exploring the origin of ring-like ion beam spatial profiles from solids irradiated by intense laser pulses was by Clark et al. [28]. Using both experimental measurements and simulations, Clark *et al.* concluded that the observed ring structures were the result of front surface-accelerated protons being deflected by large magnetic fields within the interior of the target (generated by fast electrons). However, a comment by Gaillard *et al.* [157] challenged this conclusion by pointing out that saturation effects on the ion detectors (i.e. CR-39) can account for annular profiles. This comment was subsequently addressed and corrected by Clark *et al.* [158].

The proton beam divergence is represented by cone half-angle θ_D, calculated using $\theta_D = \tan^{-1}(r_D/x)$ where x is the stack to RCF distance and r_D is the radius of the circle created by the proton beam spatial profile on the RCF. Moreover, by fitting a circle to the proton beam profile and calculating the ratio of the proton beam circumference to the circumference of the circular fit, the circularity of the beam can be quantified. Importantly for the investigations presented in this thesis, the uniformity of the proton beam can be quantified using statistical methods (i.e. standard deviation and coefficient of variance - see Chapter 5).

To extract the proton energy spectrum, the following steps are performed. First, a calibration of proton dose to optical density is performed for the specific RCF type (in this case HD-810) used. This was performed by Dr. J. S. Green using the MC40 cyclotron at the University of Birmingham. To maintain the high spatial resolution of RCF (i.e. ~ 1 μm) both the calibrated and experimentally exposed film are scanned using a high-resolution optical scanner (Nikon CoolScan 3000), with a spatial resolution > 600 pixels/inch to ensure fidelity of the high resolution film detail.

The total energy deposited, E_T, within each RCF layer is calculated from the

summation of the proton dose measured (using a conversion factor obtained from the calibrated film), together with the mass of the RCF active layer contained within each pixel:

$$E_T = d_L \rho_L \sum_{i=1}^{N} (D_i A_i) \tag{4.12}$$

where N is the total number of pixels in the region of scanned RCF for which the proton dose has been calculated, D_i is the proton dose deposited in the i^{th} pixel and A_i is the area of the i^{th} pixel, d_L and ρ_L are the thickness density, respectively of the RCF active layer.

The proton energy spectrum is calculated using Eq. 4.12, assuming that the dose contribution in a given RCF layer by higher energy protons is negligible and that the protons stopped within each respective layer deposit all their energy

$$N_p = \frac{E_T}{E_{PK} \Delta E} \tag{4.13}$$

where N_p is the number of protons stopped in a given layer, E_{PK} is the central Bragg peak proton energy for a given layer and ΔE is the energy difference due to the thickness of the RCF layer (i.e. the energy difference between protons stopped in the front and rear of the RCF active layer).

4.5 Numerical modelling

Experimental observations and measurements provide the foundation on which an understanding of laser-solid interactions is built upon. However, the large range of parameters (i.e. laser parameters and target composition) that govern the physical processes necessitate the use of a variety of numerical tools to both interpret experimental findings and to explore new ideas and directions for research. While analytical models provide important details for predicting specific scalings (i.e. proton energy with laser intensity) and understanding key concepts, the extreme complexity of laser-solid interactions requires a more complete numerical treatment. When these simulation tools are used in conjunction with

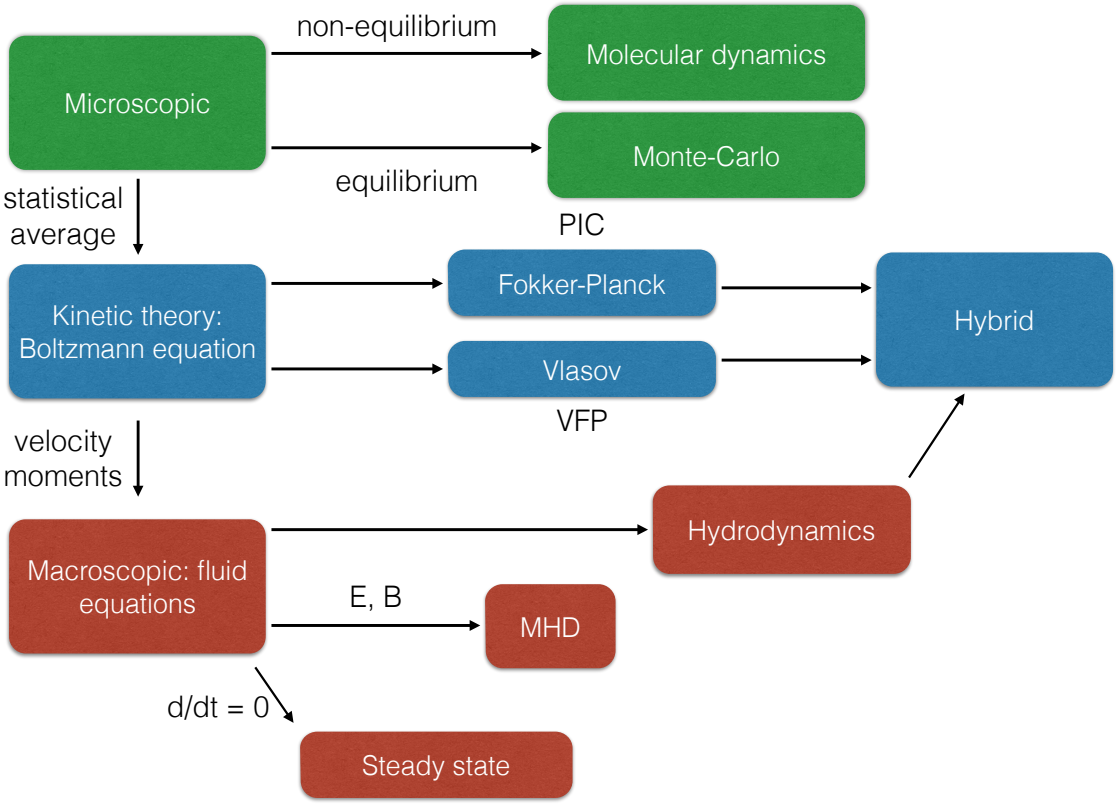

Figure 4.5: Schematic of common numerical methods used in both plasma and laser-plasma simulations (adapted from Gibbon [45]).

experimental data and analytical calculations, a rich description of the underlying physical phenomena emerges.

Within the context of high-intensity laser-solid interactions, two approaches to numerical simulation have been most widely used: 1) hydrodynamic (i.e. fluid); and 2) kinetic (i.e. particle). In Fig. 4.5, the relationship between a range numerical techniques is illustrated schematically (adapted from Gibbon [45]), displaying the wide variety and scope of numerical methods – the kinetic theory and macroscopic (i.e. fluid equations) paths are of particular relevance to laser-plasma interactions. In addition, a key step has been highlighted which shows the relationship between kinetic and fluid approaches when applied to a 'hybrid' code, as is used in the investigations presented in Chapters 5, 6 and 7.

Finally, it is also important to note that microscopic effects (i.e. at the molecular level, corresponding to condensed matter physics and quantum mechanical

effects) are simulated using molecular dynamics techniques (i.e. quantum molecular dynamics (QMD) simulations - see Chapter 3). Simulations of this kind, while not normally considered important for intense laser-solid interactions, can in-fact play a defining role for conditions relevant to fast electron and applications such as fast ignition, as will be demonstrated in Chapter 5, 6 and 7.

4.5.1 Hydrodynamic simulations: HELIOS

The hydrodynamic approach to modelling laser-solid interactions treats the plasma as a fluid using the macroscopic variables of density, pressure and fluid velocity. Hydrodynamic simulations are of particular use in simulating dynamic, large-scale plasmas, particularly when strong collisions are expected to dominate the plasma behaviour. Strong collisions occur when a particle undergoes many collisions during the timescale of interest; an alternative description is that the mean free path of a particle is small compared to the plasma dimension. For a collisional plasma, the local particle distribution function can be approximated by a Maxwellian distribution and the system is described as being in local thermodynamic equilibrium (LTE). By contrast, if collisions are weak (and thus the electron distribution cannot be described by a Maxwellian), then the hydrodynamic approach breaks down and the plasma must be treated kinetically (see section 4.5.2).

Hydrodynamic simulations are governed by three key equations which are solved for particle velocity, $\mathbf{v}$, density, ρ, pressure, P, and total energy ϵ of the system. The equations are defined by:

$$\frac{\partial}{\partial t} + \nabla \cdot (\rho \mathbf{v}) = 0 \tag{4.14}$$

$$\rho \frac{\partial \mathbf{v}}{\partial t} + \rho \cdot (\mathbf{v} \cdot \nabla)\mathbf{v} = -\nabla P \tag{4.15}$$

$$\frac{\partial \epsilon}{\partial t} + \nabla \cdot (\mathbf{v}(\epsilon + P)) = 0 \tag{4.16}$$

In conjunction with these equations, an appropriate Equation of State (EOS) is used, given by:

$$P = f\left(\epsilon - \frac{1}{2}\rho\mathbf{v^2}\right) \tag{4.17}$$

The EOS can take the form of an ideal gas (i.e. $P = (\gamma - 1)(\epsilon - \frac{1}{2}\rho)$, where γ is the ratio of the specific heat capacity at constant pressure to the specific heat capacity at constant volume between the electrons and ions) or more sophisticated models such as the SESAME tables [159] and QEOS model [160], which combine experimental measurements with both analytical theory and numerical simulations to generate wide parameter-range equation of state tables.

Although hydrodynamic codes do not directly include a laser (i.e. through solving Maxwell's equations), a laser is typically defined and incorporated into the code as a heating source term (using a prescribed model). In addition, magnetic field dynamics are included (via Ohm's law), which also act to determine the electric field dynamics. In this case, the hydrodynamic code is known as a magnetohydrodynamic (MHD) code.

Hydrodynamic codes are most commonly characterised due to the technique employed to solve the fluid equations of motion (i.e. Eq. (4.14), Eq. (4.15) and Eq. (4.16)). This can be either Eulerian and Lagrangian, which are determined by the technique by which each code maps the fluid components to a simulation grid. For a Eulerian code, the simulation grid is spatially fixed and calculates the fluid variables at a given point in space for all times. By contrast, a Lagrangian hydrodynamic code utilises a simulation grid which propagates with the fluid flow, where each cell corresponds to a separate fluid element.

The hydrodynamic code utilised in the investigations presented in this thesis is the 1-D Lagrangian radiation-magnetohydrodynamics code HELIOS-CR [51]. HELIOS solves the hydrodynamic equations – in Lagrangian form (i.e. the spatial grid moves with the fluid, where electrons and ions are assumed to be co-moving) – for a range of simulation geometries (i.e. planar, cylindrical, and spherical). In addition, the code enables 'targets' (i.e. solids or plasmas) to be composed of a single or multi-layer material by defining regions containing

unique material properties. The evolution of the material's properties are described by EOS and opacity databases that are generated under the assumption of local thermodynamic equilibrium (LTE), as well as those generated for non-LTE plasmas. Moreover, pressure contributions to the hydrodynamic equations come from electrons, ions, radiation, and from magnetic fields. Both the electron and ion distributions are assumed to be Maxwellian, defined by their respective temperatures, T_i and T_e, and the energy transport can be treated using either a one-temperature ($T_i = T_e$) or two-temperature ($T_i \neq T_e$) model.

Material EOS properties are based on either SESAME tables [159] or PROPACEOS tables [51], and opacities are included through tabulated PROPACEOS data. For inclusion of a laser source, the energy deposition is calculated using an inverse Bremsstrahlung model, together with the condition that the beam doesn't propagate beyond the critical surface. In planar geometry (i.e. that representative of a laser-solid experiment), laser light is transported along a given trajectory with incidence angle θ_i. Other simulation geometries can also be accounted for (i.e. spherical geometry, in which a multi-ray, conical beam model is used to describe laser propagation [51]), but do not feature in the investigations presented in this thesis.

Additionally, and key to the investigations presented in Chapter 7, HELIOS also includes the capability to deposit energy into the plasma using ion beams, utilising a Monte-Carlo algorithm to calculate the ion stopping profiles in conjunction with a ray-tracing algorithm to determine the particle (i.e. ion) trajectories. This enables the hydrodynamics (i.e. temperature and density profiles) of proton-irradiated solids to be simulated.

4.5.2 Hybrid-PIC electron transport simulations: ZEPHYROS

For laser-solid interactions, the most widely used simulation method is kinetic simulations, which make few initial assumptions and approximations, and thus can be envisaged as a 'numerical experiment', offering key insights into the laser-

plasma interaction dynamics.

The most simple kinetic description of a plasma utilises a single particle velocity distribution, $f(\mathbf{r}, \mathbf{v})$. The distribution evolution is described using the Vlasov equation which is given as:

$$\frac{\partial f}{\partial t} + \mathbf{v} \cdot \frac{\partial f}{\partial x} + q\left(\mathbf{E} + \frac{\mathbf{v}}{c} \times \mathbf{B} \cdot \frac{\partial f}{\partial \mathbf{p}}\right) = 0 \tag{4.18}$$

where $\mathbf{r}$ is the spatial dimensions, $\mathbf{E}$ is the electric field, $\mathbf{B}$ is the magnetic field, $\mathbf{p}$ is the momentum and $\mathbf{v}$ is the velocity.

The velocity distribution function $f(\mathbf{r}, \mathbf{v})$ is 6-dimensional (3 spatial and 3 velocity components) and therefore the general solution of Eq. (4.18) is practically unsolvable for most realistic experimental conditions. Furthermore, even for 1D simulation geometry, two or three velocity components are required to correctly incorporate the electron motion and coupling to Maxwell's equations, resulting in a complicated 3-D or 4-D simulation code.

Over the years, the most popular method by which to numerically solve the Vlasov kinetic equation is the Particle-in-Cell (PIC) technique [161]. In this method, rather than solving Eq. (4.18) as it stands, the distribution function is represented using discrete, statistically weighted particles, known as macro-particles. Each macro-particle is described using a charge q_i and mass m_i and are moved according to the Newton-Lorentz equation [45]:

$$\frac{d}{dt}\left(\gamma_i \mathbf{v_i}\right) = +\frac{q_i}{m_i}\left(\mathbf{E} + \frac{\mathbf{v_i}}{c} \times \mathbf{B}\right) \tag{4.19}$$

where $\gamma_i = (1 - v_i^2/c^2)$ and $i = 1, ..., N$ is the number of macro-particles.

When the Vlasov equation (Eq. (4.18)) is solved using computational particles (i.e. macro-particles), the resulting code is known as a *collisionless* PIC code. By contrast, a *collisional* PIC code accounts for collisions by including Fokker-Planck collisional operators (for electron and ion species) on the right hand-side of the Vlasov equation, which can account for (to first order) effects such as resistivity [38].

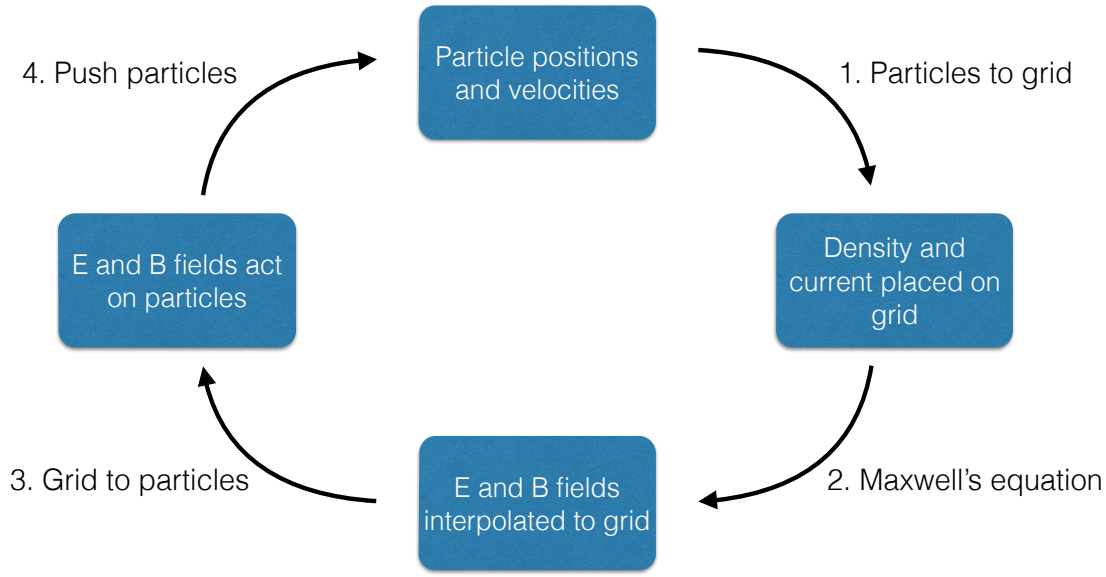

Figure 4.6: Illustration of the particle-in-cell (PIC) algorithm.

The core PIC algorithm follows the steps outlined below, as shown schematically in Fig. 4.6.

Initially, the particles are moved using the Lorentz equation (i.e. Eq. (4.19)). The density and current source terms (required to enable integration of Maxwell's equations) are obtained by interpolating the local particle positions and velocities onto the simulation grid, given respectively by:

$$\rho(\mathbf{r}) = \sum_{j=1}^{N} q_j S\left(\mathbf{r_j} - \mathbf{r}\right) \tag{4.20}$$

$$\mathbf{J}(\mathbf{r}) = \sum_{j=1}^{N} q_j \mathbf{v}_j S\left(\mathbf{r_j} - \mathbf{r}\right) \tag{4.21}$$

where $S\left(\mathbf{r_j} - \mathbf{r}\right)$ is a function which describes the shape of the macro-particle; there are a variety of descriptions of the macro-particle shape, including spline and 'Cloud-in-Cell', with each representing varying degrees of accuracy.

Once $\rho(\mathbf{r})$ and $J(\mathbf{r})$ are defined at the simulation grid points, Maxwell's equations are solved to obtain updated electric and magnetic fields. These updated fields are then interpolated back to the particle positions, acting to push the particles via the Lorentz equation, thus completing the cycle for a single temporal time-step. This process is then re-iterated for the required number of time-steps.

While PIC codes are extremely powerful in simulating a vast array of laser-plasma interactions (i.e. electron acceleration [162] and harmonic generation [163]), the method can become computationally expensive when applied to fast electron transport in solids. Within this context, the key challenge is resolving the large disparity in both spatial and temporal scales; a fully collisional PIC code must resolve the cold electron Debye length ($<$ nm) and plasma frequency ($<$ fs) to inhibit the onset of numerical artefacts (for example, numerical heating [161]), while simultaneously resolving the fast electron propagation distance ($\sim$ hundred μm), Debye length ($\sim$ μm) and pulse duration ($\sim$1 - 10 ps).

A model that has been widely used to address these issues is the so-called 'hybrid' code. In the context of laser-solid interactions and fast electron transport, 'hybrid' refers to the key feature of this technique; the background plasma is treated as a fluid (i.e. hydrodynamically) while the fast electrons are treated kinetically (i.e. via PIC algorithms, as outlined above). Hybrid-PIC codes can be characterised by the method they use to solve Maxwells equations, typically adopting one of two techniques: 1) explicit hybrid-PIC codes, in which a leap-frog algorithm [161] is used; and 2) implicit hybrid-PIC codes, which employ an alternate-direction iterative (ADI) [161] algorithm. While explicit hybrid-PIC codes offer excellent capability at simulating electron transport in dense plasma (i.e. solids), a key advantage of an implicit scheme is that low-density plasma physics (i.e. laser-plasma interactions) can also be included in the simulation [164].

In essence, a hybrid-PIC code circumvents the computational limitations of a collisional PIC code by sacrificing a degree of accuracy to produce a reduced model which is relatively quick to compute, and which only needs to resolve the fast electron scale properties (i.e. propagation distance, Debye length and pulse

duration). This is implemented by making a number of key assumptions.

The main assumption made is that the fast electron population number is small in comparison to the background electron population number (i.e. $n_f \ll n_b$, where n_f is the number of fast electrons and n_b is the number of the background electrons). Note that despite the fast electron number being small in relation the to the background electron number, the current density of the fast electron population can be significant. Furthermore, hybrid-PIC codes also demand that even in the absence of fast electrons, the fluid description of the background plasma is valid on the spatial and temporal scales of interest. This means that the very small length and time scales of the background plasma can be ignored, and thus much larger simulation time-steps can be used enabling more realistic simulations to be performed.

Additionally, if the fast electron population is small, then electrostatic (and magnetostatic) arguments can be made for current neutrality to be conserved (see Chapter 3):

$$\mathbf{j}_f + \mathbf{j}_b = \frac{\nabla \times \mathbf{B}}{\mu_0} \tag{4.22}$$

where f denotes the fast electrons and b denotes the background electrons.

A hybrid-PIC code calculates the electric field via Ohm's law, which in this context is described by:

$$\mathbf{E} = \eta \mathbf{j}_b \tag{4.23}$$

When coupled with current neutrality, and neglecting $\nabla \times \mathbf{B}$ contributions, this becomes:

$$\mathbf{E} = -\eta \mathbf{j}_f + \frac{\eta}{\mu_0} \nabla \times \mathbf{B} \tag{4.24}$$

$$\rightarrow \mathbf{E} = -\eta \mathbf{j}_f \tag{4.25}$$

Using Ohms Law to describe the electric field reduces Maxwell's induction

equation, and thus a resistive magnetic field is generated as:

$$\frac{\partial \mathbf{B}}{\partial t} = \eta \nabla \times \mathbf{j}_f + \nabla \eta \times \mathbf{j}_f + \frac{\eta}{\mu_0} \nabla^2 \mathbf{B} - \frac{1}{\mu_0} \nabla \eta \times \mathbf{B} \tag{4.26}$$

$$\rightarrow \frac{\partial \mathbf{B}}{\partial t} = \eta \nabla \times \mathbf{j}_f + \nabla \eta \times \mathbf{j}_f \tag{4.27}$$

While the background electrons are treated hydrodynamically, the fast electron population is described kinetically utilising the Vlasov equation, which is solved via the PIC method (as outlined previously). Additionally, collisions are included using the Fokker-Planck collisional operators [165], which account for angular fast electron scattering from background ions and electrons, together with drag generated by the background electrons, incorporated using a Monte-Carlo algorithm.

An important component of the hybrid-PIC method, and key to the results presented in this thesis, is that the temperature-dependant resistivity must be prescribed as an input parameter. This can be done using a theoretical model (e.g. Spitzer model or Lee-More model), an empirically measured resistivity (i.e. aluminium resistivity measured by Milchberg *et al* [90]) or using a combination of theory and simulation (i.e. QMD calculations coupled with the Kubo-Greenwood equation − see Chapter 3). Although the resistivity is not calculated self-consistently (unlike a purely kinetic model), the great strength of the hybrid method is that it is relatively straight-forward to incorporate a resistivity model that accounts for the 'warm dense matter' regime (i.e. 1 - 50 eV, see Chapter 3). This capability is fundamentally important for the results described in Chapters 5, 6 and 7.

A variety of hybrid-PIC codes have been developed in recent years, including the first hybrid-PIC code applied to fast electron transport in solids by Davies *et al.*[106], PARIS by Gremillet *et al.* [113], LSP [164] and PETRA [166]. For the results presented in this thesis, the hybrid-PIC code ZEPHYROS is used, which was written and developed by Dr A. P. L. Robinson, and has been employed extensively [23, 39, 167] to simulate conditions relevant to fast electron transport in dense plasma.

Chapter 5

Fast Electron Transport in Carbon

5.1 Introduction

In this chapter, experimental results are presented that demonstrate the importance of the choice of target material in controlling sheath accelerated protons. Example measurements of the spatial-intensity distribution of the beam of multi-MeV protons accelerated from the rear surface of three different target materials irradiated by an intense laser pulse are presented. Furthermore, a model is developed to infer the initial two-dimensional (2D) fast electron density distribution at the target rear surface, and hence the fast electron transport pattern within the target, from the measured 2D proton beam dose distribution. The model is applied to determine the fast electron transport pattern in diamond, which produces an unusual proton beam profile - cusp-like intensity structures at the centre of an otherwise smooth beam. Moreover, the results are compared with previous investigations of fast electron transport in carbon [39] at higher laser-drive intensities, and the electron transport properties are explained using hybrid-PIC simulations together with an analysis of the resistive filamentation instability growth rate. The results presented highlight the defining role that lattice structure, and thereby electrical resistivity at low temperatures (i.e. 'warm dense matter' regime), have in determining fast electron transport properties.

5.2 Experiment

The experiment is performed using the Vulcan laser at the Rutherford Appleton Laboratory, Oxfordshire. In this arrangement, the laser delivers 1.053 μm pulses with an on target energy of 60 J and duration $\tau_L = 1$ ps (full width at half maximum, FWHM). The p-polarised pulses were focused to a FWHM focal spot of 8 μm diameter. The resulting peak intensity is calculated to be 7×10^{19} Wcm^{-2}. The key diagnostic set-up was arranged in the configuration shown schematically in Fig. 5.1. Three different target samples were used: silicon, single-crystalline diamond and vitreous carbon, each of 300 μm thickness and lateral dimension 3 mm $\times$ 3 mm, with highly polished surfaces. While single-crystalline diamond contains a highly ordered face-centred-cubic lattice structure, vitreous carbon exists in a highly disordered (i.e. amorphous) structure and thus the experiment explores differences in electron transport between the two extreme states. The fast electron transport pattern inside the target is diagnosed by recording and analysing the spatial-intensity profile of sheath accelerated proton beams using passive stacks of 5 cm x 5 cm radiochromic dosimetry film (RCF) positioned 6 cm from the rear of the target, as shown in Fig. 5.1.

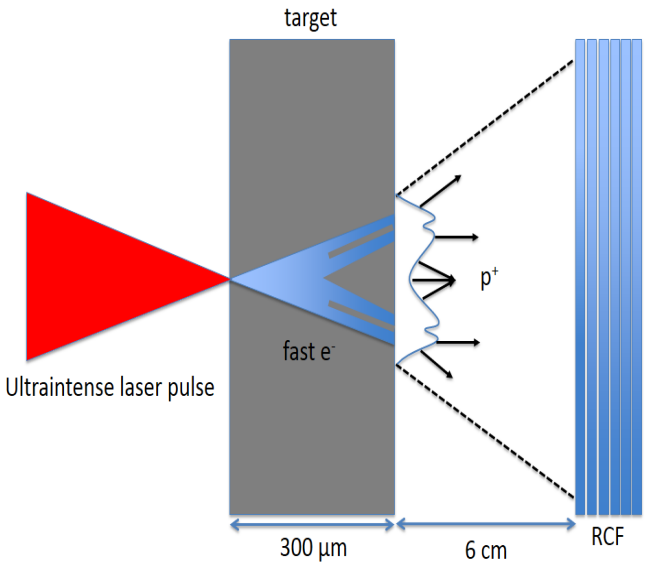

Figure 5.1: Schematic of the diagnostic approach. A high power laser pulse is focused (to a peak intensity equal to 7×10^{19} Wcm^{-2}) onto the front surface of the solid target. Fast electrons are generated in the focal region and propagate through the target, creating a sheath layer, with a multi-TV/m field at the target rear surface. The spatial-intensity dose distribution of the resulting beam of accelerated protons is measured using a stack of dosimetry radiochromic film (RCF).

The accelerated protons are produced as a result of an electrostatic sheath field established at the target rear surface by the fast electrons originating in the laser focal region at the target front surface. Due to the rapid nature of the proton acceleration, any large spatial modulations in the sheath field strength, resulting from modulations or instabilities in the fast electron density, and thus the transport pattern, are mapped into the expanding proton beam intensity distribution [37]. Therefore, by measuring the spatial intensity dose distribution of the sheath accelerated protons, we can infer the electric sheath properties and fast electron propagation dynamics.

Fig. 5.2 shows example experimentally measured proton spatial intensity profiles for (a) 300 μm-thick silicon, (b) 300 μm-thick diamond and (c) 300 μm-thick vitreous carbon, all for peak laser intensity equal to 7×10^{19} Wcm^{-2}. The example proton profiles correspond to a proton energy of 5 MeV in all cases, with similar features observed throughout the RCF stack (i.e. at all proton energies).

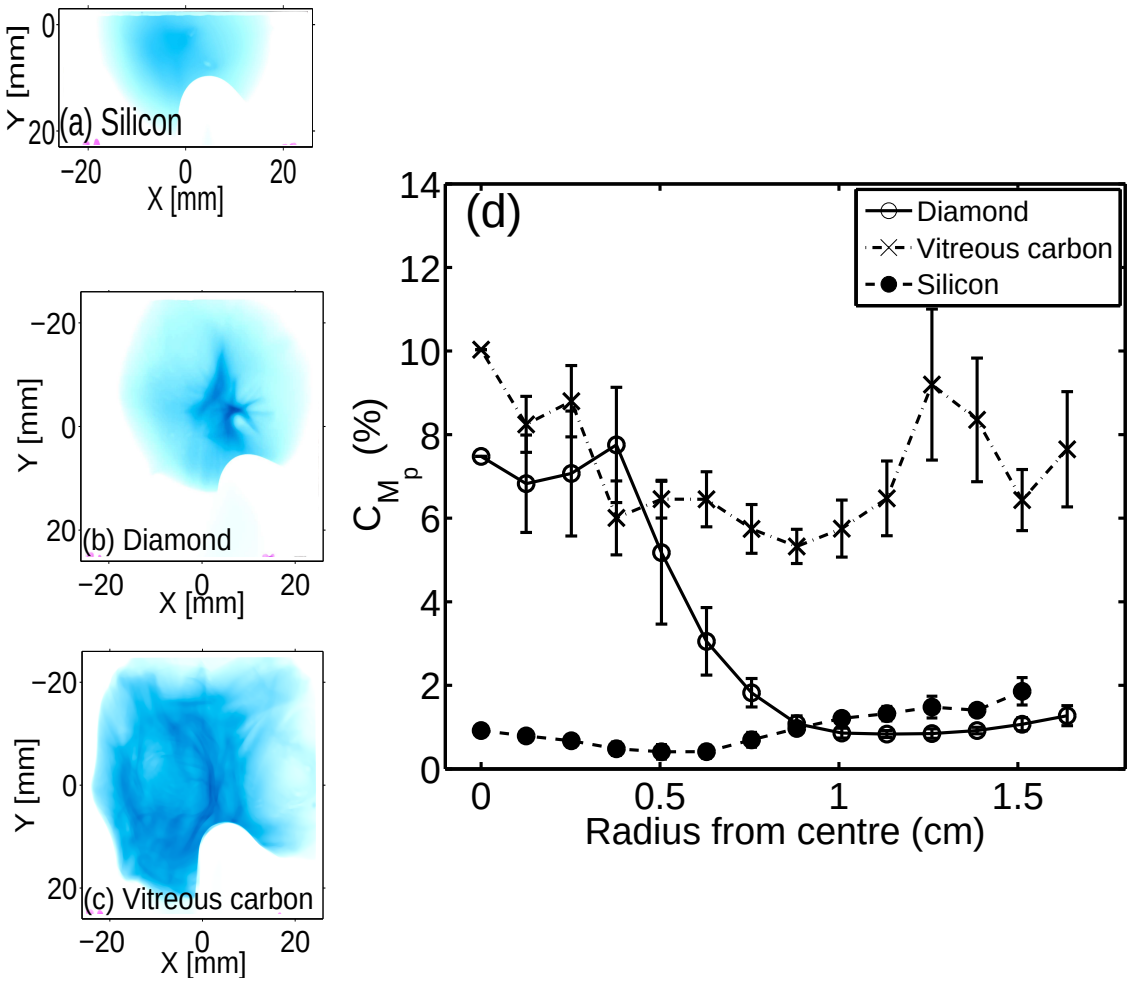

Figure 5.2: Experimental results. Representative measurements of the spatial-intensity dose distribution of protons (at an example energy of 5 MeV) for (a) 300 μm silicon (lower half of the proton beam), (b) 300 μm diamond, and (c) 300 μm vitreous carbon. A small portion of the proton beam on the bottom-right in each image is blocked. (d) Coefficient of variation of the proton dose as a function of radius from the centre of the beam.

The proton beam profiles are distinctly different for the three different target materials. Importantly, the results emphasise the acute sensitivity of sheath-accelerated protons to the different fast electron transport properties within the three materials.

As shown in Fig. 5.2(a), the measured proton beam profile for silicon is circular and highly uniform, reflecting smooth fast electron transport. The corresponding measurement for vitreous (disordered, or glassy-like) carbon shows a highly structured beam intensity profile, with cusp-like features extending to the beam profile edge (Fig. 5.2(c)). As discussed in McKenna *et al.* [39], this structure arises due to filamentation of the fast electron beam during propagation through the target, giving rise to multiple hot-spots in the fast electron density distribution at the target rear-surface, and thus multiple regions of high proton emission within the sheath. The proton front from these sources overlap downstream in the detector plane giving rise to the measured cusp-like features across the beam. Interestingly, the measurements with diamond, as shown in Fig. 5.2(b), for the same laser drive parameters, including peak intensity of 7×10^{19} Wcm^{-2}, produces an unusual proton beam distribution with a fairly circular profile and uniform distribution at large radii, but with strong cusp-like structure at the centre. Repeat laser shots were taken on each of the target materials and the results are fully reproduced.

To quantify the degree of structure or variation across each proton beam, the coefficient of variation of the dose (converted from optical density) across each RCF image is calculated. The coefficient of variation C_p quantifies the percentage statistical variation (standard deviation σ_p) in the proton beam dose relative to the mean M_p of the sampled region, as follows:

$$C_p = \frac{\sigma_p}{M_p} \times 100 \tag{5.1}$$

For multiple angles $N_\theta = 90$, in the lower left quadrant of each proton beam profile, C_p is calculated in sampling regions of 30 $\times$ 30 pixel dimension. The mean across the N_θ angular selections is calculated, giving the mean coefficient

of variation, C_{Mp}, at a given radius, r, as:

$$C_{Mp}(r) = \frac{\sum_{k=1}^{N_\theta} C_p(k,r)}{N_\theta} \tag{5.2}$$

where $k = 1, 2, ..., N_\theta$. The calculation is then performed as a function of radius from the beam center, to quantify the proton beam dose variation radially across the beam profile. Higher values of C_{Mp} correspond to regions of strong dose variation or structure.

This analysis is performed on the measured proton beams for each target type, for the three examples shown in Fig. 5.2(a - c), and the results are shown in Fig. 5.2(d). The error bars correspond to statistical variations across multiple angular samples, with large error bars indicative of angular inhomogeneity in the proton beam dose profile and small error bars corresponding to regions of high angular homogeneity. The resulting structure-radius profiles reflect what is visually observed in each 2D proton dose profile measurement. A low dose variance value is obtained for silicon and a high value for vitreous carbon for all radii. In the case of diamond, the structure or degree of dose variation at the centre of the beam is similar to the vitreous carbon, but with increasing radius the variation decreases to a value more similar to silicon.

Given that lattice structure has been identified as playing an important role in defining fast electron transport patterns [39], it is particularly interesting to compare the proton beam profiles for diamond and silicon, which both have the same diamond-cubic lattice structure. As a starting point, the unusual case of diamond is investigated: a smooth proton beam with structure limited to the beam centre. This will provide a basis for exploration of the underlying transport physics, described later in this chapter.

5.3 Analytical modelling

The analytical model developed to investigate the 2D mapping of the fast electron density distribution into the spatial-intensity distribution of the beam of accelerated protons builds upon previous work reported in [39, 133, 136]. By

performing a systematic investigation of various initial fast electron density and hence electric field profiles, their subsequent spatial and temporal evolution, and the final mapping into the 2D proton profile at the detector, it is found that the proton beam spatial-intensity distribution measured for the diamond targets is explained by an annular fast electron beam with a filamented electric sheath field distribution.

The electric field profile and final proton spatial-intensity distribution are calculated as follows. First, an initial sheath diameter, d_0, equal to $\sim$300 μm is assumed for the fast electron beam arriving at the target rear surface. This corresponds to ballistic transport of the fast electrons through the $L = 300\mu$m thick target, with the inital sheath diameter d_0 given by:

$$d_0 = 2L \tan \theta_{1/2} \tag{5.3}$$

where $\tan \theta_{1/2}$ is the effective half angle of divergence, equal to 26° [120, 124]. Fast electron transport is typically not ballistic due to the effects of self-generated fields, but an 'effective' transport angle, which averages over differences in local beam divergence within the target, is found to provide a good approximation of the beam transport - see for example Coury *et al.* [137]. A 2D spatial grid of cell dimensions 1000 x 1000, with 1 μm cell resolution, is defined to represent the rear target surface. The 2D sheath grid is populated with $n_s = 30$ 'sub-sheaths' to represent individual filaments, each assigned a random relative field strength of R_i, normalised between $0 < R_i < 1$.

As reported in McKenna *et al.* [39], the cusp-like features across the full proton beam for the case of vitreous carbon results from a random distribution of these filaments across the sheath surface, as expected from the stochastic nature of fast electron beam filamentation within the target. However, for the interesting case of the diamond measurement shown in Fig. 5.2(b), we find that we can reproduce the measured proton beam spatial-intensity profile only when the filaments are arranged in an annular pattern and furthermore when there is some degree of asymmetry in the distribution.

The filaments are positioned in a circle of diameter d_0 centred on $x = y =$

0. The spatial-intensity profile of each filament is described using a Gaussian function $f_i(x, y, t)$:

$$f_i(x, y, t) = R_i exp\left(-\left(\left(\frac{(x + x_i)^2)}{2W_i^2}\right) + \left(\frac{(y + y_i)^2)}{2W_i^2}\right)\right) \tag{5.4}$$

where $W_i(t)$ is the expanding Gaussian half width with $i = 1, 2, ..., n_s$.

$$W_i(t > 0) = W_i(t - \Delta t) + v_\perp(t)\Delta t \tag{5.5}$$

The transverse expansion velocity $v_\perp$ across the 2D grid is initially set to c in agreement with previous studies of sheath expansion for similar laser conditions [168, 169]. The value of $v_\perp$ decreases exponentially with time, with $1/e = 1.6$ ps, consistent with optical probe reflectometry measurements of sheath expansion [170]:

$$v_\perp(t) = c\left(0.94 \exp\left(-\frac{t}{1.6ps}\right) + 0.06\right) \tag{5.6}$$

The sheath field spatial distribution is calculated in 100 fs temporal steps as it expands over the predefined 2D grid for a total duration of 2 ps. The magnitude of the field, $E_0.G(t)$, increases with the rising Gaussian temporal profile, $G(t)$, of the laser pulse to a maximum value E_0 at $t_p \approx \tau_L$. Thereafter, the field strength follows an exponential decrease with $1/e = 1.6$ ps.

$$G(t) = \exp\left(-\frac{4ln(2)(t - t_p)^2}{\tau_L^2}\right); \qquad [t < t_p] \tag{5.7}$$

$$G(t) = \exp\left(-\frac{(t - t_p)}{1.6\text{ps}}\right); \qquad [t > t_p] \tag{5.8}$$

The annular group of filaments evolve as individual subsheaths and spread radially along the target rear surface with velocity $v_\perp$, gradually coalescing to form a total electric sheath field $F(x, y, t)$:

$$F(x, y, t) = \sum_{i=1}^{n_s} f_i(x, y, t) \tag{5.9}$$

The spatial and temporal evolution of the sheath field magnitude, $E(x, y, t)$, is calculated using:

$$E(x, y, t) = E_0 G(t) F(x, y, t) \tag{5.10}$$

To produce protons for acceleration by this field, a uniform layer of hydrogen is defined on the target rear surface and the electric sheath field $E(x, y, t)$ ionises the hydrogen, via field ionisation. The resulting protons are accelerated at each time step by the evolving electric sheath field. The expanding ion front is calculated from the local electric sheath field profile, and the protons are accelerated in the direction normal to this ion front. Finally, the protons are translated from the target grid to detector grid using polar coordinates to extrapolate the local gradients from the ion front surface into the angular mapping of the protons. The detector plane is defined as a 6 cm $\times$ 6 cm spatial grid positioned 6 cm from the target rear surface (i.e. equal to the distance between the target and RCF stack in the experiment).

Two example results from the modeling are shown in Figs. 5.3 and 5.4. The first case, Fig. 5.3, involves a ring of filaments while the second case, investigating a uniform annular sheath profile (i.e. without filamentary structures), is shown in Fig. 5.4.

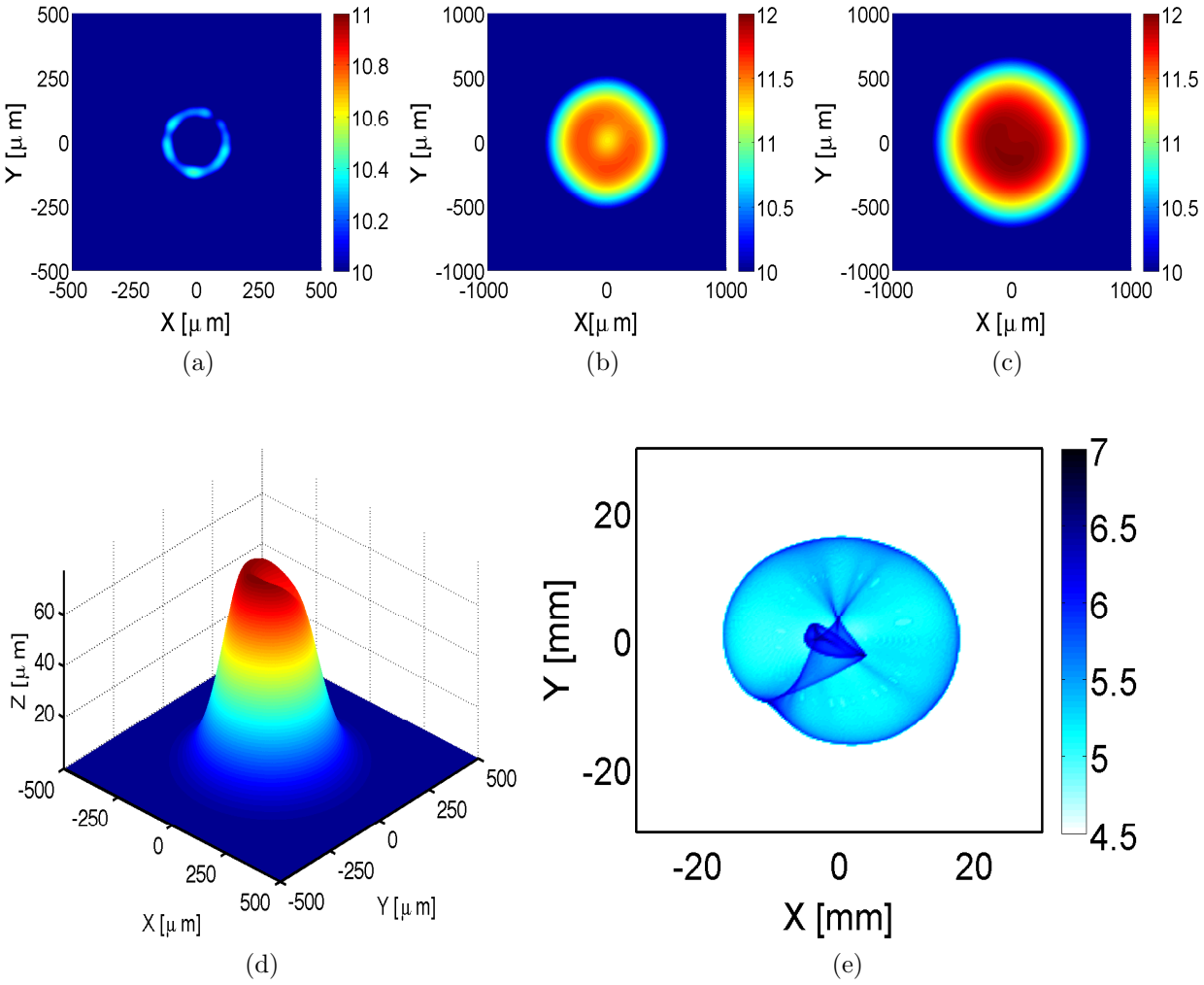

Figure 5.3: Analytical modelling of sheath field dynamics for an annular ring of filaments. (a), (b) and (c) show results for the time evolution of the $\log_{10}$ sheath field (Vm^{-1}) at time steps of 300 fs, 700 fs and 1000 fs respectively. (d) shows the 3-D proton acceleration front, the local gradients of which give rise to the final 2-D proton spatial profile shown in (e).

In Figure 5.3(a), (b) and (c) we plot the electric sheath field at time intervals of 300 fs, 700 fs and 1000 fs. Fig. 5.3(d) shows the final proton acceleration front and Fig. 5.3(e) shows the resulting proton beam spatial-intensity distribution. The initial $n_s = 30$ filaments, of 1 μm FWHM width, merge after 300 fs (Fig. 5.3(a)) into a ring spatial profile of diameter $\sim$ 400 μm. This annular structure then radially expands with velocity $v_\perp$ until the peak electric field strength at the peak of the laser pulse (i.e. at $t_p \approx \tau_L = 1000$ fs), shown in Fig. 5.3(b) and (c) for 700 fs and 1000 fs respectively. The final ion front is shown in Fig. 5.3(d)

and reflects the spatial uniformity of the accelerating surface which generates the final proton spatial-intensity profile shown in Fig. 5.3(e). This profile is in good agreement with the experimentally measured beam for diamond, displayed in Fig. 5.2(b). The protons accelerated by the fast electron hot-spots in the ring superimpose to produce cusp-like structures at the center of the beam, whereas the beam intensity profile is relatively smooth at large radii, and the overall beam is quite circular. The edges of the initial annular distribution, which have the largest field gradients, are maintained throughout the temporal evolution. Since the protons are accelerated normal to the local gradients at the sheath surface, these large spatial field gradients produce large divergence angles in the proton beam, which creates the relatively high degree of circularity in the final beam profile.

As in Fig. 5.3, Fig. 5.4(a), (b) and (c) correspond to the electric sheath field at time intervals of 300 fs, 700 fs and 1000 fs respectively, while Fig. 5.4 (d) shows the final proton acceleration front and Fig. 5.3(e) gives the resulting proton beam spatial intensity distribution. Fig. 5.4 reveals that an annular profile *without* filamentary structure gives rise to a cylindrically symmetric proton beam spatial-intensity profile containing a ring-like feature within it.

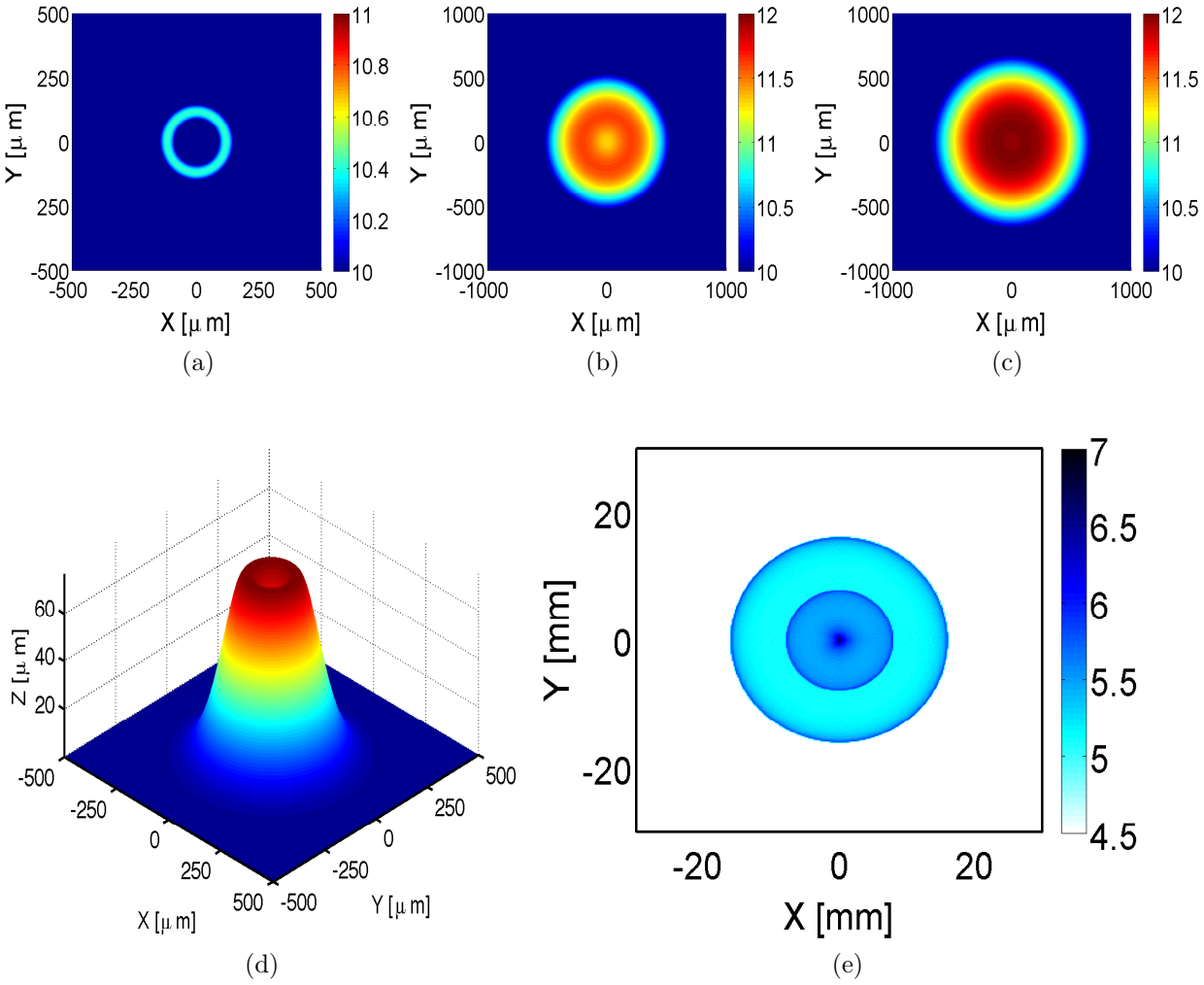

Figure 5.4: Analytical modelling of sheath field dynamics for a uniform ring. (a), (b) and (c) show the $\log_{10}$ sheath field (Vm^{-1}) at time steps of 300 fs, 700 fs and 1000 fs respectively. (d) shows the 3-D proton acceleration front, the local gradients of which give rise to the final 2-D proton spatial profile shown in (e).

To compare the model calculations of proton beam uniformity with the experimentally measured proton distributions, the previously described radial statistical analysis is performed on the model result in Fig. 5.3(e). The results are shown in Fig. 5.5 alongside the corresponding experimental profile for diamond (from Fig. 5.2(b)). Good quantitative agreement is found. Whilst there are some differences in the statistical variation between the experimental and model proton beams at certain radii, particularly between 0 cm and 0.5 cm, the overall features of the experimental result are well reproduced.

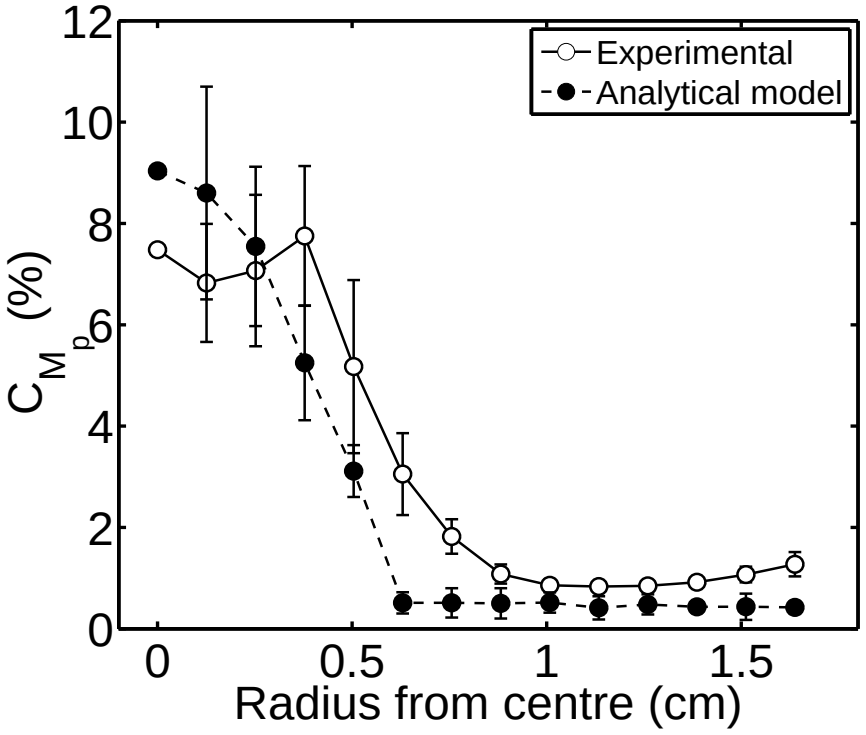

Figure 5.5: Coefficient of variation of the proton beam intensity as a function of radius. Good overall agreement is obtained between the model calculations (Fig. 5.3(e)) and experiment (Fig. 5.2(b)).

The different proton beam spatial-intensity profiles result from differences in the fast electron transport patterns within the target. As it propagates, the fast electron beam is subject to a number of different transport instabilities and the effects of self-generated fields. In a recent investigation, reported in McKenna *et al.* [39], performed at a higher peak laser intensity (2×10^{20} Wcm^{-2}) smooth proton beams were obtained for diamond targets (across the full proton beam area) and structured beams were measured for vitreous carbon. The difference between the two results was explained by the higher resistivity of vitreous carbon at relatively low temperatures of 1-50 eV. The differences in resistivity of the two carbon targets was attributed to the different degree of ordering of the carbon ions (i.e. the lattice structure). The distinctly different proton beam profile measured with diamond for the lower peak laser intensity (7×10^{19} Wcm^{-2}) in the present work points to a different fast electron beam transport pattern within the target. Therefore, the underlying electron transport physics underpinning

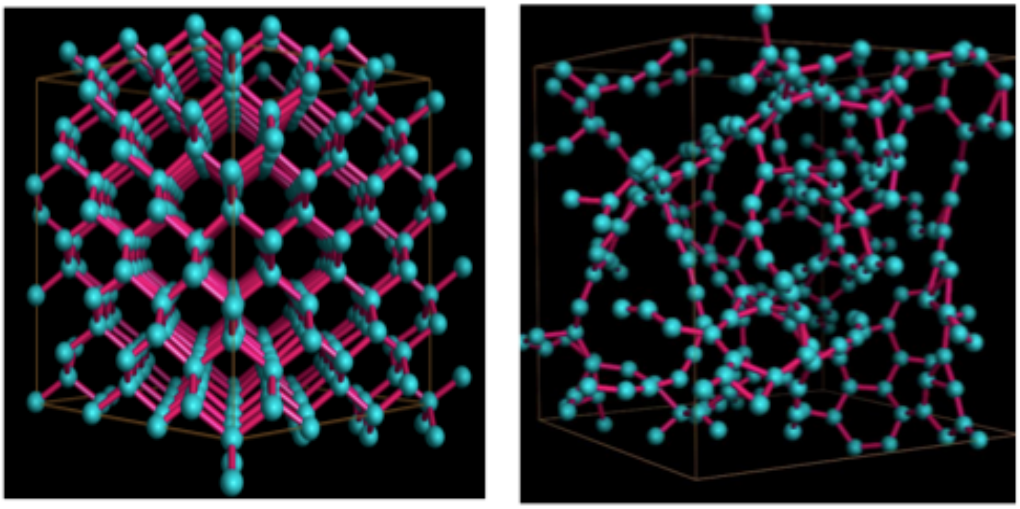

(a) Diamond (b) Vitreous carbon

Figure 5.6: Configuration of: (a) ordered diamond lattice structure; and (b) amorphous vitreous carbon structure. Reproduced with permission of Dr M. P. Desjarlais, Sandia National Laboratory.

these experimental observations is now investigated.

5.4 Numerical simulations

Firstly, the properties of the two extreme lattice structure states examined in this study (i.e. diamond - tetrahedral lattice; Fig. 5.6(a), and vitreous carbon - amorphous structure; Fig. 5.6(b)) are explored and differences in resistivity between the two materials in their transition from cold-solid, through warm dense matter state to eventual hot plasma are evaluated. Crucially, it is the ionic structure of the material which determines the resistivity-temperature profile in the transient warm dense matter regime.

First, the ionic structure of each carbon allotrope is simulated. These simulations were performed by Dr M. P. Desjarlais of Sandia National Laboratory. The ionic configurations are calculated using quantum molecular dynamics (QMD) simulations utilising the plane-wave density functional code VASP [91, 92]. The atomic configurations of each allotrope were obtained by performing the DFT simulations at a fixed temperature of 300 K, corresponding to the ionic structure

at room temperature. Next, the electronic temperature was varied from 0.025 to 20 eV in subsequent static Kubo-Greenwood conductivity calculations [85] using the previously sampled atomic configurations at 300 K.

Fig. 5.7 shows the resulting resistivity as a function of temperature for both carbon allotropes. Diamond (blue curve in Fig. 5.7) is strongly insulating at room temperatures due to the large energy separation (i.e. band gap) between its valence and conductance bands. However, the electrical resistivity decreases sharply with temperature as soon as the electrons are ionised above the material band gap. The dip in the diamond resistivity represents ionisation of the 2s-shell electrons. By contrast, the resistivity of vitreous carbon, which is relatively low at room temperature, drops only weakly with increasing temperature. In the transient WDM regime ($\sim$10 eV), the electrical resistivity of diamond is nearly two orders of magnitude less than that of vitreous carbon. At temperatures greater than $\sim$100 eV the resistivity decreases for both materials, representing a transition to a Spitzer resistivity.

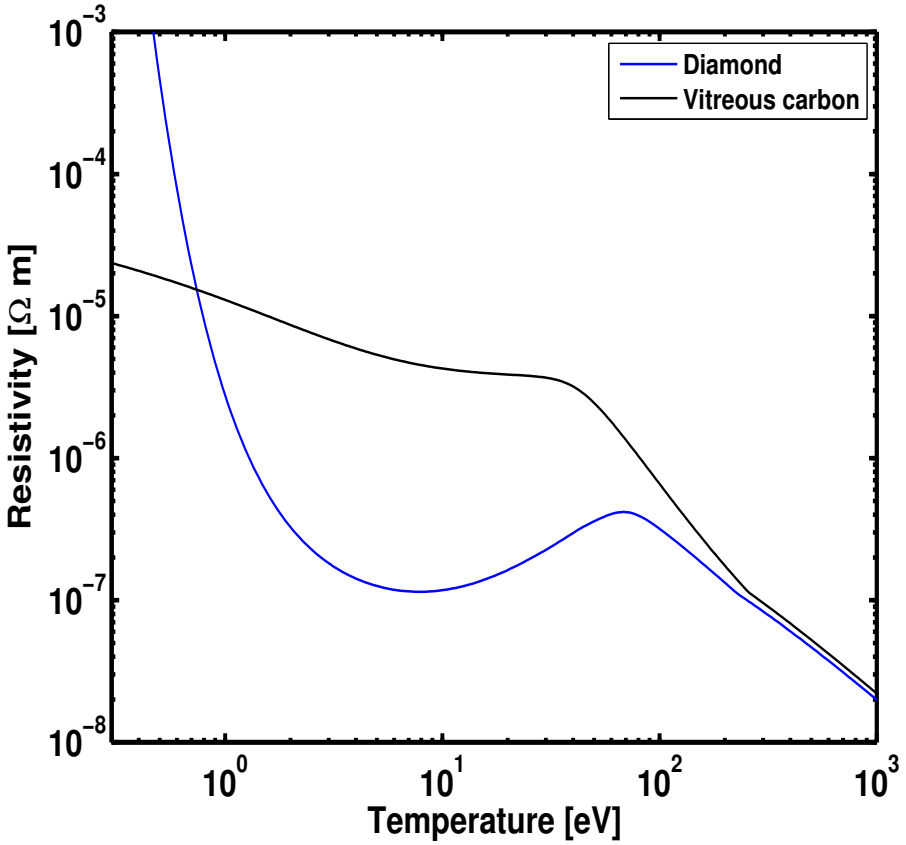

Figure 5.7: Calculations of the resistivity of carbon. The blue curve is the *ab initio* QMD calculation coupled with the Kubo-Greenwood equation for diamond while the black curve is the same calculation performed for vitreous carbon.

The origin of the effect of ionic ordering on electrical conductivity is understood by considering the electron mean free path, which fundamentally determines the shape of the resistivity-temperature curve in the transient, non-equilibrium WDM regime. If the ions are in an amorphous, disordered state (i.e. vitreous carbon) then electrons scatter incoherently from the lattice sites, resulting in an electron mean free path that is limited to the mean interionic distance which results, in turn, to a high resistivity. Conversely, if the ions are in a well-ordered geometric lattice (i.e. the face centred cubic diamond lattice) then coherent scattering of the electrons occurs, resulting in constructive interference of the scattered electron wave functions from multiple lattice sites. This gives rise to a mean free path considerably longer than the mean interionic distance. Thus, for an ordered arrangement of ions the material resistivity is lower than for a dis-

ordered material of the same atomic element, and similar density. At very high temperatures (> 100 eV) the scattering cross sections decrease with increasing mean electron energy - typical of Coulomb scattering processes as the material transitions to a plasma state - and hence the resistivity decreases regardless of ionic ordering.

To explore the effect that lattice ordering has on the propagation of fast electrons, the calculated resistivity-temperature profiles from Fig. 5.7 are incorporated into a 3D hybrid-PIC code, specifically the ZEPHYROS particle-based hybrid code [23, 167] to investigate fast electron propagation in each target material. ZEPHYROS uses a particle-in-cell treatment for the fast electrons and a static fluid background for the cold target, closely following the original hybrid method developed by J. R. Davies [106]. A 200 μm $\times$400 μm $\times$400 μm simulation box was used, with 1 μm cell resolution. The laser-to-fast electron conversion efficiency was set to 0.3, with laser pulse duration of 1 ps and laser wavelength of 1 μm, matching the experimental parameters. The number of macroparticles was set to 200 million, with the electron injection half angle set to 50° and an initial target temperature of 1 eV. A relativistic Maxwellian distribution of electron energies was used with mean temperature equal to 1.3 MeV and 6.2 MeV, for simulations at peak laser intensities equal to 5×10^{19} Wcm^{-2} and 5×10^{20} Wcm^{-2} respectively.

Fig. 5.8 shows the hybrid-PIC simulation results. Fig. 5.8(a) and (b) correspond to fast electron density plots at 1.4 ps for intensities of 5×10^{19} Wcm^{-2} for diamond and vitreous carbon respectively, while Fig. 5.8(c) and (d) represent simulations at 5×10^{20} Wcm^{-2}, again for diamond and vitreous carbon respectively. Firstly, electron transport in vitreous carbon produces a fast electron beam that is strongly filamented at both intensities (see Figs. 5.8(b) and (d)), which in turn will result in a structured proton beam spatial intensity profile, as demonstrated both in this study and in previous work (see Fig. 5.2(c) and [39]). Interestingly, diamond produces different transport properties upon changing the laser-drive intensity between 5×10^{19} Wcm^{-2} and 5×10^{20} Wcm^{-2}. From Fig. 5.8(a) note that the fast electrons propagate in a beam with many small filaments, with highest

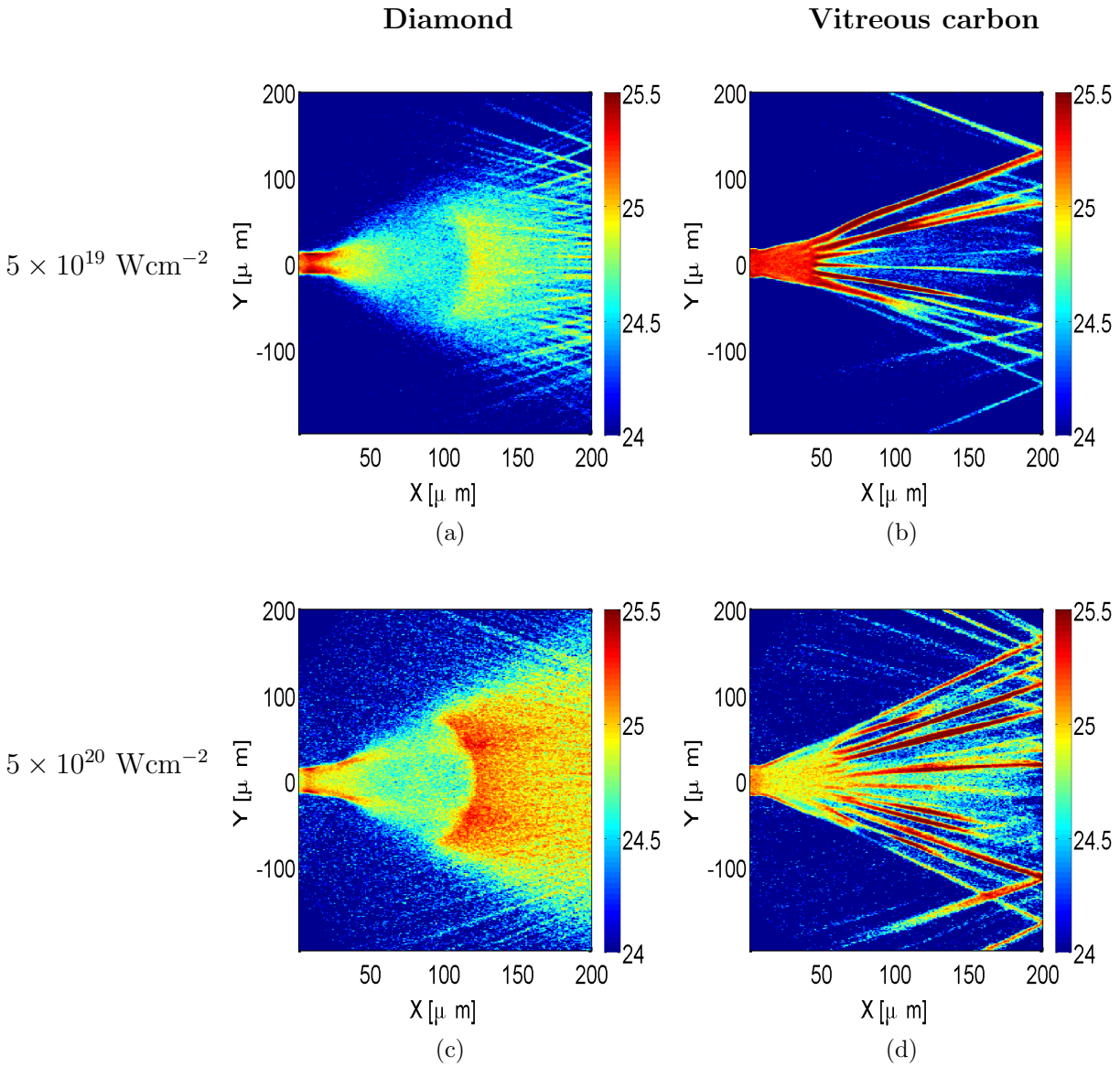

Figure 5.8: Hybrid-PIC simulation results. (a) and (c) show the x-y midplane plots of the $\log_{10}$ fast electron density(m^{-3}) at 1.4ps after irradiation of diamond by a laser pulse of intensity 5×10^{19} Wcm^{-2} and 5×10^{20} Wcm^{-2} respectively. (b) and (d) corresponding simulation results for vitreous carbon irradiated with a peak laser intensity of 5×10^{19} Wcm^{-2} and 5×10^{20} Wcm^{-2} respectively.

electron densities located in the centre of the beam (correlating with the experimental measurement - see Fig. 5.2(b)). Conversely, increasing the laser intensity to 5×10^{20} Wcm^{-2} produces a smooth electron transport profile, similar to that reported both experimentally and numerically in [39].

5.5 Resistive instability growth rate

To explain the response of the fast electron transport pattern to target resistivity, specifically to the magnitude of the resistivity in the transient warm dense regime, together with the effect of laser-drive intensity, the resistive filamentation growth rate of both diamond and carbon is calculated using a linear resistivity analysis, based on the work of Gremillet *et al.* [113] and Robinson *et al.* [114].

In this model, specific assumptions are made: 1) the fast electron beam is initially uniform in the transverse direction; and 2) the background material exhibits constant resistivity. Furthermore, the fast electron beam is assumed to be mono-energetic and uniform in the x-direction and have infinite extent in both the x-direction and y-direction. While these assumptions are not fully representative of the complex transport properties (i.e. the target will exhibit temperature and therefore resistivity gradients in multiple directions), the simplified model enables the salient features of fast electron transport in materials with different resistivity to be demonstrated. Firstly, the fast electrons are given a fluid description. The subsequent linearised fluid equations are [114]:

$$\frac{\partial n_1}{\partial t} + n_{f,0}\frac{\partial u_{y,1}}{\partial y} = 0 \tag{5.11}$$

$$\frac{\partial u_{y,1}}{\partial t} = \frac{e u_{x,0} B_z}{\gamma m_e} \tag{5.12}$$

$$\frac{\partial B_z}{\partial t} = e u_{x,0} \eta \frac{\partial n_1}{\partial y} \tag{5.13}$$

Solutions are then sought of the following form:

$$n_1 = n_{f,0} N(t) cos(k_p y) \tag{5.14}$$

$$u_{y,1} = U(t) sin(k_p y) \tag{5.15}$$

$$B_z = B(t) sin(k_p y) \tag{5.16}$$

where $k_p = 2\pi/\lambda$ is the wavenumber of the perturbation. Combining these equations together results in a single ordinary differential equation (ODE) for N:

$$\frac{\partial^3 N}{\partial t^3} - \alpha N = 0 \tag{5.17}$$

where:

$$\alpha = \frac{e^2 u_{x,0}^2 n_{f,0} k_p^2 \eta}{\gamma m_e} \tag{5.18}$$

This has the solution:

$$N = N(0) \exp(\alpha^{1/3} t) \tag{5.19}$$

Thus, the electron beam is unstable to an exponentially growing filamentation mode governed by $\exp(\alpha^{1/3} t)$.

If the calculation is repeated assuming that the beam has a small but finite transverse temperature (i.e. energy) spread, denoted by $T_{f,\perp}$, then:

$$\frac{\partial^3 N}{\partial t^3} + \beta \frac{\partial N}{\partial t} - \alpha N = 0 \tag{5.20}$$

where

$$\beta = \frac{k_p^2 e T_{f,\perp}}{\gamma m_e} \tag{5.21}$$

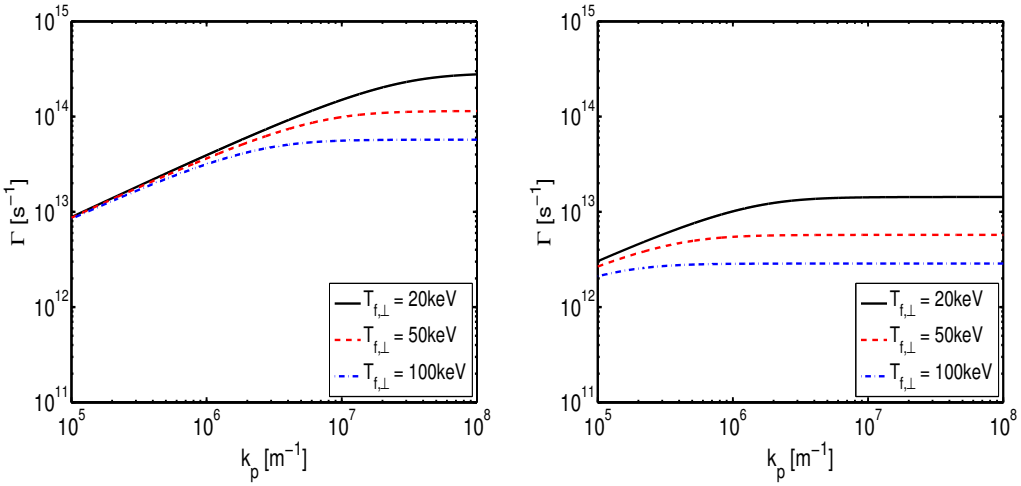

(a) Vitreous carbon (b) Diamond

Figure 5.9: Resistive instabilitiy growth rate as a function of wavenumber for: (a) vitreous carbon; and (b) diamond, for various transverse electron temperatures.

This also has an exponentially growing mode ($\exp(\Gamma t)$), where [114]:

$$\Gamma = (\alpha/2 + \sqrt{D})^{1/3} - (\sqrt{D} - \alpha/2)^{1/3} \tag{5.22}$$

and $D = (\beta/3)^3 + (\alpha/2)^2$. The growth rate is evalulated using appropriate parameters corresponding to the experimental conditions. Firstly, the fast electron density and velocity are estimated as $n_{f,0} = 10^{26}$ m^{-3} and $u_{x,0} \approx c$ respectively. Furthermore, over the temperature range of 1- 50 eV, the vitreous carbon target has a resistivity of approximately $\eta_{vit} = 4 \times 10^{-6}$ Ωm, whereas for diamond this is approximately $\eta_{dia} = 2 \times 10^{-7}$ Ωm.

Using these values, the growth rate Γ is calculated as a function of k_p for both materials. In addition to the previous values, $\gamma = 14$ (corresponding to an intensity of 5×10^{20} Wcm^{-2}). The results are shown in Fig. 5.9(a) and (b), for vitreous carbon and diamond respectively, for various values of transverse electron temperature $T_{f,\perp}$.

The concept of 'e-folding' is used to describe the trends in Fig. 5.9(a) and (b), defined as the parameter values over which the magnitude of an exponentially varying quantity changes by a factor of e. In the calculations described, the exponentially varying quantity Γ varies with perturbation wavenumber k_p.

It is found that the resistive filamentation grows at a rate of approximately one e-folding per 10 fs for vitreous carbon for lower transverse temperatures (black line in Fig. 5.9(a) - corresponding to $T_{f,\perp} = 20$ keV). For higher transverse temperatures (for example $T_{f,\perp} = 100$ keV - blue line in Fig. 5.9(a)) the growth rate will still have an e-folding time of less than 100 fs. Conversely, in the case of diamond there will be one e-folding per 100 fs, even for low transverse temperatures (black line in Fig. 5.9(b) - corresponding to $T_{f,\perp} = 20$ keV). Therefore, for fast electron transport driven by a picosecond laser, the filamentation has little time to develop in the case of diamond and thus strong filamentation is expected in vitreous carbon but little (or no) filamentation in diamond. Importantly, these calculations were performed for an intensity of 5×10^{20} Wcm^{-2}. Also note that although a maximum resistive instability growth rate has been predicted by other authors [113], the simple model applied here does not fully reproduce this feature, although a saturation value is achieved for all cases explored. This most likely arises due to the simplified assumptions used (i.e. constant resistivity and transverse beam temperature).

Next, the resistive filamentation growth rate is calculated for both carbon allotropes at two intensity values: $\gamma = 14$ (corresponding to an intensity of 5×10^{20} Wcm^{-2}) and $\gamma = 4$ (corresponding to an intensity of 5×10^{19} Wcm^{-2}), while fixing the transverse temperature at $T_{f,\perp} = 20$ keV. Correlating with Fig. 5.9, the calculations (shown in Fig. 5.10) reveal that the resistive filamentation growth rate is much greater for vitreous carbon (red lines in 5.10) than for diamond (black lines in 5.10). Taking vitreous carbon, the time for one e-folding of the resistive filamentation instability is of the order of a few tens of femtoseconds for both intensities, which means that strong filamentation should occur for electron transport driven by a picosecond laser pulse — this is what is observed experimentally (see Fig. 5.2(d)) and in the hybrid-PIC simulations presented in Fig. 5.8 at both 5×10^{19} Wcm^{-2} and 5×10^{20} Wcm^{-2}. By contrast, the e-folding time for diamond is approximately a few hundred femtoseconds, and therefore the beam is much less likely to filament for a picosecond duration pulse.

Interestingly, the effect of reducing the laser intensity is to increase the re-

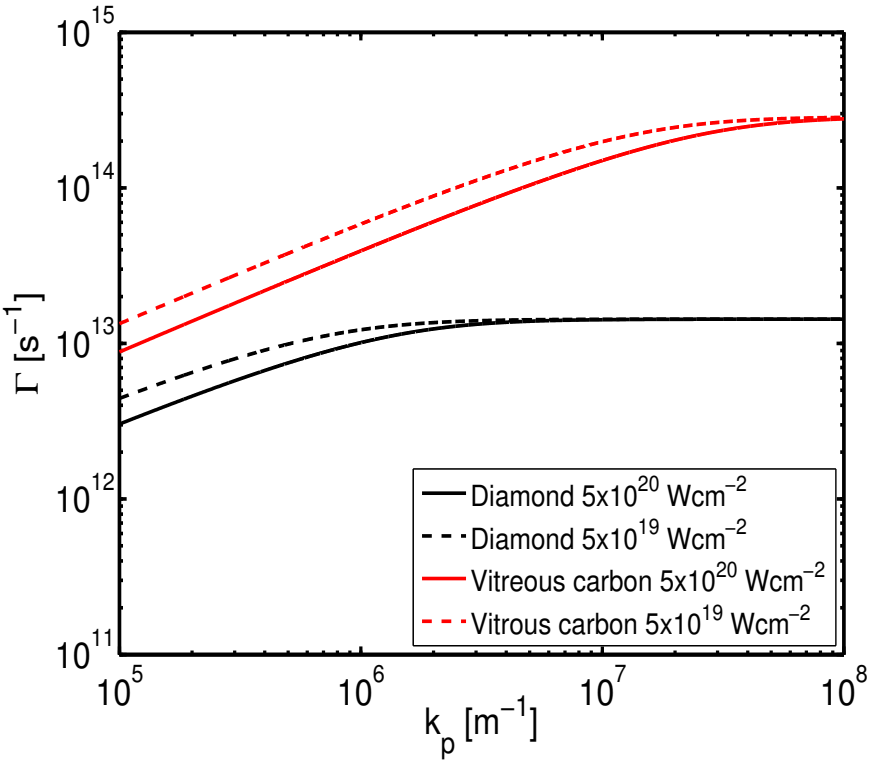

Figure 5.10: Resistive instabilitiy growth rate as a function of wavenumber for vitreous carbon (red solid and dotted lines) and diamond (black solid and dotted lines) for two intensity regimes: 5×10^{19} Wcm^{-2} - dotted lines and 5×10^{20} Wcm^{-2} - solid lines.

sistive filamentation growth rate in both allotropes. To explore the intensity dependence of the filamentation growth rate in more detail, the growth rate is calculated as a function of laser-drive intensity between the range of 1×10^{18} - 1×10^{21} Wcm^{-2}, while defining $T_{f,\perp} = 20$keV and $k_p = 1 \times 10^4$ m^{-1}, for both allotropes.

The result of this calculation, shown in Fig. 5.11, highlights the variation of the filamentation growth rate as a function of intensity for both allotropes. For vitreous carbon, increasing intensity results in an overall decrease in the filamentation growth rate. While diamond exhibits a similar trend, the overall reduction is not as significant as that in vitreous carbon. Nevertheless, reducing the laser-drive intensity to 5×10^{19} Wcm^{-2} from 5×10^{20} Wcm^{-2} gives rise to an overall reduction of the resistive filamentation growth rate of approximately 35%. This may account for the increase in beam filamentation observed both numerically (via the hybrid-PIC simulations - Fig. 5.8) and experimentally (Fig. 5.2(b)) for

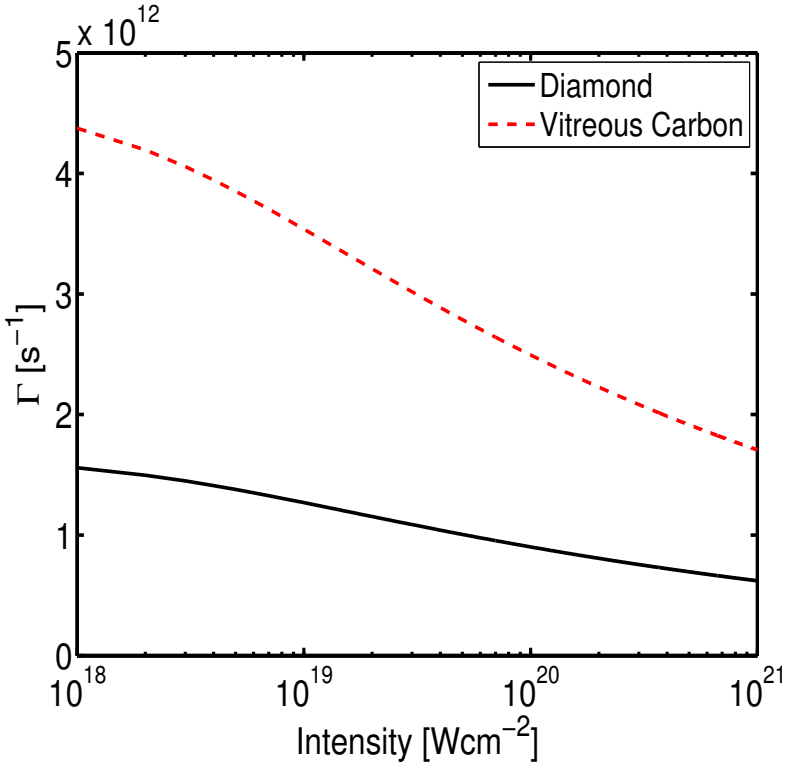

Figure 5.11: Resistive instability growth rate as a function of laser intensity for vitreous carbon (red line) and diamond (black line).

diamond at the lower intensity case of 5×10^{19} Wcm^{-2}.

5.6 Conclusions

To conclude this chapter, firstly a model has been developed to investigate the mapping of the initial 2D fast electron density distribution at the target rear surface into the spatial-intensity distribution of the beam of accelerated protons. This model takes account of the fast electron sheath field evolution, field ionisation and expansion, and projection of the resulting proton front to the detector plane. Building on a recent fast electron investigation [39], measurements of proton beam spatial-intensity distributions for three example targets are presented. The case of diamond, irradiated at a peak intensity equal to 7×10^{19} Wcm^{-2}, is selected due to the unusual feature of structure occurring only at the centre of an otherwise smooth proton beam profile, and the analytical model is applied to infer the initial fast electron density distribution at the target rear surface. The measured beam

profile is reproduced using an annular fast electron density distribution with a filamentary structure.

In addition, results are presented that demonstrate the role that lattice structure has in defining electron transport properties. By performing numerical simulations, utilising a hybrid-PIC code, on two allotropes of carbon, diamond and vitreous carbon, the important role that material lattice structure has in defining fast electron transport is established. Furthermore, the effect of both low temperature resistivity and laser-drive intensity is investigated using an analytical model of the resistive filamentation instability. These results show the importance of considering lattice structure, and thereby low temperature resistivity, in fast electron transport, as well as the key role that laser-drive parameters have in defining electron beam transport properties. The role of both low temperature resistivity and laser-drive parameters are investigated in more detail in Chapter 6.

Finally, investigations of fast electron transport in silicon revealed that, while possessing the same lattice structure as diamond, for the same laser-drive intensity strikingly different fast electron transport properties are produced; a smooth proton beam rather than the centrally-located caustic structures present in diamond. This further demonstrates the role that cold material properties have in fast electron transport. In the following chapters, fast electron transport in silicon will be explored in greater detail.

Chapter 6

Fast Electron Transport in Silicon

6.1 Introduction

In the preceding chapter, it was demonstrated that the material's lattice structure in a transient state of warm dense matter, at temperatures in the range 1-100 eV, is a key factor in defining the resistivity and thus in determining the fast electron beam pattern.

The influence of resistivity in the 1-100 eV temperature regime (i.e. low temperature resistivity) has been acknowledged but largely overlooked in fast electron transport research. Particle-in-cell and hybrid-PIC simulations of intense laser-solid interactions often assume a high initial target temperature ($\sim$100 eV) where the Spitzer formula adequately describes the resistivity. This is usually implemented using a collisional particle-in-cell model [38], which calculates the resistivity through field ionisation and collisions of plasma particles, resulting in a resistivity which varies as $\eta \sim Z/T^{3/2}$. However, the Spitzer model is only applicable for fully ionised, non-degenerate plasmas and is not valid below temperatures of $\sim$100 eV. In an ultraintense laser solid interaction, the target's electrons transition from room temperature (0.025 eV) to plasma temperatures on a femtosecond timescale, while the temperature of the ions increases over a much longer (typically tens of picoseconds) timescale. Furthermore, during ultraintense laser irradiation (for laser parameters typical of the investigations in this thesis), only the first $\sim$10 μm of a solid density target is heated to a sufficiently high

temperature to be accurately described by the Spitzer resistivity [80]. Beyond $\sim$10 μm, the temperature varies between 1 and 100 eV and hence the fast electrons propagate through matter in which the resistivity cannot be described by the Spitzer model.

Since the transport of high currents of fast (MeV) electrons in solids (created by ultra-intense laser irradiation of a solid target) underpins a number of important applications, there has been significant effort devoted to optimising control of the electron beam transport - recent work has included the use of target engineering [167, 171] and multiple laser pulses [172]. Additionally, an ability to completely change the fast electron beam transport pattern could fundamentally alter the implementation and realisation of applications such as fast ignition-ICF and tailored ion beams for use in medicine and industry.

In this chapter, the role that low-temperature resistivity has in defining new fast electron beam transport patterns is investigated. The chapter is organised as follows: in the section 6.2, the influence of low-temperature resistivity on fast electron transport is investigated and the extent to which the choice of resistivity model influences the predicted beam transport properties is revealed. Specifically, the case of silicon is explored and it is shown that resistively generated magnetic fields arising from the low-temperature (few eV) region of the resistivity-temperature profile define the global fast electron transport properties. In section 6.3, using a hybrid-PIC code, the influence of the laser-drive parameters on the properties of fast electron transport in silicon is investigated numerically. Moreover, the potential ability to optically tune and tailor the electron beam transport pattern through variation of laser pulse duration, energy and focal spot size is demonstrated and discussed.

6.2 Part 1 - The role of low temperature resistity in defining fast electron transport

Within the context of fast electron propagation in solids, previous work has demonstrated that a range of physical phenomena depend strongly on target re-

sistivity; for example electric-field inhibition [97], resistive transport instabilities [113] and self-generated resistive magnetic fields [107]. As previously highlighted, although the overall importance of target resistivity in defining fast electron beam transport is widely acknowledged, the influence of resistivity at relatively low temperatures (i.e. from room temperature to ∼50 eV) has been largely unexplored. This is due mainly to the fact that many experimental studies [38] have been performed with relatively thin targets, in the tens-of-micron range, where resistivity is adequately described by the Spitzer resistivity [80]. For fast electron transport investigations over longer distances (i.e. thicker targets ≥40 μm), for which less heating of the bulk target occurs, the resistivity evolution at lower temperatures must be accounted for.

In this section, it is demonstrated that completely new types of fast electron transport patterns can be created by a more accurate understanding and control of the target resistivity-temperature profile at low temperatures. This is illustrated by predicting, using 3D-hybrid-PIC modelling, and then experimentally verifying a signature of annular fast electron beam transport in silicon. Moreover, through detailed comparison with the hybrid-PIC simulations, it is concluded that this transport pattern arises due to resistive magnetic fields generated by a dip in the resistivity-temperature profile at a few eV. Furthermore, the results presented demonstrate the importance of properly accounting for low-temperature resistivity in investigations of fast electron transport.

6.2.1 Simulations

To begin with, the influence that the choice of resistivity model has on fast electron transport is explored by performing simulations for silicon using three different resistivity-temperature models, shown in Fig. 6.1.

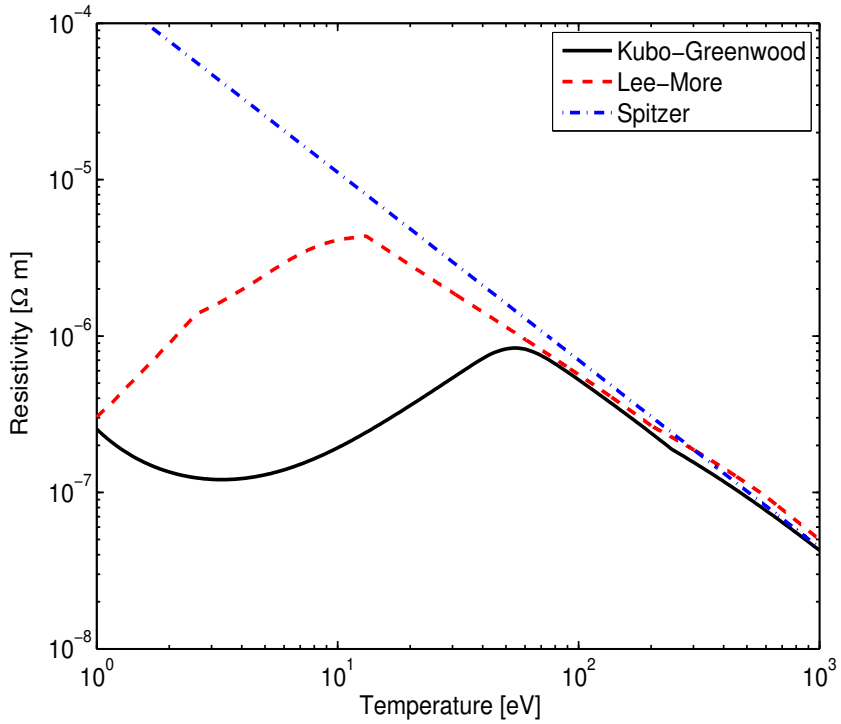

Figure 6.1: Calculations of the resistivity of silicon as a function of temperature for three resistivity models: Black - *ab initio* QMD calculations coupled with the Kubo-Greenwood equation; Red - the Lee-More model; Blue - the Spitzer model.

The first resistivity model utilised is the widely-used Spitzer model [80] (Fig. 6.1 - blue line), which describes the resistivity of a high temperature and fully ionised, non-degenerate plasma. The second model investigated is the Lee-More model [79](Fig. 6.1 - red line), which is a wide-range density-temperature resistivity calculation developed to provide an analytical correction to the Spitzer resistivity model at low temperature (∼1-10 eV). The calculation is based upon the Thomas-Fermi ionisation model [173] but, crucially, does not account for the effect of material lattice structure on resistivity, and is therefore of limited validity in describing the resistivity of insulator-conductor (and semiconductor-conductor) transitions. A more accurate determination of the low-temperature resistivity of silicon is achieved using *ab initio* quantum molecular dynamic (QMD) simulations, based on density functional theory (DFT). The Vienna *Ab initio* Simulation Program (VASP), a plane-wave DFT code [91, 92], is used to perform the QMD calculations. These simulations were performed by Dr M. P. Desjarlais of Sandia

National Laboratory. To produce the resistivity-temperature profile, shown as the black line in Fig. 6.1, the silicon atomic configurations were obtained by performing the DFT simulations at a fixed temperature of 300 K, corresponding to the ionic structure at room temperature. Next, the electronic temperature of the electron sub-system was varied from 0.025 to 20 eV in subsequent static Kubo-Greenwood conductivity calculations [85] using the previously sampled atomic configurations at 300 K. As shown in Fig. 6.1, the three resistivity profiles differ greatly at temperatures below 50 eV.

The form of the QMD-Kubo-Greenwood resistivity-temperature profile in the low-temperature regime is important, as will be demonstrated below, and is understood in the following way. The minimum at ∼3.5 eV in the QMD-Kubo-Greenwood profile corresponds to excitation and ionisation of the outer valence electrons above the silicon bandgap of 1.12 eV. This produces an increase in the number of charge carriers in the conduction band and an overall reduction in the resistivity. Thereafter, the resistivity rises to peak at ∼50 eV. This temperature represents a transition from electron-phonon scattering to electron-ion collisions, with the subsequent resistivity peak corresponding to a minimum in the electron mean free path. Due to the rapid nature of the heating driven by the ultrashort fast electron bunch, the background electrons are heated, but the ions, temporarily (on picosecond timescales) remain cold and retain their initial lattice structure, justifying our choice of sampling the atomic configurations at 300 K in the DFT simulations. The highly ordered face-centred cubic diamond crystal structure of silicon influences the electron mean free path and therefore the material resistivity in the warm dense state [39]. As the temperature increases beyond ∼50 eV, ionisation processes begin to dominate, and scattering cross sections decrease with increasing mean electron momentum, giving rise to the Spitzer resistivity as the material transitions to an ionised plasma.

To investigate how sensitive fast electron beam transport is to low-temperature resistivity, simulations are performed using the QMD-Kubo-Greenwood, Lee-More and Spitzer resistivity-temperature models incorporated into the 3D particle-based hybrid code ZEPHYROS [23, 167]. ZEPHYROS treats the fast electrons

using a PIC algorithm (i.e. kinetically) and the background (cold) target using a hybrid, fluid approximation, as in the original hybrid method developed by Davies [106]. Key to the description of the background material, and crucial to this investigation, is the prescription of a resistivity-temperature profile − this feature of the hybrid-PIC method is exploited by incorporating the resistivity-temperature calculations of Fig. 6.1 as an input parameter in the simulations. A 200 μm × 400 μm × 400 μm simulation grid is used, with a cell resolution of ΔX = ΔY = ΔZ = 1 μm. The laser-to-fast electron energy conversion factor is set to 0.3, with a laser pulse duration of 1 ps and wavelength equal to 1 μm. The total number of macro-particles is set to 2×10^8 (2×10^7 macro-particles are injected at each timestep), with the electron injection half-angle set to 50° [137]. In all cases the initial target temperature is set equal to 1 eV, except for simulations involving the Spitzer model. In this case, the target temperature is initialised at 100 eV to circumvent electron transport inhibition problems in the simulation, arising due to the large resistivity values at low temperatures. A relativistic Maxwellian distribution of electron energies is used with mean temperature equal to 1.3 MeV and 6.2 MeV, for simulations at peak laser intensities equal to 5×10^{19} Wcm^{-2} and 5×10^{20} Wcm^{-2}, respectively. These temperatures are determined from ponderomotive scaling [65]. The temperature evolution of the resistivity is prescribed through the calculated resistivity curves for each model, as described above and shown in Fig. 6.1. Example simulation results are shown in Fig. 6.2.

The fast electron population is injected at the left side of the simulation box, which represents a laser-spot focal region, centred at [X, Y, Z] = [0, 0, 0], and propagates in the X-direction. Snapshots of the fast electron density in the [X, Y] plane at Z = 0 (i.e. cut-away side view) and in the [Y, Z] plane at X = 200 μm (i.e. the target rear surface) are shown for four given sets of simulation parameters. Figs. 6.2(a - b), (c - d) and (e - f) correspond to the use of the Spitzer, Lee-More and QMD-Kubo-Greenwood resistivity-temperature profiles, respectively, for electron beam parameters corresponding to a fixed laser intensity equal to 5×10^{20} Wcm^{-2}. Figs. 6.2(g - h) is the corresponding result for the QMD-Kubo-Greenwood case at a lower laser intensity of 5×10^{19} Wcm^{-2}.

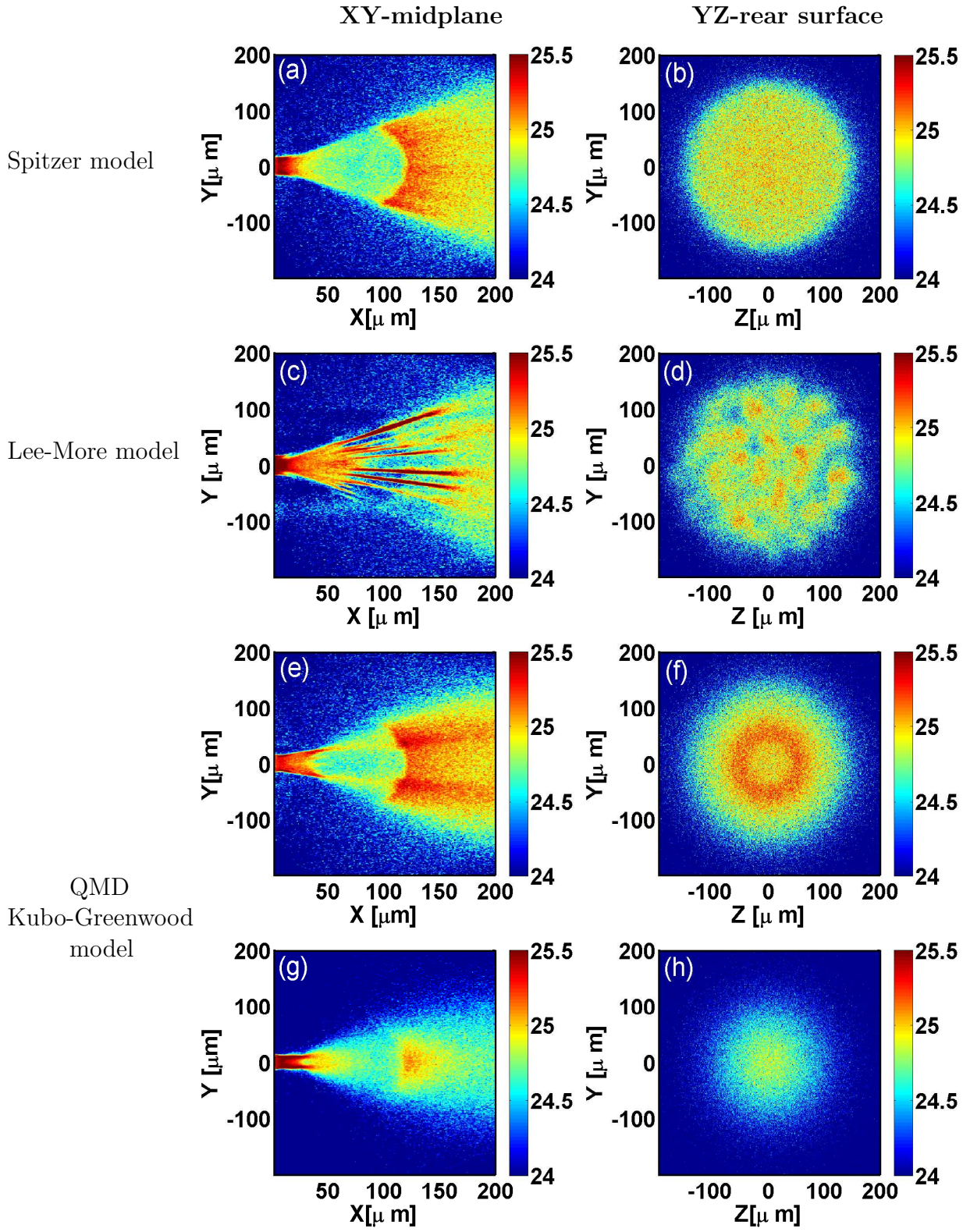

Figure 6.2: Hybrid-PIC simulation results showing $\log_{10}$ fast electron density maps (m^{-3}) in the [X-Y] mid-plane and rear surface [Y-Z] plane, 1.4 ps after laser irradiation: (a - b) Spitzer; (c - d) Lee-More, and (e - f) QMD-Kubo-Greenwood models; all for peak intensity equal to 5×10^{20} Wcm^{-2}. (g - h) Corresponding simulation result for the QMD-Kubo-Greenwood resistivity-temperature calculations at 5×10^{19} Wcm^{-2}.

Comparing the results for the three different resistivity models, it is clear that three distinctly different fast electron transport patterns are obtained. Using the Spitzer model, with an initial target temperature of 100 eV (noting that all three resistivity models converge to the same resistivity at high temperatures), results in smooth electron transport and a relatively uniform fast electron density distribution at the target rear side (Fig. 6.2(a - b)). As previously stated, the Spitzer model is not valid at WDM temperatures. Test simulations at an initial starting temperature of 1 eV resulted in an unphysical high magnetic field strength (due to the orders of magnitude higher resistivity at the lower temperature - blue line in Fig. 6.1) in the region of the electron source, which prevents beam propagation. As shown in Fig. 6.2(c - d), the Lee-More model correction to the Spitzer resistivity at low temperature results in strongly filamented fast electron beam transport, leading to a highly non-uniform and structured rear-surface fast electron distribution. In contrast, the Kubo-Greenwood approach, which includes the QMD simulations of low temperature resistivity, produces a distinctly different electron transport profile. A hollowing of the fast electron beam is produced (similar to that described in reference [109]), resulting in an annular fast electron density at the target rear surface, as shown in Figs. 6.2(e - f). Moreover, it is observed that the beam hollowing effect is dependant upon laser intensity. Fig. 6.2(g - h) shows corresponding simulation results for an order of magnitude lower laser intensity, 5×10^{19} Wcm^{-2}, for which relatively smooth beam transport occurs, with no spatial modulations or annular features in the fast electron density distribution at the target rear surface. Moreover, note that there is evidence of the seeding of the beam hollowing effect at X = 40 μm at both intensities, but in the lower intensity case this modulation does not develop during beam propagation deeper into the target.

6.2.2 Experiment

The numerical demonstration of remarkably different electron transport properties upon variation of both the resistivity model employed and peak laser-drive intensity requires experimental verification. To do this, the Vulcan laser (Target

Area Petawatt, TAP) at the Rutherford Appleton Laboratory, UK, is utilised. The laser delivers pulses of 1.055 μm wavelength light, in a (0.8 $\pm$ 0.2) ps duration (full width at half maximum, FWHM) pulse with a maximum pulse energy (on target) of 300 J. The Vulcan pulse is directed to the f/3 off-axis parabolic mirror by a turning mirror of one metre diameter, and the p-polarised pulses are focused onto the target front surface at an incident angle of 33°, producing a measured 4.5 μm diameter (FWHM) spot. This produces a calculated peak intensity of 6.8×10^{20} Wcm^{-2}.

The targets used in the experimental investigation are silicon of 300 μm-thickness, lateral dimensions of 3 mm $\times$ 3 mm and highly polished surfaces (to minimise the production of structure in the proton beam arising due to spatial structures on the target rear-surface [149]). The fast electron transport patterns within the targets are diagnosed by employing measurements of the spatial-dose distribution of the beam of protons accelerated by the sheath field established by the arrival of the fast electrons at the target rear surface [37, 39, 133]. A magnified schematic of this arrangement is shown in Fig. 6.3 (as discussed in Chapter 4). Since the 2-D fast electron density profile is mapped into the sheath field, it is therefore directly mapped into the intensity distribution of the resulting proton beam. The spatial-dose distribution is measured at discrete proton energy values, determined by the Bragg peak deposition in each layer, by using a stack of dosimetry film (radiochromic film, RCF). The RCF stack is positioned 6 cm from the rear surface of the target and centred on the target normal.

Additionally, the focal spot spatial profile is characterised and the 2D spatial-intensity map and corresponding horizontal lineout are displayed in Fig. 6.4(a) and (b) respectively. Previous work [37, 149] has demonstrated that the spatial-intensity profile of the laser focus can be directly mapped into the fast electron beam pattern, and thus imprinted into the accelerated ion beam spatial distribution. Therefore, by ensuring that the laser spot at best focus exhibits a Gaussian spatial profile, the resulting proton spatial profile can be attributed to electron transport properties inside the target alone.

The proton spatial profiles across a range of peak laser-drive intensities are

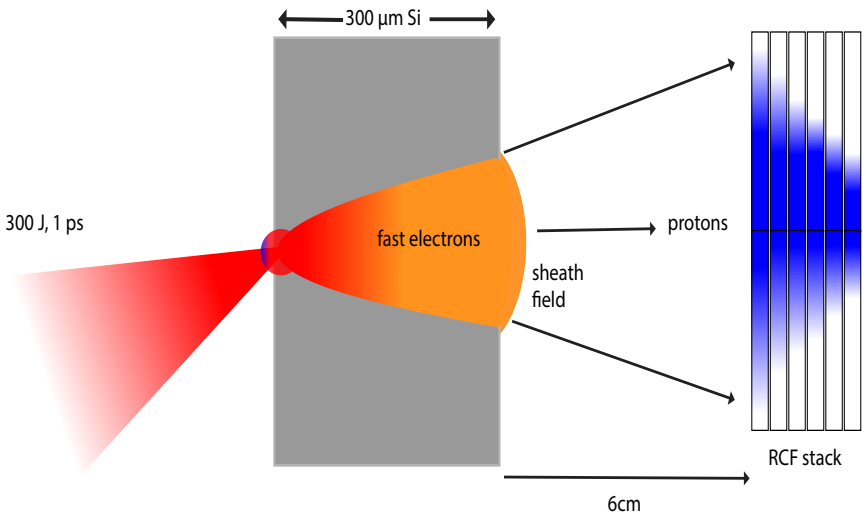

Figure 6.3: Key proton diagnostic schematic. The ultraintense Vulcan pulse, of peak intensity 6.8×10^{20} Wcm^{-2}, is focussed onto the front surface of the silicon target samples. A large current of relativistic electrons are produced which propagate through the target. Reaching the target rear surface, they create an electric field sheath layer, with typical field strengths of multi-TV/m, which ionises the rear-surface and accelerates ions. The spatial profile of the fast electron transport is mapped into the electric sheath distribution, which in turn is mapped into the accelerated ions. The spatial-intensity dose distribution of the resulting beam of accelerated protons is measured using a stack of dosimetry radiochromic film (RCF)

compared. For brevity, representative proton beam dose profiles are selected at a proton energy of 7.3 MeV and are displayed in Fig. 6.5(a - c) as a function of peak laser intensity between the range of 6×10^{19} Wcm^{-2} and 6.8×10^{20} Wcm^{-2} (respective laser pulse energies of 26 J and 300 J). Note that this is for a fixed value of the other laser parameters i.e. pulse duration and focal spot radius - the influence of pulse duration and focal spot radius on fast electron transport in silicon is explored numerically in part 2. The smooth proton beam measured at 6×10^{19} Wcm^{-2}, Fig. 6.5(a), is indicative of smooth electron transport within the target. The slight intensity enhancement in the beam centre may be indicative of the onset of structure, either filamentation or ring-like distributions, in the fast electron beam. As the peak laser intensity is increased to 4×10^{20} Wcm^{-2},

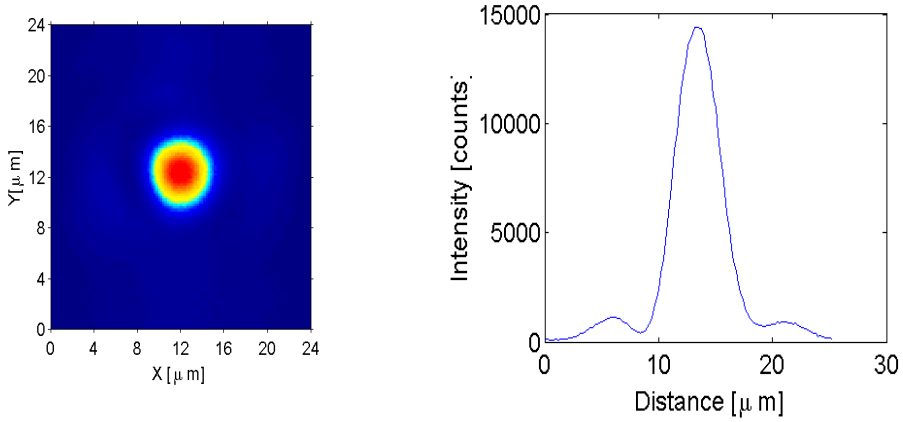

Figure 6.4: Focal spot spatial-intensity distribution of the Vulcan laser: (a) 2-D intensity map of the laser-spot at best focus and (b) corresponding horizontal lineout of the spatial profile.

Fig. 6.5(b), the overall size of the beam grows and ring-like structures start to form within the beam, close to the centre. At the highest intensity accessible, Fig. 6.5(c), a clear annular-profile is measured in the proton beam distribution. From these results, it is concluded that the fast electron beam transport pattern is sensitive to the peak laser intensity and that a ring-like pattern emerges at the highest intensity accessible, in agreement with simulation results with the QMD Kubo-Greenwood model, shown in Figs. 6.2(e - h).

It is important to note that the features displayed in the example protons beam measurements in Fig. 6.5 are representative of spatial features that are present at all energies in the proton beam (i.e. throughout the RCF stack). By way of example, Fig. 6.6 displays the full proton beam profile for the highest intensity explored (6.8×10^{20} Wcm^{-2}) across a range of proton energy (from 1 to 22.1 MeV).

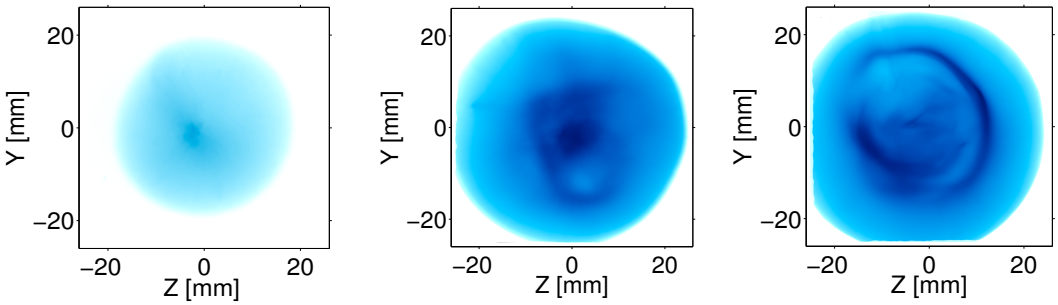

Figure 6.5: Representative example measured proton spatial-intensity distributions at a proton energy of 7.3 MeV for peak laser intensity equal to: (a) 6×10^{19} Wcm^{-2}; (b) 4×10^{20} Wcm^{-2}; and, (c) 6.8×10^{20} Wcm^{-2}.

For lower proton energies (i.e. 1 - 3 MeV) the proton dose is at the highest value − the annular structure is present but largely obscured due to the very high proton dose (see Fig. 6.6(a)). At higher proton energies, the annular structure is clearly visible, as evidenced by the proton beam profiles at both 9.4 MeV and 22.1 MeV (Fig. 6.6(e) and (f) respectively). Interestingly, the ring structure accounts for the highest proton dose region for each beam energy. This indicates that the annular proton beam was produced by the region of the sheath field possessing the greatest electric field strength, which in turn indicates that the ring was generated by the region of the fast electron beam containing the highest current density. This point is important when the mechanism which induces the formation of the annular transport pattern is explored, described below in section 6.2.3.

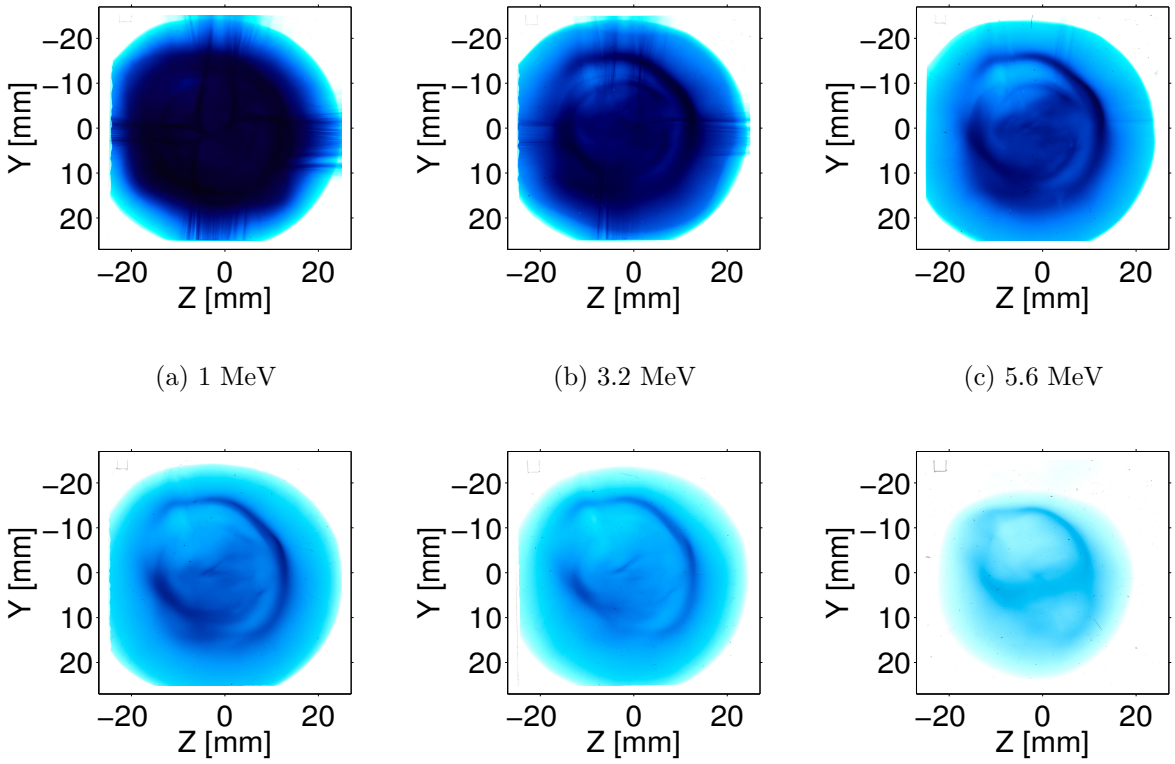

(a) 1 MeV (b) 3.2 MeV (c) 5.6 MeV

(d) 7.3 MeV (e) 11.1 MeV (f) 20 MeV

Figure 6.6: Example experimentally measured proton beam, giving energy and spatial characteristics of the beam. The observed annular feature is present throughout the stack, from lower proton energies ((a) 1 MeV) to much higher proton energies ((f) 22 MeV).

To enable a more direct and comprehensive comparison between the experimentally measured proton beams and the numerically simulated fast electron transport patterns from Fig. 6.2, the analytical model used to investigate fast electron transport in carbon allotropes (see Chapter 5) was employed. The model, which computes the evolution of the 2-D electric sheath field, the proton front and the projection of the resulting beam of multi-MeV protons onto the detector plane was developed and modified such that the initial 2-D electric field distribution is calculated using the rear-surface fast electron density distribution results from the ZEPHYROS simulations.

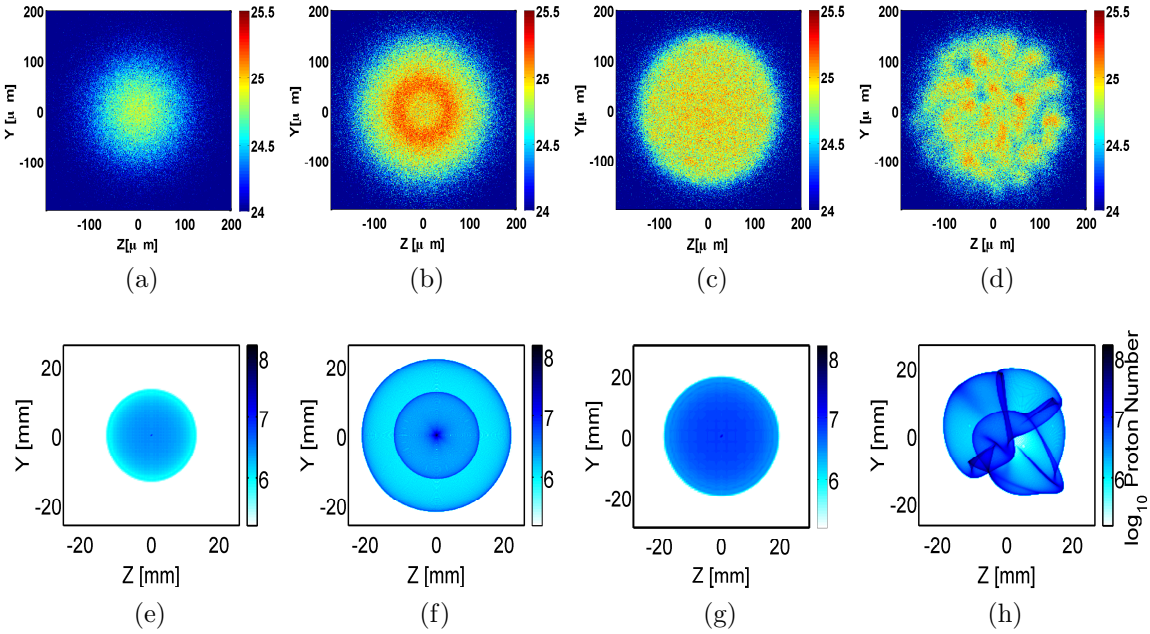

Figure 6.7: Analytical model calculations of the proton spatial distribution resulting from the rear-surface fast electron density distributions from the ZEPHYROS simulations. (a, e) 5×10^{19} Wcm^{-2} QMD-Kubo-Greenwood profile; (b, f) 5×10^{20} Wcm^{-2} QMD-Kubo-Greenwood profile; (c, g) 5×10^{20} Wcm^{-2} Spitzer profile; (d, h) 5×10^{20} Wcm^{-2} Lee-More profile

For clarity, the rear-surface fast electron density profiles (from Fig. 6.2) are replotted in Figs. 6.7(a - d). Below them, in Figs. 6.7(e - h), is the corresponding analytically calculated proton beam spatial-intensity distributions arising from the fast electron density maps for the Kubo-Greenwood resistivity model applied to the low and high intensity cases, and the Spitzer and Lee-More resistivity models applied to the high laser intensity simulation results, respectively. Considering the Spitzer result (Figs. 6.7(c) and (g)) first, the predicted proton beam is smooth, with a uniform spatial distribution resulting from the uniform electric sheath profile calculated from the hybrid simulations. Interestingly, a distinctly different proton spatial profile is predicted using the Lee-More model (at a peak laser intensity of 5×10^{20} Wcm^{-2}): the highly disrupted and filamented fast electron beam profile (Fig. 6.7(d)) results in an irregular proton beam with strong cusp-like structures within it, as shown in Fig. 6.7(h). Proton beams with this type of structure, driven by a filamented fast electron density distribution at the

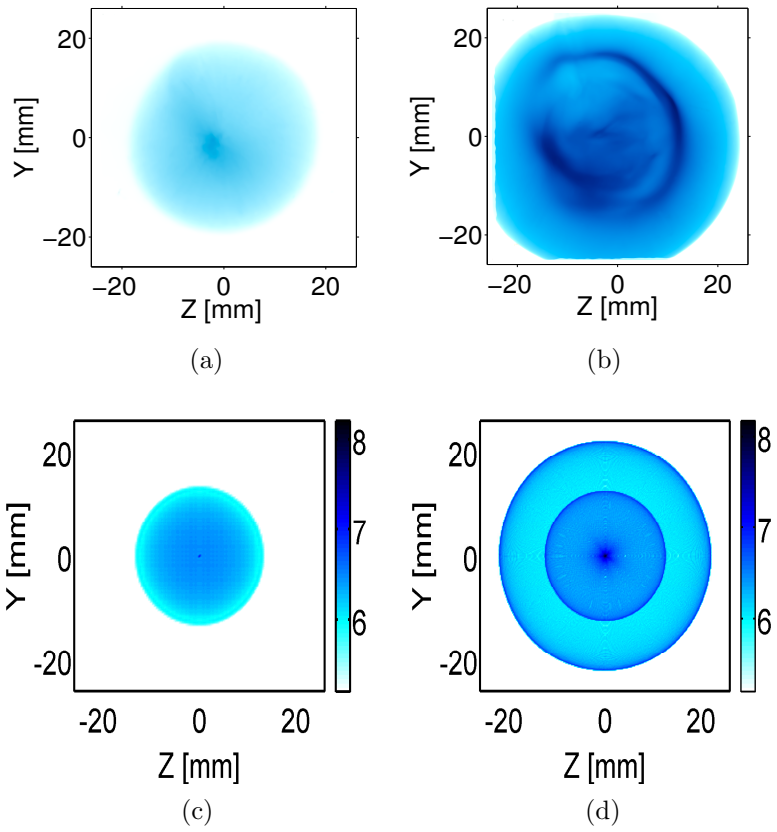

Figure 6.8: (a - b) Representative example measured proton spatial-intensity distributions at 7.3 MeV for peak laser intensity equal to: (a) 6×10^{19} Wcm^{-2}; and (b) 6.8×10^{20} Wcm^{-2}. (c - d) Analytical model calculations of the proton beam spatial distribution resulting from the *ab initio* QMD Kubo-Greenwood simulations at (d) 5×10^{19} Wcm^{-2}; and (f) 5×10^{20} Wcm^{-2}.

target rear surface, were observed in vitreous carbon and described in detail in Chapter 5.

For a closer comparison between the experimentally measured proton beams and the simulation predictions, the simulation cases in closest agreement with the experimental results are focussed on – the *ab initio* QMD Kubo-Greenwood resistivity calculation at peak laser intensities of 5×10^{19} Wcm^{-2} and 5×10^{20} Wcm^{-2}.

Displayed in Fig. 6.8, excellent qualitative agreement is found between the experimental and analytical results for the lower laser intensity (Figs. 6.8(a) and (c) respectively), for which smooth electron transport results in a uniform proton beam. Excellent agreement is also found between the experimental and simulated proton beams at the higher laser intensity, displayed in Figs. 6.8(b) and (d) re-

spectively. In this case, the annular fast electron beam observed in the simulations results in a ring-like structure in the proton beam, correlating closely with what was measured experimentally: a clear annular-profile in the proton beam distribution. Furthermore, these proton beam measurements contrast sharply with the distinctly different proton beam profiles, without annular features, which are predicted using the fast electron density distributions simulated with the other resistivity-temperature profiles.

6.2.3 The mechanism inducing annular transport

To understand why low-temperature resistivity plays such an important role in defining fast electron transport patterns, the way in which evolving temperature, and therefore resistivity, gradients subsequently lead to magnetic field patterns which strongly influence electron propagation is explored. The growth rate of the self-generated, resistive magnetic field is described by:

$$\frac{\partial \mathbf{B}}{\partial t} = \eta \nabla \times \mathbf{j}_f + \nabla \eta \times \mathbf{j}_f \tag{6.1}$$

where $\mathbf{j}_f$ is the fast electron current density and η is the target resistivity. The first term on the right hand side of Eq. (6.1) produces an azimuthal magnetic field which forces electrons towards regions of high current density. The resulting pinching action can, in principle, both collimate the beam [107] and lead to filamentation if seeded by non-uniformities in the current density across the beam. The second term arises from resistivity gradients in the target and generates a field that pushes electrons towards higher resistivity regions [109]. As described by Davies [109], the latter effect can lead to a hollowing of the fast electron beam. In this scenario, as the beam density is initially centrally peaked (following a typical Gaussian laser-spot profile), the highest collisional return current is drawn, and therefore the largest degree of target heating occurs, on-axis. As the beam propagates into a region of the target in which resistivity decreases with increasing temperature (the Spitzer regime is considered by Davies [109]), the target becomes less resistive on-axis than at larger radii, which could lead to beam hollowing if

the field due to the second term in Eq. (6.1)) exceeds the collimating effect of the field due to the first. For this investigation of fast electron transport in silicon, it is found to be the dip in the QMD-Kubo-Greenwood resistivity profile (Fig. 6.1) at low temperatures, centred at ∼3.5 eV, combined with the action of the second term in Eq. (6.1) which is a key factor in inducing the observed annular structure.

To illustrate this, the hybrid-PIC simulations are examined in greater detail, specifically focussing on the temperature, magnetic field and resistivity profiles. In Fig. 6.9, example ZEPHYROS hybrid-PIC simulation results are displayed of silicon target heating and resulting magnetic field generation (all at an example time step of 1.4 ps after the start of the laser pulse) using the QMD Kubo-Greenwood resistivity profile. Figs. 6.9(a) and (c) respectively represent 2-D temperature and corresponding magnetic field maps at a laser drive intensity of 5×10^{19} Wcm^{-2}, while Figs. 6.9(b) and (d) show the corresponding temperature and magnetic field profiles for a laser drive intensity of 5×10^{20} Wcm^{-2} respectively.

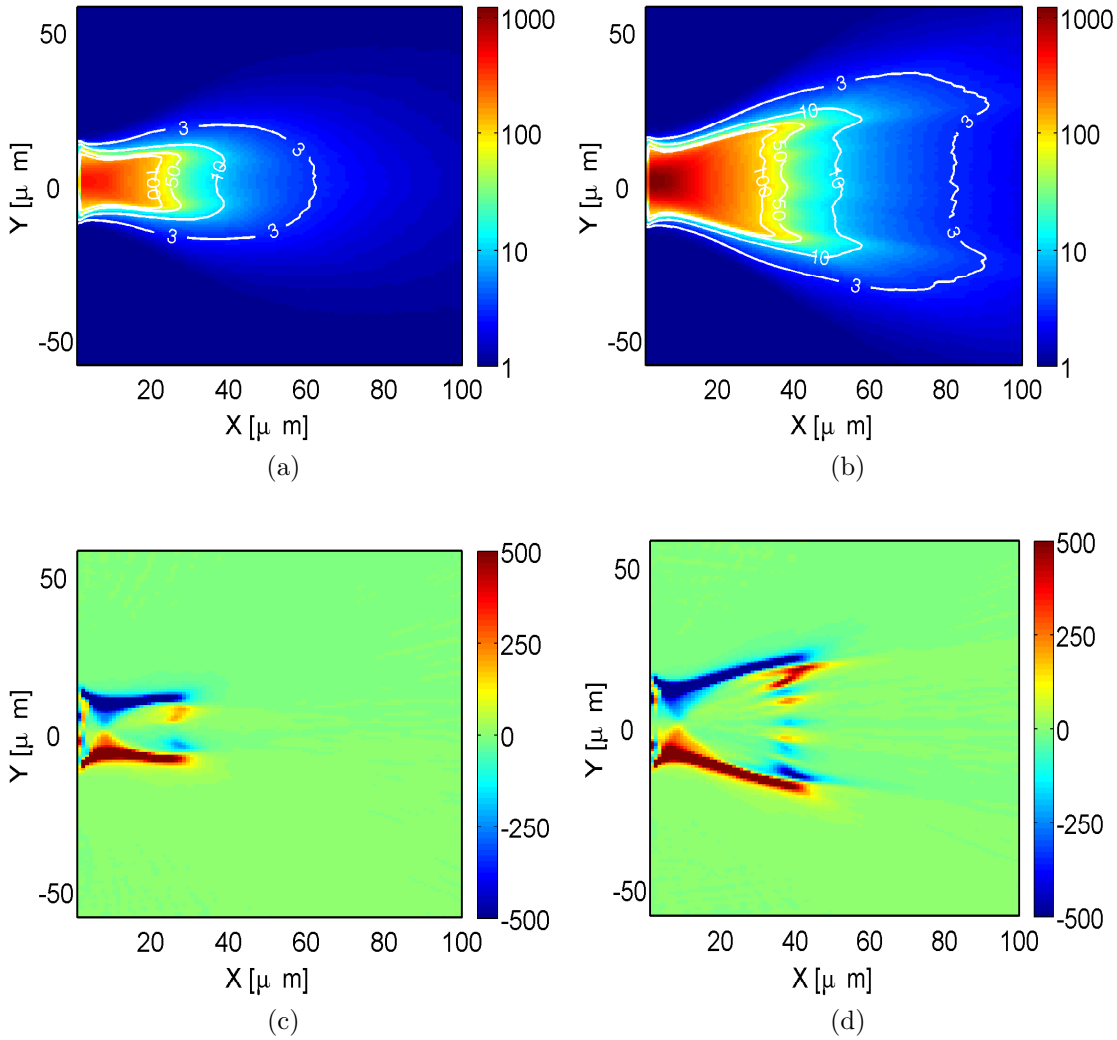

Figure 6.9: Hybrid-PIC simulation results using the QMD-Kubo-Greenwood resistivity-temperature model (outputs all at an example simulation time equal to 1.4 ps after the start of the laser pulse): (a - b) $\log_{10}$ 2-D target temperature map (in eV) with selected isothermal contours for the 5×10^{19} Wcm^{-2} and 5×10^{20} Wcm^{-2} cases respectively; (c - d) 2-D map of magnetic flux density (B_Z component in Tesla), for the 5×10^{19} Wcm^{-2} and 5×10^{20} Wcm^{-2} cases respectively, showing a reversal in magnetic field direction inside the edge of the beam.

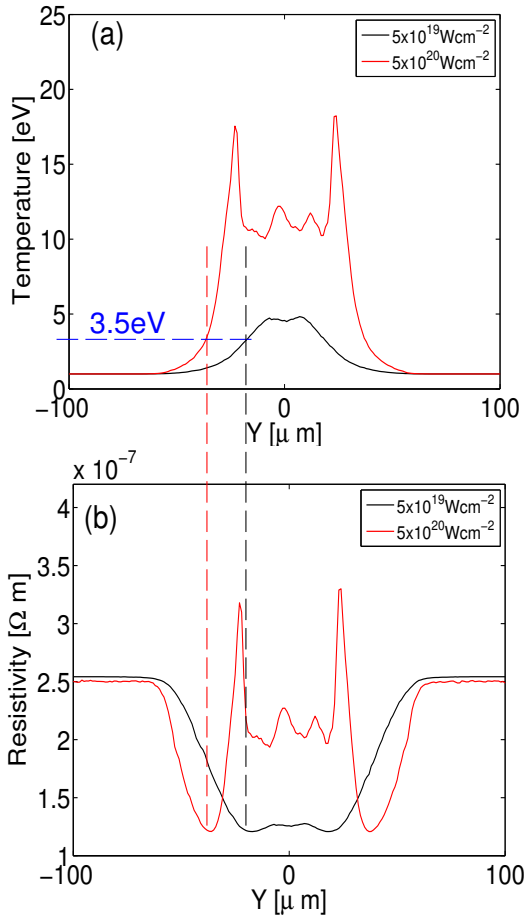

Figure 6.10: Hybrid-PIC simulation results using the QMD-Kubo-Greenwood model (outputs all at an example simulation time equal to 1.4 ps after the start of the laser pulse). Transverse (a) temperature, and (b) resistivity, profiles at 50 μm depth for 5×10^{19} Wcm^{-2} and 5×10^{20} Wcm^{-2}. Dashed vertical lines for both laser intensity cases illustrate that a dip in the resistivity profile, which seeds beam hollowing, arises at a temperature of about 3.5 eV.

Examining the low intensity case (i.e. 5×10^{19} Wcm^{-2} - Fig. 6.9(a)) first, it is found that there is substantial heating (up to several hundred eV) in the region immediately in-front of the laser focus (i.e. over the first $\sim$20 μm of the target). At greater depths, beyond $\sim$30 μm, the temperature falls rapidly and, at around 40 μm depth, has reduced to a value of $\sim$8 eV. The spatial temperature profile also reveals the onset of a lobe-like structure, located at the edge of the 10 eV isotherm, suggesting the onset of beam hollowing. The heating profile extends deeper into the target as evidenced by the extension of the 3 eV isotherm

to ∼60 μm. The corresponding magnetic field profile, shown in Fig. 6.9(c), is generated by the resistivity gradients produced by the temperature gradients in Fig. 6.9(a). Interestingly, the 2-D magnetic field profile reveals the strong collimating magnetic field component enveloping the fast electron beam together with the hollowing field component, arising at a depth of ∼30 μm. Importantly, however, the magnitude of this hollowing component is significantly less than the collimating, 'pinching' component. The balance between these two sources of resistive magnetic field growth are key to producing annular fast electron transport, as is discussed below.

Next, the 2-D temperature map of the high intensity case of 5×10^{20} Wcm^{-2}, displayed in Fig. 6.9(b), is explored. In this case, the induced heating extends much deeper into the target than the 5×10^{19} Wcm^{-2} intensity case. For example, the 3 eV isotherm extends to a depth of ∼90 μm while the 10 eV isotherm propagates to ∼55 μm. A 'spiked' spatial profile, emerging towards the edge of the electron beam, is also observed, indicative of strong beam hollowing. The magnetic field profile which arises from these temperature, and thereby resistivity, gradients is shown in Fig. 6.9(d). As in the low intensity case (Fig. 6.9(c)), there is a strong collimating magnetic field component which encases the electron beam. However, in contrast to the low intensity case, the hollowing field component, seeded at depth of ∼40 μm and generated just inside the edge of the collimating field, exhibits a field magnitude that is comparable to that of the collimating component, and actually exceeds it at slightly greater depths (i.e. ∼50 μm).

It is this hollowing field, as it begins to dominate over the collimating component, that seeds annular fast electron transport; the subsequent onset of the strong annular transport pattern in the high intensity case is understood as follows. Initially the highest temperature is on-axis for the Gaussian profile beam. At the edge of the beam, where the temperature drops to ∼3.5 eV, the resistivity gradient changes sign, as shown in Fig. 6.10(d), due to the dip in the resistivity-temperature profile (dashed lines are shown in Fig. 6.10 to illustrate this correlation for both laser intensity cases). Due to the second term in Eq. (6.1), this change in resistivity gradient drives a magnetic field reversal (see Figure 6.9(d)),

resulting in a perturbation in the beam current density, producing a localised increase near the edge of the beam. Subsequently, the resulting increased return current, and therefore rate of Ohmic heating in this region, drives a localised increase in resistivity for temperatures above ∼3.5 eV (up to tens of eV - see Fig. 6.1) and the region near the edge of the beam remains more resistive than at the centre (see the resistivity spikes in Fig. 6.10(b), which grow as the simulation evolves). This, together with the pinching effect of the magnetic field arising from the first term in Eq. (6.1), due to the higher current density, leads to strong positive feedback which sustains the annular transport pattern as the beam propagates through the remainder of the target. This explains why, for the high intensity case, the annular structure fully develops, while for the lower intensity case the resulting current density perturbation is not large enough to drive the annular transport pattern to the target rear-surface.

Finally, it is also interesting to note that the simulation result for the case of the Lee-More resistivity profile results in strong filamentation of the fast electron beam (Fig. 6.2(c - d)). The significantly higher resistivity in the 1-50 eV temperature range in this case, compared to the Kubo-Greenwood profile, results in a higher resistive instability growth rate [113], as described in Chapter 5.

6.2.4 The influence of target thickness and electron refluxing on annular transport

Building upon the investigation of electron transport in thick (300 μm) silicon, the role of target thickness on influencing fast electron transport is addressed by exploring electron transport in thinner silicon targets. Specifically, transport in 40 μm thick silicon targets is investigated to determine the influence that electron refluxing [58] has on fast electron beam transport dynamics. In addition, potential limitations of using proton emission as a diagnostic of electron transport in thin targets driven by an ultraintense picosecond laser pulse are indicated.

The experimental measurements displayed in Fig. 6.5 were obtained over a range of laser intensities, from 6×10^{19} Wcm^{-2} to 6.8×10^{20} Wcm^{-2} for 300 μm-

thick silicon targets, in which the subsequent transport patterns are explained by the generation of an additional magnetic field component which opposes the azimuthally collimating field component, acting to seed an annular transport pattern. The origin of this hollowing field component is due to a reversal in the resistivity gradient at a depth of ∼40 μm - see Fig. 6.9 - and thus one might expect the annular profile to be observable for targets with thickness of the order of $\sim$ 40 μm. However, there is an important practical reason for choosing thick targets: the diagnostic approach works best for thick targets for which there is little or no fast electron beam refluxing occurring within the target.

The fast electrons injected at the front side of the target leave the region of the focal spot and propagate through the target until they reach the rear surface. There, they establish the quasi-electrostatic sheath field which ionises the target rear-surface and subsequently drives ion acceleration. However, the strength of this field is large enough such that the majority of the fast electrons are reflected at the target rear-surface and directed back into the target. Once these reflected electrons reach the front surface of the target, a similar sheath potential forms which acts to reflect the fast electrons to propagate back into the target, returning to the rear surface. The resulting effect is that the fast electrons recirculate (i.e. reflux), as described by Sentoku *et al.* [174]. For thin targets, with thickness of the order of 30-40 μm, the fast electrons can circulate multiple times within the target over the duration of the laser pulse. This acts to disrupt the spatial distribution of the sheath field formed at the rear target surface, due to the arrival of energetic electrons that have recirculated multiple times. Thus for thinner targets (i.e. 30-40 μm), the use of proton emission as a diagnostic of the 'first pass' electron transport pattern can be misleading, since the resulting proton beam is a time-integrated measurement of the changing sheath distribution produced by the refluxing electrons. By using 300 μm thick targets, the effect of refluxing is minimised for fast electron transport and proton emission using a $\sim$ 1 ps laser pulse. Over the duration of the laser pulse, which governs the time over which the electric sheath field grows and accelerates ions [58], the resulting proton beam is predominantly produced by the 'first-pass' (i.e.

first propagation) of the fast electrons across the target.

To illustrate this, simulations are performed of fast electron transport in thin silicon targets of 40 μm thickness.The effects of fast electron refluxing are investigated by performing the simulations with and without reflective boundaries, which corresponds to refluxing turned on or off respectively. These simulations are performed using the ZEPHYROS hybrid-PIC code, with the same parameters as described previously. The simulations were performed at intensities of 5×10^{19} Wcm^{-2} and at 5×10^{20} Wcm^{-2}, and the results are shown in Fig. 6.11.

Fig. 6.11(a) shows the case for a peak laser intensity of 5×10^{19} Wcm^{-2} with no refluxing (i.e transmissive simulation boundaries). In this case an annular beam profile is produced, but with a very small diameter. The corresponding case at the higher laser intensity of 5×10^{20} Wcm^{-2} with no refluxing is shown in Fig. 6.11(b), again revealing an annular profile of small radius, albeit with a slightly larger radius that the lower intensity case. However, as shown in Fig. 6.11(c) and (d), when refluxing occurs the annular-structure is 'washed out' by the refluxing electrons.

To further demonstrate this effect, an experimental measurement of the proton beam spatial-intensity profile, generated using the Vulcan laser, of a 40 μm-thick silicon target at peak laser-drive intensity of 6×10^{19} Wcm^{-2}, is displayed in Fig. 6.12 . The measurement is in agreement with the simulation result of Fig. 6.11(c) $-$ there is no annular structure, due to the influence of fast electron refluxing on the measured spatial distribution of sheath accelerated protons. Moreover, the edges of the ion beam spatial distribution are not well defined which is a direct result of the 'halo' of fast electrons which expand to large radii, as shown in Fig. 6.11(c). This effect is a direct consequence of the refluxing electrons.

6.2.5 Summary - Part 1

To summarise this section, it was demonstrated that a more accurate treatment of low temperature resistivity, using *ab initio* QMD calculations, is important for describing fast electron transport physics as well as for interpreting experimental

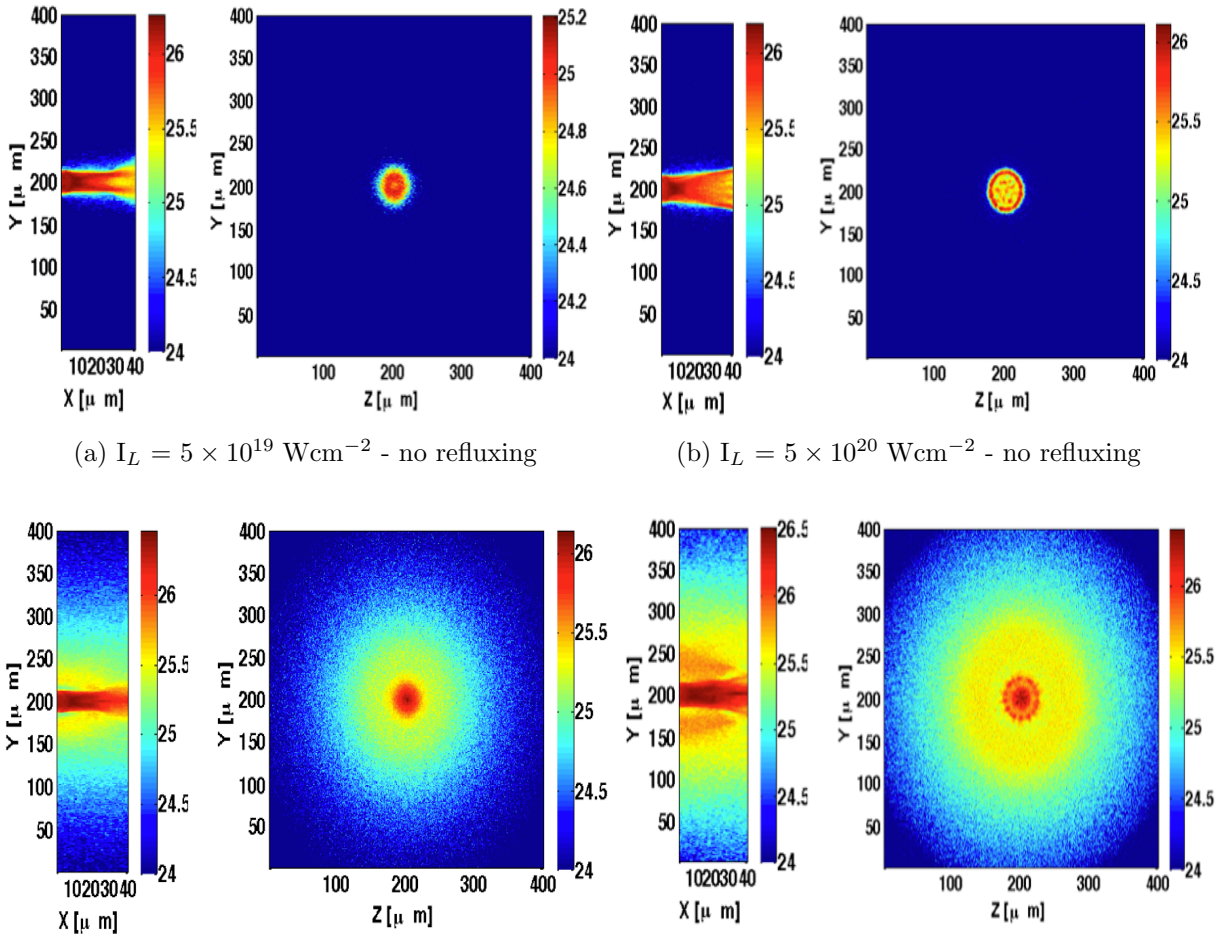

(a) $I_L = 5 \times 10^{19}$ Wcm^{-2} - no refluxing

(b) $I_L = 5 \times 10^{20}$ Wcm^{-2} - no refluxing

(c) $I_L = 5 \times 10^{19}$ Wcm^{-2} - refluxing

(d) $I_L = 5 \times 10^{20}$ Wcm^{-2} - refluxing

Figure 6.11: Hybrid-PIC simulation results, using the QMD-Kubo-Greenwood resistivity-temperature profile, for 40 μm thick silicon targets (outputs all at an example simulation time equal to 1.4 ps after the start of the laser pulse). In all cases the $\log_{10}$ electron density (m^{-3}) is plotted for the [X, Y] mid-plane (left panel) and [Y Z] rear-pane (right panel): Intensity of 5×10^{19} Wcm^{-2} for the case of no refluxing (a) and refluxing (c), and intensity of 5×10^{20} Wcm^{-2} for the case of no refluxing (b) and refluxing (d).

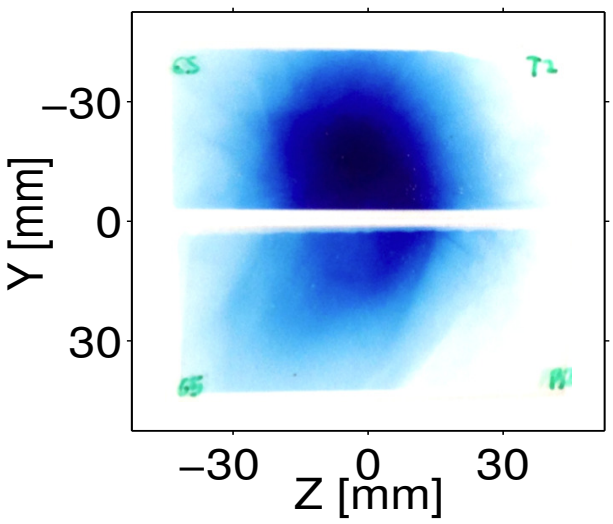

Figure 6.12: Example experimental proton beam spatial intensity measurement (at an example energy of 7.3 MeV) of 40 μm thick silicon irradiated at a peak laser intensity of $I_L = 6 \times 10^{19}$ Wcm^{-2}.

results. Moreover, it was demonstrated that the shape of the low-temperature region of the resistivity curve can profoundly alter the fast electron transport pattern through the key role that resistivity has in producing resistively generated magnetic fields − these fields subsequently act to influence the fast electron beam. It was also shown, using both numerical simulations and experimental results, that refluxing can have an impact upon the interpretation of proton emission measurements within the context of diagnosing fast electron transport.

The results presented indicate a potential route to enabling tunable beam patterns; by variation of laser-drive parameters to create a desired resistivity profile evolution in space and time. In the following section, we explore this idea by investigating the influence that laser-drive parameters have on annular transport.

6.3 Part 2 - The influence of laser-drive parameters on annular fast transport in silicon

Part 1 demonstrated that resistively generated magnetic fields, induced by the low-temperature (few eV) region of the resistivity-temperature profile, account

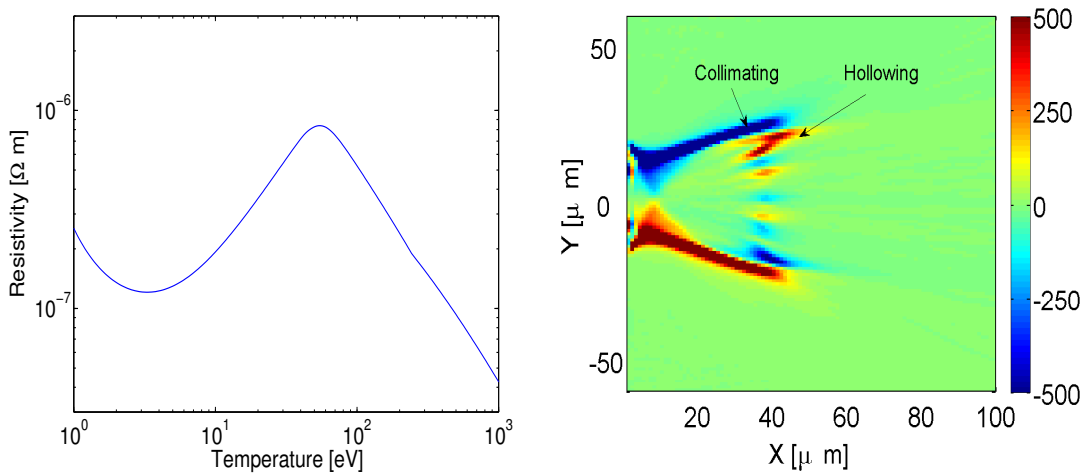

(b)

Figure 6.13: (a) Electrical resistivity of silicon as a function of target temperature, based on *ab initio* QMD calculations coupled with the Kubo-Greenwood equation and (b) example hybrid-PIC simulation result showing the 2D magnetic flux density (B_Z component in Tesla) generated in the interaction of a laser pulse of intensity 5×10^{20} Wcm^{-2} with a silicon target. The resistively generated magnetic field exhibits a collimating component which acts to limit the divergence of the beam and a hollowing component arising from a reversal in the magnetic field direction inside the edge of the beam.

for the transformation of the fast electron beam transport pattern from a uniform Gaussian-like spatial profile to an annular electron beam profile. Key to these results was the use of a resistivity model which was calculated using DFT simulations of the ionic structure, coupled with the Kubo-Greenwood equation to calculate the resistivity; this particular model was found to agree most closely with the experimental measurement of annular beam transport.

In this section, the sensitivity of annular fast electron beam transport to the parameters of the drive laser pulse is investigated numerically using 3D hybrid-PIC simulations. It is demonstrated that changes to the size of the ring and the density of the electrons forming it are produced upon variation of the laser-drive parameters, and these trends are quantified as a function of laser pulse energy, duration and focal spot radius. In addition, the observed variation of the beam transport patterns is explained by considering the effect that the pulse parameters have on the temporal and spatial dynamics of the resistively generated magnetic fields.

The numerical modelling presented in this section is performed using the same particle-based 3D-hybrid code used previously: the ZEPHYROS [23, 167] hybrid-PIC code. The majority of simulation parameters are kept fixed at the same values as those used in the previous section. However, this investigation involves the numerical exploration of the sensitivity of annular transport to laser intensity by controlling the drive laser pulse parameters. Thus, the variation of laser pulse energy E_L, focal spot radius r_L and laser pulse duration τ_L and the corresponding variation of the range of peak laser pulse intensities, I_L, and the subsequent influence on the annular electron beam transport, is investigated. The range of parameter values explored will be described below.

The silicon resistivity-temperature profile used, presented in Fig. 6.13(a), is based on a QMD-Kubo-Greenwood calculation [85, 91, 92] as discussed in detail in Part 1, where it was demonstrated that the dip in resistivity at a few eV leads to a reversal in the resistivity gradient near the edges of the fast electron beam, which in turn generates a hollowing magnetic field component which seeds a ring electron beam structure (see Fig. 6.13(b)). Since this model was shown to agree most closely with the experimental observation of an annular electron beam, this particular model will be used throughout this investigation.

6.4 Modelling Results

Before presenting the simulation results, two key parameters which are used to characterise and quantify the degree of annular transport present in the simulations, and which will be referred to when explaining the observed trends, are defined. The first of these parameters determines the inner radius of the annulus at the simulation rear-surface (corresponding to a target rear-surface) i.e. at X = 200 μm. Quantitatively, this is defined by the ratio at which the fast electron density increases by a factor of 5 with respect to the axial electron density. The second parameter calculates the ratio of the fast electron density in the annulus to the axial position (i.e. at [X, Y, Z] = [200,0,0]), again at the simulation rear-surface. Together, these parameters effectively quantify the magnitude of

2×10^{20} Wcm^{-2} 2.5×10^{20} Wcm^{-2} 3.3×10^{20} Wcm^{-2} 5×10^{20} Wcm^{-2} 1×10^{21} Wcm^{-2}

A

$\tau_L = 1$ ps
$r_L = 3.5$ μm

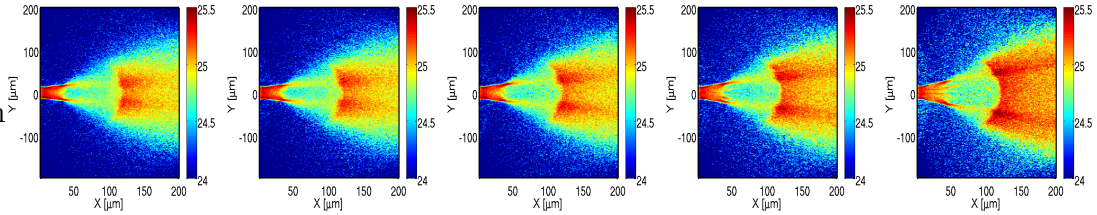

(a) $E_L = 78$ J (b) $E_L = 96$ J (c) $E_L = 128$ J (d) $E_L = 192$ J (e) $E_L = 384$ J

B

$E_L = 192$ J
$\tau_L = 1$ ps

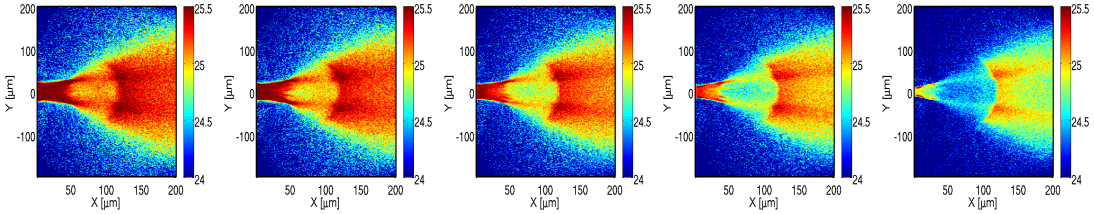

(f) $r_L = 5.5$ μm (g) $r_L = 5$ μm (h) $r_L = 4.3$ μm (i) $r_L = 3.5$ μm (j) $r_L = 2.5$ μm

C

$E_L = 192$ J
$r_L = 3.5$ μm

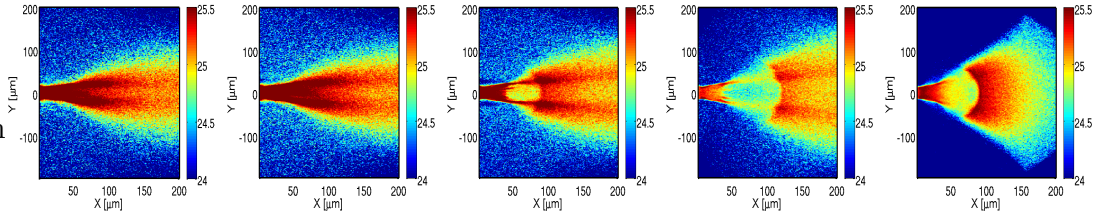

(k) $\tau_L = 2.5$ ps (l) $\tau_L = 2$ ps (m) $\tau_L = 1.5$ ps (n) $\tau_L = 1$ ps (o) $\tau_L = 0.5$ ps

Figure 6.14: 2D maps of the fast electron beam density ($\log_{10}$), in units of m^{-3}, in the [X-Y] mid-plane of the simulation, for three laser pulse parameter scans: (a-e) variation of E_L (top row); (f-j) variation of r_L (middle row); (k-o) variation of τ_L (bottom row). The value of the varied parameter is given below each panel.

the radius of the ring and the annulus-to-axial contrast ratio.

To enable a detailed exploration of the sensitivity of annular transport to laser pulse parameters, a detailed series of three simulation scans are performed, described as follows: (A) variation of laser pulse energy, E_L in the range 78 - 384 J, for fixed focal spot radius $r_L = 3.5$ μm and fixed laser pulse duration $\tau_L = 1$ ps; (B) variation of r_L in the range 2.5 - 5.5 μm, for fixed $E_L = 192$ J and $\tau_L = 1$ ps; and, (C) variation of τ_L in the range 0.5 - 2.5 ps, for fixed $E_L = 192$ J and $r_L = 3.5$ μm. This particular range of parameter values were chosen such that the peak laser pulse intensity, I_L, was varied in the range 2×10^{20} - 1×10^{21} Wcm^{-2} for all three scans.

To demonstrate the overall trends observed in the simulations, Fig. 6.14 presents the fast electron density in the [X, Y] mid-plane at an example time

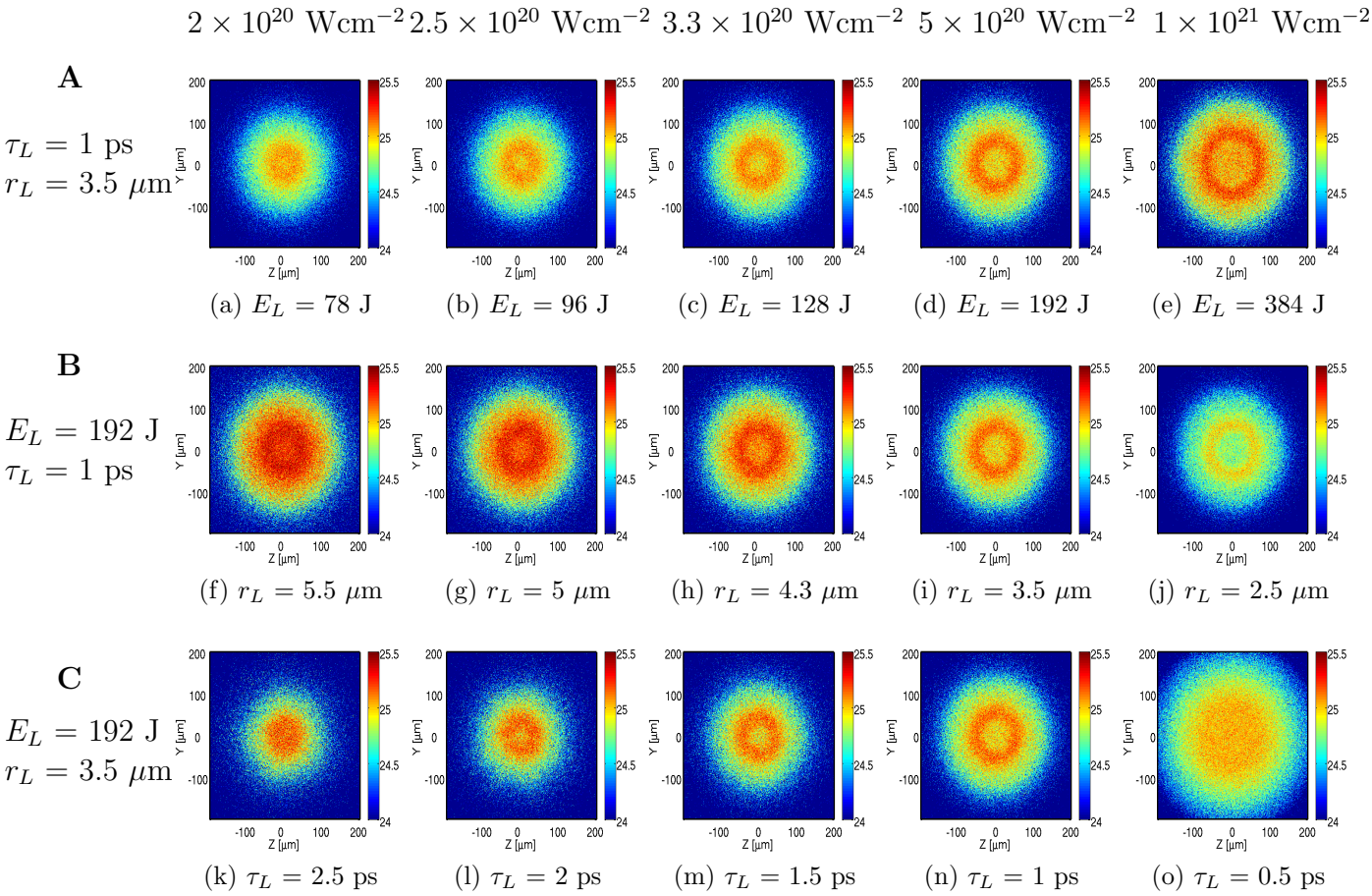

(a) $E_L = 78$ J (b) $E_L = 96$ J (c) $E_L = 128$ J (d) $E_L = 192$ J (e) $E_L = 384$ J

(f) $r_L = 5.5$ μm (g) $r_L = 5$ μm (h) $r_L = 4.3$ μm (i) $r_L = 3.5$ μm (j) $r_L = 2.5$ μm

(k) $\tau_L = 2.5$ ps (l) $\tau_L = 2$ ps (m) $\tau_L = 1.5$ ps (n) $\tau_L = 1$ ps (o) $\tau_L = 0.5$ ps

Figure 6.15: Same as Fig. 6.14, but for the rear surface [Y-Z] plane

of τ_L + 0.4 ps. Note that this time is selected because the full population of electrons has been initiated in the simulation and has propagated at least 100 μm across the target, with the majority having reached the rear surface. Scan A is presented in the top row (Fig. 6.14(a - e)), B in the middle row (Fig. 6.14(f - j)), and C in the bottom row (Fig. 6.14(k - o)). In addition, we also present the corresponding simulation outputs for the [Y, Z] rear-plane snapshots (corresponding to target rear-surface) − these results are displayed in Fig. 6.15.

Firstly, the results of scan A (i.e. the laser energy scan) are described. From Figs. 6.14 (a - e), it is found that increasing the pulse energy from 78 J to 384 J, which increases the injected electron current, produces an increase in the overall divergence of the fast electron beam, and therefore an increase in the radius of the annular feature. Conversely, scan B reveals that by decreasing the focal spot radius from $r_L = 5.54$ μm to 2.48 μm, which acts to increase the intensity over the same range as scan A, the overall increase in both beam divergence

and the radius of the ring is smaller than that of scan A. In this case, the fixed pulse energy together with the increasing intensity (through decreasing spot radius) corresponds to fewer injected electrons at the focal-spot 'absorption' region, centred at [X, Y, Z] = [0, 0, 0], as the focal spot radius decreases. This results in the decreasing fast electron beam density (for increasing laser intensity) observed in Figs. 6.14(f - j). As will be explained, the decrease in fast electron density, and therefore current density, has a direct effect on the target temperature and resistivity temporal evolution, and thus on the electron transport properties. In scan C, Figs. 6.14(n - k), for fixed laser energy and spot radius, significant change to the electron beam transport is observed for variation of the pulse duration. As τ_L increases over the range of 1 ps to 2.5 ps, which corresponds to an intensity decrease of 5×10^{20} to 2×10^{20} Wcm^{-2}, see Figs. 6.14(n - k), the overall beam divergence and radius of the annular structure decrease. This leads to a more uniform beam transport pattern for longer pulse durations (see Fig. 6.14(k) for 2.5 ps). Moreover, it is interesting to note that loss of annular structure is also observed for reducing τ_L to 0.5 ps. As will be explained, this is a result of the reduction of the collimating component of the resistive magnetic field which varies with pulse duration. As an aside, note that the annular transport is relatively stable along the length of propagation, until significant refluxing has occurred at the target rear surface; recent work demonstrated that fast electron refluxing can create perturbations of the resistive magnetic field which, in turn, act to modify the fast electron propagation [136], also demonstrated in part 1.

To describe these trends in more detail, the rear-surface simulation outputs (from Fig. 6.15) are analysed using the previously defined parameters that quantify the variation of the size of the annulus, and the relative fast electron density within the ring, as a function of laser intensity I_L for each of the three laser parameter scans. The annular radius is defined as the distance from the centre of the rear-surface in the simulation, at [Y, Z] = [0, 0], to the inner annulus of the ring structure. The results of this analysis are presented in Fig. 6.16(a). In addition, the ratio of the fast electron density in the annulus to the density at the centre of the beam, at [Y, Z] = [0, 0], is shown in Fig. 6.16(b).

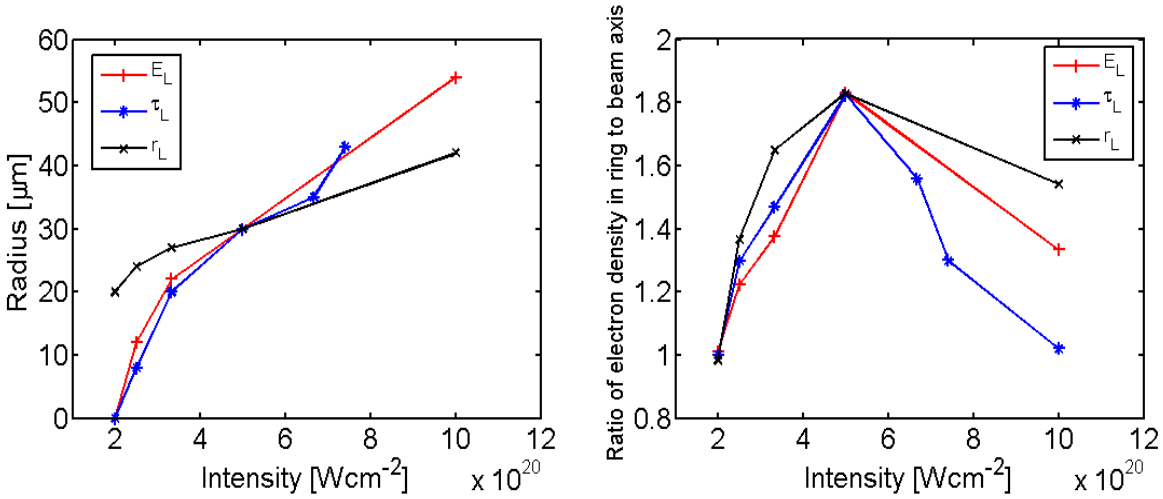

(a) (b)

Figure 6.16: (a) Inner radius of the annulus at the target rear surface as a function of I_L, for the three parameter scans shown in Fig. 6.14 and Fig. 6.15. (b) Ratio of the fast electron density in the annulus to the density on-axis (i.e. at [200,0,0]) as a function of I_L, for the same three parameter scans.

6.4.1 Overall effect of laser intensity

To begin the discussion, the variation of the size (i.e. radius) of the ring structure across the range of peak laser-drive intensities is explored. Fig. 6.16(a) reveals that increasing peak laser intensity induces an increase in the ring radius for each laser parameter (i.e. laser energy, focal spot radius and pulse duration). These trends are understood within the framework of the resistive generation of large magnetic fields. As described previously, the magnetic field reversal that drives the beam hollowing effect occurs towards the edge of the fast electron beam, where Ohmic heating of the background material is of the order of a few eV. The radius of the ring is, to first order, defined by the overall beam divergence which is in turn defined by the angular distribution of the electron source. Note that in these simulations, this is fixed at a constant value. Moreover, the beam divergence is also determined by the magnitude of the collimating magnetic field component, which is predominantly determined by the electron current density and is strongest in regions of high current density. Regions of highest current density occur within the first few tens of microns from the target front surface,

and in this region the beam can be approximated as a cylinder. To understand the influence of these strong magnetic fields on fast electron transport a simple analytic model is used, which describes the resistive azimuthal magnetic field that envelopes a uniform cylindrical electron beam.

An intense laser pulse interacting with a solid target produces a bunch of fast electrons, the number of which, N_f, depends upon the percentage conversion of laser energy into fast electron energy, $\eta_{L\rightarrow e}$, the laser energy, E_L, and the temperature of the fast electron beam, k_BT_f, which scales ponderomotively [65] in these simulations:

$$k_BT_f = 0.511[(1 + 0.73I_{18}\lambda_{\mu m}^2)^{1/2} - 1]\text{MeV} \tag{6.2}$$

where I_{18} is the laser intensity in units of 10^{18} Wcm^{-2} and $\lambda_{\mu m}$ is the laser wavelength in μm. The number of fast electrons is given by:

$$N_f = \frac{\eta_{L\rightarrow e}E_L}{k_BT_f} \tag{6.3}$$

Eq. (6.3) describes the number of electrons N_f contained within a cylinder of base equal to the radius of the focal spot, r_L, and length given by the pulse length $\tau_L c$. The volume of the fast electrons is thus given by $V = \pi r_L^2 c\tau_L$. The corresponding fast electron density, n_f, is calculated as:

$$n_f = \frac{N_f}{\pi r_L^2 c\tau_L} \tag{6.4}$$

where c is the speed of light. The current density of the beam, $\mathbf{j}_f$, is given by:

$$\mathbf{j}_f = -en_f\mathbf{v}_f \tag{6.5}$$

where $\mathbf{v}_f = \sqrt{k_BT_e/m_e}$ and m_e is the electron mass.

Thus, the resistively generated magnetic field, $\mathbf{B}$, is given by:

$$\frac{\partial \mathbf{B}}{\partial t} = \frac{\eta \mathbf{j}_f}{r_f} \tag{6.6}$$

$$\frac{\partial \mathbf{B}}{\partial t} = \frac{-e\eta}{r_f} \frac{\mathbf{v}_f}{\pi r_L^2 c \tau_L} \frac{\eta_{L\rightarrow e} E_L}{k_B T_f} \tag{6.7}$$

where η is the resistivity and t is the time. The magnitude of the magnetic field can be estimated from Eq. (6.6) as:

$$\partial \mathbf{B} \approx \frac{\eta j_f \tau_L}{r_f} \tag{6.8}$$

From the simulation results, note that electron beam hollowing is not seeded until a depth of $\sim$40 μm. As described by Eq. (6.7), there is an inverse dependence of the magnitude of the collimating magnetic field on the fast electron energy T_f, which arises due to the reduction in the current density as T_f is increased (Eq. (6.5)). Since T_f scales ponderomotively with the square root of the laser intensity (Eq. (6.2)), as the peak laser intensity is increased the magnetic field strength, and hence it's focussing effect, decreases, which acts to increase the overall beam divergence. Thus the radius of the ring induced by the hollowing component of the field formed near the edge of the beam increases with I_L.

Analysis of the ratio of the electron density in the annulus to the axial density, shown in Fig. 6.16(b), for all three laser pulse parameter scans, reveals that the ratio of the electron density in the annulus to the axial density is highest for $I_L = 5 \times 10^{20}$ Wcm^{-2}. By decreasing the laser intensity, the overall beam temperature T_f is reduced. As discussed previously, decreasing mean electron temperature acts to increase the resistively generated magnetic field strength (Eq. (6.7)), pinching the electron beam and resulting in a higher electron beam density along the beam axis. As shown in Fig. 6.15, hollowing does still occur at lower laser intensity. However, the ratio of the beam density in the annulus to axial position decreases as the collimating effects of the magnetic field dominates over the hollowing term for smaller beam radii. As the peak laser intensity increases beyond 5×10^{20} Wcm^{-2}, the growth rate of the resistive magnetic field decreases which results

in less fast electrons being directed into the ring structure − although the beam radius increases, which should enhance the contrast ratio, the lower magnitude of the hollowing magnetic field together with higher beam temperature gives rise to less electrons being present in the annular structure. Furthermore, since the local current density $\mathbf{j}_f$ in the annulus thereby decreases with increasing laser intensity (Eq. (6.5)), the rate of localised resistive heating is lower (resistive heating scales with $\mathbf{j}_f^2$) and so the reinforcing feedback condition discussed above is not established. Therefore, in this case the annular transport structure does not develop and evolve into a substantial ring feature.

6.4.2 Laser focal spot dependence

Despite the radius of the annular structure increasing with increasing I_L for all three parameter scans, Fig. 6.16(a) clearly reveals that the intensity scaling is different for variation of the laser focal spot radius when compared with variation of the laser energy E_L or pulse duration τ_L. To explain this feature, the effect that the size of the electron beam at the source (i.e. focal spot region) has on the subsequent beam transport is explored. A decrease in the beam radius r_L has two principle effects: (1) fast electron current density $\mathbf{j}_f$ increases and thus $\mathbf{B}$ increases (Eq. (6.7)), acting to reduce the divergence of the electron beam; and, (2) the radius at which hollowing is seeded decreases. Both effects influence the radius of the beam annulus downstream, and each are considered in turn.

From Eq. (6.7), the magnitude of the magnetic field is inversely proportional to the beam radius r_f and is thus strongest in regions where $\mathbf{j}_f$ is highest. This occurs particularly at the electron source, and the size of this region is determined by the size of the laser focal spot. By first examining the simulation results at 5×10^{20} Wcm^{-2} (which is common to all three parameter scans) as a reference point for a focal spot radius of $r_L = 3.5$ μm, it is found that decreasing the focal spot radius to 2.5 μm (corresponding to an increased intensity of 1×10^{21} Wcm^{-2}) increases $\mathbf{j}_f$ at the source by approximately a factor of two, resulting in a peak magnetic field strength increase also of a factor of two. Examining the transport properties of the fast electron beam, the simulation reveals a reduction

of the radius of the annulus which corresponds to an overall beam divergence angle reduction of $\sim 36\%$, compared to the simulations at the same intensity in scans A and C for which $r_L = 3.5$ μm. Similarly, an increase in r_L from 3.5 μm to 4.3 μm ($I_L = 3.3{\times}10^{20}$ Wcm^{-2}) results in a 50% decrease in $\mathbf{j}_f$ (and hence magnetic field $\mathbf{B}$) at the source, which contributes to the $\sim 35\%$ increase in the ring divergence in the simulation results (again compared to the simulations at the same intensity in scans A and C).

The influence that variation of the focal spot radius has on the depth at which the annular transport pattern is seeded is explored in more detail in Fig. 6.17. In this figure, the transverse intensity profiles of the drive laser pulse are shown in Fig. 6.17(a) and (d) for the energy and focal spot scans (A and B), respectively. Note lineout profiles of scan C are very similar to those of scan A, and are thus not considered here. For each scan, three example peak laser intensities are considered: 2×10^{20} Wcm^{-2}, 5×10^{20} Wcm^{-2} and 1×10^{21} Wcm^{-2} (displayed as the black, red and blue plots, respectively) and the FWHM for each case is marked with a correspondingly coloured horizontal line. The corresponding target temperature and resistivity profiles (along the Y-axis) at X = 50 μm (depth at which the annular transport evolves) are shown in Fig. 6.17(b) - (c) and Fig. 6.17(e) - (f) for scan A and B respectively. The red dotted line highlights the temperature at 3.5 eV and the corresponding reversal in the resistivity gradient at the edges of the beam which seeds annular transport. From these plots, it is demonstrated that the radius at which seeding of the annular transport occurs increases with intensity for scan A (and C), but decreases slightly with intensity for scan B, due to the change in r_L. For example, at a peak intensity of $I_L = 2 \times 10^{20}$ Wcm^{-2}, the radius at which annular transport is seeded is $\sim 35\%$ larger in scan B than in scan A, due to the larger r_L, which contributes to the larger annular profile at the rear of the simulation box.

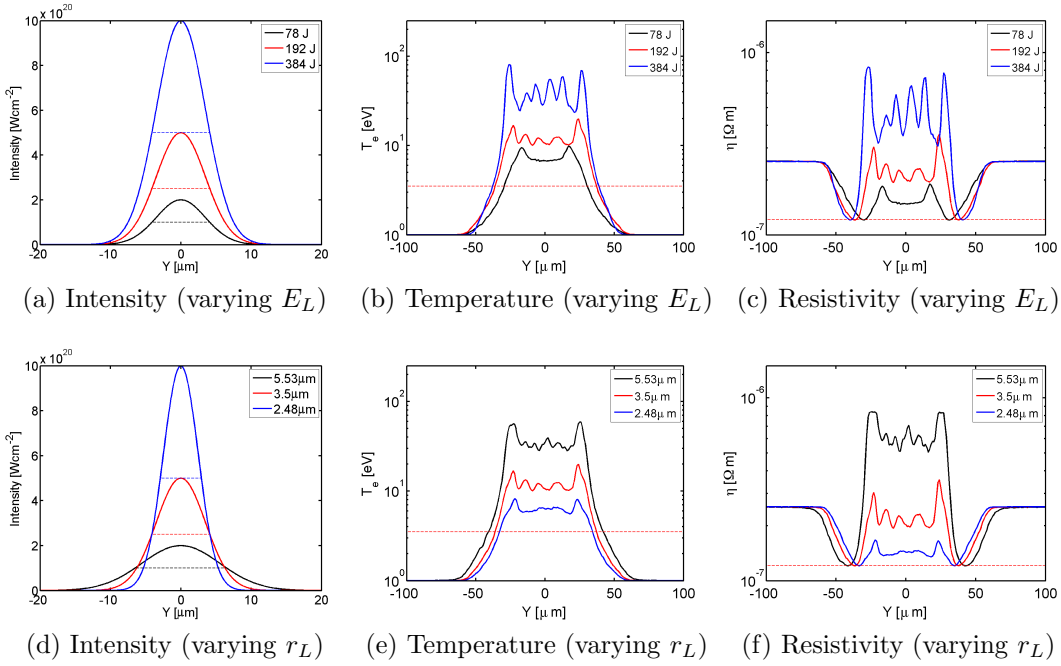

(a) Intensity (varying E_L) (b) Temperature (varying E_L) (c) Resistivity (varying E_L)

(d) Intensity (varying r_L) (e) Temperature (varying r_L) (f) Resistivity (varying r_L)

Figure 6.17: Variation of (a) the laser pulse intensity, (b) the target temperature at X = 50 μm and (c) electrical resistivity at X = 50 μm along the Y-axis, all for three example peak intensities (2×10^{20} Wcm^{-2}-black, 5×10^{20} Wcm^{-2}-red and 1×10^{21} Wcm^{-2}-blue) obtained by variation of E_L (values given). (d-f) Same as (a-c), for the same three peak intensities, but for variation of r_L (values given). Dotted lines in (a) and (d) highlight the FWHM of the intensity distributions. Dotted lines in (b) and (e) mark the important 3.5 eV target temperature, and in (c) and (f) mark the corresponding turning points in the target resistivity which seeds annular fast electron beam transport.

It is interesting to note that the simulation profiles displayed in Fig. 6.17 exhibit sharp, spike-like structures in the target temperature and resistivity profiles. These features grow at the edge of the electron beam and are a consequence of the local increase in the electron beam density, which in turn drives an increase in the collisional return current due to more fast electrons being deflected to that region by the magnetic field. As discussed in Part 1, this mechanism drives a localised increase in resistivity for temperatures greater than ~3.5 eV. Thus, regions of the target located near the edge of the electron beam remain more resistive than regions located in the centre of the electron beam, which acts to reinforce the annular transport profile (via the positive-feedback mechanism outlined previously) as the fast electrons propagate through the rest of the target.

It is also interesting to highlight that reducing r_L for a fixed E_L and τ_L has

the result of significantly reducing the overall heating of the target (Fig. 6.17(e)). This occurs because I_L, and therefore T_f (see Eq. (6.2)), increases, which for a fixed total fast electron energy (which is assumed in these simulations to be 30 %) reduces the total number of fast electrons injected into the target. Thus, the target heating is reduced since Ohmic heating scales as $\mathbf{j}_f^2$.

Moreover, the results presented in Fig. 6.17 reveal a general trend of the onset of filamentation of the fast electron beam as the laser energy is increased as evidenced by the oscillatory, 'spiked' structures becoming visible across the beam in Fig. 6.17(b - c). This effect is a direct consequence of the background electrons being heated to temperatures between ∼3.5 eV and ∼70 eV, corresponding to an increase in resistivity (Fig. 6.13) which in turn leads to a higher resistive instability growth rate, as demonstrated in Chapter 5.

6.4.3 Influence of laser pulse duration

The influence of laser pulse duration on the formation and evolution of the annular transport pattern is now examined. Firstly, to aid understanding of why the annular structure is 'washed out' for the $\tau_L = 0.5$ ps case in scan C, the spatial profile of the resistively generated magnetic field as a function of τ_L is examined by extracting lineouts along the Y-direction (i.e. transverse, or radial, profile) of the simulation grid, at the X-axis position at which the magnetic field extends. This position varies as a function of τ_L and is defined as the position at which the magnitude of the collimating magnetic field is reduced by 50%. For the temporal cases examined this represents depths of 45 μm, 50 μm, 55 μm, 60 μm and 65 μm for $\tau_L = 0.5$ ps, 1 ps, 1.5 ps, 2 ps and 2.5 ps respectively. The resulting field profiles are shown in Fig. 6.18(a) for transverse beam radius up to 80 μm (i.e. Y = 0 corresponds to the centre of the beam) for each of the five simulation cases.

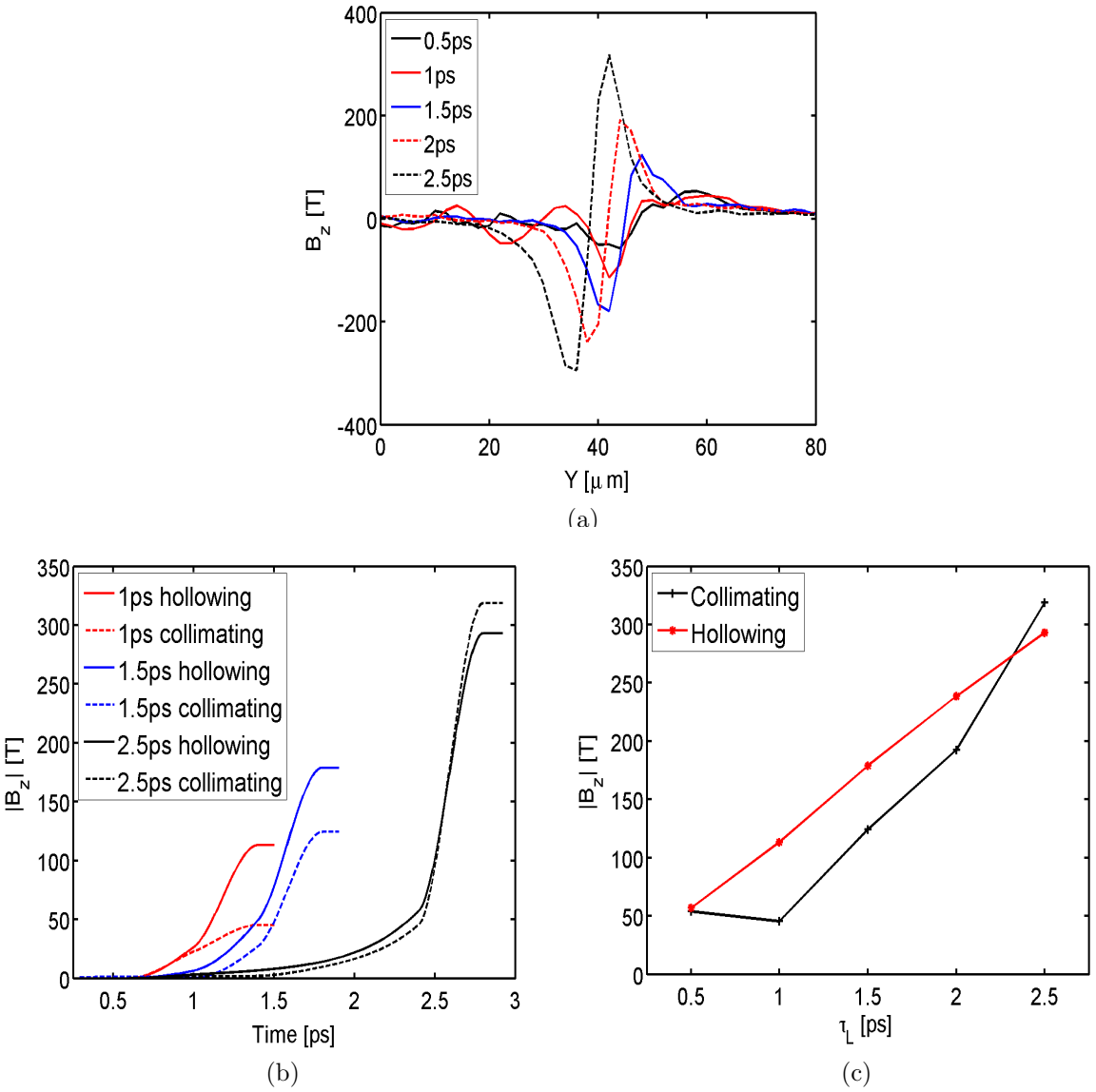

Figure 6.18: (a) Variation of the self-generated resistive magnetic field as a function of beam radius (Y-axis) at the penetration depth over which the magnetic field extends: 45 μm, 50 μm, 55 μm, 60 μm and 65 μm for τ_L = 0.5 ps, 1 ps, 1.5 ps, 2 ps and 2.5 ps respectively. (b) Magnitude of the collimating and hollowing magnetic field components as a function of time for given τ_L. (c) Magnitude of the collimating and hollowing magnetic field components as a function of τ_L.

The results highlight the complex interplay between laser pulse duration and the generation of both the collimating magnetic field, which envelopes the beam and drives electrons toward the beam axis (represented by positive B_Z values in Fig. 6.18(a), and hollowing magnetic field which forms inside the edge of the beam and acts to push electrons away from the beam axis (represented by neg-

ative B_Z in Fig. 6.18(a)). The key to initiating and propagating an annular fast electron structure is to obtain a balance between these opposing components of the magnetic field.

With reference to Eq. (6.7), the magnitude and growth rate of the resistive magnetic field depend on both the fast electron current density $\mathbf{j}_f$ and the duration of the electron bunch t, which is governed by the duration of the drive laser pulse [99]. The transverse lineouts of the magnetic field, shown in Fig. 6.18(a), reveal both the collimating ('pinching') component and oppositely-directed hollowing component, at each selected τ_L. It is found that the amplitude of both field components increases as the pulse duration increases, which is a direct consequence of the longer duration over which the field grows (see Eq. (6.7)). Moreover, a general trend of a decrease in the difference between the field amplitudes as the pulse duration is increased is observed. This point is reinforced by Fig. 6.18(b) which shows the temporal evolution of both magnetic field components for three example τ_L, and Fig. 6.18(c), which shows the magnitude of both components as a function of pulse duration.

The greatest difference in magnetic field strength between the two components is observed for $\tau_L = 1$ ps, which explains the resulting strong annular transport patterns observed at that intensity. As the pulse duration increases, this difference decreases as the collimating magnetic field begins to dominate over the hollowing field. Eventually, for τ_L above 2 ps, there is a switch over in the dominant field component. The consequence of the collimating field becoming stronger than the hollowing field is that the annular transport pattern is no longer sustained, as evidenced by the uniform fast electron spatial profile observed in Fig. 6.15(k). Moreover, for the shortest pulse duration explored (i.e. $\tau_L = 0.5$ ps), the amplitude of the peak collimating and hollowing magnetic fields is approximately equal, in addition to the overall magnitude of each component not being sufficient to significantly influence the fast electron transport, as evidenced by the loss of annular transport and increase in beam divergence (see Fig. 6.15(o)). In general, the optimum conditions for initialising a strong, well-defined annular transport pattern occur when the magnitude of the hollowing resistive magnetic field com-

ponent is greater than the collimating component. Moreover, increasing the laser pulse duration reduces the transverse extent of the location of the peak magnitude of each field component (i.e. the Y-axis position of each component decreases), reinforcing the reduction of the radius of the annular structure. This effect is a direct consequence of the increasing collimating field which acts to decrease the overall beam divergence.

6.4.4 Summary - Part 2

To summarise the work presented in this section, the annular transport patterns of fast electron beams in silicon, arising from oppositely-directed azimuthal components of the self-generated resistive magnetic field, have been investigated as a function of the parameters of the drive laser pulse, using a 3D hybrid-PIC code. The results demonstrate that there is an optimum laser peak intensity range for transporting fast electrons within an annular structure produced in this way. The size of the annulus is found to increase with peak intensity, due to a decrease in the magnitude of the collimating magnetic field which defines the overall beam divergence. An optimum laser intensity is found for enhancing the annulus-to-axial electron density contrast ratio, determined by the relative strength of the resistive magnetic field components — the hollowing component should be high to deflect electrons into the annulus, but the collimating component should not be so high as to produce a strongly collimated beam. The resulting balance between these magnetic field components explains the observed optimum laser drive intensity. Furthermore, it is found that the size of the annular profile is sensitive to the laser focal spot size, which enables some degree of tuning of the annular transport pattern for a fixed beam temperature or drive laser intensity.

6.5 Conclusions

At the beginning of this chapter, it was highlighted that low-temperature resistivity is a feature which, while acknowledged, has been widely overlooked in fast electron transport. This chapter has challenged this oversight by demonstrating the importance of low-temperature resistivity on influencing the global fast electron transport properties in solid density targets. This has been demonstrated both experimentally and numerically, revealing that annular electron transport patterns observed in silicon are explained by using a more accurate calculation of the low-temperature region of the resistivity-temperature profile: QMD simulations coupled with the Kubo-Greenwood equation. Furthermore, it was also demonstrated that the annular transport pattern can be controlled and optimised optically; by varying the laser-drive parameters the key dependencies of the transport pattern to laser energy, focal spot radius and pulse duration was demonstrated.

In the next chapter, these results are built upon by exploring the effect that target resistivity gradients, induced by preheating the target with laser-driven protons, have on influencing fast electron beam transport.

Chapter 7

Fast Electron Transport in Preheated Silicon

7.1 Introduction

The results presented in Chapters 5 and 6 demonstrate the effect that low-temperature (1 - 50 eV) electrical resistivity has on fast electron transport in solids. The results can be summarised as follows: firstly, in Chapter 5, the importance of lattice structure in determining low-temperature resistivity was demonstrated, and the subsequent role that lattice structure has in defining fast electron beam filamentation; and secondly, in Chapter 6, new fast electron transport patterns, specifically annular beam transport, can be generated depending on the shape of the resistivity-temperature profile at temperatures as low as a few eV. In addition, the potential to optically 'tune' fast electron transport through variation of the laser drive parameters was also explored (see Chapter 6, Part 2). These results point to a tantalising potential capability; predictive control of fast electron beam transport via target material choice (i.e. through the material's lattice structure) and by variation of the laser-drive parameters (i.e. altering the temporal and spatial evolution of temperature and resistivity gradients). These two factors may play an important role in providing much needed control of fast electron transport for applications.

In this chapter, this work is built upon by investigating a radically different

approach to understanding and controlling fast electron transport: exploring fast electron transport in a preheated solid. Although the previous investigations involved electron propagation through a solid undergoing Ohmic heating driven by the return current electrons (induced by the forward-streaming 'fast' electrons), which occurs on a femtosecond timescale, the bulk solid is initially in a cold state (i.e at room temperature, $\sim$ 0.025 eV) when the fast electrons are produced. In this chapter, the extent to which the initial target temperature, and spatial gradients in temperature and lattice disorder, influence fast electron transport is explored. By using a laser-driven proton beam to preheat solid-density silicon samples to temperatures above the melting temperature (i.e. $>$ 0.145 eV), thus melting the lattice on tens-of-picoseconds timescales, the transport properties of fast electrons which propagate through a solid containing significant initial temperature, and therefore resistivity, gradients is explored. Experimental measurements of sheath-accelerated protons are used to diagnose the fast electron transport, together with 1-D hydrodynamic simulations to determine the proton-induced spatial-temperature gradients created in the silicon targets. The experimental results are compared to simulations performed using a newly developed 3-D hybrid PIC code, which has been modified to explore the influence of temperature and resistivity lattice melt on fast electron transport.

7.2 Experimental arrangement

The Vulcan laser (Target Area West, TAW) is used to experimentally investigate the influence that initial temperature gradients have on fast electron transport. Utilising the dual-beam capability of TAW, two short-duration laser pulses are employed; the first beam (B8) delivered pulses of 1.055 μm wavelength in a τ_{B8} =10 ps duration (full width at half maximum, FWHM) pulse, with a maximum pulse energy (on target) of 250 J; the second laser pulse (B7), delivered 1.055 μm wavelength light in a duration of τ_{B7} = 1 ps (FWHM), with a maximum on-target energy of 60 J. For both B7 and B8, the p-polarized pulses were focused using separate f/4 off-axis parabolic mirrors, at incident angles of 13° and

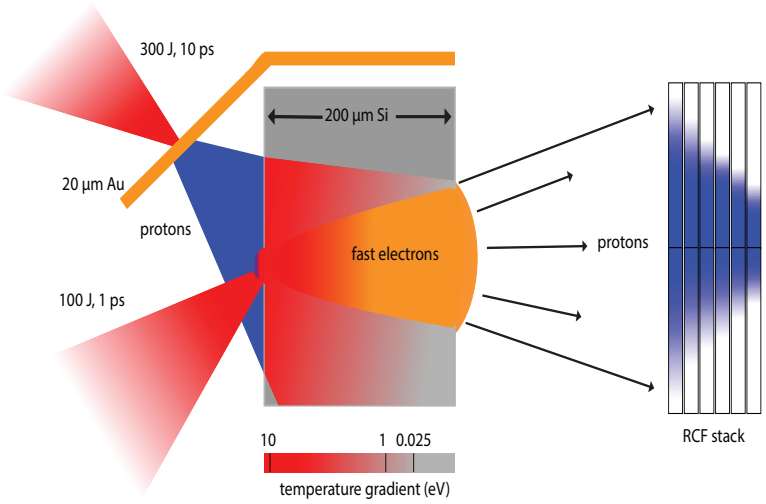

Figure 7.1: Experiment arrangement. The interaction of a 250 J, 10 ps pulse (B8) with 20 μm-thick gold targets produces a TNSA-proton beam which is incident onto 200 μm-thick silicon samples, heating the target to temperatures ranging from $\sim$ 10 eV at the front surface to $\sim$ 1 eV at greater depths. The fast electron beam is generated by the interaction of a second pulse (B7), of energy and duration equal to 60 J and 1 ps respectively, with the preheated silicon. The subsequent fast electron transport is diagnosed by measuring the spatial-dose distribution of the sheath-accelerated protons from the preheated target using a stack of RCF film.

20° respectively, with respect to target normal; B8 produced a focal spot radius of 12 μm (FWHM) while B7 was focussed to a spot radius of 8 μm (FWHM), corresponding to calculated peak intensities of $I_{B8} = 1.5 \times 10^{19}$ Wcm^{-2} and $I_{B7} = 7 \times 10^{19}$ Wcm^{-2} respectively.

Fig. 7.1, which represents a top-view schematic of the experimental setup, displays the spatial orientation of both beams (together with their respective target samples). This particular arrangement is chosen as it provides sufficient space to enable the second laser pulse (B7), which generates the fast electrons, to be incident onto the preheated silicon target without obstruction. The experiment is conducted as follows; firstly, the proton beam (which preheats the silicon target) is generated by the interaction of the B8 pulse (250 J, 10 ps) with 20 μm-thick gold targets. The resulting TNSA-proton beam propagates over a distance of 1100 μm (the longitudinal 'stand-off' distance between the laser focal position on the gold foil and the primary heated target) to the surface of the primary target,

producing a range of incident angles determined by the divergence of the protons beam; this produces an irradiated front surface area of ~ 1000 μm diameter. In this investigation, 200 μm-thick silicon, of 3×3 mm lateral dimensions, is used as the primary target which is heated by the proton beam, and through which the fast electrons propagate.

Once the proton beam arrives at the target front surface and deposited energy into the primary silicon sample, giving rise to significant heating of the target, the fast electron source is generated by the interaction of the second pulse (B7 - of respective energy and pulse duration equal to 60 J and 1 ps) with the pre-heated silicon target. Thus, the fast electrons propagate through a solid that exhibits large spatial temperature gradients, induced by the proton beam energy deposition. Moreover, heating the target to temperatures above ~ 0.15 eV gives rise to melting of the lattice, typically on timescales of tens-of-picoseconds; this represents the time for heated electrons to transfer energy, via electron-phonon coupling [40], to the target lattice.

To enable investigation of the effect of proton-induced lattice melt on fast electron propagation, the temporal separation between the arrival of the protons and the fast electron drive laser beam is varied; this is achieved by varying the time delay between the B8 and B7 pulses. The relative beam timing between B7 (fast electron source) and B8 (proton source) is characterised using a high dynamic range optical streak camera (Hammamatsu C7700), which measured the temporal separation between the B7 and B8 pulses, $\Delta\tau$, to within an error of $\Delta\tau \pm 7$ ps. By varying the temporal separation between the two beams, within the range of tens-of-picoseconds up to ~ 100 ps, the degree of induced lattice melt at different time steps can be varied.

The fast electron transport patterns inside the preheated silicon samples are diagnosed by measuring the spatial-dose distribution of the proton beam accelerated by the sheath field established at the target rear surface by the the fast electrons[37, 39**?**]; this technique was used extensively in the experimental investigations presented in Chapter 5 and 6. The 3-D electron transport inside the target produces a 2-D fast electron density profile on the target rear-surface,

which is then mapped into the sheath field. Since this sheath field ionises and accelerates protons, it's spatial profile is directly mapped into the spatial-dose distribution of the resulting proton beam profile. The proton beam profile is measured at discrete energy values, determined by the Bragg peak deposition in each layer, using a stack of dosimetry film (radiochromic film, RCF). The RCF stack is positioned 6 cm from the rear surface of the target and centred on the target normal.

7.3 Characterising the proton-induced heating profile

Before presenting the experimentally measured proton beam spatial-intensity profiles, and thus fast electron transport patterns inside the silicon targets, the proton-induced temperature gradients in the silicon sample is first characterised. Under strong heating, a solid-density sample undergoes hydrodynamic expansion, a process characterised by a decrease in density with simultaneous increase in temperature. A useful way to understand this process is by considering the confinement time, τ_C, of the sample, defined as the time over which the target density stays close to solid density; this gives an indication of the time scale over which significant hydrodynamic expansion occurs, and is approximately given by the ratio of the spatial dimension of the heated sample, L, to the ion sound speed, c_s (see Eq 2.38 - Chapter 2):

$$\tau_C \approx \frac{L}{c_s} \tag{7.1}$$

By way of example, a confinement time of $\tau_C \approx 100$ ps is achieved for a 20 μm thick target with a uniform temperature distribution of 5 eV. A method to produce such high temperatures, while maintaining the target at close to solid density, is to isochorically heat the sample; the energy which drives the sample heating is deposited on a timescale shorter than the time of confinement, and thus before significant hydrodynamic expansion occurs.

There are a number of ways to isochorically heat matter, including direct laser heating [175], electron heating [63] and x-ray heating (using x-rays generated by laser-solid interactions [176], Z-pinch machines[177] and free electron lasers [178]. However, the use of protons (i.e. ions) to isochorically heat solid-density matter offers important advantages due to key differences between the stopping power (and thus energy deposition profile) of protons, and photons, electrons and x-rays in solids. For photons (e.g. lasers - optical absorption), the deposited energy is proportional to the number of photons, and the energy is predominantly absorbed at the front (irradiated side) of the material (i.e. at the skin depth). For x-rays, the majority of the energy is absorbed at the target surface with some energy absorbed within the bulk of the target, exhibiting a gradual reduction in absorption at greater target depths (due to x-rays being absorbed or scattered by the medium). When fast electrons (or indeed, ions) propagate through matter, they lose energy along their propagation path [103] via both collisional and radiative effects (depending on their energy - see Chapter 3); the relative dose deposition decreases with thickness [104].

In distinct contrast, protons (or, more generally, ions) are not significantly influenced by scattering from the target's nuclei until the end of their propagation range; at this position the proton velocity is of a similar magnitude as the velocity of the target electrons (approximately 0.1 MeV for protons in solid aluminium). Thus, protons propagate through the target in straight lines with little scattering-induced transverse spread until the end of their propagation depth. Proton energy deposition increases with increasing penetration depth, with most of their energy deposited at the end of their range in a narrow peak known as the Bragg peak. Moreover, protons generated by ultrashort laser pulses interacting with solids typically exhibit a short, picosecond beam duration, enabling deposition of the beam energy on a time scale shorter than the hydrodynamic expansion time.

To determine the effect of proton heating on silicon targets, energy and spatially-resolved measurements of the 'heating' proton beam are made using stacks of passive dosimetry film (RCF), together with hydrodynamic simulations using the 1-D HELIOS-CR code, to characterise the spatial-temperature gradi-

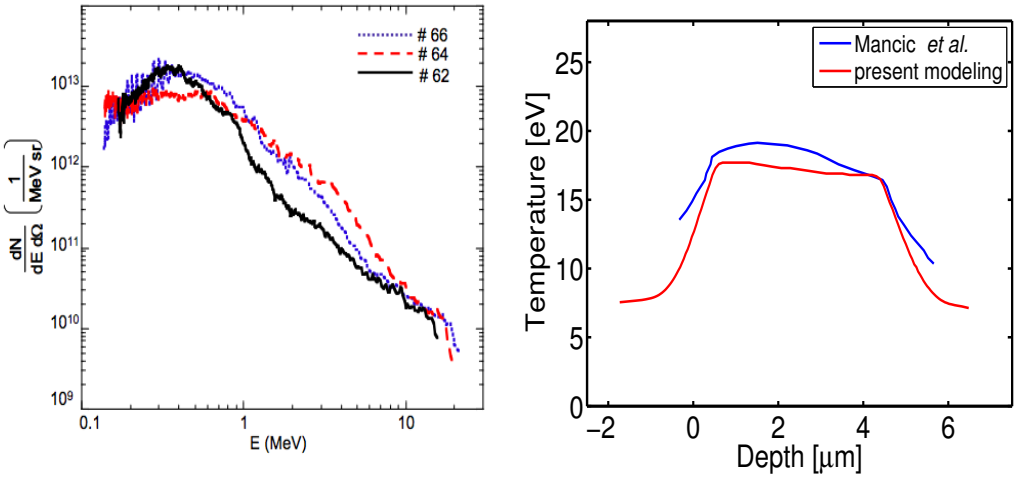

(a) Proton spectrum

(b) Heating profile calculated with HELIOS

Figure 7.2: Proton heating benchmarking calculations: (a) the experimentally measured proton spectrum is used as an input parameter into two different hydrodynamic codes; (b) spatial temperature profile of proton-heated aluminium obtained by Mancic *et al.* [179] using the 1-D hydynamic code ESTHER; (c) corresponding simulation result of the temperature profile obtained using the 1-D hydrodynamic code HELIOS.

ents induced by proton energy deposition.

To test the validity of this approach, the methodology is benchmarked against previous investigations of isochoric proton heating of solids. Firstly, the work reported by Mancic *et al.*[179] is used, in which both experimental and numerical characterisation of proton-heated aluminium is performed. In the work by Mancic *et al.*, energy and spatial measurements of laser-accelerated protons are made (using a Thomson Parabola spectrometer in conjunction with RCF stacks), and used as an input parameter in a 1-D hydrodynamic code to calculate the temperature profile induced in 5 μm aluminium targets by the laser-generated proton beam. Their results are displayed in Fig. 7.2 (a - b), showing the proton beam spectrum and corresponding temperature and density profiles respectively.

Mancic *et al.* use the 1-D hydrodynamic code ESTHER [181], together with the Bushman-Lomonosov-Fortov (BLF) multi-phase equation of state (EOS) [182], while our method inputs the proton spectrum from Fig. 7.2(a) into the 1-D hydrodynamic code HELIOS-CR[51], together with the PROPACEOS EOS model [51]. Comparing Fig. 7.2 (b) and (c), good agreements is observed be-

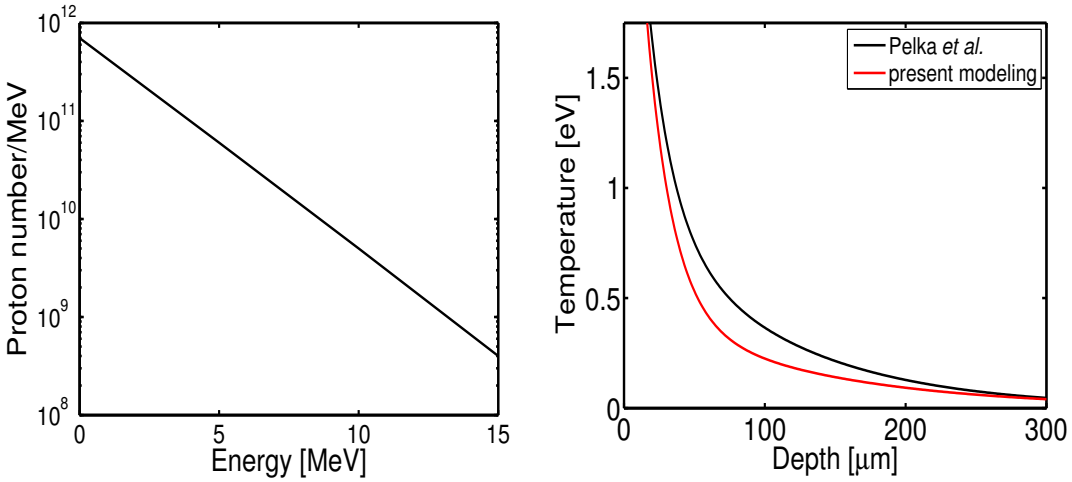

(a) (b)

Figure 7.3: Proton heating benchmarking calculations: (a) fit to an experimentally measured proton spectrum; (b) spatial-temperature profile of proton-heated carbon obtained by Pelka *et al* [180] using MULTI (red line), shown alongside the profile calculated using HELIOS (black line).

tween the two calculations. In the Mancic *et al.* work, a peak target temperature of around 18 eV is obtained, with a gradual decrease in temperature with increasing target depth (see Fig. 7.2 (b)). Using our method, a peak temperature of $\sim$ 17 eV is obtained, with a spatial-temperature profile similar to that calculated by Mancic *et al* (see Fig. 7.2 (c)). Overall, there is excellent agreement between the two methods (i.e. ESTHER with BLF EOS and HELIOS with PROPACEOS EOS).

Next, a similar benchmarking calculation is performed by comparing our methodology with results reported by Pelka *et al.*[180] in which TNSA-protons, produced by the interaction of a 1 ps, 60 J laser pulse (corresponding to peak laser intensity $\sim 7\times10^{19}$ Wcm^{-2}) with a 20 μm gold foil, heat several hundred-micron-thick carbon samples. The induced temperature profile is characterised by performing measurements of the heating proton beam using a stack of RCF film (the resulting proton spectrum is displayed in Fig. 7.3 (a)), together with the radiation-hydrodynamic code MULTI [183] and SESAME equation of state [159] tables for carbon.

The resulting temperature profile is shown in Fig. 7.3 (b) for each case: using

the experimentally measured proton spectrum input with MULTI (i.e. Pelka *et al.* - red line) and HELIOS (our approach - black line). Good agreement is found; both exhibit a similar exponential spatial-temperature profile, with temperatures of ~ 2 eV and ~ 0.2 eV achieved at depths of ~ 10 μm and 100 μm respectively. Despite the different hydrodynamic simulations codes used (i.e. MULTI and HELIOS respectively), in addition to the different equations of state used in each simulation (i.e. SESAME and PROPACEOS respectively), which may account for the discrepancy between the spatial profiles at depths in the range 50 - 200 μm, the overall agreement between the results is excellent.

7.3.1 Proton heating of silicon

Having demonstrated the relative accuracy of the methodology, hydrodynamic simulations of proton-heated silicon targets are now presented. The proton source properties, generated by the interaction of a $\tau_L = 10$ ps and $E_L = 250$ J laser pulse with 20 μm gold targets, are determined using measurements of the spatial-dose profile of the resulting TNSA-proton beam; an example proton beam spatial profile is shown in Fig. 7.4 at selected proton energies (i.e. at different layers in the stack).

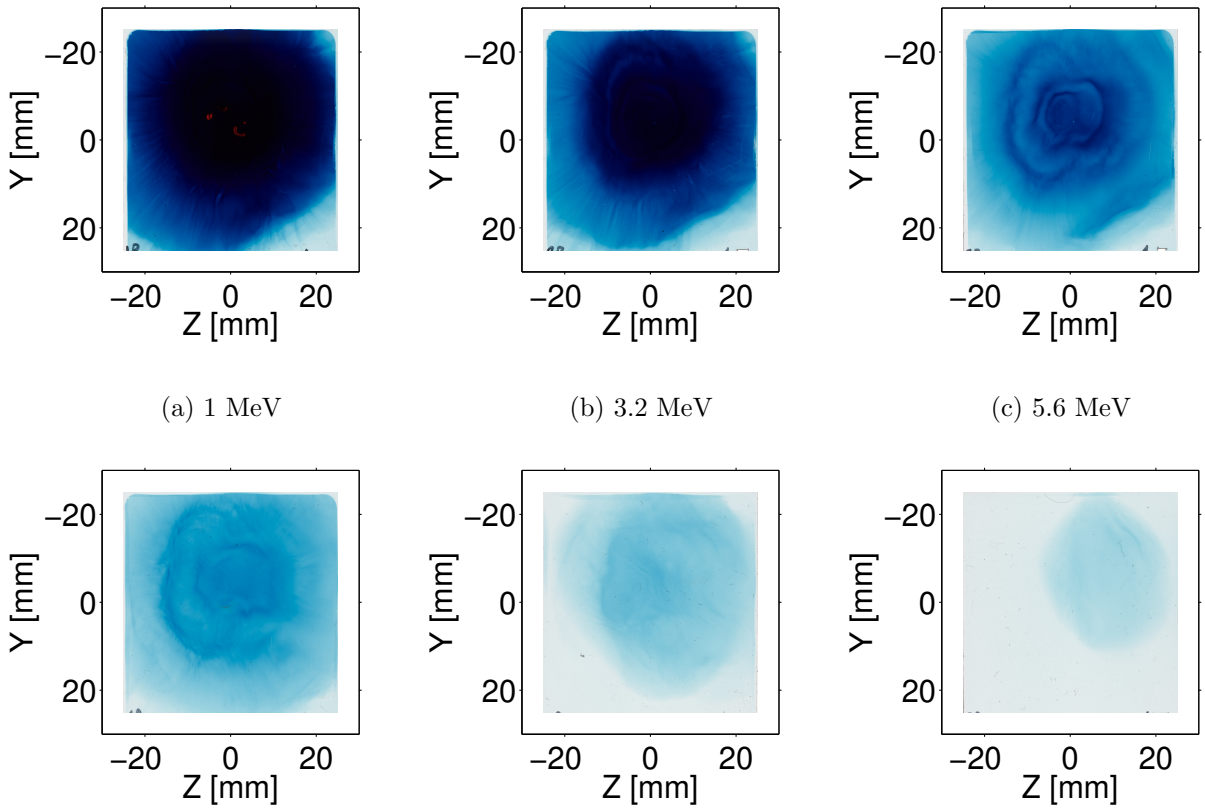

(a) 1 MeV (b) 3.2 MeV (c) 5.6 MeV

(d) 8.2 MeV (e) 10.8 MeV (f) 13 MeV

Figure 7.4: Example experimentally measured proton beam used to heat the silicon samples. The spatial-dose profile is displayed as a function of beam energy i.e. at different layers within the RCF stack.

The resulting proton spectrum is displayed in Fig. 7.5 (a), alongside the beam divergence half-angle in Fig. 7.5(b); error bars correspond to statistical variations over a series of shots (in this case four), with an on-target energy of 250 ± 15 J.

In these simulations, the silicon target grid is divided into 100 cells, with a total simulation run-time of 1.5 ns, in 0.5 ps output steps. The simulations include the effect of amplified spontaneous emission (ASE); measurements made on the Vulcan laser indicate that the level of amplified spontaneous emission (ASE) is of the order of 10^{10} Wcm^{-2} at 0.1 - 1 ns and 10^{11} Wcm^{-2} at 50 - 100 ps prior the arrival of the main B7 pulse[119], and thus we incorporate this laser profile into the simulation setup. The protons are initiated in the simulation after 1.2 ns of ASE laser heating (i.e. at a time step of 1.2 ns).

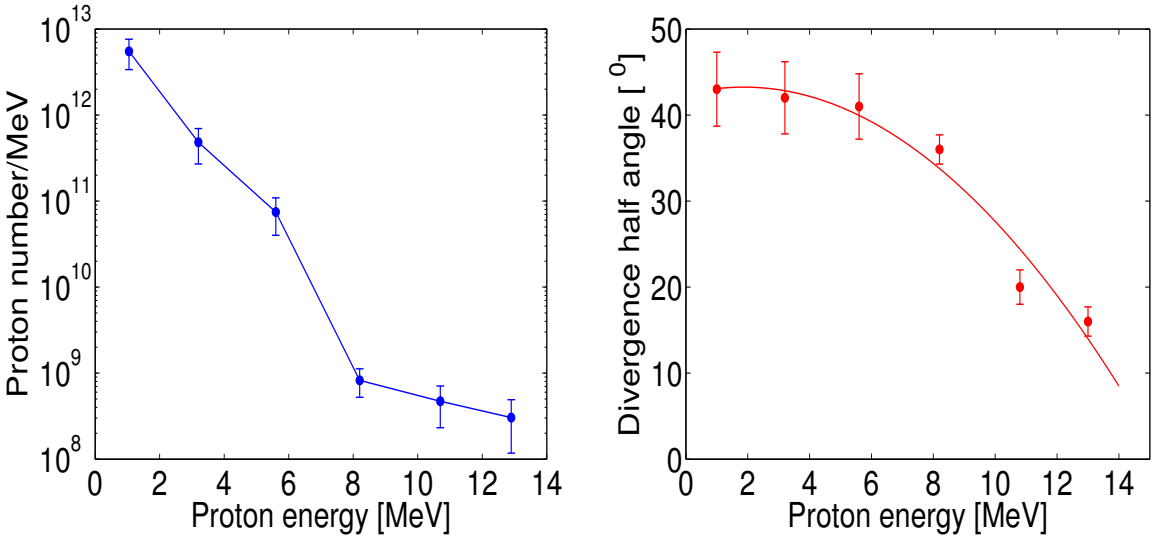

(a) Proton spectrum

(b) Beam divergence half-angle

Figure 7.5: Experimentally measured properties of the heating proton beam: (a) proton spectrum; and (b) beam divergence half-angle; error bars correspond to statistical variations over four shots.

At each simulation time step the proton energy and corresponding proton flux (calculated from the experimentally measured proton spectrum and divergence half angle displayed in Fig. 7.5) is included as an input parameter into HELIOS. In these simulations, the lowest and highest proton energies used are 1 MeV and 13 MeV respectively (see Fig. 7.5 (a)). As assumed in previous studies [179, 180], the relative contribution of X-rays and fast electrons (produced by the interaction of B8 with the secondary target (i.e. 20 μm-thick gold)) to the front surface and bulk heating of the primary target is not significant. Rather, it is assumed that proton-induced heating, due to the energy deposition profile (i.e. Bragg peak) and relatively high directionality (over the 'standoff' distance 1100 μm) of the proton beam, is the dominant heating mechanism. The proton beam exhibits a high flux of low energy (1 - 5 MeV - Fig. 7.4 (a - c)) protons, which is a direct consequence of the beam pulse parameters (i.e. energy and pulse duration of 250 J and 10 ps respectively). These were selected to specifically tailor the lower energy region of the proton spectrum since lower energy protons (i.e. 1 - 5 MeV) contribute most to heating of a 200 μm-thick silicon target, due to their stopping depth being less than or of the order of the target thickness (see Fig. 7.6 (b)).

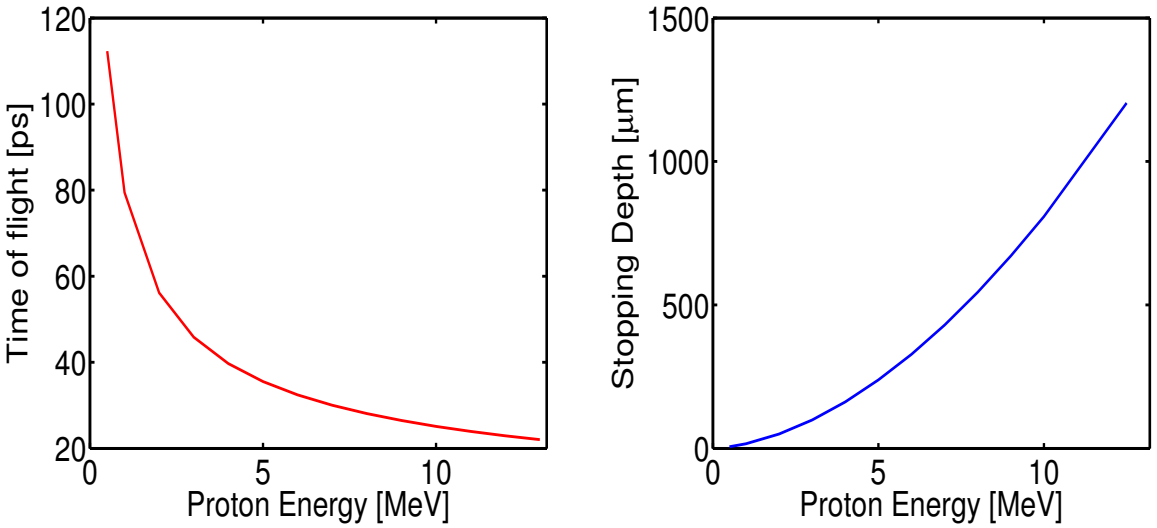

(a) Time-of-flight (b) Stopping depth

Figure 7.6: Calculations of: (a) proton time-of-flight over a propagation distance of 1100 μm; and (b) proton stopping depth calculations in silicon using the PSTAR program.

The proton stopping power is calculated from collisional stopping powers, evaluated using Bethe's stopping-power formula [103], implemented within the hydrodynamic code [51]; this calculation is similar to that used in the PSTAR program [102] - the PSTAR program was used to calculate the example proton stopping depth in silicon, displayed in Fig. 7.6 (b).

To accurately model the experimental configuration, the simulations account for the 1100 μm longitudinal separation between the proton source and target sample (shown in Fig. 7.1) by calculating the time of flight for each proton energy (shown in Fig. 7.6 (a)). The time of flight gives the temporal off-set for each proton energy. For example, protons of energy 1 MeV and 13 MeV arrive at the secondary target after approximately 100 ps and 20 ps respectively (corresponding to simulation time steps of 1.3 ns and 1.22 ns respectively), giving the proton beam temporal spread of $\sim$ 80 ps. Thus, for HELIOS simulations starting at $t = 0$ ps, initial heating of the material will begin after $\sim$ 20 ps (i.e. the time at which the fastest electrons arrive at the target), with the total proton beam energy deposited, and thus peak temperature achieved, 100 ps after the initialisation of the protons in the simulation.

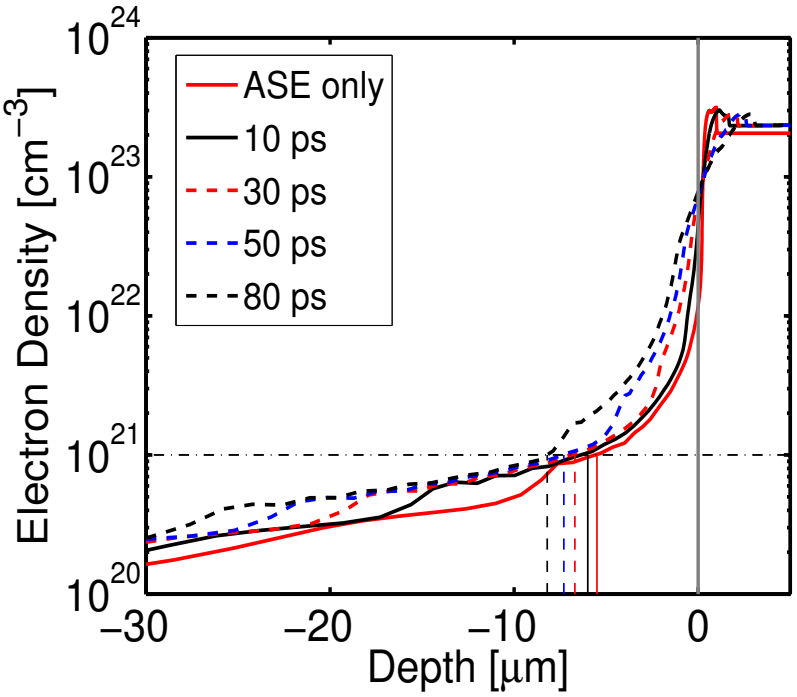

Figure 7.7: 1-D HELIOS hydrodynamic simulation results. Electron density profiles at the front surface of the silicon target at given simulation times, driven by the B7 laser ASE in conjunction with the proton heating driven by B8. The critical density surface for each time step is highlighted by the short vertical lines − the grey vertical and black horizontal lines correspond to the location of the original target surface and critical density respectively.

To demonstrate that the electron source (i.e. the front surface of the silicon target) remains largely unperturbed during proton heating, simulation results of the electron density profiles, which correspond to front surface plasma expansion, at various simulation time steps are presented. The expansion profiles, at given simulation times of 1.2 ns (ASE-only), 1.22 ns, 1.25 ns, 1.27 ns and 1.3 ns, corresponding to proton heating times, t_{heat}, of 0 ps, 10 ps, 30 ps, 50 ps an 80 ps respectively, are displayed in Fig. 7.7. For simulations including ASE-only (Fig. 7.7 - solid red curve), the main action of the ASE is to generate a low-density pre-plasma region at the target front surface, in addition to driving a shock wave into the overdense target (giving rise to compression of the first few micron depth of the target by ~ 10 %); this density profile is common to all shots (i.e. with and without proton heating).

Once protons are initiated in the simulation and arrive at the target (with the

highest energy protons reaching the target after 20 ps), the protons act to induce a relatively small enhancement of the front-side pre-plasma expansion profile, an effect which increases with time, from $t_{heat} = 10$ ps to $t_{heat} = 80$ ps. This results in a slightly longer plasma scale length, compared to the case of ASE-only heating. However, it is important to emphasise that the resulting density perturbation is only of the order of a few microns. To demonstrate this, the spatial position of the critical density surface (i.e. the location of the fast electron source) is displayed in Fig. 7.7 for each time step (i.e. t_{heat}) by the short vertical lines (with colour and line-style representative of each time step − the grey vertical and black horizontal lines correspond to the location of the original target surface and critical density respectively). It is found that over the maximum duration of proton heating explored (i.e. $t_{heat} = 80$ ps), the critical surface (and thus electron source) extends by ~ 2.5 μm, while for $t_{heat} = 30$ ps the critical surface extends by only ~ 1 μm, an expansion which is not expected to significantly influence the subsequent fast electron transport properties. Furthermore, Fig. 7.7 also reveals that, excluding the density perturbation in the first few μm of the target, the bulk target remains at solid density, thus highlighting the isochoric properties of proton heating.

The temporal heating profile of silicon is displayed in Fig. 7.8 at selected proton heating time-steps, t_{heat}, of 10 ps, 30 ps, 50 ps and 80 ps after the arrival of the most energetic (13 MeV) protons. It is clearly evident that the sample is significantly heated under the action of the protons, transitioning from room temperature (~ 0.025 eV) to temperatures of 1 - 10 eV (i.e. 'warm dense' temperatures [**?**]). For example, a time separation of $\Delta t_{7\rightarrow 8} = 30$ ps between B7 and B8 corresponds to a proton heating time of $t_{heat} = 10$ ps by the highest energy protons (10 - 13 MeV) − these protons are not stopped entirely within the target as their Bragg peak, and thus stopping depth, is much greater (~ 1200 μm) than the thickness of the sample (i.e. 200 μm − see Fig. 7.6). However, due to collisions with the target electrons, these protons do deposit some energy, giving rise to the relatively weak temperature increase for $t_{heat} = 10$ ps (i.e. the dotted black line in Fig. 7.8). For $t_{heat} = 30$ ps (solid black line in Fig. 7.8), the lower

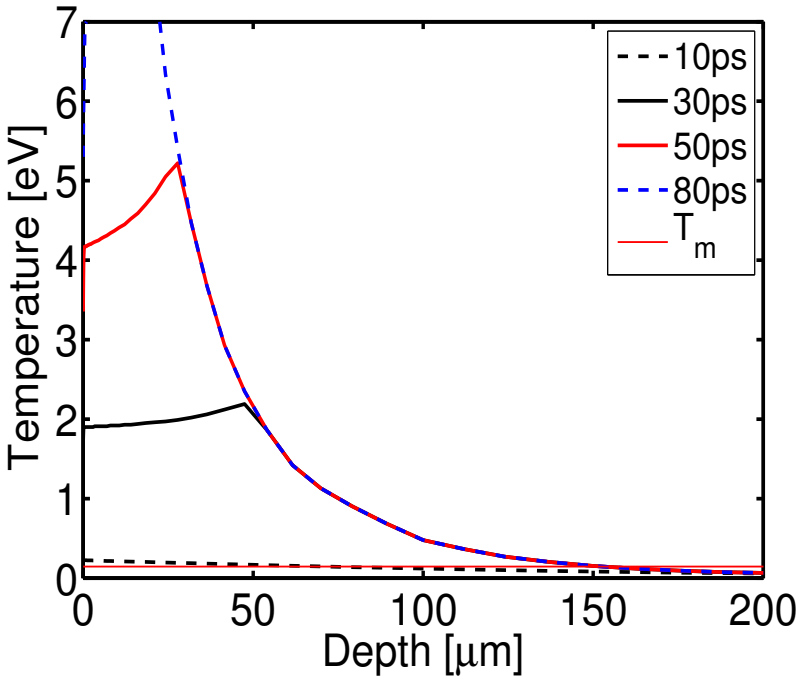

Figure 7.8: 1-D HELIOS hydrodynamic simulation results. Target temperature spatial profiles in the bulk of the target at given proton heating times of 10 ps, 30 ps, 50 ps and 80 ps. Also shown is the melting temperature of silicon (thin solid red line).

energy protons (3 - 7 MeV) will have arrived at the target and deposited their energy, resulting in the sharp rise in temperature to $\sim$ 2 eV at depths between 0 - 50 μm, reducing to $\sim$ 0.5 eV at 100 μm depth. Heating for longer times (i.e. t_{heat} = 50 ps - solid red line in Fig. 7.8, and t_{heat} = 80 ps - dashed blue line in Fig. 7.8) results in strong target heating to temperatures $\sim$ 7 eV in the first 20 μm of the target and an exponentially decreasing temperature profile, to around 0.5 eV at 100 μm depth. For the case of t_{heat} = 80 ps, all of the protons will have arrived at the target and deposited their energy. In particular, the low energy protons, due to their higher flux and shorter stopping depth, give rise to the observed increase in temperature. Note that the y-axis of Fig. 7.8 is truncated to a temperature of $\sim$ 7 eV. Since the lower cut-off energy of the proton detector (i.e. RCF stacks) is 1 MeV, the contribution of $<$ 1 MeV protons (which will act to heat the target to higher temperatures in the first few microns) is not included in the heating calculations.

Crucially, the proton heating investigated in these simulations occurs on

timescales of 30 - 80 ps; significant lattice heating, and thus lattice-melt, is predicted to occur for heating durations of the order of tens of picoseconds [40]. Thus, for these time steps, a wide range of spatial-temperature (and thus lattice-melt) profiles, at different $\Delta t_{7\rightarrow 8}$, will be produced by proton heating. As demonstrated in Chapter 6, resistively generated magnetic fields depend strongly on spatial resistivity gradients which effect the propagation of fast electrons. Thus, proton-induced temperature (and thereby resistivity) gradients would be expected to significantly influence fast electron transport properties. Proton emission results of electron transport in proton-preheated silicon are now presented.

7.4 Experimental results

The experimentally measured proton beam spatial-intensity distributions shown in Fig. 7.9 represent protons accelerated from the primary (i.e. proton heated) silicon target at different t_{heat}, thus enabling investigation of the effect of lattice-melt (i.e. resistivity gradients) on electron transport.

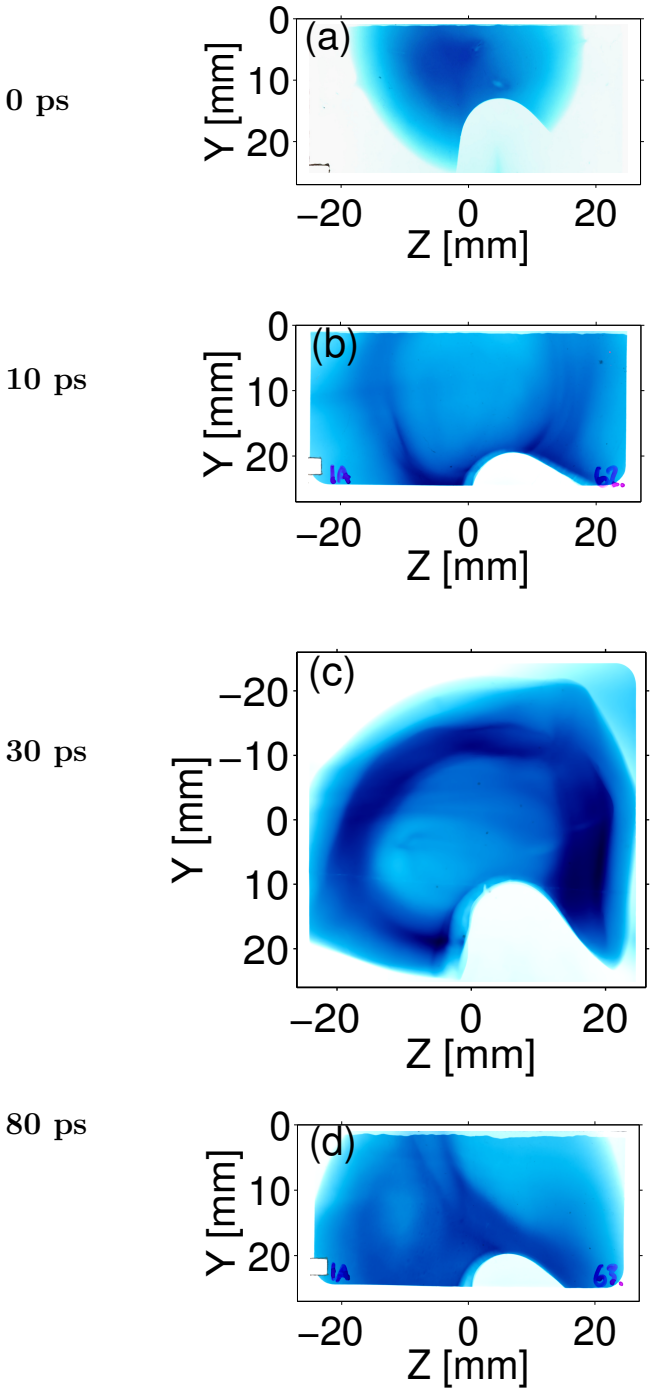

Figure 7.9: Example measured proton spatial-dose distributions at 3.3 MeV for peak laser intensity equal to 7×10^{19} Wcm^{-2}, for proton heating times of (a) 0 ps - unheated (b) 10 ps (c) 30 ps and (d) 80 ps.

The proton emission measurements shown in Fig. 7.9 correspond to an energy of 3.3 MeV; this proton energy was selected such that the proton dose for each time step was similar, enabling a more representative comparison to be made

between the results. The measurements in Fig. 7.9 (a - d) represent $\Delta t_{7\rightarrow 8}$ of 0 ps, 30 ps, 50 ps and 100 ps, corresponding to t_{heat} of 0 ps (i.e. unheated), 10 ps, 30 ps and 80 ps respectively. Initially, for unheated silicon (Fig. 7.9 (a)) the proton beam exhibits a smooth, homogenous spatial distribution, in agreement with the results presented in both Chapter 5 and Chapter 6, where such proton beam spatial-dose profiles were attributed to uniform electron transport at a laser-drive intensity of $\sim 7 \times 10^{19}$ Wcm^{-2}. However, as the target is pre-heated by the TNSA-proton beam, distinct changes in the proton spatial-intensity distribution occur (which are directly correlated to changes in the fast electron transport inside the target). After $t_{heat} = 10$ ps (Fig. 7.9 (b), representing heating by the most energetic protons (i.e. 13 MeV)) there is evidence of the onset of an annular structure in an otherwise smooth beam profile. Preheating for $t_{heat} = 30$ ps (Fig. 7.9 (c)), at which point the majority of the 3 - 8 MeV protons will have heated the target, results in the observation of a distinct ring profile in the proton spatial-intensity distribution. Preheating the target for $t_{heat} = 80$ ps (Fig. 7.9 (d)) gives rise to caustic structures in the proton beam spatial-intensity profile, indicative of the onset of fast electron beam filamentation (see Chapter 5).

The key finding of these measurements is that annular proton beam spatial-intensity profiles are obtained for $t_{heat} = 30$ ps, while filamentation occurs at $t_{heat} = 80$ ps. As discussed in detail in Chapter 6, annular proton beams measured from thick (i.e. 200 μm) silicon targets are primarily driven by annular fast electron transport within the target which, in turn, is generated by strong, resistively generated magnetic fields. Thus, the proton emission measurements displayed in Fig. 7.9 (a - d) present strong evidence that proton-heating induces spatial and temporal changes in the target resistivity, which subsequently drive magnetic field generation within the silicon targets. As previously demonstrated in Chapter 6, these resistive magnetic fields are generated by spatial variation of resistivity gradients as a consequence of target heating. Therefore, to explain the effect of proton-induced temperature (and thereby resistivity) gradients, we now perform hybrid-PIC simulations of fast electron transport in a preheated solid.

7.5 Modelling - 3D-hybrid PIC simulations

Simulating fast electron transport in an isochorically preheated solid is a particularly challenging problem. To enable this capability, the particle-based 3D-hybrid code ZEPHYROS [23, 167], as used in Chapter 5 and 6, is developed to investigate fast electron transport under temperature-gradient conditions. The code modification, made by Dr A. P. L. Robinson, enables simulation of the influence of lattice melt on fast electron transport. This is performed by incorporating a transition between two different resistivity-temperature profiles across the target grid, executed by prescribing multiple resistivity curves, each corresponding to a different degree of lattice structure (produced by proton-induced lattice melt), throughout the target simulation box. Therefore, resistivity-temperature profiles corresponding to disordered and ordered silicon are used, including an interpolation between them. As demonstrated in Chapter 5, the resistivity-temperature profile of a disordered solid is distinctly different from the ordered lattice case of the same element, due to the influence of the lattice structure on the electron mean free path, and thus resistivity.

Firstly, the silicon resistivity-temperature profile that was presented in Chapter 6 is utilised. Hybrid-PIC simulations performed with this profile, calculated using QMD simulations combined with the Kubo-Greenwood equation [85, 91, 92], correlated well with the experimental observation of annular electron transport, subsequently explained by the generation of a hollowing magnetic field component by a dip in the resistivity at a few eV. This curve was modelled by simulating the silicon ionic configurations at 300 K, and thus represents a well ordered lattice structure (i.e. diamond face-centred-cubic structure). Next, the resistivity profile for 'disordered' silicon is calculated using the same QMD Kubo-Greenwood approach as was performed to obtain the 'ordered' silicon resistivity profile. Crucially, however, the configurations are now simulated at 4 eV (i.e. $\sim$46,000 K) which corresponds to disordered silicon; the high temperature of the silicon ions, which is considerably greater than the melting temperature of silicon (0.145 eV), gives rise to amorphous, 'glassy'-like silicon. Both the ordered (red

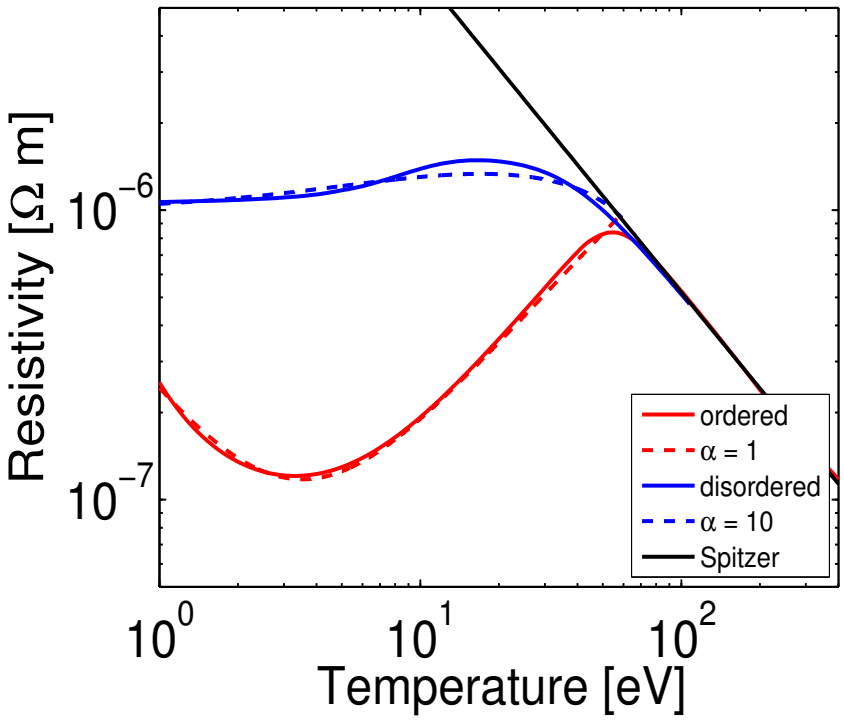

Figure 7.10: Calculations of the resistivity-temperature profile of silicon for different lattice structures. Ordered silicon (solid red line) is plotted alongside disordered silicon (solid blue line), together with numerical fits to the low temperature region of each resistivity profile (dotted red line and dotted blue line for the ordered and disordered models respectively). The curves converge to the Spitzer resistivity profile (solid black line) at temperatures greater than 60 eV

curve) and disordered (blue curve) resistivity-temperature profiles are shown in Fig. 7.10. Alongside these profiles, numerical fits to the low temperature (i.e. 1 - 60 eV) region of each curve (dotted red curve - ordered; dotted blue curve - disordered) are plotted.

A model equation is formulated which scales the resistivity between the ordered and disordered curves for an appropriate choice of 'lattice order' parameter α, and has the following form:

$$\eta(T) = \beta \frac{\Gamma(T)}{\Omega(T)} \tag{7.2}$$

where η is the resistivity, $\beta = 0.11$ and T is the temperature in eV. The functions

Γ(T) and Ω(T) are given by:

$$\Gamma(T) = (C_1\alpha^3T^3) - (C_2\alpha^5T^3) - (C_3\alpha^4T^4) - (C_4\alpha^6T^2) + (C_5\alpha^6T) + (C_6\alpha^9) + C_7 \tag{7.3}$$

$$\Omega(T) = (C_8\alpha^3T^2) + (C_9\alpha^6T) + (C_{10}\alpha^8) \tag{7.4}$$

where $C_1 = 1.2 \times 10^{-7}$, $C_2 = 1.1 \times 10^{-9}$, $C_3 = 1.2 \times 10^{-10}$, $C_4 = 1 \times 10^{-9}$, $C_5 = 1.33 \times 10^{-6}$, $C_6 = 9 \times 10^{-9}$, $C_7 = 4 \times 10^{-7}$, $C_8 = 0.75$, $C_9 = 8 \times 10^{-2}$ and $C_{10} = 1 \times 10^{-2}$.

These model equations are cast in this form such that the prescription of the lattice order parameter, α, varies the resistivity curve between the ordered and disordered profiles. To show the effect of changing this α-value, Fig. 7.11 displays the resistivity curves that arise upon varying α between 1 (ordered) and 10 (disordered).

Throughout the simulation grid, a desired resistivity curve is allocated to each cell (i.e. grid point) and calculated in the following way: initially, the low temperature region of the resistivity-temperature profile (in the range 1 - 60 eV) is calculated using the desired α-value and incorporated within a 3-D matrix that corresponds to an α-value at each each simulation grid point - this matrix is then included as an input parameter into ZEPHYROS; for temperatures greater than 60 eV, the resistivity profile follows the Spitzer model.

The majority of the simulation parameters are the same as those used in the simulations performed in Chapter 6, briefly restated for clarity. A 200 μm $\times$ 400 μm $\times$ 400 μm simulation grid, with a cell resolution of ΔX = ΔY = ΔZ = 1 μm is used, and the electron population is injected at [X, Y, Z] = [0, 0, 0]. The laser-to-fast electron energy conversion factor is set to 0.3, with a laser pulse duration of 1 ps, wavelength equal to 1 μm and focal spot radius $r_L = 8$ μm. In addition, the peak laser intensity is equal to $I_L = 7 \times 10^{19}$ Wcm^{-2}. The electrons propagate in the X-direction with an exponential energy distribution, with mean temperature T_f given by ponderomotive scaling [65]. The electrons are injected

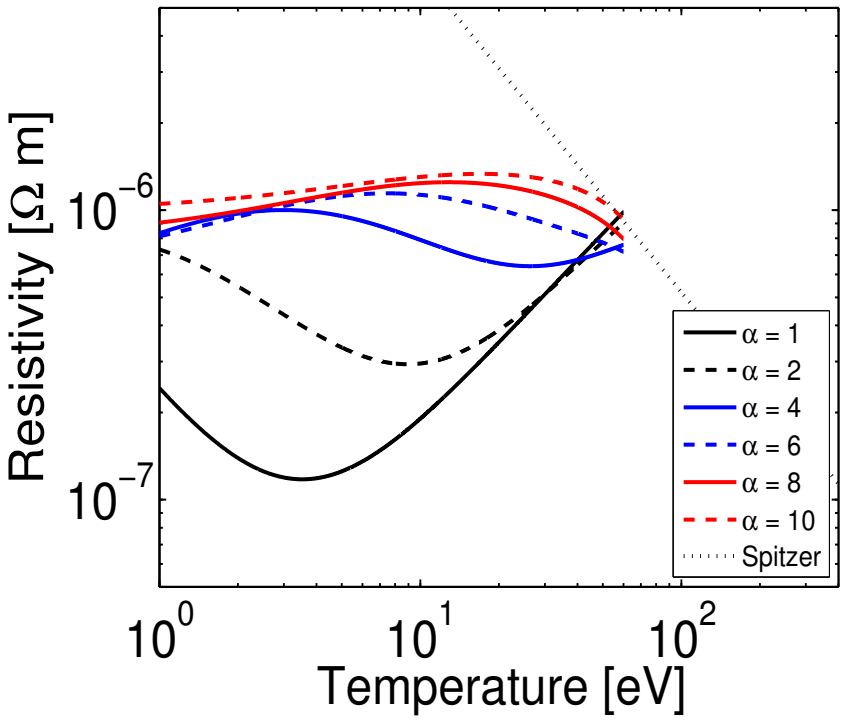

Figure 7.11: Resistivity-temperature profiles calculated using various α-parameter values; $\alpha = 1$ corresponds to ordered silicon (solid black line) while $\alpha = 10$ corresponds to disordered silicon (dotted red line); the Spitzer resistivity profile is also displayed (broken black line).

with a uniform angular distribution over a cone subtended by a half-angle of 50° [137] and in all cases the initial target temperature is set equal to 1 eV.

Initial benchmarking tests demonstrated that prescribing each cell in the simulation box with an α-parameter value of one (corresponding to ordered silicon) and ten (corresponding to disordered silicon) exactly reproduced simulation results performed by incorporating the resistivity curves separately, as done in the previous version of the code used in Chapter 5 and 6. Importantly, for simulations corresponding to pre-heated silicon, an α-parameter value is assigned using the spatial temperature profile calculated from the HELIOS simulations of proton-heated silicon (Fig. 7.8). The 1-D spatial profile obtained from the hydrodynamic simulations is incorporated into the 3-D α-parameter matrix and included as an initial input parameter. Fig. 7.12 (a) and (b) displays the [X,Y] mid-plane profile and axial line-out of the α-parameter values used in the simulation, respectively. Physically, this represents proton-induced lattice disordering (i.e. $\alpha = 10$) over

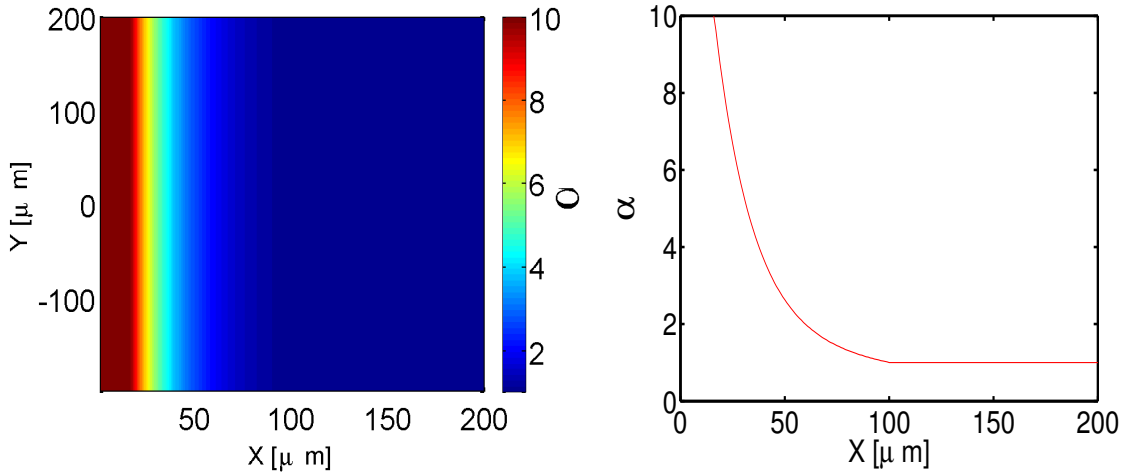

Figure 7.12: α-parameter value (calculated using the HELIOS temperature profile from Fig. 7.8) used for the proton-preheated Zephyros simulations: (a) [X,Y] mid-plane plot; and (b) axial lineout of the α-parameter.

the first 20 μm of the target, with an exponentially decreasing gradient (corresponding to an increase in lattice order) until a depth of 100 μm, at which point the target lattice is well-ordered (i.e. $\alpha = 1$).

Simulation results corresponding to two example cases are shown in Fig. 7.13(a - d). For the case of a non-graded, uniform target resistivity profile (corresponding to no proton pre-heating), Fig. 7.13(c - d) displays the fast electron density in the [X-Y] mid-plane and rear surface [Y-Z] plane respectively, while the case of a proton-induced temperature-gradient profile, using the spatial α-parameter distribution from Fig. 7.12, is displayed in Fig. 7.13(a - b) for the [X-Y] mid-plane and rear surface [Y-Z] plane fast electron density profiles respectively. In both cases, the simulation time is equal to 1.4 ps. Importantly, the only difference between these simulations is the inclusion of a temperature, and thus resistivity, gradient in the simulations shown in Fig. 7.13(a - b); all other parameters are the same for both simulations.

The results demonstrate key differences in the fast electron propagation properties between uniform silicon (i.e. 'cold-start' – no proton heating) and proton pre-heated silicon (i.e. including longitudinal temperature, and thus resistivity, gradients – Fig. 7.12). For the case of ordered silicon (Fig. 7.13(c - d)), the fast

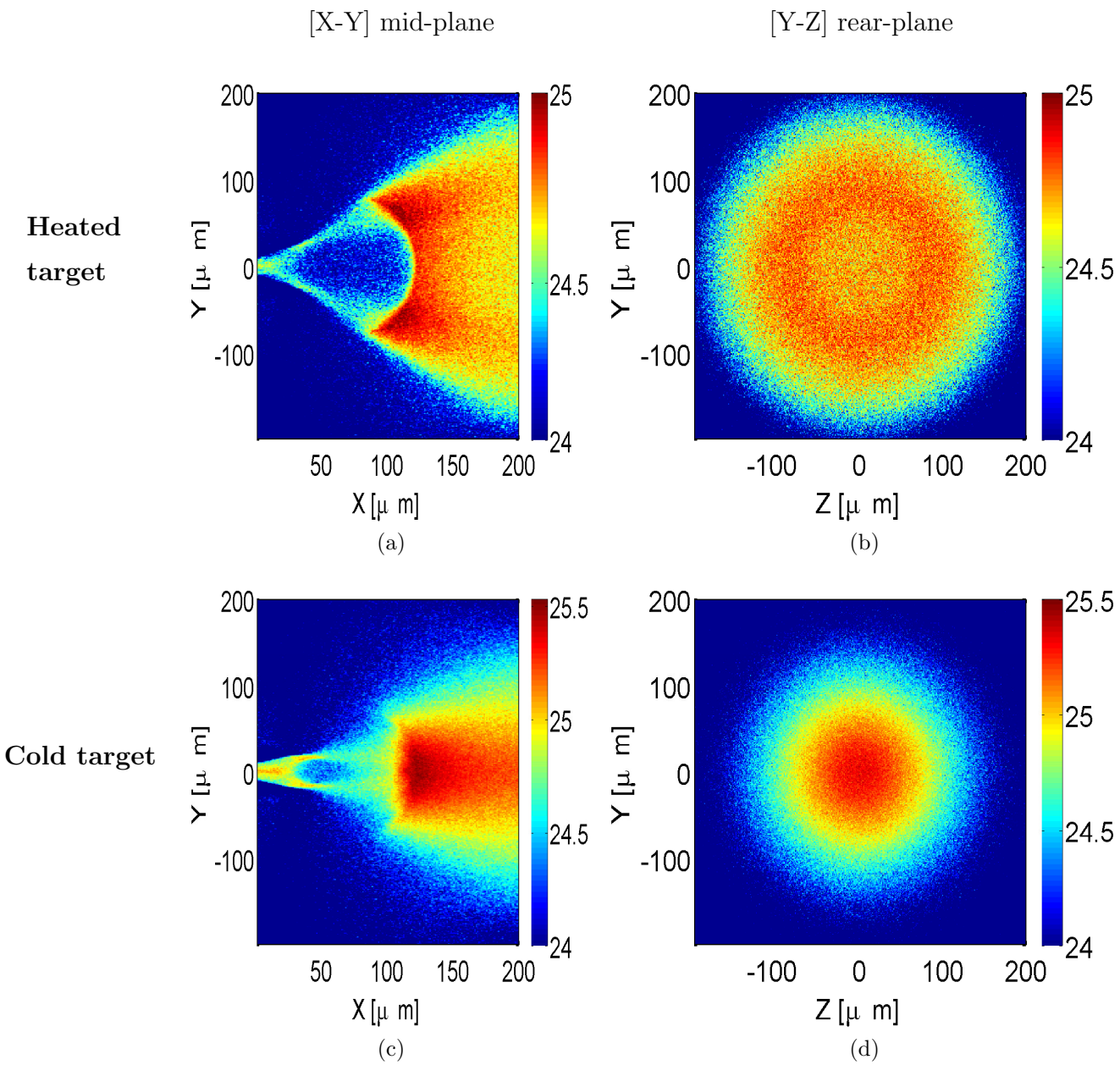

Figure 7.13: 3D Hybrid-PIC simulation results showing $\log_{10}$ fast electron density maps (m^{-3}) in the [X-Y] mid-plane and rear surface [Y-Z] plane, 1.4 ps after laser irradiation: (a - b) 'heated' target (i.e. containing temperature gradients); (c - d) 'cold' target (i.e. ordered silicon); all for peak intensity equal to 7×10^{19} Wcm^{-2}.

electron transport pattern is relatively homogenous at the target rear-surface, in agreement with previous results (see Chapter 6).

In distinct contrast, the fast electron transport pattern obtained for a silicon target containing initial proton-induced temperature (and therefore resistivity) gradients (Fig. 7.13(a - b)) is significantly different to the transport properties arising from transport in ordered (i.e. initially 'cold') silicon (Fig. 7.13(c - d)). For the 'heated' case, the fast electron beam divergence is approximately 30% larger than that of the 'cold' case (i.e. containing no longitudinal temperature gradients), and a ring-like structure emerges in the fast electron beam, which propagates to the target rear-surface (see Fig. 7.13(b)). As described in Chapter 6, an annular fast electron spatial-density profile at the target rear-surface results in an annular proton beam spatial-intensity profile. Thus, the annulus observed in the simulation of fast electron transport in silicon containing an initial longitudinal temperature gradient (Fig. 7.13(b)) is in qualitative agreement with the experimental result displayed in Fig. 7.9(c).

Interestingly, the mechanism inducing annular transport in the 'heated' case is distinctly different to the mechanism governing annular transport in ordered, uniform silicon at higher laser intensities (i.e. $I_L = 5 \times 10^{20}$ Wcm^{-2} - see Chapter 6), in which beam hollowing originated from a dip in the resistivity-temperature profile (at temperatures of a few eV). This subsequently led to a reversal in the resistivity gradient near the edges of the fast electron beam, which in turn generates a hollowing magnetic field component which seeds an annular electron beam structure. For that case, the depth at which hollowing was seeded was of the order of 50 μm. However, for the 'heated' case explored here (i.e. longitudinal proton-induced resistivity gradients) the onset of beam hollowing occurs at shallower depths of around ~ 20 μm (see Fig. 7.13(a)).

To explore the origin of this beam hollowing in more detail, Fig. 7.14 shows simulation results of the 2-D magnetic field and resistivity profiles (in the [X-Y] mid-plane) which correspond to the fast electron density results shown in Fig. 7.13(a) and (c) respectively. The results are understood within the framework

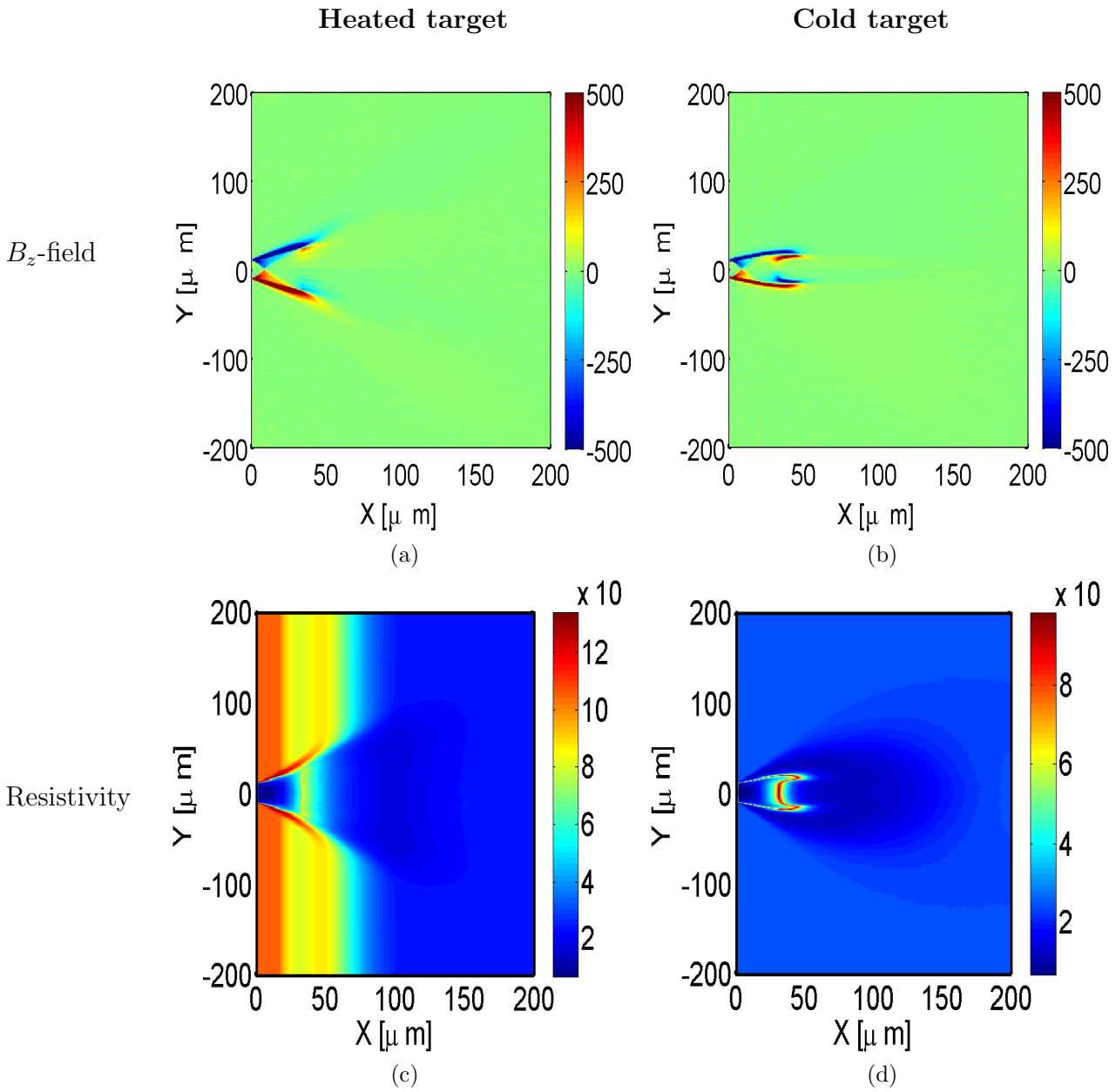

Figure 7.14: 3D Hybrid-PIC simulation results (outputs all at an example simulation time equal to 1.4 ps after the start of the laser pulse): (a - b) [X-Y] mid-plane 2-D map of magnetic flux density (B_Z component in Tesla) for the cases of proton heated and cold silicon respectively; (c - d) [X-Y] mid-plane 2-D map of resistivity, η, (in units of 10^{-7} Ωm) for the proton heated and cold cases respectively.

of the resistively generated magnetic field, $\mathbf{B}$, given by:

$$\frac{\partial \mathbf{B}}{\partial t} = \eta \nabla \times \mathbf{j}_f + \nabla \eta \times \mathbf{j}_f \tag{7.5}$$

The magnetic field is principally generated by two components; the first ($\eta \nabla \times \mathbf{j}_f$) pinches the electrons into regions of highest current density, while the second ($\nabla \eta \times \mathbf{j}_f$) seeds magnetic field growth from regions containing resistivity gradients, subsequently driving electrons into regions of highest resistivity.

Examining the uniform (i.e. 'cold') silicon case first (Figs. 7.14(b) and (d)), it is observed that the global fast electron transport properties are dominated by a collimating azimuthal magnetic field which acts to 'pinch' the fast electron beam up to depths of X = 50 μm (Fig. 7.14(b)). While the onset of beam hollowing occurs at depths of $\sim$ 50 μm into the target (Fig. 7.13(c)) the resulting density perturbation is not significantly strong to sustain annular transport, and thus the electron beam transport is uniform at the target rear-surface (Fig. 7.13(d)).

By contrast, the 2-D resistivity and magnetic field maps (Figs. 7.14(a) and (c) respectively) arising from fast electron transport in the proton heated (i.e. resistivity gradient) target profile are markedly different, and are understood as follows. The injected fast electron beam has the highest current density along the beam axis (i.e. Y = 0), and thus strongest target heating occurs along the axial, longitudinal direction (due to Ohmic heating varying with $\mathbf{j_r}^2$). This, in turn, results in a reduction in the magnitude of the resistivity along the beam axis (see Fig. 7.14(c)). Consequently, the longitudinal resistivity gradient (induced by proton heating) gives rise to regions of higher resistivity, in addition to strong resistivity gradients, located at the edge of the fast electron beam (see the localised channels of high resistivity in Fig. 7.14(c)). Combined, these effects result in the generation of a de-collimating magnetic field (arising from $\nabla \eta \times \mathbf{j}_f$) which acts to expel electrons from the centre of the beam towards the beam edge (where the resistivity is higher). Thus, the higher resistivity regions at the beam edge essentially act as a resistivity 'channel', guiding the fast electrons from the injection region (i.e. X = 0 μm, corresponding to the focal spot position) into a hollowed, annular pattern which propagates into the target. Furthermore, the

corresponding increase in current density at the beam edge results in the generation of a 'pinching' magnetic field (via $\eta\nabla\times\mathbf{j}_f$) around the ring-structure, and thus the annular electron beam is maintained through to the target rear-surface (Fig. 7.13(b)). Moreover, since the de-collimating magnetic field is seeded close to the target front-surface (i.e. from X = 0 - 20 μm), the resulting electron beam divergence will increase due to resistive 'channeling' occurring over a relatively large distance (i.e. from X = 0 - 75 μm − see Fig. 7.14(c)) − this explains the larger beam divergence observed for fast electron transport in 'heated' targets than in 'cold' targets (i.e. Figs. 7.13(b) and (d) respectively).

It is particularly interesting to note that annular fast electron transport induced by resistively generated magnetic fields was predicted by Robinson and Sherlock [184]. The main results reported in that work involved the use of a 'core fibre' of high resistivity, surrounded by a 'cladding' region of lower resistivity material, such that a collimating magnetic field was induced at the resistivity boundary, leading to collimation of fast electron transport. However the authors also briefly consider the inverse case (i.e. a low resistivity core and high resistivity cladding) and find that a portion of the fast electron beam is hollowed. The results presented in this chapter, while realised in a different way (i.e. utilising proton-heating induced lattice-melt, and thus resistivity gradients, rather than embedding layers of different resistivity within the target), clearly demonstrate this numerical prediction.

The interplay of proton-induced longitudinal temperature gradients, lattice melt and resistivity gradients, with target heating and magnetic field generation driven by the fast electrons, is an extremely complex and dynamic process. While this investigation has focussed on the most simple case of fast electron transport in a longitudinal temperature profile, the capability of inducing resistivity gradients in a target by proton-deposition, prior to the arrival and propagation of the fast electron population, may provide an alternative approach to other methods of resistive guiding of fast electrons, such as the use of 'structured collimator' [167, 171, 184] targets, 'magnetic switchyard' schemes [23], or more recent work exploring the concept of elliptical magnetic mirrors [185]. In addition, the work

presented in this chapter reinforces the conclusions of Chapters 5 and 6 − electron transport in solids is significantly influenced by material lattice structure, and the accurate inclusion of the low-temperature resistivity is of key importance to understanding the electron transport properties.

7.6 Conclusions

In this chapter the effect of the initial target temperature, and thus effect of gradients in lattice melt, on the physics of fast electron transport has been investigated. By using TNSA-proton beams to isochorically heat silicon for several tens-of-picoseconds, prior to the propagation fast electrons through the pre-heated target, the influence of resistivity gradients, generated by proton-induced lattice melt, on fast electron transport properties is explored. The experimental observation of an annular proton beam after $t_{heat} = 30$ ps of proton pre-heating, which corresponds to annular electron transport within the target, is in excellent qualitative agreement with 3-D hybrid-PIC simulations of fast electron transport in a target containing an initial temperature (and thus, resistivity) gradient.

Chapter 8

Conclusions and Future Work

8.1 Summary of results

The underlying objective of this PhD project, and therefore this thesis, was to "...obtain a clearer understanding of the fundamental relationship between material properties and fast electron transport". The subsequent investigations have principally evaluated the influence that low-temperature (i.e. 1 - 60 eV) electrical resistivity has on the transport properties of fast electrons in solids. Utilising a programme of experimental investigations and numerical simulations, new insights into the interplay between material properties, resistivity and fast electron transport have been achieved. This final chapter presents the key results of each investigation and discusses the results within the context of fast electron transport research as a whole. Finally, potential directions for future research are given.

8.2 Fast electron transport in carbon

Building upon previous work [39], the investigation presented in Chapter 5 explored fast electron transport in carbon utilising experimental measurements of sheath-accelerated proton beams (at a laser-drive peak intensity of $I_L = 7 \times 10^{19}$ Wcm^{-2}). It was demonstrated that diamond exhibits an unusual proton beam spatial-intensity; centrally located filamentation within a surrounding radially

smooth bream profile. To explain this, an analytical model was developed and applied to understand the origin of this feature, which in turn enables the initial fast electron density distribution at the target rear surface to be inferred. It was found that the measured proton beam spatial-intensity profile for diamond is produced using an annular fast electron density distribution containing regions of density filaments − this suggests the onset of filamentation, in competition with a self-generated magnetic field structure which drives annular electron beam transport within diamond. Moreover, experimental measurements of fast electron transport in vitreous carbon revealed a filamented proton beam spatial-intensity profile, in agreement with previous work [39].

Additionally, the investigation compared experimentally measured sheath-accelerated proton beam spatial-intensity profiles with those generated via analytical modelling, demonstrating a potential method by which to tailor the fast electron transport to produce a desired proton beam spatial-intensity distribution. Potential applications of laser-driven ion sources, such as laser-driven proton oncology [146] and ion-driven FI [35], are likely to benefit from an ability to tune the proton beam spatial-intensity profile, particularly when a homogenous proton beam is required.

Finally, by numerically investigating fast electron transport in two carbon allotropes − diamond and vitreous (amorphous) carbon − at two different peak laser intensities (i.e. $I_L = 5 \times 10^{19}$ Wcm^{-2} and $I_L = 5 \times 10^{20}$ Wcm^{-2}) using 3-D hybrid-PIC simulations, material lattice structure is demonstrated to be significantly influential in defining the fast electron transport properties.

8.3 Fast electron transport in silicon

The work presented in Chapter 6 addresses two main factors which influence the global fast electron transport properties in solid density targets: 1) the importance of the shape of the resistivity-temperature profile; and 2) 'optical' control of the fast electron transport via changing the laser-drive parameters.

In section 1, it was demonstrated that a more accurate treatment of low-

temperature resistivity − using *ab initio* QMD calculations − is key to describing the subsequent fast electron transport properties. Moreover, it was demonstrated that even subtle features in the low-temperature region (i.e. 1 - 10 eV) of the resistivity-temperature profile can profoundly alter the fast electron transport pattern through the key role that resistivity has in producing resistively generated magnetic fields.

In section 2, the annular transport patterns of fast electron beams in silicon were investigated as a function of the laser-drive pulse parameters, using a 3D hybrid-PIC code. The results presented demonstrate that an optimum laser peak intensity range exists for transporting fast electrons within an annular structure (generated in this way). The overall size of the annulus was found to increase with peak intensity (as a consequence of a decrease in the magnitude of the collimating magnetic field which defines the overall beam divergence). Moreover, an optimum laser intensity is found by which enhancement of the annulus-to-axial electron density contrast ratio is achieved, determined by the relative strength of the resistive magnetic field components. Finally, the size of the annular profile is sensitive to the laser focal spot size, which enables some degree of tuning of the annular transport pattern for a fixed beam temperature or drive laser intensity.

The results presented in this chapter provide a new understanding of the origin of annular transport patterns − such patterns have been observed in several previous experimental studies with different target materials [110, 124, 186]. More practically, generation of such annular electron beam profiles may be important for applications. It has been demonstrated [98] that an annular beam structure can enable the propagation of an electron beam of higher current when compared to a uniform beam, as a consequence of the current-limiting Alfvén limit increasing by a factor r/R in the case of an annular beam, where r is the radius of the beam and R is the width of the annulus, thus enabling propagation of a higher electron beam current in a ring structure. For direct application to fast ignition, J. R. Davies [187] showed that the resistive decay of the return current, which can inhibit the propagation of the fast electron beam required for fast ignition, can be compensated for by propagating the electron beam in an annular structure.

Additionally, the results highlight the possibility of producing annular beams of sheath-accelerated protons, driven by annular fast electron beam transport. An important application of annular proton beams was demonstrated by Temporal *et al* [188], in which, for a proton-driven fast ignition scheme [35], an annular proton driver-beam, when used in conjunction with a secondary uniform proton beam, can reduce the total energy required for ignition by almost a factor of two when compared to using a single uniform proton beam.

Finally, the results also highlight the potential to produce and control annular beams of fast electrons for advanced approaches to fast ignition-ICF (in addition to other applications), for example using a silicon-tipped cone to generate a ring-transport profile to seed annular transport patters, and thus potentially reduce the overall energy requirements for fusion gain.

8.4 Fast electron transport in pre-heated silicon

Building upon the insights developed in the previous investigations, the results reported in Chapter 7 explore the role that temperature gradients and lattice melting have on fast electron transport. By using a laser-driven TNSA proton beam to preheat solid-density silicon samples to temperatures above the melt-temperature (i.e. > 0.145 eV), thereby melting the silicon lattice on timescales of tens-of-picoseconds. By varying the temporal separation between proton-heating and the arrival of the fast electron beam (utilising a second laser pulse), the degree of lattice melt, and thus resistivity gradients, at the time at which fast electrons propagate through the target was varied. Experimental measurements of sheath-accelerated protons, used to diagnose the fast electron transport within the target, demonstrated an annular proton beam after $t_{heat} = 30$ ps of proton pre-heating, with filamentation occuring after $t_{heat} = 80$ ps. Utilising 1-D hydrodynamic simulations, the proton-induced spatial-temperature gradient generated in the silicon targets was characterised and incorporated into a 3-D hybrid PIC code, modified to explore the influence of temperature gradients, and therefore lattice melt, on fast electron transport. The simulation results revealed an annular

electron beam, generated by resistive magnetic fields, in excellent qualitative agreement with the experimental results. Previous schemes of using resistivity gradients to influence fast electron transport via magnetic fields typically involve the use of structured targets containing regions of different resistivity [171, 184**?**]. The technique presented in Chapter 7 explores an alternative approach to inducing resistivity gradients, by using proton-induced heating to melt the target lattice, thereby changing there resistivity and thus the magnetic field growth. Perhaps more importantly, the results again emphasise the key role of lattice structure, material effects and low-temperature resistivity in defining fast electron transport properties.

8.5 Future work

The progression of high intensity laser-plasma interactions is closely linked with the development of new laser technology. As lasers become increasingly more powerful, the range of physics that can be explored becomes considerably greater. With large scale facilities such as the Extreme Light Infrastructure (ELI) [189] and proposed Vulcan 20 PW, in addition to new facilities such as APOLLON in France, due to come on-line in the coming years, the future of intense laser-solid interactions is extremely promising. In addition, the ever increasing development of more powerful computational resources will inevitably result in the realisation of more complex simulations, thus increasing the predictive capability of simulations to both interpret results and indicate potential new avenues for exploration. In the more interim future, the work presented in this thesis can be developed in a number of ways.

The investigation of the influence of lattice structure on fast electron transport (i.e. Chapter 5) revealed that the onset of electron beam filmentation is determined by the material resistivity in the low-temperature region of the resistivity-temperature profile, in addition to dependence on the laser-drive intensity. Therefore, a detailed study of the material and laser parameters that define when beam filamentation occurs would provide key information on the criteria which give rise

to the growth or mitigation of filamentation − such results will be important for applications. For example, by using targets consisting of layers of materials with different lattice structure, the depth at which filamentation is seeded may be determined.

In Chapter 3, the main mechanisms which give rise to resistivity were discussed, namely: 1) lattice vibrations (i.e. electron-phonon scattering); 2) lattice dislocations (i.e. lattice vacancies); and 3) impurities. Thus, exploration of fast electron transport in silicon is particularly interesting since, given that silicon is a semiconductor, doping of silicon (or other semiconductors) may enable the generation of tailored resistivity-temperature profiles for desired fast electron transport properties. Therefore, a detailed study of fast electron transport in semiconductors, both pure and doped, combined with variation of the laser-drive parameters, may demonstrate controlled temporal and spatial evolution of the resistivity for a specific fast electron beam application.

Moreover, a numerical development of this work would involve performing full-scale fast ignition simulations. Utilising a hybrid-PIC code such as ZEPHYROS [23, 167] will enable some of these proposed ideas to be tested numerically; for example embedding diamond and silicon within the gold cone-tips in a cone-guided fast ignition simulation, thus exploring the propagation of smooth or annular fast electron beams in compressed DT fuel.

Finally, the results presented in Chapter 7 represent the first investigation of fast electron transport in a solid pre-heated by sheath-accelerated proton beams. Despite the key result of annular electron transport (evidenced by an annular proton beam spatial-intensity profile), which was supported and explained using 3-D hybrid-PIC simulations, the investigation nevertheless represents a 'proof-of-principle' study. The physics of proton-heated solids is a field in it's own right, but when investigated in combination with fast electron propagation our understanding of both fast electron transport and states of warm dense matter will inevitably advance. Looking forward, a relatively simple development would be to explore the influence of asymmetrical temperature (and thus resistivity) gradients on fast electron transport, both experimentally and numerically − this

may reveal ways in which to manipulate the fast electron transport such that the sheath-accelerated proton beam can be tailored for a given application. A more fundamental development would be to explore the proton-induced lattice melt in more detail by utilising X-ray measurements [190] − this will provide a measurement of the target temperature for benchmarking with simulations, in addition to information on the proton heating-induced structural modification of the target lattice.

In the coming years, the combination of higher power lasers and increased numerical simulation capability should result in remarkable breakthroughs in our understanding of energy transport in dense plasma and solids, and in the realisation of applications, particularly work related to ICF. Furthermore, it is my opinion that the results presented in this thesis are only the beginning of a clearer and more fundamental knowledge of the role that material properties have on fast electron transport − I sincerely look forward to what is ahead.

Bibliography

[1] T. H. Maiman. Stimulated radiation in ruby. *Nature*, **187**: 4736, (1960).

[2] J. P. Gordon *et al.* The maser — new type of microwave amplifier, frequency standard, and spectrometer. *Phys. Rev.*, **99**: 1264, (1955).

[3] Canberra Times, Saturday April 11$^{\text{th}}$, (1964).

[4] D. S. Jin *et al.* Collective excitations of a bose-einstein condensate in a dilute gas. *Phys. Rev. Lett.*, **77**: 420, (1996).

[5] F. J. McClung and R. W. Hellwarth. Giant optical pulsations from ruby. *Journal of App. Phys.*, **33**: 828, (1962).

[6] L. E. Hargrove *et al.* Locking of he-ne laser modes induced by synchronous intracavity modulation. *Appl. Phys. Lett.*, **5**: 4, (1964).

[7] C. Kapetanakos. Filamentation of intense relativistic electron beams propagating in dense plasmas. *Appl. Phys. Lett.*, **25**: 484, (1974).

[8] R. Decoste and B. H. Ripin. High-energy ion expansion in laser-plasma interactions. *Phys. Rev. Lett*, **40**: 34, (1978).

[9] C. Joshi *et al.* Quantitative measurements of fast ions from co_2 laser produced plasmas. *Appl. Phys. Lett.*, **34**: 625, (1979).

[10] D. Strickland and G. Mourou. Compression of amplified chirped optical pulses. *Opt. Commun.*, **56**: 219, (1985).

[11] R.E. Kidder. Application of lasers to the production of high-temperature and high-pressure plasma. *Nucl. Fusion*, **8**: 3, (1968).

[12] J. Nuckolls *et al.* Laser compression of matter to super-high densities: Thermonuclear applications. *Nature*, **239**: 139, (1972).

[13] J. Nuckolls. Early steps toward inertial fusion energy (ife) (1952 to 1962). *LLNL Report*, UCRL-ID-131075, (1998).

[14] J. Lindl. Development of the indirectdrive approach to inertial confinement fusion and the target physics basis for ignition and gain. *Phys. Plasmas*, **2**: 3933, (1995).

[15] J. Meyer ter Vehn. On energy gain of fusion targets: the model of kidder and bodner improved. *Nucl. Fusion*, **22**: 561, (1982).

[16] J. D. Kilkenny *et al.* A review of the ablative stabilization of the rayleigh-taylor instability in regimes relevant to inertial confinement fusion. *Phys. Plasmas*, **1**: 1379, (1994).

[17] M. Tabak *et al.* Ignition and high gain with ultra powerful lasers. *Phys. Plasmas*, **1**: 1626, (1994).

[18] S. Atzeni *et al.* Targets for direct-drive fast ignition at total laser energy of 200 400 kj. *Phys. Plasmas*, **14**: 052702, (2007).

[19] K. A. Tanaka *et al.* Studies of ultra-intense laser plasma interactions for fast ignition. *Phys. Plasmas*, **7**: 2014, (2000).

[20] P. A. Norreys *et al.* Experimental studies of the advanced fast ignitor scheme. *Phys. Plasmas*, **7**: 3721, (2000).

[21] R. Kodama *et al.* Nuclear fusion: Fast heating scalable to laser fusion ignition. *Nature*, **418**: 933, (2002).

[22] S. Atzeni. Inertial fusion fast ignitor: Igniting pulse parameter window vs the penetration depth of the heating particles and the density of the precompressed fuel. *Phys. Plasmas*, **6**: 3316, (1999).

[23] A. P. L. Robinson *et al.* Focusing of relativistic electrons in dense plasma using a resistivity-gradient-generated magnetic switchyard. *Phys. Rev. Lett*, **108**: 125004, (2012).

[24] G.D. Tsakiris *et al.* Laser induced electron acceleration in the presence of static electric and magnetic fields in a plasma. *Phys. Rev. Lett*, **46**: 1202, (1981).

[25] F. Begay and D.W. Forslund. Acceleration of multi-species ions in CO_2 laser-produced plasmas: Experiments and theory. *Phys. Fluids*, **25**: 1675, (1982).

[26] A. P. Fews *et al.* Plasma ion emission from high intensity picosecond laser pulse interactions with solid targets. *Phys. Rev. Lett*, **73**: 1801, (1994).

[27] F. Beg *et al.* A study of picosecond laser-solid interactions up to 10^{19} W/cm^2. *Phys. Plasmas*, **4**: 447, (1997).

[28] E. L. Clark *et al.* Measurements of energetic protons transport through magnetized plasma form intense laser interaction with solids. *Phys. Rev. Lett.*, **84**: 670, (2000).

[29] R. A. Snavely *et al.* Intense high energy proton beams from petawatt laser irradiation of solids. *Phys. Rev. Lett.*, **85**: 2945, (2000).

[30] A. Maksimchuk *et al.* Forward ion acceleration in thin films driven by a high-intensity laser. *Phys. Rev. Lett.*, **84**: 18, (2000).

[31] S. C. Wilks *et al.* Energetic proton generation in ultra-intense laser solid interaction. *Phys. Plasmas*, **8**: 2, (2001).

[32] L. Robson *et al.* Scaling of proton acceleration driven by petawatt laser plasma interactions. *Nature Physics*, **3**: 58, 2007.

[33] T. E. Cowan *et al.* Ultra-low emittance, multi-MeV proton beams from a laser virtual-cathode plasma accelerator. *Phys. Rev. Lett.*, **92**: 20, (2004).

[34] M. Borghesi *et al.* Fast ion generation by high intensity laser irradiation of solid targets and applications. *Fusion Sci. Technol.*, **49**: 412, (2006).

[35] M. Roth *et al.* Fast ignition by intense laser accelerated proton beams. *Phys. Rev. Lett.*, **86**: 436, 2001.

[36] R. A. Snavely *et al.* Laser generated proton beam focusing and high temperature isochoric heating of solid matter. *Phys. Plasmas*, **14**: 092703, (2007).

[37] J. Fuchs *et al.* Spatial uniformity of laser-accelerated ultrahigh-current MeV electron propagation in metals and insulators. *Phys. Rev. Lett.*, **91**: 255002, (2003).

[38] Y. Sentoku *et al.* Dynamic control over mega-ampere electron currents in metals using ionization-driven resistive magnetic fields. *Phys. Rev. Lett.*, **107**: 135005, (2011).

[39] P. McKenna *et al.* Effect of lattice structure on energetic electron transport in solids irradiated by ultraintense laser pulses. *Phys. Rev. Lett.*, **106**: 185004, (2011).

[40] S. Mazevet *et al.* Ab-initio simulations of the optical properties of warm dense gold. *Phys. Rev. Lett.*, **95**: 085002, (2005).

[41] L. V. Keldysh. Ionization in the field of a strong electromagnetic wave. *Soviet Physics JETP*, **20**: 1307, (1965).

[42] H. R. Reiss. Unsuitability of the keldysh parameter for laser fields. *Phys. Rev. A.*, **82**: 023418, (2010).

[43] M. V. Ammosov *et al.* Tunnel ionization of complex atoms and of atomic ions in an alternating electromagnetic field. *Soviet Physics JETP*, **64**: 1191, (1986).

[44] M. Hegelich *et al.* MeV ion jets from short-pulse-laser interaction with thin foils. *Phys. Rev. Lett.*, **89**: 085002, (2002).

[45] P. Gibbon. *Short pulse laser interaction with matter, an introduction.* Imperial College Press, 2005.

[46] J. D. Dawson. Lasers and accelerators. *IEEE Transaction on Nuclear Science*, **26**: 4217, (1979).

[47] S. Eliezer. *The interaction of high-power lasers with plasmas.* Institute of Physics Publishing, (2002).

[48] F. Pegoraro *et al.* Photon bubbles and ion acceleration in a plasma dominated by the radiation pressure of an electromagnetic pulse. *Phys. Rev. Lett.*, **99**: 065002, (2007).

[49] S. V. Bulanov *et al.* Interaction of an ultrashort, relativistically strong laser pulse with an overdense plasma. *Phys. Plasmas*, **1**: 745, (1994).

[50] A. Henig *et al.* Enhanced laser-driven ion acceleration in the relativistic transparency regime. *Phys. Rev. Lett.*, **103**: 1–4, (2009).

[51] J. J. MacFarlane *et al.* HELIOS-CR — a 1-D radiation-magnetohydrodynamics code with inline atomic kinetics modeling. *Journal of Quantitative Spectroscopy and Radiative Transfer*, **99**: 381, (2006).

[52] W. Kruer. *The Physics Of Laser Plasma Interactions.* Frontiers in Physics, Westview Press, (2003).

[53] D. D. Meyerhofer *et al.* Resonance absorption in high-intensity contrast, picosecond laser-plasma interactions. *Phys. Fluids*, B **5**: 2584, (1993).

[54] A. Kemp *et al.* Hot-electron energy coupling in ultraintense laser-matter interaction. *Phys. Rev. Lett.*, **101**: 075004, (2008).

[55] F. Brunel. Not-so-resonant, resonant absorption. *Phys. Rev. Lett.*, **59**: 52, (1987).

[56] W. L. Kruer and K. Estabrook. JxB heating by very intense laser light. *Phys. Fluids*, **28**: 430, (1985).

[57] M. Santala *et al.* Effect of the plasma density scale length on the direction of fast electrons in relativistic laser-solid interactions. *Phys. Rev. Lett.*, **84**: 1459, (2000).

[58] M. N. Quinn *et al.* Refluxing of fast electrons in solid targets irradiated by intense, picosecond laser pulses. *Plasma Phys. Control. Fusion*, **53**: 025007, (2011).

[59] Y. Ping *et al.* Absorption of short laser pulses on solid targets in the ultra relativistic regime. *Phys. Rev. Lett.*, **100**: 085004, (2008).

[60] M. H. Key *et al.* Hot electron production and heating by hot electrons in fast igniter research. *Phys. Plasmas*, **5**: 1966, (1998).

[61] K. B. Wharton *et al.* Experimental measurements of hot electrons generated by ultraintense laser-plasma interactions on solid-density targets. *Phys. Rev. Lett.*, **81**: 822, (1998).

[62] J. Myatt *et al.* High-intensity laser interactions with mass-limited solid targets and implications for fast-ignition experiments on OMEGA EP. *Phys. Plasmas*, **14**: 056301, (2007).

[63] P. M. Nilson *et al.* Bulk heating of solid-density plasmas during high-intensity-laser plasma interactions. *Phys. Rev. E.*, **79**: 016406, (2009).

[64] J. R. Davies. Laser absorption by overdense plasmas in the relativistic regime. *Plasma Phys. Control. Fusion*, **51**: 014006, (2009).

[65] S. C. Wilks *et al.* Absorption of ultrashort, ultra-intense laser light by solids and overdense plasmas. *IEEE Journal of Quantum Electronics*, **33**: 1954–68, (1997).

[66] B. Bezzerides *et al.* Randomness, maxwellian distributions, and resonance absorption. *Phys. Rev. Lett.*, **44**: 651, (1980).

[67] P. Gibbon. Efficient production of fast electrons from femtosecond laser interaction with solid targets. *Phys. Rev. Lett.*, **73**: 664, (1994).

[68] L. M. Chen *et al.* Hot electron generation via vacuum heating process in femtosecond laser-solid interactions. *Phys. Plasmas*, **8**: 2925, (2001).

[69] F. Jüttner *et al.* Das maxwellsche gesetz der geschwindigkeitsverteilung in der relativtheorie. *Annalen der Physik*, **339**: 856, (1911).

[70] D. Forslund *et al.* Theory of hot-electron spectra at high laser intensity. *Phys. Rev. Lett.*, **39**: 284, (1977).

[71] P. Gibbon and A. R. Bell. Collisionless absorption in sharp-edged plasmas. *Phys. Rev. Lett.*, **68**: 1535, (1992).

[72] S. C. Wilks *et al.* Absorption of ultra intense laser pulses. *Phys. Rev. Lett.*, **69**: 9, (1992).

[73] M. Haines *et al.* Hot-electron temperature and laser-light absorption in fast ignition. *Phys. Rev. Lett.*, **102**: 045008, (2009).

[74] C. D. Chen *et al.* Bremsstrahlung and K_α fluorescence measurements for inferring conversion efficiencies into fast ignition relevant hot electrons. *Phys. Plasmas*, **16**: 082705, (2009).

[75] P. Drude. Zur elektronentheorie der metalle. *Annalen der Physik*, **306**: 566, (1900).

[76] R. O. Simmons and R. W. Balluffi. Measurements of the high-temperature electrical resistance of aluminum: Resistivity of lattice vacancies. *Phys. Rev.*, **117**: 62, (1960).

[77] C. Kittel. *Introduction to Solid State Physics*. Wiley, New York, (1996).

[78] N. W. Ashcroft and N. D. Mermin. *Solid State Physics*. Saunders College, (1976).

[79] Y. T. Lee and R. M. More. An electron conductivity model for dense plasmas. *Phys. Fluids*, **27**: 1273, (1984).

[80] L. Spitzer and R. Härm. Transport phenomena in a completely ionized gas. *Phys. Rev.*, **89**: 5, (1953).

[81] R. W. Lee *et al.* Finite temperature dense matter studies on next-generation light sources. *J. Opt. Soc. Am.*, **20**: 1, (2003).

[82] J. M. Ziman. A theory of the electrical properties of liquid metals. *Philos. Mag.*, **6**: 1013, (1961).

[83] G. A. Rinker. Electrical conductivity of a strongly coupled plasma. *Phys. Rev. B.*, **31**: 4207, (1985).

[84] R. Cauble and W. Rozmus. Two-temperature frequency-dependent electrical resistivity in solid density plasmas produced by ultrashort laser pulses. *Phys. Rev. E.*, **52**: 2974, (1995).

[85] M. P. Desjarlais *et al.* Electrical conductivity for warm, dense aluminium plasmas and liquids. *Phys. Rev. E.*, **66**: 025401, (2002).

[86] R. Latter. Temperature behavior of the thomas-fermi statistical model for atoms. *Phys. Lett.*, **99**: 1854, (1955).

[87] F. J. Rogers *et al.* Phase shift contributions to the partition function of a system of interacting particles. *Phys. Lett.*, **34**: 127, (1971).

[88] P. H. Lee. *PhD dissertation.* University of Pittsburgh, (1977).

[89] A. P. L. Robinson. *PyPhys Routines.* Central Laser Facility, (2012).

[90] H. Milchberg *et al.* Resistivity of a simple metal from room temperature to 10^6 k. *Phys. Rev. Lett.*, **61**: 2364, (1988).

[91] G. Kresse and J. Hafner. *Ab initio* molecular dynamics for liquid metals. *Phys. Rev. B.*, **47**: 558, (1965).

[92] G. Kresse and J. Furthmüller. Efficiency of *ab initio* total energy calculations for metals and semiconductors using a plane-wave basis set. *Comput. Mat. Sci.*, **6**: 15, (1996).

[93] N. D. Mermin. Thermal properties of the inhomogeneous electron gas. *Phys. Rev.*, **137**: 1441, (1965).

[94] D. Vanderbilt. Soft self-consistent pseudopotentials in a generalized eigenvalue formalism. *Phys. Rev. B.*, **41**: 7892, (1990).

[95] R. Kubo. Statistical-mechanical theory of irreversible processes. i. general theory and simple applications to magnetic and conduction problems. *J. Phys. Soc. Jpn.*, **12**: 570, (1957).

[96] H. J. Monkhorst and J. D. Pack. Special points for brillouin-zone integrations. *Phys. Rev. B.*, **13**: 5188, (1976).

[97] A. R. Bell *et al.* Fast electron transport in high intensity short pulse laser solid experiments. *Plasma Phys. Control. Fusion*, **39**: 653, (1997).

[98] H. Alfvèn. On the motion of cosmic rays in interstellar space. *Plys. Rev.*, **55**: 425, (1939).

[99] A. R. Bell *et al.* Fast electron transport in laser-produced plasmas and the kalos code for solution of the vlasov-fokker-planck equation. *Plasma Phys. Control. Fusion*, **48**: R37, (2006).

[100] M. Honda *et al.* Collective stopping and ion heating in relativistic-electron-beam transport for fast ignition. *Phys. Rev. Lett.*, **85**: 2128, (2000).

[101] Y. Sentoku *et al.* Three-dimensional particle-in-cell simulations of energetic electron generation and transport with relativistic laser pulses in overdense plasmas. *Phys. Rev. E.*, **65**: 046408, (2002).

[102] M. Berger *et al.* Stopping-power and range tables for electrons, protons, and helium ions. *http://physics.nist.gov*, (2010).

[103] H. Bethe. Zur theorie des durchgangs schneller korpuskularstrahlen durch materie. *Annalen der Physik*, **397**: 325, (1930).

[104] H. Bethe. Bremsformel für elektronen relativistischer geschwindigkeit. *Z. Phys.*, **76**: 293, (1932).

[105] S. Seltzer and M. Berger. Bremsstrahlung spectra from electron interactions with screened atomic nuclei and orbital electrons. *Nuc. Inst. Meth. Phys. Res. Sec. B: Beam Interactions with Materials and Atoms*, **12**: 95, (1985).

[106] J. R. Davies *et al.* Short-pulse high-intensity laser-generated fast electron transport into thick solid targets. *Phys. Rev. E.*, **56**: 7193, (1997).

[107] A. R. Bell and R. J. Kingham. Resistive collimation of electron beams in laser-produced plasmas. *Phys. Rev. Lett.*, **91**: 035003, (2003).

[108] J. R. Davies. Electric and magnetic field generation and target heating by laser-generated fast electrons. *Phys. Rev. E.*, **68**: 056404, (2003).

[109] J. R. Davies *et al.* Electron beam hollowing in laser-solid interactions. *Plasma Phys. Control. Fusion*, **48**: 1181, (2006).

[110] P. A. Norreys *et al.* Observation of annular electron beam transport in multi-terawatt laser-solid interactions. *Plasma Phys. Control. Fusion*, **48**: L11, (2006).

[111] E. Weibel. Spontaneously growing transverse waves in a plasma due to an anisotropic velocity distribution. *Phys. Rev. Lett.*, **2**: 83, (1959).

[112] R. Jung *et al.* Study of electron-beam propagation through preionized dense foam plasmas. *Phys. Rev. Lett.*, **94**: 195001, (2005).

[113] L. Gremillet *et al.* Filamented transport of laser- generated relativistic electrons penetrating a solid target. *Phys. Plasmas*, **9**: 941, (2002).

[114] A. P. L. Robinson *et al.* Effect of transverse density modulations on fast electron transport in dense plasmas. *Plasma Phys. Control. Fusion*, **50**: 065019, (2008).

[115] A. Dubietis *et al.* Powerful femtosecond pulse generation by chirped and stretched pulse parametetric amplification in bbo crystal. *Opt. Comms.*, **80**: 437, (1992).

[116] J. Collier *et al.* Evaluation of an ultrabroadband high-gain amplification technique for chirped pulse amplification facilities. *Applied Optics*, **38**: 7486, (1999).

[117] D. J. Maas *et al.* High precision optical characterization of semiconductor saturable absorber mirrors. *Optics Express*, **16**: 7571, (2008).

[118] D. E. Spence *et al.* Regeneratively initiated self-mode-locked ti:sapphire laser. *Optics Letters*, **16**: 1762, (1991).

[119] I. O. Musgrave *et al.* High precision optical characterization of semiconductor saturable absorber mirrors. *Central Laser Facility Annual Report*, 2009-2010: 152, (2009).

[120] J. S. Green *et al.* Effect of laser intensity on fast-electron-beam divergence in solid-density plasmas. *Phys. Rev. Lett.*, **100**: 015003, (2008).

[121] R. B. Stephans *et al.* K_α fluorescence measurement of relativistic electron transport in the context of fast ignition. *Phys. Rev. E.*, **69**: 066414, (2004).

[122] K. L. Lancaster *et al.* Measurements of energy transport patterns in solid density laser plasma interactions at intensities of 5×10^{20} Wcm^{-2}. *Phys. Rev. Lett.*, **98**: 125002, (2007).

[123] X. H. Yuan *et al.* Spatially resolved x-ray spectroscopy using a flat hopg crystal. *Nuc. Inst. and Meth.*, **653**: 145, (2011).

[124] M. Storm *et al.* High-current, relativistic electron- beam transport in metals and the role of magnetic collimation. *Phys. Rev. Lett.*, **102**: 23500, (2009).

[125] M. Borghesi *et al.* Observations of collimated ionization channels in aluminum-coated glass targets irradiated by ultraintense laser pulses. *Phys. Rev. Lett.*, **83**: 4309, (1999).

[126] M. Tatarakis *et al.* Plasma formation on the front and rear of plastic targets due to high-intensity laser-generated fast electrons. *Phys. Rev. Lett.*, **81**: 999, (1998).

[127] L. Gremillet *et al.* Time-resolved observation of ultrahigh intensity laser-produced electron jets propagating through transparent solid targets. *Phys. Rev. Lett.*, **83**: 5015, (1999).

[128] J. S. Green *et al.* Single shot, temporally and spatially resolved measurements of fast electron dynamics using a chirped optical probe. *Journal of Instrumentation*, **9**: P03003, (2014).

[129] V. L. Ginzburg. *Transition Radiation and Transition Scattering. The Adam Hilger Series on Plasma Physics.* Hilgor, Bristol, (1990).

[130] V. L. Ginzburg. Radiation by uniformly moving sources (vavilov-cherenkov effect, transition radiation, and other phenomena). *Phys.-Usp*, **39**: 973, (1996).

[131] J. Zheng *et al.* Theoretical study of transition radiation from hot electrons generation in the laser-solid interactions. *Phys. Plasmas*, **10**: 2994, (2003).

[132] J. J. Santos *et al.* Fast electron transport in ultra-intense laser pulse interaction with solid targets by rear-side radiation diagnostics. *Phys. Rev. Lett.*, **89**: 025001, (2002).

[133] M. N. Quinn *et al.* On the investigation of fast electron beam filamentation in laser-irradiated solid targets using multi-mev proton emission. *Plasma Phys. Control. Fusion*, **53**: 124012, (2011).

[134] P. Mora and T. Grismayer. Rarefaction acceleration and kinetic effects in thin-foil expansion into a vacuum. *Phys. Rev. Lett*, **102**: 145001, (2009).

[135] P. Gibbon. Resistively enhanced proton acceleration via high-intensity laser interactions with cold foil targets. *Phys. Rev. E.*, **72**: 026411, (2005).

[136] X. H. Yuan *et al.* Effect of self-generated magnetic fields on fast-electron beam divergence in solid targets. *New J. Phys.*, **12**: 063018, (2010).

[137] M. Coury *et al.* Injection and transport properties of fast electrons in ultraintense laser-solid interactions. *Phys. Plasmas*, **62**: 712, (2013).

[138] P. Mora. Plasma expansion into a vacuum. *Phys. Rev. Lett.*, **90**: 185002, (2003).

[139] P. Mora *et al.* Thin foil expansion into vacuum. *Phys. Rev. E*, **72**: 056401, (2005).

[140] M. Passoni *et al.* Theory of light-ion acceleration driven by a strong charge separation. *Phys. Rev. Lett.*, **101**: 115001, (2008).

[141] J. Schreiber *et al.* Analytical model for ion acceleration by high-intensity laser pulses. *Phys. Rev. Lett.*, **97**: 045005, (2006).

[142] J. E. Crow *et al.* The expansion of a plasma in vacuum. *Journal of Plasma Physics*, **14**: 65, (1975).

[143] J. Denavit. Collisionless plasma expansion in vacuum. *Phys. Fluids*, **22**: 1384, (1979).

[144] J. Fuchs *et al.* Laser-driven proton scaling laws and new paths towards energy increase. *Nat. Phys.*, **2**: 48, (2006).

[145] M. Passoni *et al.* Charge separation effects in solid targets and ion acceleration with a two-temperature electron distribution. *Phys. Rev. E*, **69**: 0264011, (2004).

[146] V. Malka *et al.* Practicability of proton therapy using compact laser systems. *Medical Physics*, **31**: 1587, (2004).

[147] P. K. Patel *et al.* Isochoric heating of solid density matter with ultrafast proton beam. *Phys. Rev. Lett.*, **91**: 125004, (2003).

[148] C. M. Brenner *et al.* High energy conversion efficiency in laser-proton acceleration by controlling laser-energy deposition onto thin foil targets. *App. Phys. Lett.*, **104**: 1123, (2014).

[149] M. Schollmeier *et al.* Laser beam-profile impression and target thickness impact on laser-accelerated protons. *Phys. Plasmas*, **15**: 053101, (2008).

[150] M. Roth *et al.* Laser accelerated ions and electron transport in ultra intense laser matter interaction. *Laser Part. Beams*, **23**: 95, (2005).

[151] M. Borghesi *et al.* Multi-MeV proton source investigations in ultra intense laser foil interaction. *Phys. Rev. Lett.*, **92**: 055003, (2004).

[152] F. Nürnberg *et al.* Radiochromic film imaging spectroscopy of laser-accelerated proton beams. *Rev. Sci. Inst.*, **80**: 033301, (2009).

[153] R. J. Clarke *et al.* Nuclear activation as a high dynamic range diagnostic of laser-plasma interactions. *Nucl. Inst. Meth. Phys.*, **585**: 117, (2008).

[154] P. McKenna *et al.* Characterization of proton and heavier ion acceleration in ultrahigh-intensity laser solid interactions with heated target foils. *Phys. Rev. E.*, **70**: 036405, (2004).

[155] GAFCHROMIC®. http://online1.ispcorp.com/_layouts/Gafchromic/index.html.

[156] http://www.srim.org.

[157] S. Gaillard *et al.* Comment on "measurements of energetic proton transport through magnetized plasma from intense laser interactions with solids". *Phys. Rev. Lett.*, **96**, (2006).

[158] E. Clark *et al.* Clark *et al.* reply. *Phys. Rev. Lett.*, **96**: 249202, (2006).

[159] S. P. Lyon and J. D. Johnson. SESAME: The Los Alamos National Laboratory Equation of State database. *LANL Report No. LA-UR- 92-3407*, (1992).

[160] R. M. More. Dopant a new quotidian equation of state (QEOS) for hot dense matter. *Phys Plasmas*, **31**: 3059–3078, (1988).

[161] C. K. Birdsall and A. B. Langdon. *Plasma physics via computer simulation.* Taylor and Francis, New York, (1991).

[162] S. P. D. Mangles *et al.* Monoenergetic beams of relativistic electrons from intense laser plasma interactions. *Nature*, **431**: 535, 2004.

[163] S. V. Bulanov *et al.* Interaction of electromagnetic waves with plasma in the radiation dominated regime. *Plasma Phys. Reports*, **30**: 196–213, 2004.

[164] D. R. Welch *et al.* Simulations of intense heavy ion beams propagating through a gaseous fusion target chamber. *Phys. Plasmas*, **9**: 2344, (2002).

[165] A. G. R. Thomas *et al.* A review of Vlasov-Fokker-Planck numerical modeling of inertial confinement fusion plasma. *J. Comput. Phys.*, **231**: 1051, (2012).

[166] J. Honrubia and J. Meyer ter Vehn. Three-dimensional fast electron transport for ignition-scale inertial fusion capsules. *Nucl. Fusion*, **46**: L25–L28, (2006).

[167] S. Kar *et al.* Guiding of relativistic electron beams in solid targets by resistively controlled magnetic fields. *Phys. Rev. Lett.*, **102**: 055001, (2009).

[168] E. Brambrink *et al.* Modeling of the electrostatic sheath shape on the rear target surface in short-pulse laser-driven proton acceleration. *Laser and Particle Beams*, **24**: 061301, (2006).

[169] P. McKenna *et al.* Lateral electron transport in high-intensity laser irradiated foils diagnosed by ion emission. *Phys. Rev. Lett*, **98**: 145001, (2007).

[170] P. Antici. *Laser-acceleration of high-energy short proton beams and applications, PhD thesis.* Ecole Polytechnique, (2007).

[171] B. Ramakrishna *et al.* Laser-driven fast electron collimation in targets with resistivity boundary. *Phys. Rev. Lett.*, **105**: 135001, (2010).

[172] R. R. Scott *et al.* Controlling fast-electron-beam divergence using two laser pulses. *Phys. Rev. Lett.*, **109**: 015001, (2012).

[173] S. Atzeni and J. Meyer ter Vehn. *The physics of inertial fusion: beam plasma interaction, hydrodynamics, hot dense matter*. Oxford University Press, Oxford, (2004).

[174] Y. Sentoku *et al.* High energy proton acceleration in interaction of short laser pulse with dense plasma target. *Phys. Plasmas*, **10**: 2009, (2003).

[175] P. Audebert *et al.* Heating of thin foils with a relativistic-intensity short-pulse laser. *Phys. Rev. Lett.*, **89**: 265001, (2002).

[176] T. S. Perry *et al.* Absorption experiments on x-ray-heated mid-z constrained samples. *Phys. Rev. E.*, **54**: 5617, (1996).

[177] J. J. MacFarlane *et al.* X-ray absorption spectroscopy measurements of thin foil heating by Z-pinch radiation. *Phys. Rev. E.*, **66**: 046416, (2002).

[178] S. M. Vinko *et al.* Creation and diagnosis of a solid-density plasma with an x-ray free-electron laser. *Nature*, **482**: 59, (2012).

[179] A. Mancic *et al.* Isochoric heating of solids by laser-accelerated protons: Experimental characterization and self-consistent hydrodynamic modeling. *High Energy Density Physics*, **6**: 21, (2010).

[180] A. Pelka *et al.* Ultrafast melting of carbon induced by intense proton beams. *Phys. Rev. Lett.*, **105**: 265701, (2010).

[181] J.P. Colombier *et al.* Hydrodynamic simulations of metal ablation by femtosecond laser irradiation. *Phys. Rev. B.*, **71**: 165406, (2005).

[182] A. V. Bushman *et al.* Equations of state for metals at high energy density. *Inst. Chem. Phys.*, (1992).

[183] R. Ramis *et al.* MULTI-fs – a computer code for laser-plasma interaction in the femtosecond regime. *Comp. Phys. Comm.*, **183**: 637, (2012).

[184] A. P. L. Robinson and M. Sherlock. Magnetic collimation of fast electrons produced by ultraintense laser irradiation by structuring the target composition. *Phys. Plasmas*, **14**: 083105, (2007).

[185] A. P. L. Robinson *et al.* Elliptical magnetic mirror generated via resistivity gradients for fast ignition inertial confinement fusion. *Phys. Plasmas*, **20**: 062704, (2013).

[186] J. A. Koch *et al.* Experimental measurements of deep directional columnar heating by laser-generated relativistic electrons at near-solid density. *Phys. Rev. E* ., **65**: 016410, (2001).

[187] J. R. Davies. Alfvén limit in fast ignition. *Phys. Rev. E.*, **69**: 065402, (2004).

[188] M. Temporal *et al.* Experimental measurements of deep directional columnar heating by laser-generated relativistic electrons at near-solid density. *Phys. Plasmas*, **15**: 052702, (2008).

[189] H. Backe *et al.* Proposal for a European Extreme Light Infrastructure (ELI). *http://www.extreme-light-infrastructure.eu/pictures/ELI-scientific-case-id17.pdf.*

[190] A. Mancic *et al.* Picosecond short-range disordering in isochorically heated aluminum at solid density. *Phys. Rev. Lett.*, **104**: 035002, 2010.